Sur de nouveaux composes hydroxyfluores nanostructures à base d'aluminium : synthèses, structures & propriétés acides (Lewis/Bronsted)

Damien Dambournet

THESE

Présentée à

L'UNIVERSITE BORDEAUX I

ECOLE DOCTORALE DES SCIENCES CHIMIQUES

par

Damien DAMBOURNET

POUR OBTENIR LE GRADE DE

DOCTEUR

Spécialité : **PHYSICO-CHIMIE DE LA MATIERE CONDENSEE**

****

SUR DE NOUVEAUX COMPOSES HYDROXYFLUORES NANOSTRUCTURES A BASE D'ALUMINIUM : SYNTHESES, STRUCTURES & PROPRIETES ACIDES (LEWIS/BRONSTED)

****

M. WINFIELD John. M., Professeur, Université de Glagow, UK	*Rapporteur*
M. LEBLANC Marc, Professeur, Université du Maine, Le Mans	*Rapporteur*

Devant la commission d'examen formée de :

M. DELMAS Claude, Directeur de Recherche, ICMCB, Pessac	*Président*
M. SECHERESSE Francis, Professeur, Université de Versailles, Versailles	*Examinateur*
M. TRESSAUD Alain, Directeur de recherche, ICMCB, Pessac	*Co-directeur de thèse*
M. GRAVEREAU Pierre, Professeur, ICMCB, Pessac	*Examinateur*
Mme. BRUNET Sylvette, Chargé de recherche, Faculté des sciences, Poitiers (Invité)	*Invité*
M. DEMOURGUES Alain, Chargé de recherche, ICMCB, Pessac (Invité)	*Co-directeur de thèse*
M. KEMNITZ Erhard, Professeur, Humboldt Université, Berlin, Allemagne (Invité)	*Invité*
M. LAVALLEY Jean-Claude, Professeur émérite, LCS, Caen (Invité)	Invité

REMERCIEMENTS

Ce travail de thèse a été réalisé à l'Institut de Chimie de la Matière Condensée de Bordeaux, ICMCB. J'aimerais exprimer ma reconnaissance à Monsieur Claude Delmas, Directeur de l'Institut, pour son accueil et pour l'honneur qu'il m'a fait en acceptant de présider mon jury de thèse.

Mes sincères remerciements s'adressent aux membres du jury pour l'intérêt qu'ils ont porté à ce travail. Je remercie tout particulièrement Messieurs John. W. Winfield et Marc Leblanc, qui ont accepté d'être les rapporteurs de cette thèse. Je remercie également le Professeur Francis Sécheresse qui, malgré son emploi du temps, a accepté de juger le travail de son ancien étudiant. Je tiens à remercier vivement le Professeur Pierre Gravereau pour ses conseils ainsi que les corrections apportées à ce manuscrit. Je remercie Sylvette Brunet pour avoir accepté de participer à ce jury. Je remercie le Professeur Erhard Kemnitz, coordinateur du réseau FUNFLUOS, pour avoir évalué ce travail et aussi permis le très bon déroulement de ce programme. Enfin, à Messieurs Alain Tressaud et Alain Demourgues qui ont assuré la direction de ces recherches, je tiens à exprimer ma profonde gratitude et mon estime la plus sincère.

Un immense merci à Alain Tressaud qui m'a fait confiance et qui m'a permis de m'épanouir durant cette thèse. Je le remercie pour sa vision du monde scientifique, pour m'avoir inculqué l'envie de communiquer mes travaux. Je le remercie vivement pour son aide lors de ma recherche d'emploi et pour m'avoir aidé à trouver ma voie.
Un immense merci à Alain Demourgues (ou Demorgues pour les intimes) avec qui j'ai vécu de très bon moments. Je tiens à remercier le grand scientifique qu'il est, avec ses idées et ses coups de génie. Enfin, je voudrais le remercier pour m'avoir fait beaucoup rire pendant ces trois années, qualité inestimable pour un directeur de thèse.
Merci à vous deux.

Je voudrais également remercier l'ensemble des personnes qui ont contribué à cette formidable ambiance de groupe avec comme mot d'ordre « rire et travail ».
Etienne Durand, notre assistant ingénieur, que je remercie pour les expériences de fluoration, le soutien logistique et technique (ce qui n'est pas une mince affaire avec moi). Je le remercie

pour son implication dans le groupe et salue sa capacité à trouver des surnoms (HP, Dambour…). Je ne n'oublierai jamais les congrès passés avec lui où j'ai eu parmi mes plus belles crises de rire.
Merci à ma copine Hélène Perrier pour tout ses joyeux moments et j'espère qu'on se retrouvera très bientôt.
Je remercie tout les occupants du bureau C12 pour m'avoir supporté : Romain qui est complètement barré, Maman qui va beaucoup me manquer, Penini avec qui j'ai eu le plaisir de travailler, Benjamin, Jay-Jay et Mélanie.
Manuel Gaudon, un brillant chercheur qui m'a aussi beaucoup fait rire avec les gaudonneries.
Jérôme Majimel, merci pour les séances de microscopie.

Mes remerciements s'adressent également à Eric Lebraud et Stanislas Pechev pour les mesures de diffraction des rayons X. Un grand merci à Stanislas Peshev et Pierre Gravereau pour m'avoir formé à la diffraction ainsi que pour leur contribution à ces travaux. Merci à Carol et Stéphane Toulin pour leur aide quotidienne. Je remercie Cathel et Denis pour leur présence au labo le week end et pendant les vacances…

Merci à l'équipe du Mans Christophe Legein, Charlotte Martineau, Jean-Yves Buzaré pour les mesures de RMN et leur implication dans ces travaux. Je remercie tout particulièrement Christophe pour sa motivation et sa redoutable efficacité et je me rappellerai longtemps de notre visite de Kyoto.

Merci à Alexandre Vimont, Marco Daturi, Hervé Leclerc et Jean-Claude Lavalley du LCS Caen pour m'avoir initié à cette belle technique qu'est la spectroscopie infrarouge. Je les remercie pour cette collaboration fructueuse. Merci à Jean-Claude Lavalley pour sa venue et son intervention à ma thèse.

Je voudrais remercier l'ensemble de nos partenaires du réseau européen FUNFLUOS pour toutes ces discussions et collaborations sans qui ce travail n'aurait pu aboutir.

Je tiens également à remercier tous ceux qui m'ont soutenu lors de ma candidature à Argonne : Alain Tressaud, Claude Delmas, Gérard Férey et Marc Leblanc.

Enfin, il me faut remercier mes parents qui ont cru en moi et m’ont permis d’effectuer une thèse. Il est clair que sans eux je n’y serai jamais arrivé. Alors c’est un grand merci de votre fils qui vous aime. Merci à ma famille qui est venue me soutenir le jour de ma soutenance, mes sœurs Domitille et Daphné. Ma marraine Donatienne à qui je veux dire que Mitch nous manque beaucoup.

Je tiens à remercier Laurent Bédikian parce que ça lui fera plaisir et pour ne pas faire de jaloux je remercie mes amis de toujours Julien et Gaël.

Je garde naturellement le meilleur pour la fin en remerciant ma femme Bettina qui m’a beaucoup soutenu et aidé durant cette période. Je la remercie de m’accompagner dans notre nouvelle vie.

Sommaire

CHAPITRE 1 :

Introduction et présentation générale

1. Introduction

Environ 85 à 90% des produits issus de l'industrie chimique proviennent de procédés catalytiques.[1] La recherche sur la synthèse et la caractérisation de nouveaux catalyseurs de plus en plus performants est d'un intérêt grandissant compte tenu des nouveaux critères environnementaux. L'utilisation des oxydes pour des applications en catalyse hétérogène dans l'industrie est très largement répandue. On peut citer par exemple l'alumine γ-Al_2O_3 qui possède des propriétés acides au sens de Lewis et de Brønsted et qui est utilisée dans de nombreux procédés de raffinage du pétrole.

Malgré les caractéristiques intrinsèques du fluor (forte réactivité et électronégativité), les matériaux fluorés restent peu utilisés dans le domaine de la catalyse du fait de leur insuffisante surface spécifique et de leur faible stabilité thermique. En effet, le caractère structurant du fluor qui très largement employé, par exemple, dans l'élaboration de solides microporeux cristallisés,[2] représente un sérieux désavantage pour l'obtention de nanomatériaux fluorés. L'un des critères majeurs lors de la sélection d'un catalyseur est sa surface spécifique qui définie la surface active du matériau. Outre un plus grand nombre de sites, une taille nanométrique permet de générer des défauts de surfaces dans lesquels le cation se trouve dans un état sous-coordonné renforçant leur caractère acide.

Le traitement d'un matériau par un réactif fluoré est couramment utilisé pour modifier ou augmenter ces propriétés acides. L'imprégnation d'une zéolithe MCM-41 avec une solution de NH_4F conduit par exemple à une augmentation de son acidité de Brønsted[3] alors qu'un traitement de fluoration par voie gaz sur de l'alumine γ-Al_2O_3 mène à des propriétés de Lewis et de Brønsted particulières.[4] Cette augmentation de réactivité est associée à l'électronégativité de l'ion fluorure qui se traduit par une augmentation de la densité de la charge partielle du cation renforçant son caractère acide de Lewis. Du point de vue de l'acidité de Brønsted, par effet antagoniste le proton d'une liaison M-OH se trouvera plus labile augmentant ainsi son caractère acide.

L'interdiction des chlorofluorocarbones (CFC) par le protocole de Montréal (1991) pour leur contribution dans la destruction de la couche d'ozone a engendré une recherche accrue pour la

[1] Chorkendorff, I. ; Niemantsverdriet, J. W. in "Concepts of modern catalysis and kinetics". *Wiley Ed.* **2003**.
[2] Loiseau, T., Férey, G. *J. Fluo. Chem.* **2007**, *128*, 413.
[3] Xu, M. ; Wang, W. ; Seiler, M. ; Buchholz, A.; Hunger, M. *J. Phys. Chem. B.* **2002**, *106*, 3202.
[4] Chupas, P.J., Grey, C.P. *J. Cata.* **2004**, 224, 69.

synthèse de substituts non chlorés.[5] La synthèse de ces hydrofluorocarbones (HFC) nécessite un catalyseur de type acide de Lewis.

Au premier abord, l'électronégativité qui traduit la capacité d'un élément à attirer des électrons, devrait traduire l'acidité intrinsèque au sens de Lewis d'un cation. Cette grandeur n'est en fait pas suffisante et il faut faire intervenir la taille du cation. La notion de gradient de champ électrique χ/r^2 permet de mieux appréhender l'acidité intrinsèque d'un cation traduisant en fait sa polarisabilité.[6] L'aluminium trivalent présente ainsi une plus forte acidité de Lewis en comparaison avec d'autres éléments de transitions tel que Ga^{3+}, Fe^{3+} ou Cr^{3+}.[6] De plus, les fluorures d'aluminium présentent une meilleure stabilité thermique et une moindre toxicité. Enfin, le fluorure d'antimoine SbF_5 est un des acides les plus forts et est très largement utilisé en synthèse organique malgré sa toxicité.[7]

De nombreux travaux relatifs à la synthèse et à la caractérisation structurale de fluorures d'aluminium ont été réalisés. Après un bref tour d'horizon autour de ces recherches, nous passerons du volume à la surface afin d'illustrer sur la base de calculs ab initio, la complexité des surfaces de ces solides. De plus, nous mettrons en avant l'importance de stabiliser des nanomatériaux associés à de grande surface spécifique et nous évoquerons les nouvelles voies de synthèse permettant d'accéder à ce type de solide. Enfin, si l'aspect « nano » est important en catalyse, une connaissance accrue de la composition chimique du solide est primordiale. Ce dernier point fera l'objet d'une discussion.

2. Etat de l'art

2.1 Synthèse et structures des fluorures d'aluminium

La cristallochimie des fluorures d'aluminium est très riche avec de nombreuses variétés allotropiques. De manière générale, ces structures résultent de la connexion d'octaèdres AlF_6 par les sommets. Les différents réseaux et leur mode de synthèse des AlF_3 sont présentés ici.

[5] Advances in Fluorine Science Vol.1 - Fluorine and the Environment: Atmospheric Chemistry, Emissions, and Lithosphere. A. Tressaud Ed., Elsevier, Amsterdam. **2006**.
[6] Francke, L. ; Durand, E. ; Demourgues, A. ; Vimont, A. ; Daturi, M. ; Tressaud, A. *J. Mater. Chem*. **2003**, *13*, 2330.
[7] Olah, G. A. *J. Org. Chem.* **2005**, *70*, 2413.

2.1.1 Mode de synthèse

Les différentes variétés allotropiques des fluorures d'aluminium sont généralement obtenues par décomposition thermique d'un précurseur.[8] Le schéma 1 résume les différentes transitions menant aux diverses variétés des AlF_3.[9] Les précurseurs utilisés requièrent des méthodes de préparation plus ou moins complexes. On peut citer les fluorures hydratés facilement obtenus par voie aqueuse et opérant avec un excès de fluor pour éviter toutes traces d'impuretés (oxydes/hydroxydes). La déshydratation du précurseur permet ainsi l'obtention d'une phase AlF_3, ici α et β-AlF_3, à température relativement basse (<350°C). Les phases α-NH_4AlF_4 ou $(NH_4)_3AlF_6$ font aussi partie de ces précurseurs synthétisés par voie aqueuse classique.
Une autre stratégie de synthèse a permis l'obtention de nouvelles phases métastables : η-, θ- et κ-AlF_3.[10] Une voie non-aqueuse a été développée pour obtenir des sels de fluoroaluminate de formule générale $MAlF_4$ ou M est un cation organique (M = pyridineH^+, $N(CH_3)_4^+$, NH_4^+). La décomposition thermique de ces sels libère une espèce volatile de type MF, générant ainsi le solide cristallisé AlF_3. L'obtention de la phase κ-AlF_3 est certainement la phase qui nécessite la méthode de préparation la plus complexe. Son précurseur β-NH_4AlF_4 est une phase métastable obtenue par réaction entre un sel de pyridinium et du formamide, qui n'est autre que le solvant, comme suit : pyridine$H.AlF_4$ + $HCONH_2$ → pyridine + CO + NH_4AlF_4.
Il est à noter que l'ensemble de ces voies mènent à des composés présentant de faibles surfaces spécifiques, inférieures à 50 m^2g^{-1}.

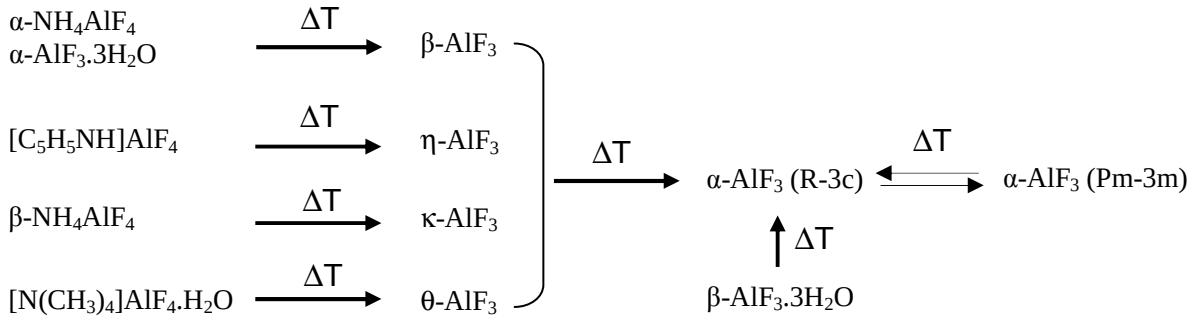

Schéma 1 : Voies de synthèses des différentes formes allotropiques AlF_3. D'après réf [9]

Il est convient ici de rappeler que l'hydroxyfluorure $Al_2[(F_{0.5},OH_{0.5})_6].H_2O$ est obtenu par précipitation dans une milieu basique.[11]

[8] Kemnitz, E.; Menz., D.H. *Prog. Solid State Chem.* **1998**, *26*, 97.
[9] T. Krahl, E ; Kemnitz. *J. Fluo. Chem.* **2006**, *127*, 663.
[10] Herron, N. ; Thorn, D.L. ; Harlow, R.L. ; Jones, G.A. ; Parise, J.B. ; Fernandez-Baca, J.A. ; Vogt, T. *Chem. Mater.* **1995**, *7*, 75.
[11] Cowley, J. M.; Scott, T. R. *J. Amer. Chem. Soc.* **1948**, *70*, 105.

2.1.2 Les réseaux des fluorures d'aluminium

α-AlF_3 : Les différentes formes allotropiques de fluorures d'aluminium conduisent irréversiblement, sous chauffage, à la phase thermodynamiquement stable[12] : α-AlF_3 (R-3c) dérivée de la structure ReO_3. Cette phase elle-même subit une transition réversible aux alentours de 450°C vers la forme cubique ReO_3 (Figure 1).

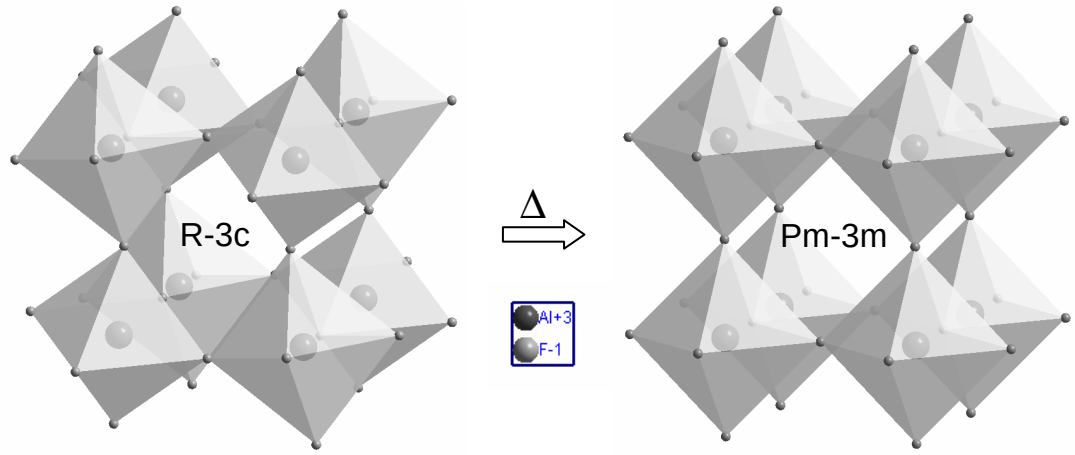

Figure 1: Evolution de la structure α-AlF_3

β-AlF_3 : L'une des variétés des fluorures d'aluminium les plus connues est la phase metastable β-AlF_3 dont la structure a été résolue par Fourquet *et al*[13]. Cette dernière cristallise dans un réseau de type bronze de tungstène hexagonal (HTB) qui présente un système de canaux à sections triangulaires et hexagonales le long de la direction c (Figure 2, gauche). Le motif de la structure α-AlF_3 est aussi ici présent (Figure 2, droite).

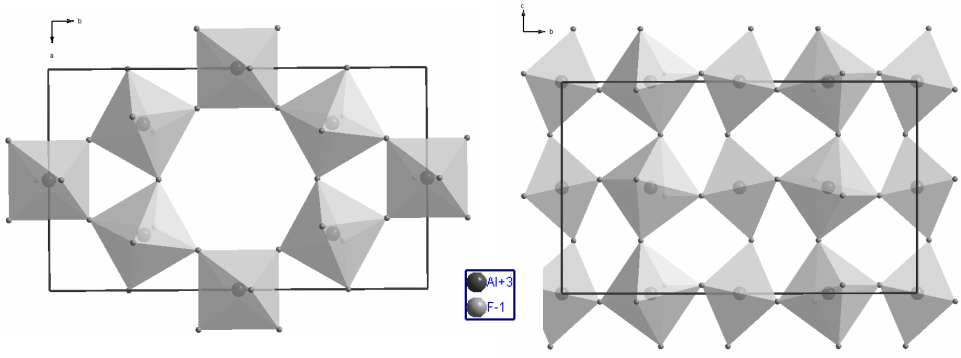

Figure 2: Projection selon [100] (gauche) et [001] de la structure β-AlF_3 (droite)

[12] Daniel, P. ; Bulou, A. ; Rousseau, M. ; Nouet, J. ; Fourquet, J.L. ; Leblanc, M. ; Burriel, R. *J. Phys.: Condens. Matter* 2. **1990,** 5663.
[13] Le Bail, A. ; Jacoboni, C. ; Leblanc, M. ; De Pape, R. ; Duroy, H. ; Fourquet, J.L. *J. Solid State Chem.* **1988**, *77*, 96.

Pyrochlore : La phase pyrochlore[14] $Al_2[(F_{0.5},OH_{0.5})_6]$ possède un réseaux de canaux dans les trois directions de l'espace. Cette structure possède des cavités à section triangulaire et hexagonale (Figure 3). Il est à noter que son homologue fluoré nommé γ- ou η-AlF_3 est obtenu par décomposition thermique de $[C_5H_5NH](AlF_4)$.[10]

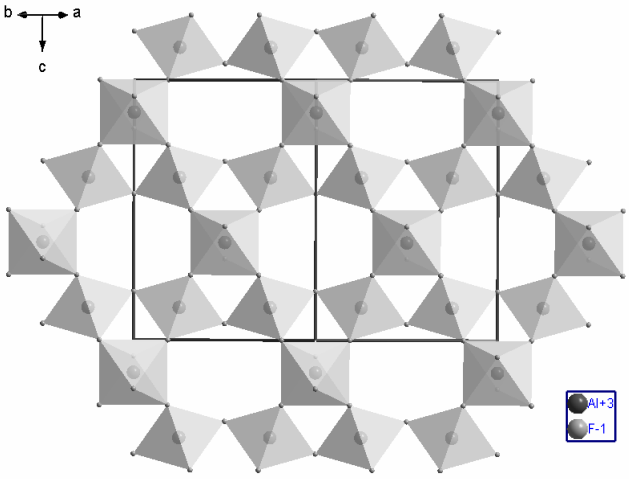

Figure 3 : Projection selon [110] de structure pyrochlore

κ-AlF_3 : Comme présenté précédemment, la dégradation thermique de la phase métastable β-NH_4AlF_4 mène à une nouvelle variété d'AlF_3.[10] La phase κ-AlF_3 est constitué d'empilements de feuillets identiques formant des canaux avec des sections triangulaires, carrés et pentagonale distordue de type bronze quadratique de tungstène (TTB) (Figure 4).

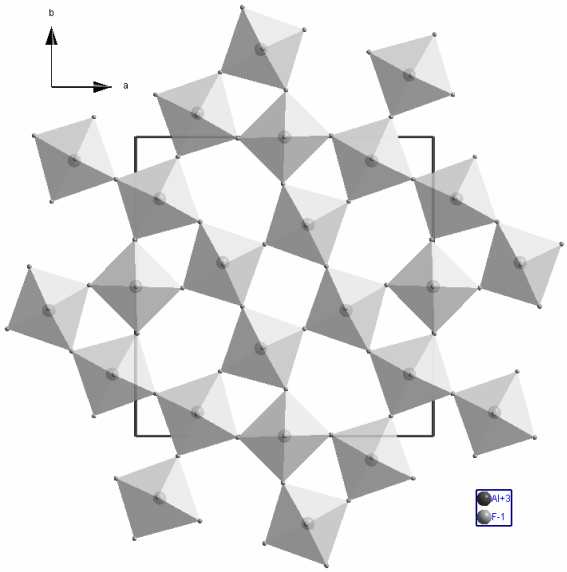

Figure 4 : Projection selon [001] de la structure κ-AlF_3

[14] Fourquet, J.L. ; Rivière, M. ; Le Bail, A. ; Nygrens, M. ; Grins, J. *Eur. J. Solid State Inorg. Chem.* **1988**, 25, 35.

θ-AlF_3 : L'agencement structurale de cette phase obtenue par décomposition thermique de $[(CH_3)_4N(AlF_4).H_2O$[15] est l'un des plus complexe parmi les réseaux AlF_3. On y distingue en effet des sections triangulaires, carrés et pentagonales (Figure 5).

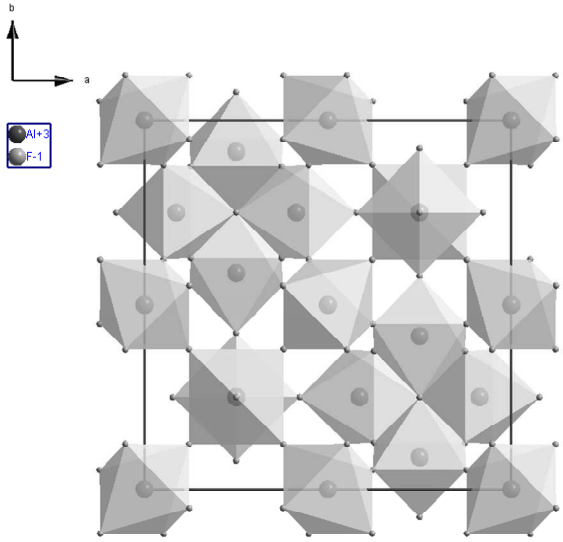

Figure 5 : Projection selon [001] de la structure θ-AlF_3

3. La réactivité des nanomatériaux

Différents paramètres interviennent dans la réactivité du solide. Ces derniers sont présentés dans cette partie. Les dernières avancées dans le domaine de la réactivité des fluorures d'aluminium y sont aussi présentées.

3.1 Effet de la taille des particules sur la structure de la surface

La taille des particules a une influence directe sur l'activité catalytique d'un solide. Les nanomatériaux ont en effet une réactivité accrue par comparaison aux matériaux dits massifs. Un exemple de l'effet de la taille sur l'activité catalytique est l'utilisation de nanoparticules d'or dans la réaction d'oxydation du CO.[16] L'or utilisé à l'état massif ne possède aucune activité alors qu'à l'état nanométrique, la réaction s'opère même à très basse température (200 K). En diminuant la taille des particules, des modifications s'opèrent sur la structure des centres réactifs, le nombre de sites présents en surface et situés au niveau des arêtes et coins des particules. Tout ceci tend à modifier l'activité catalytique.

[15]Le Bail, A. ; Fourquet, J.L. ; Bentrup, U. *J. Solid State Chem.* **1992**, *100*, 151.

[16] Haruta, M. ; Tsubota, S. ; Kobayashi, T. ; Kageyama, H. ; Genet, M.J. ; Delmon, B. *J. Catal*. **1993**, *144*, 175.

Une étude basée sur la simulation de la dynamique moléculaire de nanoparticules cubiques[17] de α-AlF_3 a permis de mettre en évidence des reconstructions de surfaces. Ces réarrangements structuraux génèrent en surface des sections triangulaires et pentagonales en plus des sections carrés (Fig 6, Inset B). Il en résulte des ions Al^{3+} en sous coordinence : tétraédrique (4c) et pentaédrique (5c, Fig 6 Inset A).

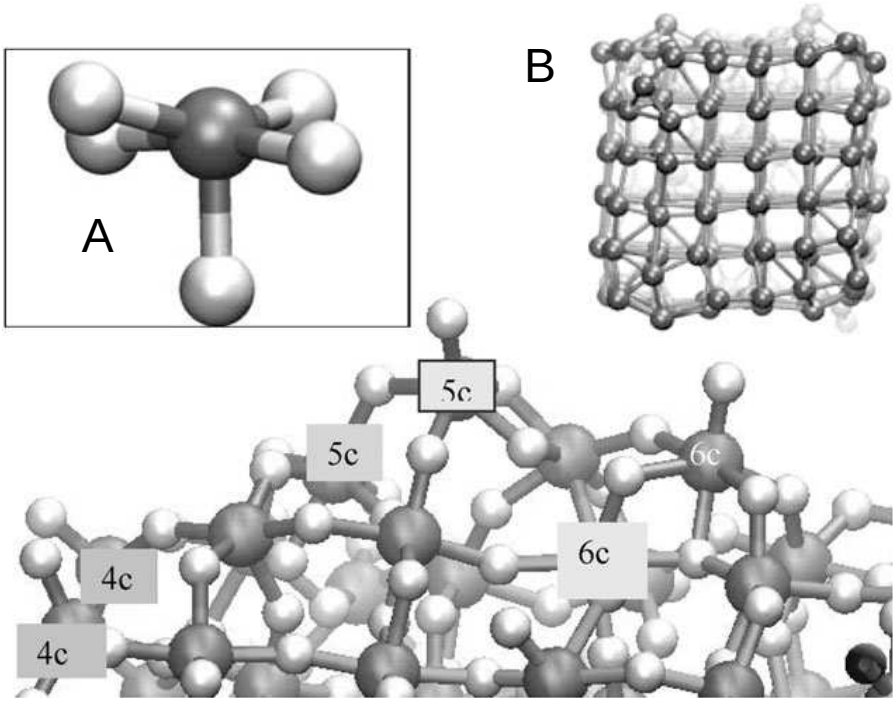

Figure 6 : Zoom au niveau d'un coin d'une nanoparticule de α-AlF_3 cubique. Les coordinences des ions Al^{3+} sont indiquées par Xc (X = 4, 5, 6). Inser A : géométrie d'un ion Al^{3+} penta-coordonné. Inser B : Réseau de l'aluminium d'une nanoparticule montrant les nouvelles sections se formant au niveau des coins et arêtes. D'après Réf [17].

Ceci a permis de mettre en évidence non seulement une reconstruction de surface ainsi qu'une localisation particulière de ce phénomène au niveau des arêtes et coins de la particule. La majorité des sites de Lewis a en effet été localisée au niveau des coins et arêtes (Figure 7 : points blancs). Cet exemple démontre parfaitement l'intérêt de la taille nanométrique en catalyse.

[17] Chaudhuri, S.; Chupas, P.; Morgan, B. J.; Madden, P. A.; Grey, C. P. *Phys. Chem. Chem. Phys.* **2006**, *8*, 5045.

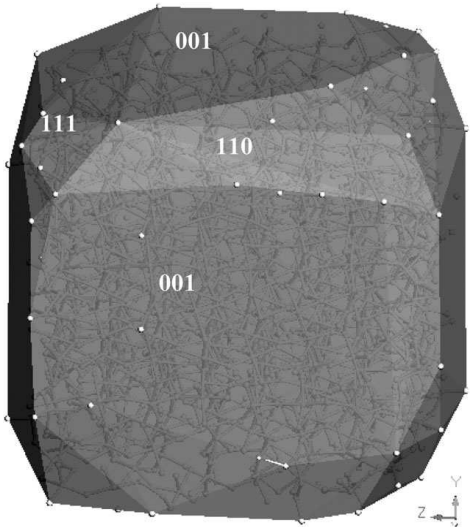

Figure 7 : Surfaces d'une nanoparticule de α-AlF_3 montrant la localisation préférentielle des sites de Lewis (points blancs) au niveau des coins et arêtes. D'après Réf [17].

3.2 Du volume à la surface

Si la surface spécifique d'un catalyseur est un des paramètres clés dans sa réactivité, la structure cristallographique y joue aussi un rôle primordial. L'activité catalytique (Tableau 1) de différentes variétés allotropiques de AlF_3 a été testées via deux réactions de fluoration[18] ci-dessous :

$$CHClF_3 + 3HF \rightarrow CHF_3 + 3HCl \quad (1)$$

$$CCl_3CF_3 + HF \rightarrow CFCl_2CF_3 + HCl \quad (2)$$

Composé	Surface spécifique ($m^2.g^{-1}$)	Conversion en CHF_3 (%)	Conversion en CCl_3CF_3 (%)
α-AlF_3	3	2	4
β-AlF_3	53	49	10
η-AlF_3	58	4	12
θ-AlF_3	64	10	11
κ-AlF_3	19	50	45

Tableau 1 : Activité catalytique de diverses formes de AlF_3. D'après réf [18].

[18] Herron, N.; Farneth. W. E. *Adv Mater*. **1996**, *12*, 8.

Malgré une faible surface spécifique, la phase κ-AlF_3 est la plus active. Ceci démontre en première approximation que la structure cristalline engendre une structure de surface différente pour chaque variété allotropique. Il est donc d'intérêt d'obtenir des informations sur la structure de la surface d'un catalyseur.

L'étude théorique de la géométrie des surfaces est possible par le calcul ab initio. Ce dernier permet d'examiner les différentes configurations de terminaison d'une surface et de déterminer celle qui sera la plus stable. Une surface est en général en contact avec une atmosphère gazeuse qui va induire une modification physico-chimique des terminaisons. Il est donc d'intérêt d'étudier la stabilité d'une terminaison en présence d'une atmosphère donnée. Ainsi les structures des terminaisons de surfaces de α- et β-AlF_3 ont été étudiées par Wander en fonction du potentiel chimique du fluor contrôlé en jouant sur la pression partielle et la température.

La phase α-AlF_3 est proche de la structure corundum α-Al_2O_3. En se basant sur la stabilité de la surface 0001 de α-Al_2O_3, Wander et al[19] ont étudié la structure de la surface (0001) de α-AlF_3. Pour ce faire, différentes terminaisons ont été proposées (Figure 8).

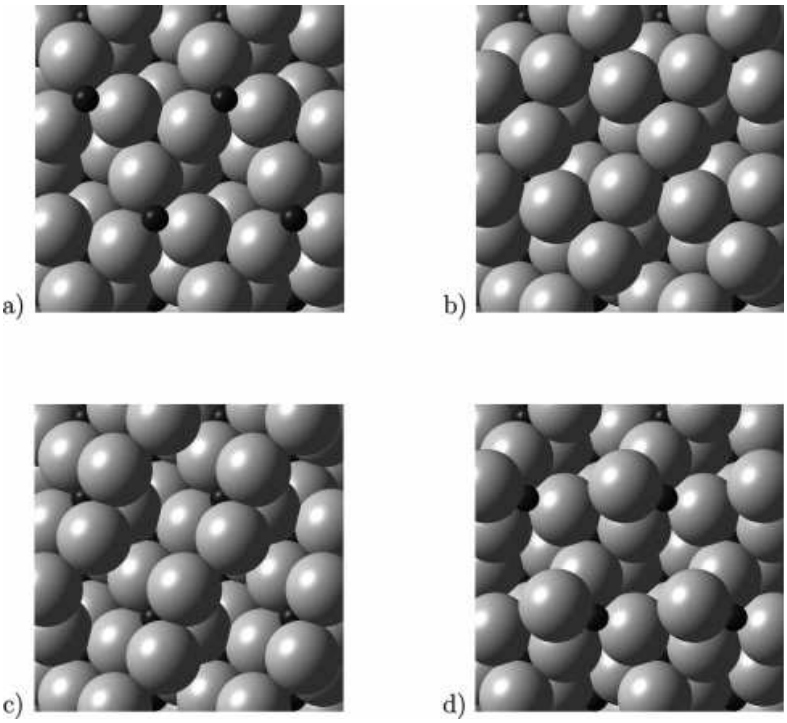

Figure 8: Les diverses terminaisons possibles de la surface (0001) de α-AlF_3, les atomes d'aluminium sont représentés en noir et les atomes de fluor en gris. a) la surface ne présente que des atomes d'aluminium (S_{Al} slab), b) 3 atomes de fluor recouvrent un atome d'aluminium (S_{3F} slab), c) 2 atomes de fluor recouvre un atome d'aluminium (S_{2F} slab), d) 1 atome de fluor recouvre un atome d'aluminium (S_{1F} slab). D'après réf [19].

[19] Wander, A.; Searle, B. G.; Bailey, C. L.; Harrison. N. M. *J. Phys. Chem. B.* **2005**, *109*, 22935.

Les énergies libres de ces terminaisons en fonction de la pression partielle de fluor montrent que la terminaison S_{2F} (Fig 8, c)) est la plus stable quelque soit les potentiels chimiques du fluor. Au niveau de la surface 0001 du α-AlF_3, les atomes d'aluminium, potentiels sites de Lewis, sont donc masqués par deux atomes de fluor rendant cette surface catalytiquement inactive.

La même étude a été effectuée sur la surface (100) de la phase β-AlF_3.[20] Cette structure étant plus complexe que celle de α-AlF_3, les calculs ont mené à deux types de terminaisons notés T1 et T6 présentant des énergies de surface proches, respectivement 1.3 et 0.8 $J.m^{-2}$. La Figure 9 présente les coupes qui permettent d'obtenir T1 et T6. Il a d'abord été considéré que la terminaison T1 ne pouvait pas être présente dans un matériau bien cristallisé.[20] Sa relative faible énergie de surface a ainsi amené les auteurs à la considérer comme un défaut de surface. Une étude plus approfondie de ces deux terminaisons a montré que T1 subissait une reconstruction de surface qui amenait son énergie libre au même niveau que celle de T6.[21] Ces deux types de surfaces sont ainsi attendus dans β-AlF_3 (100). La Figure 10 présente les structures des surfaces T1 et T6 avant et après reconstruction. La surface T6 ne montre pas de reconstruction significative lors de l'optimisation de sa structure.

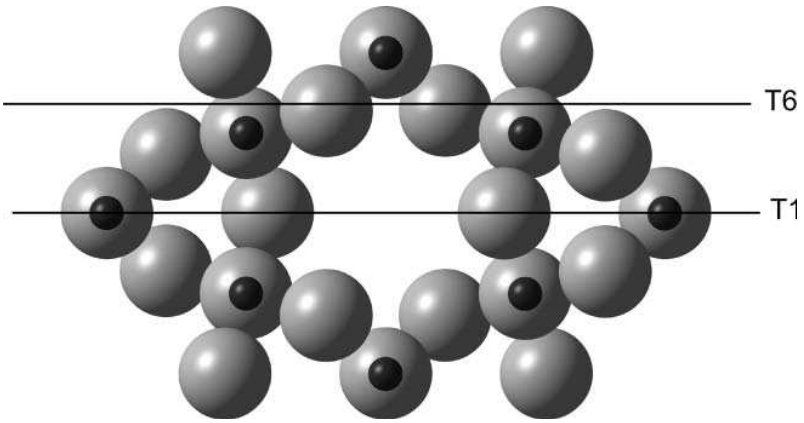

Figure 9 : Plans de coupes qui produisent les terminaisons T1 et T6. D'après la réf [20].

[20] Wander, A.; Bailey, C. L.; Searle, B. G.; Mukhopadhyay, S.; Harrison, N. M. *Phys. Chem. Chem. Phys.* **2005**, *7*, 3989.
[21] Wander, A.; Bailey, C. L.; Mukhopadhyay, S.; Searle, B. G.; Harrison, N. M. *J. Mater. Chem.* **2006**, *16*, 1906.

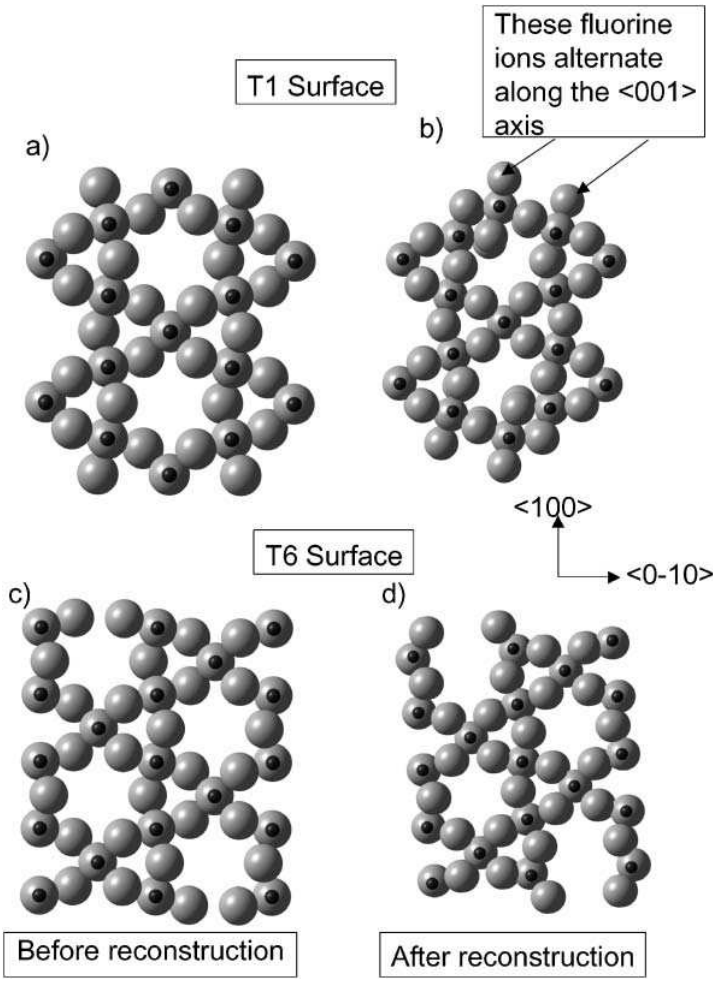

Figure 10 : Structures de la surface (100) de β-AlF_3 avant et après reconstruction. D'après la réf [21]

Dans les deux cas, les structures présentent des atomes d'aluminium en coordinence pentaédrique qui sont donc considérés comme étant des sites actifs de Lewis. L'environnement local autour des ions Al^{3+} dans T1 et T6 différent légèrement. Ces environnements sont présentés dans la figure 11.

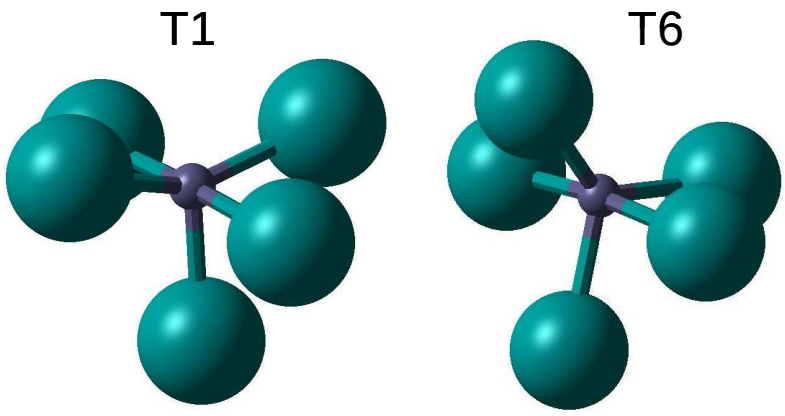

Figure 11 : Géométrie locale des ions Al^{3+} dans les surfaces T1 et T6

Une étude préliminaire a montré que les sites de type T1 étaient plus acides que ceux de type T6. Il est à noter que la thermo-désorption de l'ammoniac sur β-AlF_3 présente deux pics[22] suggérant l'existence de ces deux types de sites acides.

3.3 L'environnement et la surface

La plupart des études expérimentales sont menées dans des conditions bien particulières, souvent sous ultravide, alors que les réactions catalytiques sont effectuées dans des environnements différents. Il est ainsi possible que la structure d'une surface sous ultra-vide ne soit pas stable dans des conditions expérimentales de réactions. C'est ainsi l'un des nouveaux enjeux des calculs ab initio. Après avoir démontré l'absence de site de Lewis en surface 0001, les auteurs[23] ont étudié la surface (01-12) de α-AlF_3. Cette surface présente des sites potentiels de Lewis. Cependant sous atmosphère HF/H_2O simulant les conditions de réactions catalytiques, cette surface devient hydroxylée perdant ainsi ces centres de Lewis. Il a été prédit que l'obtention d'une surface purement fluorée ne pouvait être réalisable que dans des conditions extrêmes. L'interaction entre la surface et son environnement lié aux conditions de réactions catalytiques, est fondamentale au regard de la réactivité du solide.

4. Les nouvelles voies de synthèse

Dans le but de minimiser les propriétés structurantes du fluor et ainsi d'accéder à des composés de taille nanométrique, de nouvelles voies de synthèse ont été mises au point récemment. Ces dernières permettent d'accéder à des fluorures d'aluminium possédant de grandes surfaces spécifiques et amorphes vis-à-vis des rayons X. Dans le domaine de recherche de voies de synthèse innovante, nous présentons ici la synthèse assistée par micro-ondes.

[22] Hess, A.; Kemnitz. E. *J. Catal*. **1994**, *149*, 449.
[23] Mukhopadhyay, S.; Bailey, C.L.; Wander, A. ; Searle, B.G.; Muryn, C.A.; Schroeder, S.L.M.; Lindsay, R.; Weiher, N.; Harrison, N.M. *Surf Sci.* **2007**, 601, 4433.

4.1 Fluoration plasma d'une zéolithe

Cette méthode[24] consiste à fluorer par voie plasma radiofréquence une zéolithe riche en silicium ($H_{1.3}[Al_{1.3}Si_{22.7}O_{48}]$ H-SSZ-32, de structure type MTT) en utilisant NF_3 comme agent fluorant. Le réseau subit alors une réaction de métathèse comme suit:

$$\text{Zeolite precursor} \xrightarrow[\text{plasma}]{NF_3} AlF_3 + NO_{x(g)} + SiF_{x(g)}$$

Le fluorure d'aluminium ainsi obtenu est amorphe vis-à-vis des rayons X et possède une très grande surface spécifique de 190 $m^2.g^{-1}$. Les propriétés texturales du produit obtenu dépendent fortement du taux de silicium de départ. Plus le taux de silicium est élevé, plus la surface spécifique est importante. Le départ de l'espèce SiF_x sous forme de gaz induit une forte augmentation de la porosité puisque le précurseur présente une surface de 100 $m^2.g^{-1}$ contre 190 $m^2.g^{-1}$ après fluoration. Tout comme la voie précédente, l'obtention d'une grande surface spécifique est liée au départ d'un gaz qui engendre un matériau poreux.

4.2 La voie sol-gel

Cette méthode[25] comprenant deux étapes, mène à la préparation de fluorure d'aluminium amorphe vis-à-vis des rayons X et présentant une très grande surface spécifique, supérieure à 200 $m^2.g^{-1}$. Dans un premier temps, un alkoxide d'aluminium est fluoré par voie liquide dans un solvant organique contenant du HF anhydre. Ce procédé sol-gel mène a un alkoxy-fluorure d'aluminium de composition type $AlF_{3-x}(OR)_x$ avec une très grande surface spécifique (≅ 400 $m^2.g^{-1}$). La dernière étape permet de compléter la fluoration de l'aluminium en utilisant un agent fluorant gazeux : HCFC, CFC ou HF. Le solide ainsi obtenu « HS-AlF_3 » présente une grande surface spécifique et une très forte acidité de Lewis.
Nous avons associé cette voie à la synthèse micro-ondes de manière à obtenir des solides fluorés très divisés. Cette étude sera présentée dans le chapitre 2.

4.3 Introduction à la synthèse assistée par micro-ondes

La synthèse assistée par micro-ondes s'est développée au cours des années 80 dans le domaine de la chimie organique. De très nombreuses réactions sont ainsi effectuées via cette

[24] Delattre, J. L.; Chupas, P. J.; Grey, C. P.; Stacy, A. M. *J. Am. Chem. Soc.* **2001**, 123, 5364.
[25] Kemnitz, E.; Groß, U.; Rudiger, S.; Shekar, C. S. *Angew. Chem. Int. Ed.* **2003**, *42*, 4251.

synthèse. L'intérêt porté à cette technique est lié principalement à l'augmentation des vitesses de réaction qui dans un contexte d'économie d'énergie est très largement mis en avant.[26] L'application de cette synthèse en chimie inorganique est beaucoup plus récente mais elle a déjà prouvé qu'elle pouvait être utilisée dans la préparation d'un très grand nombre de matériaux : oxydes[27], fluorures[28], metal-organics-fragments MOF[29]… Dans la préparation de matériaux inorganiques, les avantages de cette synthèse en comparaison avec les méthodes dites conventionnelles sont nombreux : basse température, cinétique de cristallisation rapide, obtention de nanomatériaux homogènes en taille, stabilisation de nouvelles phases.

Ces différents avantages sont attribués à la particularité du chauffage, transmis directement au cœur de la solution et non par transmission du réacteur vers la solution.

La chaleur résulte de l'interaction entre l'onde et la matière. La composante du champ électrique associée à l'onde électromagnétique provoque des mouvements moléculaires par migration d'espèces ioniques et/ou par rotation d'espèces dipolaires. Les mécanismes[30] responsables de ces mouvements moléculaires sont appelés (i) mécanisme de polarisation dipolaire et (ii) mécanisme de conduction ionique. (i) Une molécule possédant un moment dipolaire, comme l'eau, est sensible au champ électrique des micro-ondes et va tenter de s'aligner sur ce dernier par un mouvement de rotation. Ces mouvements génèrent de la chaleur par friction moléculaire. (ii) Les ions contenus dans une solution vont se déplacer sous l'influence du champ électrique. Ceci aboutit à un nombre de collisions plus élevé et la génération de chaleur par conversion de l'énergie cinétique.

Le procédé de synthèse utilisé lors de nos travaux utilise l'irradiation micro-ondes comme source de chaleur. La synthèse s'effectue dans un réacteur fermé, en conditions hydrothermales. Les synthèses ont été réalisées dans un four micro-ondes, modèle MARS-5 de la société C.E.M, opérant à une fréquence de 2.45 GHz.

De manière générale, une solution contenant un précurseur métallique, un solvant et de l'acide fluorhydrique, est transvasée dans un réacteur en PTFE (100ml). Ce dernier est ensuite placé dans un dispositif (Figure 12, photo de gauche) permettant d'opérer en conditions hydrothermales avec un contrôle de la pression et de la température. Ce système (XP-1500) permet d'effectuer des synthèses à des températures maximales de l'ordre de 210°C et de

[26] Adam, D. *Nature*. **2003**, *421*, 571.
[27] Rao, K. J.; Mahesh, K. Kumar, S. *Bull. Mater. Sci*. **2005**, **28**, 19.
[28] Jacob, D.S.; Bitton, L.; Grinblat, J.; Felner, I.; Koltypin, Y.; Gedanken, A. *Chem. Mater*. **2006**, *18*, 3162.
[29] S. H. Jhung, J.-H. Lee, J. W. Yoon, C. Serre, G. Férey, J.-S. Chang. *Adv. Mater.* **2007**, *19*, 121.
[30] Kappe, C. O. *Angew. Chem. Int. Ed.* **2004**, *43*, 6250.

pressions allant jusqu'à 55 bars. Après l'étape de synthèse hydrothermale et un retour à température ambiante, un dispositif (Figure 12, photo de droite) permettant l'évaporation des solvants via un vide primaire et un flux d'argon est utilisé afin d'obtenir le matériau sous forme de poudre.

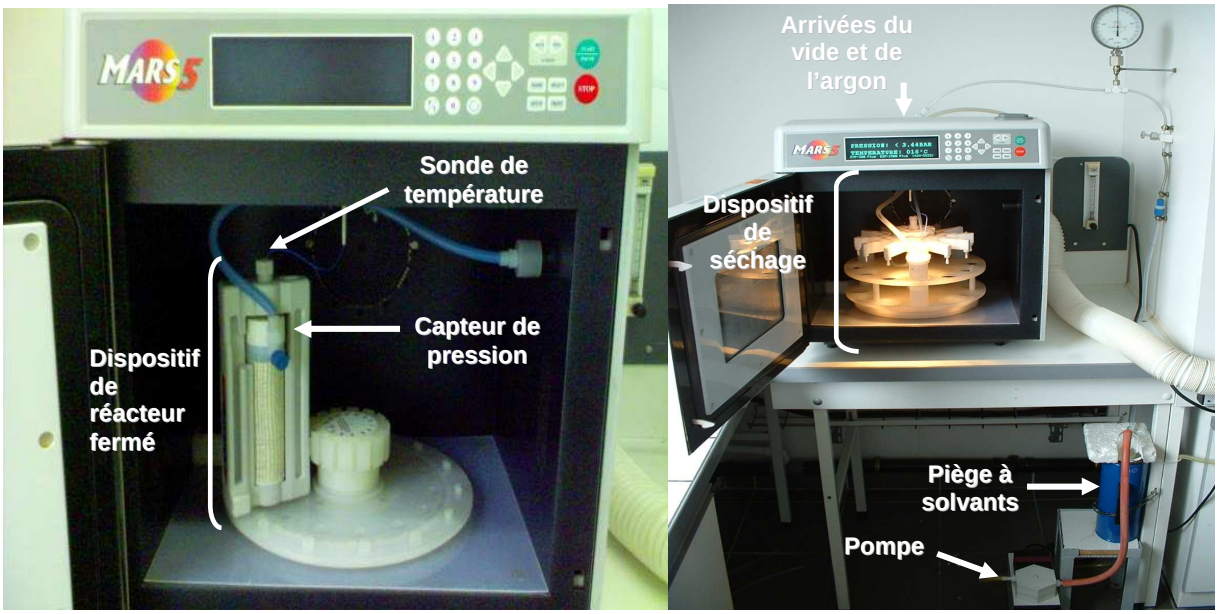

Figure 12 : Le four micro-ondes MARS-5 avec le dispositif de synthèse en conditions hydrothermales (photo à gauche) et le dispositif de séchage (photo à droite).

5. Influence de la composition chimique sur la structure et les propriétés acides

La composition chimique d'un solide a une importance considérable ainsi bien d'un point de vue structurale que sur la réactivité. Les différents anions entrant dans la composition d'un solide lui confèrent un agencement structural ainsi que des propriétés acides particulières.

Les groupements hydroxyles, potentiels sites de Brønsted, sont souvent présents dans les phases AlF_3. Ils peuvent être présents sous forme de traces ou faire partie intégrante de la structure. Lors de la préparation de ces phases, des phénomènes d'hydrolyse peuvent se produire menant à la présence d'OH dans le réseau. On peut citer l'exemple de β-AlF_3 qui quelque soit le précurseur utilisé contient des groupements OH. Compte tenu de la réaction d'hydrolyse, la déshydratation du précurseur hydrate peut s'écrire comme suit : $AlF_3 \cdot 3H_2O \xrightarrow{\Delta T} AlF_{3-x}(OH)_x + 3-x\ H_2O + x\ HF$. La dégradation du précurseur $(NH_4)_3AlF_6$ mène aussi à la présence de groupements OH[6] liée à l'utilisation d'une voie de précipitation aqueuse. Les groupements OH résultant de ces réactions d'hydrolyses sont présents en faibles quantités et ne confèrent donc pas au solide un caractère de Brønsted.

Au contraire, la phase pyrochlore s'apparente à un solide à anions mixtes: fluor et groupements OH. Ce matériau peut ainsi être considéré comme étant potentiellement un acide de Lewis et de Brønsted.

D'un point de vue structural, la présence des groupements OH dans le réseau se traduit par des distances Al-X ($X = F^-$, OH^-) plus grandes. Un autre aspect permettant d'expliquer la formation de la structure de type pyrochlore en présence de groupements OH est la tendance de ces derniers à former des angles Al-X-Al plus petits que dans les phases de type AlF_3.[31] La pyrochlore présente ainsi des angles de 141° alors que les angles des phases α- et β-AlF_3 varient entre 148 et 166°.

Si la présence d'OH permet de générer de l'acidité de Brønsted, la substitution d'ions fluorures par une espèce moins électronégative aura tendance à diminuer l'acidité de Lewis du cation environnant. Il est donc en principe possible de moduler le comportement acide d'un matériau en jouant sur sa composition chimique. Un matériau de type AlF_3 est apparenté à un acide de Lewis fort. L'incorporation de groupement OH génère une acidité de Brønsted alors que le caractère de Lewis tend à diminuer. Une large gamme d'acidité est ainsi potentiellement accessible en jouant sur le rapport F/OH.

Outre les groupements OH, la molécule d'eau est aussi potentiellement un acide de Brønsted. Il a été démontré que l'incorporation de molécules d'eau à la surface d'alumino-silicate augmentée considérablement leur acidité.[32]

La bi-fonctionnalité : Lewis/Brønsted est aussi d'intérêt dans certaines réactions catalytiques qui requièrent un effet de synergie entre ces deux acidités.[33,34]

Les composés à bases de fluorures d'aluminium peuvent ainsi avoir différents comportements acides suivant leur composition.

[31] Chupas, P. J.; Corbin, D. R. ; Rao, V. N. M.; Hanson, J. C.; Grey, C. P. *J. Phys. Chem. B.* **2003**, *107*, 8327.
[32] Garrone, E.; Onida, B.; Bonelli, B.; Busco, C.; Ugliengo, P. *J. Phys. Chem. B.* **2006**, *110*, 19087.
[33] Li, S.; Zheng, A.; Su, Y.; Zhang, H.; Chen, L.; Yang, J.; Ye, C.; Deng. F. *J. Am. Chem. Soc.* **2007**, *129*, 11171.
[34] Rimola, A. ; Tosoni, S. ; Sodupe, M. ; Ugliengo, P. *Chemical Physics Letters*. **2005**, *408*, 295.

Présentation du manuscrit

Dans ce chapitre ont été présentées les différentes structures adoptées par les fluorures d'aluminium et leur méthode de synthèse. Nous nous sommes aussi intéressés aux différents paramètres intervenants dans la réactivité de ces matériaux mettant en avant la nécessité de synthétiser des solides possédant une grande surface spécifique ainsi qu'une composition chimique bien définie. La synthèse de fluorures d'aluminium possédant des surfaces spécifiques de l'ordre de 200 $m^2.g^{-1}$ sont maintenant accessibles par de nouvelles voies consistant soit à la fluoration plasma de zéolithe ou à un procédé de type sol-gel. Cependant ces voies de synthèses mènent à des composés amorphes qui ne permettent pas ou difficilement d'établir une corrélation entre la structure/composition et la réactivité du solide.

Ces travaux de thèse se sont ainsi tournés vers la synthèse de nanomatériaux cristallisés utilisant une nouvelle méthode de synthèse : un procédé hydrothermal assisté par micro-ondes.
Les différents travaux effectués au cours de cette thèse ont fait l'objet de publications qui ont été adaptées pour s'inscrire dans ce manuscrit.
La stratégie de synthèse utilisée ici a permis de cibler les paramètres permettant : (i) la pureté phasique et (ii) l'obtention de nanomatériaux. Trois variétés allotropiques ont ainsi pu être synthétisées sous forme nanométrique. La première partie du chapitre 2 présente les trois articles relatifs à la synthèse et de la caractérisation de ces phases. Dans la deuxième partie du chapitre 2, la synthèse assistée par micro-ondes a été couplée à la voie sol-gel précédemment décrite. L'article correspondant, a permis notamment d'ouvrir des perspectives intéressantes dans la synthèse de matériaux possédant de très grande surface spécifique.
Le chapitre 3 est dédié à l'étude des propriétés acides de la phase HTB (ou β) ainsi que de son comportement thermique.
Le dernier chapitre est consacré à la conclusion relative à ces travaux.

Chapitre 2

Stabilisation de plusieurs types structuraux de composés hydroxy-fluorés à base d'aluminium

Ce chapitre concerne la préparation et la caractérisation de divers types structuraux de fluorures d'aluminium. Les trois premières parties sont relatives à l'obtention de diverses variétés obtenues par l'utilisation de précurseurs conventionnels. La dernière partie est relative aux traitements par un procédé hydrothermal assisté par micro-ondes d'un gel fluoré obtenu par une voie sol-gel non-aqueuse permettant la synthèse de matériaux à très grande surface spécifique.

2.1 Hydroxyfluorure d'aluminium nanostructuré de type HTB

Publication: *Nanostructured aluminium hydroxyfluorides derived from β-AlF_3, accepted in Chemistry of Materials.*

La première partie est consacrée à la synthèse et la caractérisation structurale d'un hydroxyfluorure d'aluminium présentant une structure de type bronze hexagonal de tungstène (HTB). Cette étude a mis en évidence l'influence du taux de fluor sur l'obtention de la variété structurale finale. Le rôle de l'isopropanol dans la stabilisation d'un matériau à grande surface spécifique a été démontré.

Une étude relative à la caractérisation micro-structurale du solide a été entreprise basée sur l'analyse de l'élargissement des pics de diffraction. Deux approches ont été utilisées : (i) l'approche de Williamson-Hall, (ii) l'analyse du profil de diffraction avec l'utilisation de la fonction de Thompson-Cox-Hastings.

Une approche combinant la résonance magnétique nucléaire et la méthode Rietveld a permis d'accéder aux environnements locaux autour de l'aluminium et du fluor.

L'étude des propriétés acides et le comportement thermique de cette phase seront détaillés dans le chapitre 3.

Nanostructured Aluminium Hydroxyfluorides Derived from β-AlF_3

Damien Dambournet,[†] Alain Demourgues,*[,†] Charlotte Martineau,[§,||] Stanislas Pechev,[†] Jérôme Lhoste,[†] Jérôme Majimel,[†] Alexandre Vimont,[‡] Jean-Claude Lavalley,[‡] Christophe Legein,[§] Jean-Yves Buzaré,[||] Franck Fayon,[⊥] and Alain Tressaud[†]

Institut de Chimie de la Matière Condensée de Bordeaux-CNRS, Université Bordeaux 1, 87 Avenue du Dr. A. Schweitzer, 33608 Pessac cedex, France, Laboratoire Catalyse et Spectrochimie, UMR 6506, CNRS-ENSICAEN-Université de Caen, Boulevard du Maréchal Juin, F-14050 Caen Cedex, France, Laboratoire des Oxydes et Fluorures, CNRS UMR 6010, IRIM2F, CNRS FR 2575, Université du Maine, Avenue Olivier Messiaen, 72085 Le Mans Cedex 9, France, Laboratoire de Physique de l'Etat Condensé, CNRS UMR 6087, IRIM2F, CNRS FR 2575, Université du Maine, Avenue Olivier Messiaen, 72085 Le Mans Cedex 9, France, and Centre de Recherche sur les Matériaux à Haute Température, CNRS UPR 4212, 1D Avenue Recherche Scientifique, 45071 Orléans Cedex 2, France

Received September 12, 2007. Revised Manuscript Received December 3, 2007

Microwave-assisted synthesis has been applied for the preparation of aluminum hydroxyfluorides derived from β-AlF_3. In the course of obtaining high-surface-area and homogeneous nanocrystallites, several key parameters have been adjusted. A relationship between the OH/F molar ratio and the stabilized allotropic forms has been pointed out. The surface area has been monitored depending on the water/isopropanol volume ratio. The microstructural properties of the as-prepared material have been thoroughly investigated highlighting X-ray line broadening arising from strains and size effects. It has been concluded from X-ray diffraction data refinements and TEM results that the prepared crystallites possess a platelet shape with an average particle size of 15 nm associated with a high surface area of 82 $m^2\ g^{-1}$. The occurrence of hydroxyl groups inside the network has been detected by FTIR spectroscopy and considered angles and bond distances are probably located in peculiar crystallographic sites, i.e., 8f (F1) and 16h (F2) Wyckoff positions. ^{19}F NMR as well as ^{27}Al high-field NMR spectroscopies are powerful tools to probe and quantify the various $AlF_{6-x}(OH)_x$ environments and confirm the preferential location of OH groups in 8f (F1) and 16h (F2) Wyckoff positions. A preliminary study using NH_3 adsorption revealed the occurrence of strong Lewis acid sites on the surface of β-$AlF_{3-x}(OH)_x$.

1. Introduction

Because of their high catalytic activity toward the halogen exchange reaction,[1] aluminum fluorides have been extensively investigated in the way that they assist the conversion of ozone-depleting[2] CFCs compounds in more environmentally acceptable compounds: HFCs. The Al−F system gives rise to numerous allotropic forms.[3] In addition to the thermodynamically stable phase α-AlF_3[3a] (space group $R\bar{3}c$) derived from the ReO_3 type structure, β-AlF_3 is the most known phase because it possesses high catalytic properties.[4] The structure has been solved by Le Bail et al.[3c] and derives from the hexagonal tungsten bronze (HTB) structure that consists of AlF_6 octahedra linked by corners and forming along the *c* direction channels with hexagonal section (Figure 1). This phase is metastable and therefore requires a multistep synthesis that conventionally consists of a thermal degrada-

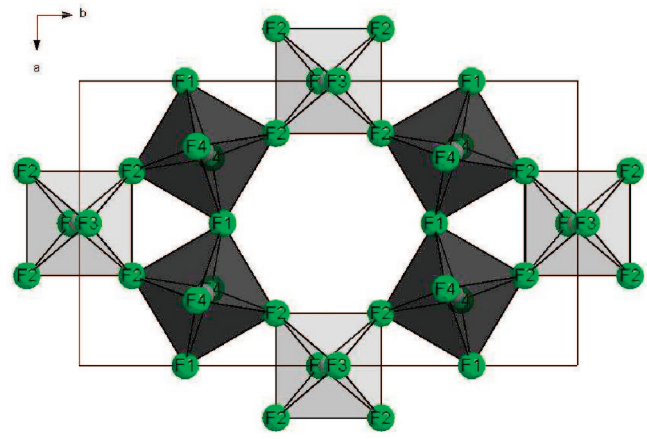

Figure 1. Network of the β-AlF_3 type structure: view along the *c* axis. The octahedra in light and dark grey denote Al1 and Al2 atom types, respectively.

* Corresponding author. E-mail: demourgues@icmcb-bordeaux.cnrs.fr.
[†] ICMCB–CNRS, Université Bordeaux 1.
[‡] Université de Caen.
[§] Laboratoire des Oxydes et Fluorures, Université du Maine.
[||] Laboratoire de Physique de l'Etat Condensé, Université du Maine.
[⊥] Centre de Recherche sur les Matériaux à Haute Température.

(1) Kemnitz, E.; Menz, D. H. *Prog. Solid State Chem.* **1998**, *26*, 97.
(2) *Fluorine and the Environment: Atmospheric Chemistry, Emissions, and Lithosphere*; Advances in Fluorine Science Series; Tressaud, A., Ed.; Elsevier: Amsterdam, 2006; Vol. 1.
(3) (a) Daniel, P.; Bulou, A.; Rousseau, M.; Nouet, J.; Fourquet, J. L.; Leblanc, M.; Burriel, R. *J. Phys.: Condens. Matter* **1990**, 5663. (b) Fourquet, J. L.; Rivière, M.; Le Bail, A. *Eur. J. Solid State Inorg. Chem.* **1988**, *25*, 535. (c) Le Bail, A.; Jacoboni, C.; Leblanc, M.; De Pape, R.; Duroy, H.; Fourquet, J. L. *J. Solid State Chem.* **1988**, *77*, 96. (d) Herron, N.; Thorn, D. L.; Harlow, R. L.; Jones, G. A.; Parise, J. B.; Fernandez-Baca, J. A.; Vogt, T. *Chem. Mater.* **1995**, *7*, 75. (e) Le Bail, A.; Fourquet, J. L.; Bentrup, U. *J. Solid State Chem.* **1992**, *199*, 151. (f) Ravez, J.; Mogus-Milankovic, A.; Chaminade, J. P.; Hagenmuller, P. *Mater. Res. Bull.* **1984**, *19*, 1311. (g) Chupas, P. J.; Chaudhuri, S.; Hanson, J. C.; Qui, X.; Lee, P. L.; Shastri, S. D.; Billinge, S. J. L.; Grey, C. P. *J. Am. Chem. Soc.* **2004**, *126*, 4756.
(4) Hess, A.; Kemnitz, E. *J. Catal.* **1994**, *149*, 449.

10.1021/cm702603b CCC: $40.75
Published on Web 01/31/2008

tion[5] of either ammonium fluoride salts (NH_4AlF_4, $(NH_4)_3AlF_6$) or aluminum trihydrate (α-$AlF_3 \cdot 3H_2O$). Unfortunately, these routes give rise to low specific surface area materials ($\sim$30 $m^2\ g^{-1}$), which drastically limits their reactivity because of a small number of active surface sites. Because of the strong electronegativity of the fluoride ions, new routes have been developed consisting either of non aqueous sol–gel[6] or plasma[7,8] fluorination processes leading to X-ray amorphous AlF_3 exhibiting high-surface-area powders (>200 and 190 $m^2\ g^{-1}$, respectively). At the same time, progress in computer calculation has enabled the improvement of theoretical surface structure and reconstruction. Wander et al. have investigated the β-AlF_3 (001) surface terminations, highlighting the occurrence of undercoordinated Al^{3+} environments, which are assumed to act as strong Lewis acid sites.[9,10] Moreover, using atomistic molecular dynamic simulations, Chaudhuri et al.[11] have shown that significant surface reconstruction occurs on cubic α-AlF_3 nanoparticles, also leading to strongly undercoordinated Al^{3+} environments, i.e., Lewis acid centers. It was therefore of great interest to develop a new route enabling the synthesis of materials presenting nanosized crystallized particles, i.e., with high surface area.

With this aim, the nonconventional route using microwave irradiation as a heating source has been used in moderate hydrothermal conditions. This peculiar process results from the interaction between the electrical field component and the matter and gives rise to two mechanisms,[12] i.e., dipolar–polarization and ionic conduction, allowing us to generate heat in the core of the solution and not transmit it through the vessel. A large number of advantages as compared to the conventional route are listed in the literature and can be summarized as follows: stabilization of novel as well as metastable phases, improvement of reaction kinetics, energy efficiency. These advantages constitute a promising area of research.[13] Some authors have already proved that this route can be used for the synthesis of well-crystallized metal fluorides through ionic liquid decomposition[14] (Fe, Co, Zn, La, Y, Sr) or novel hydride metal fluorides.[15] We report here the direct synthesis using microwave irradiation of nanosized metastable β-AlF_3 containing hydroxyl groups. The key synthesis parameters to obtain pure nanosized β-$AlF_{3-x}(OH)_x$ are presented. An accurate characterization of the samples is carried out through X-ray diffraction, FTIR spectroscopy, BET measurement, transmission electron microscopy, and ^{27}Al and ^{19}F NMR spectroscopy.

2. Experimental Section

2.1. Microwave Synthesis and Determination of the Chemical Composition. Syntheses were performed using a MARS-5 Microwave Digestion System (CEM Corp.). Temperature was regulated by percent increments of the microwave power (300 W, 2.45 GHz frequency) and controlled by an optic fiber. Internal pressure was measured by a pressure sensor. In a first step, a precursor solution was prepared as follows: 12.5 mmol of Al(III) nitrate (Sigma-Aldrich, 98% $Al(NO_3)_3 \cdot 9H_2O$) was dissolved in a water/isopropanol solution (10 mL of distilled water/10 mL of isopropanol, Sigma-Aldrich, 98%). An aqueous solution of HF (Panreac 40%) was then added in order to get an [HF]/[Al] precursor molar ratio equal to 3, which led to the precipitation of α-$AlF_3 \cdot 3H_2O$. The final volume solution did not exceed 22 mL. The precursor was placed in a closed Teflon container for microwave hydrothermal synthesis (XP-1500 plus model). Two steps were used during this process. First, the solution was heated at 373 K (288 K/min) for 10 min and then at 433 K for 2 h. The first step was required because of the occurrence of a side reaction induced by microwave irradiation: an exothermic phenomenon leading to an increase in the temperature and an internal pressure reaching about 443 K and 16–18 bar, respectively, which took place after 5 min of irradiation. The origin of this phenomenon will be discussed latter.

After heat treatment, a microwave-assisted drying was performed under a primary vacuum and argon flow at 373 K. The powder was then washed with a large amount of ethanol under nitrogen pressure and finally outgassed at 573 K under a vacuum for 4 h.

The final [F]/[Al] molar ratio was measured by electron probe microanalysis (Castaing microprobe CECAMA SX 630 apparatus) using F^- titration with specific electrode and Al^{3+} by ICPMS at the CNRS Central Service of Analysis. Although it was very difficult to get an accurate determination of the [F]/[Al] ratio, the obtained data led to a value close to 2.5 ($\pm$ 0.1) whatever the water/isopropanol solution ratio used. Considering the electroneutrality equation, this value of the [F]/[Al] molar ratio led us to consider the occurrence of hydroxyl groups stabilized within the network. This hypothesis was further confirmed by FTIR spectroscopy and will be discussed in the following. A chemical composition could thus be considered for the β phase series: $AlF_{2.5}(OH)_{0.5} \cdot xH_2O$, x being determined by thermogravimetric analysis and found in the range of 0.1–0.2. To simplify the chemical formula, the water content will not be indicated in the following.

2.2. X-ray Diffraction Analysis. Powder diffraction patterns were recorded on a PANalytical X'Pert Pro diffractometer in a Bragg–Brentano geometry ($\theta-2\theta$), using Ge(111) monochromated Cu $K\alpha_1$ radiation (λ = 1.54051Å). The investigated 2θ range was 10–110° with a step of 0.017°.

The whole pattern profile matching and the Rietveld structural refinement were performed with the FULLPROF program.[16] Individual peak profile analysis was carried out using PROFILE, version 1.4 (Socabin, Bruker AXS).

2.3. Surface Area Measurement. N_2 adsorption isotherms were performed at 77 K using an ASAP 2000 instrument from Micromeritics. The powder sample of mass around 200 mg was evacuated overnight at 573 K under 0.1 Pa prior to adsorption. The specific surface area S_{BET} was calculated from BET results applied in the P/P_o (0.03–0.25) range. The estimated standard deviation (esd) has been calculated for surface areas larger than 30 $m^2\ g^{-1}$ and is equal to 5 $m^2\ g^{-1}$.

(5) Francke, L.; Durand, E.; Demourgues, A.; Vimont, A.; Daturi, M.; Tressaud, A. *J. Mater. Chem.* **2003**, *13*, 2330.
(6) Kemnitz, E.; Groβ, U.; Rudiger, S.; Shekar, C. S. *Angew. Chem., Int. Ed.* **2003**, *42*, 4251.
(7) Delattre, J. L.; Chupas, P. J.; Grey, C. P.; Stacy, A. M. *J. Am. Chem. Soc.* **2001**, *123*, 5364.
(8) Hajime, E. K. L. Y.; Delattre, J. L.; Stacy, A. M. *Chem. Mater.* **2007**, *19*, 894.
(9) Wander, A.; Bailey, C. L.; Searle, B. G.; Mukhopadhyay, S.; Harrison, N. M. *Phys. Chem. Chem. Phys.* **2005**, *7*, 3989.
(10) Wander, A.; Bailey, C. L.; Mukhopadhyay, S.; Searle, B. G.; Harrison, N. M. *J. Mater. Chem.* **2006**, *16*, 1906.
(11) Chaudhuri, S.; Chupas, P.; Morgan, B. J.; Madden, P. A.; Grey, C. P. *Phys. Chem. Chem. Phys.* **2006**, *8*, 5045.
(12) Kappe, C. O. *Angew. Chem., Int. Ed.* **2004**, *43*, 6250.
(13) Adam, D. *Nature* **2003**, *421*, 571.
(14) Jacob, D. S.; Bitton, L.; Grinblat, J.; Felner, I.; Koltypin, Y.; Gedanken, A. *Chem. Mater.* **2006**, *18*, 3162.
(15) Thanh, S. P.; Gaslain, F.; Leblanc, M.; Maisonneuve, V. *J. Fluorine Chem.* **2000**, *101*, 161.
(16) Rodríguez-Carvajal, J. *Physica B* **1993**, *192*, 55.

2.4. Scanning Electron Microscopy. SEM pictures were obtained with a FX 600 microscope. Surface charge elimination was achieved by silver deposition.

2.5. Transmission Electron Microscopy. Transmission electron microscopy (TEM) was performed on a TECNAI F20 equipment with a field emissive gun, operating at 200 kV and with a point resolution of 0.24 nm. Fast Fourier transforms (FFT) of high-resolution transmission electron microscopy (HRTEM) images were calculated using the Gatan Digital Micrograph software. TEM samples were prepared by dissolving a few milligrams of powder in ethanol. The solution was then dipped 10 min into an ultrasonic bath so as to disagglomerate powder particles. One drop of the solution was finally deposited on a Formvar/carbon copper grid.

2.6. FTIR Spectroscopy. Infrared transmission spectra were recorded on self-supporting wafers (2 cm^2, 20 mg), which were placed into an infrared quartz cell (KBr windows) connected to a vacuum line. Samples were activated under vacuum at 573 K for one night. Spectra were recorded with a resolution of 4 cm^{-1}. The IR spectrometer was a Nicolet Nexus apparatus equipped with an extended KBr beam splitter and a mercury cadmium telluride (MCT) detector. Gaseous ammonia was dried on molecular sieves prior to use.

2.7. NMR Spectroscopy. Quantitative ^{19}F Hahn echo Magic Angle Spinning (MAS) NMR spectra were acquired on an Avance 300 Bruker spectrometer ($B_0 = 7$ T), using a 2.5 mm ^{19}F optimized CP MAS probe, operating at a ^{19}F Larmor frequency of 282.2 MHz. The 90° and 180° pulse durations were set to 4 μs (RF field 60 kHz) and 8 μs, respectively, with an interpulse delay equal to one rotor period. The recycle delay was taken to 10 s. The ^{19}F chemical shifts were referenced to $CFCl_3$ at 0 ppm. These spectra were reconstructed using the DMFIT software,[17] which allows a full reconstruction of the spectra (including the spinning sidebands) with six adjustable parameters: isotropic chemical shift δ_{iso}, chemical shift anisotropy δ_{aniso}, chemical shift asymmetry parameter η_{CS}, line width, relative line intensity, and line shape. In this study, the δ_{iso} values, the relative line intensities, and the line widths are the relevant parameters; the other parameters are not discussed at all in the following.

^{27}Al ($I = 5/2$) MAS NMR spectra were recorded using a 2.5 mm CP MAS probe at spinning speed 30–32 kHz on an Avance 750 Bruker spectrometer ($B_0 = 17.6$ T) and an Avance 300 Bruker spectrometer ($B_0 = 7$ T) operating at a ^{27}Al Larmor frequency of 195.5 and 78.2 MHz, respectively. A short pulse length of 1 μs was used to ensure quantitative excitation of the whole spin system. The recycle delay was set to 1 s and 4096 fids were accumulated. ^{27}Al spectra were referenced to a 1 M aqueous solution of $Al(NO_3)_3$. Quantitative reconstructions[18–21] of the central lines of the ^{27}Al NMR spectra were achieved taking into account the $N = 0$ spinning sideband of the satellite transitions $\langle 3/2 \rangle$ and the $N = 0$ spinning sideband of the central transition $\langle 1/2 \rangle$, which completely overlap. For each ^{27}Al NMR site, the isotropic chemical shift δ_{iso} and the quadrupolar product $\nu_{Q\eta}$ were calculated by comparison of the center of gravity $\delta_{cs}^{\langle 3/2 \rangle}$ of the Al satellite sideband with that of the central transition $\delta_{cs}^{\langle 1/2 \rangle}$, through the following equation

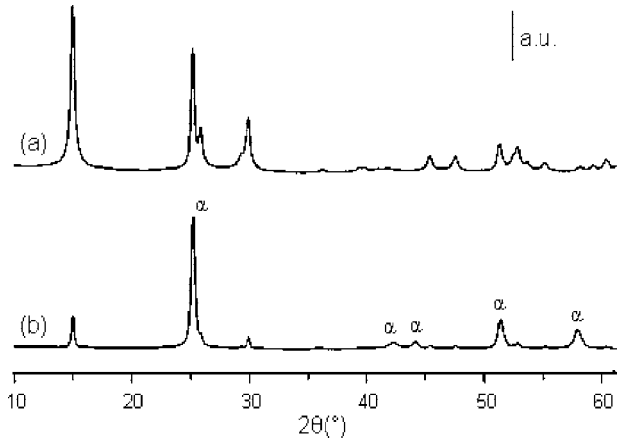

Figure 2. Effect of the aluminium precursor on the final product: X-ray diffraction powder pattern of material prepared from (a) aluminium nitrate and (b) aluminium chloride.

$$\delta_{cs}^{\langle m \rangle} = \delta_{iso} - \nu_{Q\eta}^2 \frac{[I(I+1) - 3 - 9m(m-1)]}{30\nu_0^2} \times 10^6$$

where $I = 5/2$ in the case of ^{27}Al, $\nu_0 = 195.5$ MHz (for the 17.6 T spectrometer) and $\nu_{Q\eta} = \nu_Q\sqrt{1+\eta_Q^2/3}$.[20]

^1H Hahn echo MAS NMR spectra were acquired on an Avance 300 Bruker spectrometer ($B_0 = 7$ T), using a 2.5 mm ^{19}F optimized CP MAS probe, operating at a Larmor frequency of 300 MHz for ^1H. They result in a broad unresolved peak between 0 and 10 ppm (referenced to ^1H in TMS at 0 ppm) that did not aid our analysis. These spectra are then neither shown nor discussed in the following.

3. Results and Discussion

3.1. Key Parameters of the Microwave-Assisted Route toward High-Surface-Area (HSA) β-$AlF_{3-x}(OH)_x$. *3.1.1. Nature of the Aluminum Precursor: Influence on the Final Allotropic Forms and Occurrence of a Secondary Reaction during the Microwave Process.* The effect of the Al^{3+} precursor has been investigated by comparing, in the conditions described above, aluminum nitrate (Sigma-Aldrich, 98% $Al(NO_3)_3 \cdot 9H_2O$) and aluminum chloride (Sigma-Aldrich, 98% $AlCl_3 \cdot 9H_2O$) precursor. The powder X-ray diffraction patterns of the as-prepared samples are shown in Figure 2. Pure β phase could be prepared by using nitrate precursor, in good agreement with JCPDS-ICDD file 84–1672, whereas the chloride precursor led to the stabilization of the thermodynamically stable phase α-AlF_3 (JCPDS-ICDD file 44–0231) as the major phase. As previously introduced, the use of nitrate as precursor leads to secondary reactions, which are characterized by an increase in the temperature and the pressure inside the vessel. Microwave-assisted synthesis is known to be able to induced side reactions. For instance, nitric acid was used to study the kinetics of the decomposition of organic substances under microwave irradiation. [22] One can assume that the reaction implying nitrate and isopropanol must be involved in the exothermic phenomenon observed. To confirm this hypothesis, we first recovered the

(17) Massiot, D.; Fayon, F.; Capron, M.; King, I.; Le Calvé, S.; Alonso, B.; Durand, J.-O.; Bujoli, B.; Gan, Z.; Hoatson, G. *Magn. Reson. Chem.* **2002**, *40*, 70.
(18) Massiot, D.; Bessada, C.; Coutures, J. P.; Taulelle, F. *J. Magn. Reson.* **1990**, *90*, 231–242.
(19) Alemany, L. B.; Massiot, D.; Sherriff, B. L.; Smith, M. E.; Taulelle, F. *Chem. Phys. Lett.* **1991**, *177*, 301–306.
(20) Massiot, D.; Müller, D.; Hübert, Th.; Schneider, M.; Kentgens, A. P. M.; Coté, B.; Coutures, J. P.; Gessner, W. *Solid State Nucl. Magn. Reson.* **1995**, *5*, 175–180.
(21) Stebbins, J. F.; Kroeker, S.; Lee, S. K.; Kiczenski, T. J. *J. Non-Cryst. Solids* **2000**, *275*, 1–6.
(22) Kubrakova, I. V.; Khamizov, R. Kh. *Russ. Chem. Bull., Int. Ed.* **2005**, *54*, 1413–1417.

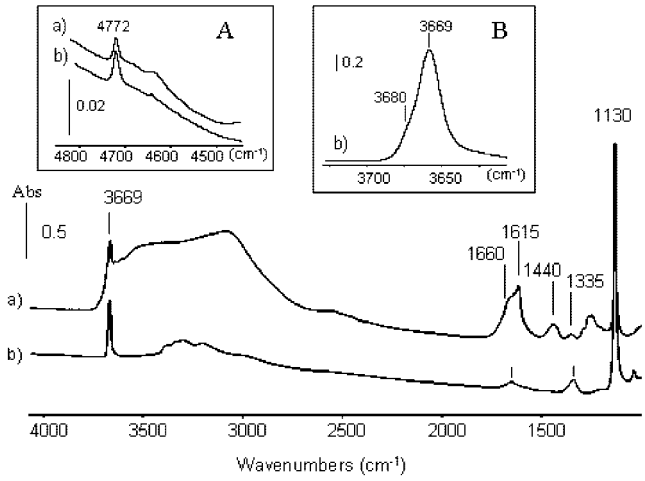

Figure 3. Infrared spectra of HSA β-$AlF_{3-x}(OH)_x$ (a) before and (b) after activation at 573 K. (Inset A: ($\delta+\nu$)OH region. Inset B: ν(OH) region).

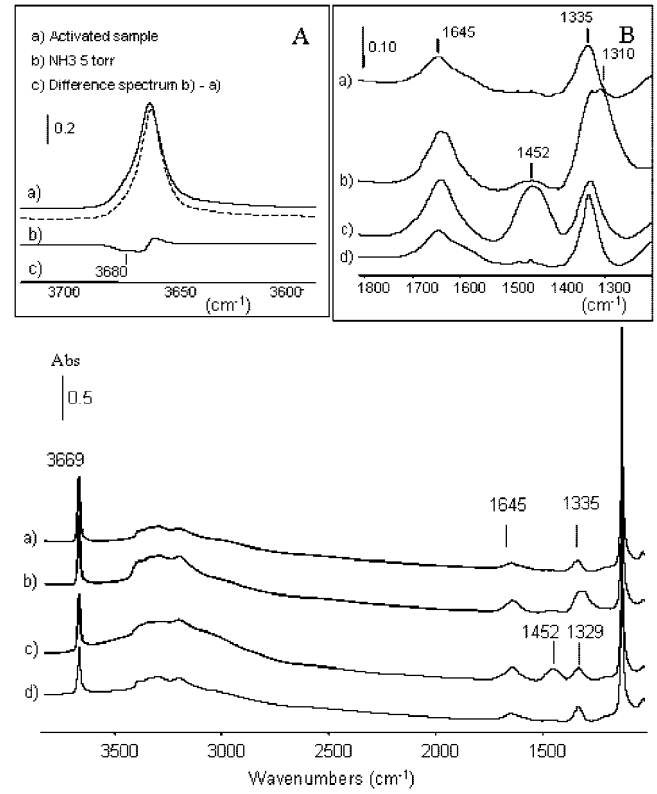

Figure 4. Infrared spectra of HSA β-$AlF_{3-x}(OH)_x$ recorded (a) after activation at 573 K, (b) after introduction of 5 Torr of NH_3 followed by evacuation at RT, (c) after introduction of $P_e = 1$ Torr of water followed by evacuation at RT, and (d) after evacuation at 573 K. Inset A: ν(OH) region. Inset B: zoom on the 1800–1250 cm^{-1} region.

remaining filtrate after microwave-assisted synthesis for analysis using a coupled gas chromatography/mass spectrometry performed by the CNRS Central Service of Analysis (SCA Vernaison). The analysis showed the presence of acetone and other products, which confirmed that isopropanol was oxidized during the synthesis.

It was interesting to then identify the redox couple at the origin of the partial oxidative process. In this aim, FTIR spectroscopy was performed on a sample prepared from nitrate, i.e., pure β-$AlF_{3-x}(OH)_x$. IR spectra of the sample before and after activation at 573 K are displayed in Figure 3. The IR spectrum of the sample before any activation (Figure 3a) exhibits many bands due to either bulk vibration or surface groups with impurities like water. After activation at 573 K, the latter is almost removed. According to Vimont et al., [23] the bands detected at 4772, 3669, and 1130 cm^{-1} are ascribed to $\nu+\delta$(OH), ν(OH), and δ(OH) of bridged Al−OH, respectively, confirming the presence of OH groups substituting fluoride ions into the network.

Before activation, supplementary bands are observed in particular in the 1700–1200 cm^{-1} region (Figure 3a). They could be due to adsorbed water or to impurities resulting from the synthesis mode. The occurrence of a weak band at 5270 cm^{-1} (not shown) unambiguously reveals the presence of water ($\nu+\delta(H_2O)$ mode). Therefore, the band at 1615 cm^{-1} with a shoulder at about 1660 cm^{-1} mainly characterizes the $\delta(H_2O)$ mode of water species, which are also responsible for the broadband near 3200 cm^{-1} ($\nu(H_2O)$).

Nevertheless, other bands like those at 1440 and 1335 cm^{-1} cannot be assigned to adsorbed water. Taking into account the preparation mode of the sample, nitrate-derived species could be considered. Infrared band frequencies of nitrate species depend on their structure. In particular, bridged species are characterized by a couple of $\nu(NO_3)$ bands near 1200 and 1600–1650 cm^{-1}. After activation at 573 K, two bands are still present at 1335 and 1645 cm^{-1} in addition to a broadband between 3400 and 3000 cm^{-1} (Figure 3b). Taking into account that the latter unambiguously characterizes the presence of NH_x species, we can deduce from the frequency of the bands at 1345 and 1635 cm^{-1} the occurrence of coordinated NH_3 species.

To check such an assignment, NH_3 has been adsorbed on the activated sample (Figure 4b). It is clear that the intensity of all NH_x bands has notably increased, confirming the presence of residual ammonia species onto the activated sample. The band near 1330 cm^{-1} is assigned to the $\delta s(NH_3)$ mode of coordinated NH_3 species; its frequency increases with the strength of the coordination sites.[24] Its position at 1335 cm^{-1} in the spectrum of the activated sample reveals the presence of very strong Lewis acid sites, in agreement with previous results on the β phase.[24] The strength of the NH_3 coordination is such that activation under a vacuum at 573 K is not sufficient to completely eliminate NH_3 species that can be localized on the outer surface or trapped into the HTB channels during the synthesis process. Ammonia addition at room temperature gives rise to a supplementary $\delta s(NH_3)$ band at 1310 cm^{-1} (Figure 4b, inset B), revealing the presence of weaker Lewis acid on the surface. Furthermore, the inset B of Figure 4d shows that evacuation at 573 K eliminates the NH_3 coordinated species adsorbed on these sites.

The addition of ammonia at room temperature gives also rise to a weak band at 1452 cm^{-1} assigned to ammonium

(23) Vimont, A.; Lavalley, J. C.; Francke, L.; Demourgues, A.; Tressaud, A.; Daturi, M. *J. Phys. Chem. B* **2004**, *108*, 3246.

(24) Busca, G. *Phys. Chem. Chem. Phys.* **1999**, *1*, 723.

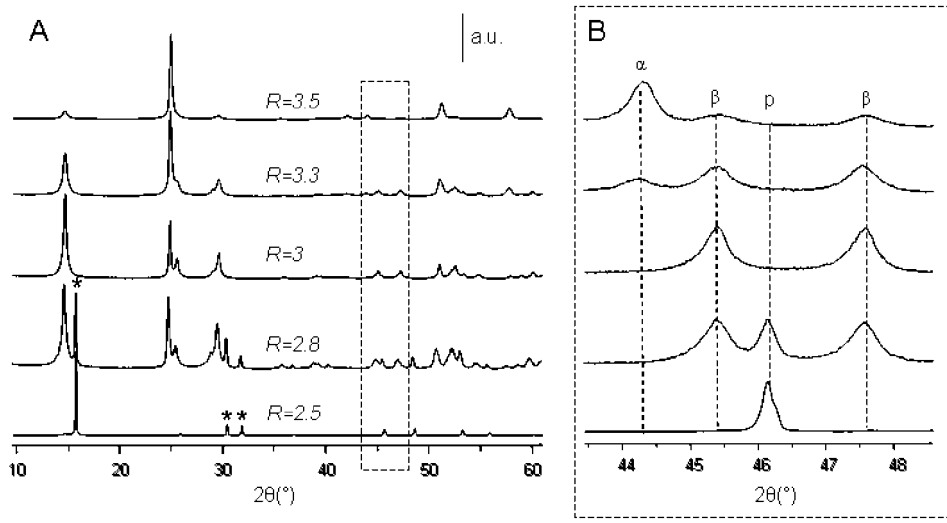

Figure 5. Evolution of the X-ray diffraction powder patterns as a function of the R = [HF]/[Al] precursor molar ratio: (A) global view where asterisks account for the main lines of the pyrochlore phase, (B) zoom, α, β, and p are assigned to α-AlF_3, β-AlF_3, and pyrochlore type structures, respectively.

species (Figure 4b, inset B). The formation of such species requires the presence of surface hydroxyl groups or residual water species. The difference spectrum before and after NH_3 adsorption at room temperature (Figure 4c, inset A) reveals the presence of a shoulder near 3680 cm^{-1}, which disappears after NH_3 sorption, whereas the strong band at 3669 cm^{-1} is not perturbed. NH_3 sorption has then highlighted the presence of surface OH groups on the activated sample; their frequency (3680 cm^{-1}), which is slightly higher than that of the bulk OH groups (3669 cm^{-1}), has been ascribed to the absence of the confinement effect occurring in the bulk. [24]

Water addition on the sample precovered with NH_3 leads to an increase in the intensity of the band at 1452 cm^{-1} because of the ammonium species, whereas the other band at 1310 cm^{-1} decreases (Figure 4c). This result shows that water converts NH_3 coordinated species into ammonium species and explains why the intensity of the 1440 cm^{-1} band is relatively intense in the spectrum of the nonactivated sample (Figure 3a).

Therefore, FTIR spectroscopy clearly shows that nitrate is reduced during the synthesis into ammonium ions. Furthermore, the thermodesorption of ammonium species shows the presence of strong Lewis acid sites. The importance of such species acting as initiators of the synthesis of the HTB-type structure is clearly illustrated in the present hydrothermal process. The exothermic redox reaction involving NO_3^- as the oxidizer and isopropanol as the reducing agent plays a key role in this synthesis, with the help of ammonium ions as templates for the stabilization of pure β-$AlF_{3-x}(OH)_x$. It is a similar process that occurs in conventional routes, i.e., the thermal degradation of either hydrate $AlF_3 \cdot 3H_2O$ or ammonium aluminum hexafluoride $(NH_4)_3AlF_6$,[5] in which molecules such as water or ammonium ions are involved in the formation of HTB-type structure.

3.1.2. [HF]/[Al] Precursor Molar Ratio: Relationships between the OH/F Content and the Nature of the Final Allotropic Form. To optimize the synthesis results, we varied the R = [HF]/[Al] precursor molar ratio from 2.5 to 3.5 using aluminum nitrate as precursor and a water/isopropanol solvent ratio equal to 1. Figure 5 shows the evolution of the powder X-ray diffraction patterns as a function of the [HF] content. Three domains can be distinguished: (i) for $R < 3$, (ii) $R = 3$, and (iii) $R > 3$. For lower ratio values, i.e., R = 2.5, hydroxyfluorides exhibiting the pyrochlore type structure with the $AlF_{1.5}(OH)_{1.5} \cdot xH_2O$ chemical composition[3b] are obtained as the major phase; an increase in the [HF] concentration up to $R = 2.8$ leads to a mixture of two phases: the β and pyrochlore forms. As described in the synthesis procedure, pure β form could be obtained using a precursor molar ratio equal to 3. Finally, higher [HF] contents lead to the appearance of the α-AlF_3 phase as an impurity. A zoom on the 43–49° 2θ range is presented in Figure 5B; it clearly shows the crucial influence of the [HF] content on the nature of the stabilized phase. This part of the diffractogram also accounts for the phase purity because in the 23–25° 2θ range, the α-AlF_3 main line cannot be clearly distinguished, because of the proximity of the β (002) reflection line.

Table 1. Correlation between the Al−X−Al angles and Building Units Present in the Hydroxy-Fluorides Series

phase	Al−X−Al (X = F or OH) bond angles (deg)	building units (*n*-membered rings)
α-AlF_3	158	4
β-AlF_3	148–148–166	3−6−4
pyrochlore $AlF_{1.5}(OH)_{1.5}$	141	3−6

The structural sequence of these various phases can be also related to the number of hydroxyl groups inside the framework, which is strongly dependent on the [HF]/[Al] precursor molar ratio. It appears that for increasing amounts of HF, the presence of fluoride ions favors, in a first step, the formation of the pyrochlore $AlF_{1.5}(OH)_{1.5}$, then β-$AlF_{3-x}(OH)_x$, and finally, the α-AlF_3 phase. Chupas et al. have described the structures of the aluminum fluoride allotropic forms by taking into account simple building units $(Al-F-)_n$, where n is the

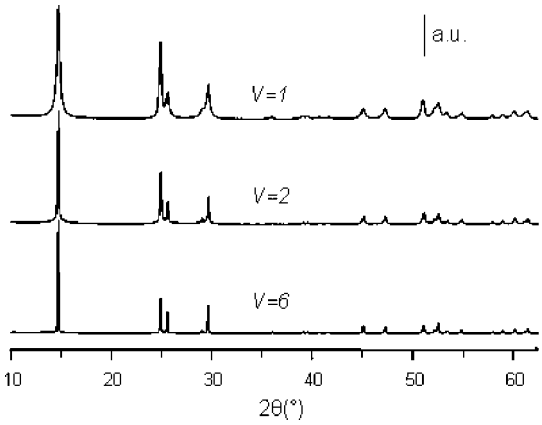

Figure 6. Dependence of the X-ray diffraction powder pattern with the volume ratio of solvents $V = V_{water}/V_{isopropanol}$.

number of units forming the ring.[25] Table 1 summarizes the building units present in the α, β, and pyrochlore phases with the corresponding Al−X−Al angles. β-AlF_3 exhibits three- and six-membered rings in the *a*, *b* plane, as well as four-membered rings in the *b*, *c* plane.The α-AlF_3 phase exhibits four-membered rings, whereas the pyrochlore presents three- and six-membered rings. Thus, hydroxyl groups, because of the presence of hydrogen atoms, favor small Al−X−Al (X = F or OH) angles, as typically found in the three-membered rings. This assumption is consistent with our observation that an increase in the [HF] content leads to the following sequence: pyrochlore → β-$AlF_{3-x}(OH)_x$ → α-AlF_3. Low [HF] contents favor small Al−X−Al angle, as found in the three- and six-membered rings of the pyrochlore phase. When passing from the pyrochlore to the β phase, the number of hydroxyl groups decreases, and conversely, the Al−X−Al angles of the three- and six-membered rings increase. The appearance of four-membered rings in the β phase corresponds to an even higher Al−X−Al angle of 166°. Finally, the α-AlF_3 network shows Al−X−Al angles of only 158°, lower than the four-membered ring angle found in the β form but larger than the three- and six-membered rings, because the framework consists of a denser packed stacking. Therefore, by tuning the [HF]/[Al] precursor molar ratio, a correlation between the types of the building units, the Al−X−Al angle and the OH/F final content can be established.

3.1.3. Influence of the Solvent Ratio: Monitoring the Surface Area by Limiting the Crystallization Kinetics. As shown previously, pure HTB phase can be obtained using nitrate as Al precursor and a [HF]/[Al] precursor molar ratio equal to 3. To get high-surface-area materials, we have tuned the volume ratio of the used solvents $V = V_{water}/V_{isopropanol}$, ranging from $V = 6$ to $V = 1$. The evolution of the powder X-ray diffraction patterns as a function of the volume ratio *V* has been represented in Figure 6. As can be observed, the increase in isopropanol content leads to a broadening of the X-ray diffraction peaks. In a first approximation, this can be ascribed to a decrease in the particle size. This trend was confirmed by measuring the surface area. As revealed by the BET method, the surface area of the materials

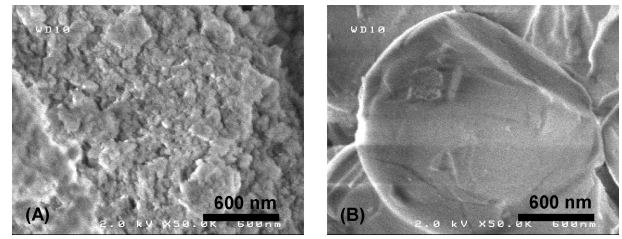

Figure 7. Scanning electron micrographs of (A) high- and (B) low-surface-area β-$AlF_{3-x}(OH)_x$.

Table 2. Surface Areas of β-$AlF_{3-x}(OH)_x$ Materials

sample	water/isopropanol volume ratio	surface area ($m^2\ g^{-1}$)
HSA	1	82
MSA	2	49
LSA	6	3

increases with increasing isopropanol rates and corresponds to 3, 49, and 82 $m^2\ g^{-1}$ for $V = 6$, 2, and 1, respectively. The materials have been named as low (LSA), medium (MSA), and high (HSA) surface area, as reported in Table 2. The effect of the isopropanol on the crystallization growth is clearly highlighted on the scanning electron micrographs represented in Figure 7, illustrating the drastic change in both the particle size and their morphology. Whereas LSA β-$AlF_{3-x}(OH)_x$ exhibits very large particles, HSA β-$AlF_{3-x}(OH)_x$ consists of nanosized particles. Therefore, by varying the solvent medium, we can monitor the surface area, and an aqueous medium favors the crystallization growth, whereas the presence of isopropanol limits its kinetics.

3.2. Structural Investigation of β-$AlF_{3-x}(OH)_x$. *3.2.1. Microstructural Characterization of the High-Surface-Area Material: From Williamson−Hall Approach to Global Profile Refinement.* The microstructural features (coherent domain size and strains) of the samples of the β-$AlF_{3-x}(OH)_x$ series were extracted from the additional broadening of the Bragg peaks with respect to the instrumental one. For our diffractometer, this instrumental contribution to the line broadening was previously established for XRD patterns of standard LaB_6 powder.

Initial profile matching (Le Bail fit) of the diffraction pattern of HSA β-$AlF_{3-x}(OH)_x$ using an isotropic model of the size and strain line broadening did not gave satisfactory results: $cR_p = 12.8\%$, $cR_{wp} = 15.7\%$, $\chi^2 = 3.96\%$. One can see in Figure 8 that the full width at half maximum (fwhm) of some experimental peaks is smaller than the calculated one, (002), whereas for other lines it is larger, (200), (130). This *hkl*-dependent line broadening suggests some anisotropy related to the sample intrinsic microstrains or crystallite shape.

The following parts will be devoted to the analysis of the anisotropic line broadening and microstructural effects in HSA β-$AlF_{3-x}(OH)_x$. Our approach was based on two integral-breadth methods: Williamson−Hall[26] and whole pattern profile matching.

3.2.1.1. Williamson−Hall Approach. The Williamson−Hall method is a good starting point of the microstructural

(25) Chupas, P. J.; Corbin, D. R.; Rao, V. N. M.; Hanson, J. C.; Grey, C. P. *J. Phys. Chem. B* **2003**, *107*, 8327.

(26) Williamson, G. K.; Hall, W. H. *Acta Metall. Sin.* **1953**, *1*, 22.

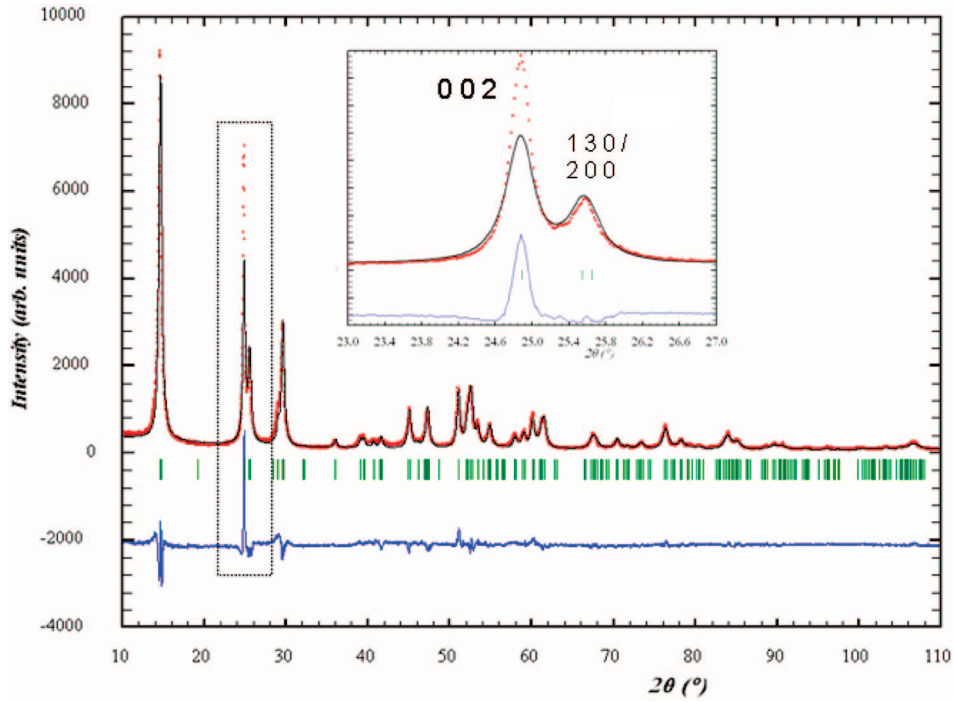

Figure 8. Initial profile matching of the diffraction pattern of HSA β-AlF$_{3-x}$(OH)$_x$ using isotropic model. Experimental X-ray diffraction powder pattern (red curve) compared to the Rietveld-refined profile (black curve) and the difference curve (blue curve). The vertical bars correspond to the positions of the Bragg reflections. Inset: zoom on the (002) reflection line.

characterization because it allows one to identify the relative contribution of each size or strain effects to the broadening of the X-ray diffraction peaks. Here, a simplifying assumption makes all diffraction peaks considered to be Lorentzian. In that case, the observed integral breadth (β_{obs}) can be adjusted for the instrumental broadening contribution (β_{ins}) by a simple substraction of the latter so the sample intrinsic part is obtained: $\beta_{samp} = \beta_{obs} - \beta_{ins}$. Moreover, β_{samp} is the sum of the size and the strain broadening contributions through the following relation: $\beta_{samp} = \lambda/(L \cos\theta) + 4(\tan\theta)\epsilon$ or $\beta_{samp} \cos\theta = A + B \sin\theta$, where $A = \lambda/L$ and $B = 4\epsilon$. So when a diagram $\beta_{samp} \cos\theta = f(\sin\theta)$ is dressed for a number of diffraction peaks, the average crystallite size $\langle L \rangle$ and strains $\langle \epsilon \rangle$ can be easily evaluated from the ordinate at the origin A and the slope B, respectively.

A Williamson−Hall diagram for HSA β-AlF$_{3-x}$(OH)$_x$ was dressed with selected peaks (Figure 9). We focused our attention on the well-resolved lines that could be suitably separated for an individual profile fit. Among them are some of the most badly fitted ones by the isotropic size and strain broadening model (Figure 8). Despite the limited number of data for the Williamson−Hall diagram, two series of points are distinguished, each one being fitted with a linear regression. The first one is related to (00l) line (or at least line l-index high toward h and k), and the second one to the (hk0) lines. The two fits are parallel, so one has to consider the strain-related contribution to the line broadening as being isotropic. On the other hand, the plot gives good evidence for anisotropic size-related broadening of the Bragg peaks. The large peaks overlap in the diffraction pattern makes the (h00) and (0k0) lines absent from our Williamson−Hall diagram. So the determination of the anisotropy direction is rather tricky

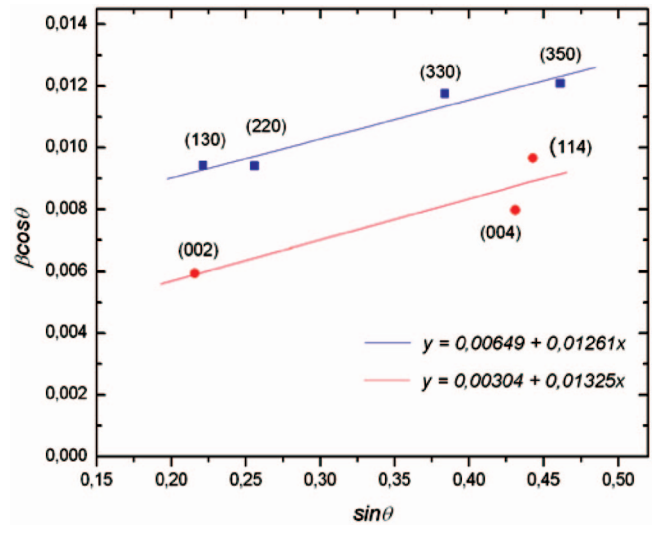

Figure 9. Williamson−Hall plots of HSA β-AlF$_{3-x}$(OH)$_x$.

with regard to the orthorhombic symmetry of the unit cell. However, the (00l) lines being sharper, this is an indication for a large domain size along the [001] direction. The simplest shape model compatible with that observation is a needle along the c axis. The approximate values of the limit dimensions deduced from the Williamson−Hall diagram correspond to a $\langle L00l \rangle / \langle Lhk0 \rangle$ ratio around 2.

3.2.1.2. Global Profile Refinement. This method offers the possibility to get a much more fine analysis of the microstructure and to calculate accurate values for the microstrains and the crystallite size.[27] The peak profiles are fitted using the pseudo-Voigt function of Thompson−Cox−Hastings,[28] which allows refining separately the angular dependence of both Lorentzian (H_L) and Gaussian (H_G) components of fwhm. So, for a given diffractometer with

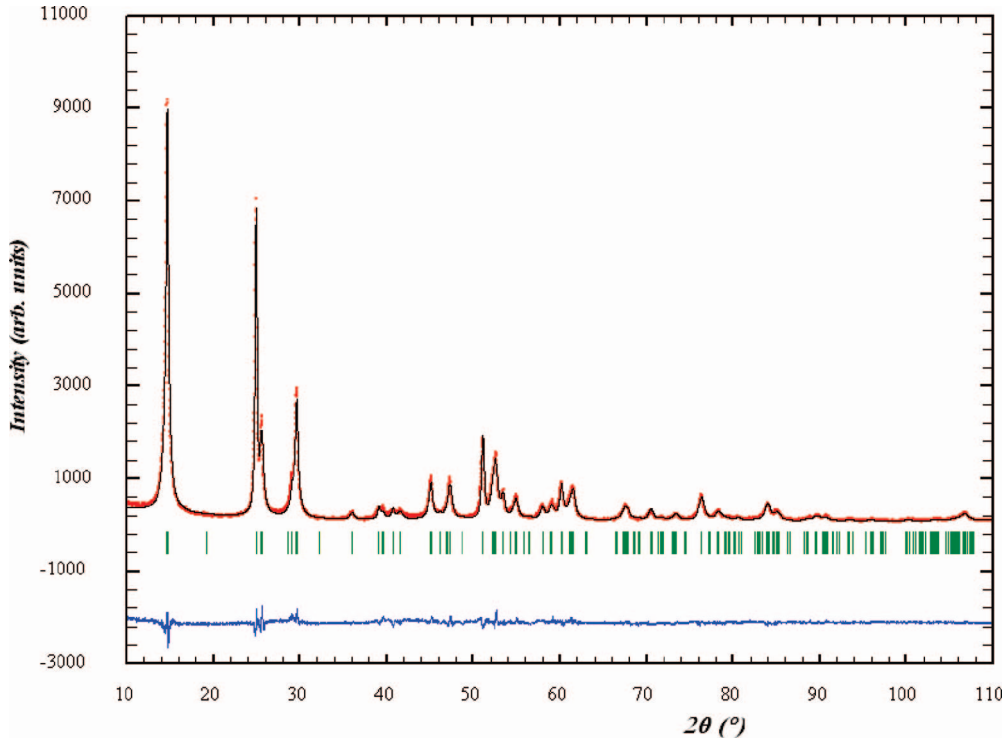

Figure 10. Final profile matching of the diffraction pattern of HSA β-$AlF_{3-x}(OH)_x$ using an anisotropic size model, i.e., platelet running in the *b*, *c* plane. Experimental X-ray diffraction powder pattern (red curve); Rietveld-refined profile (black curve), and difference curve (blue curve). The vertical bars correspond to the positions of the Bragg reflections.

previously defined instrumental resolution function, the sample contributions to the line profile are calculated as follows

$$H_G^2 = (U_{\text{strain\_iso}} + (1-\xi)^2 D^2_{\text{strain\_aniso}}) tg^2\theta + \frac{G_{\text{size\_iso}}}{\cos^2\theta}$$

$$H_L = (X_{\text{strain\_iso}} + \xi D_{\text{strain\_aniso}}) tg\theta + \frac{Y_{\text{size\_iso}} + F_{\text{size\_aniso}}}{\cos\theta}$$

where $U_{\text{strain\_iso}}$, $X_{\text{strain\_iso}}$, $G_{\text{size\_iso}}$, and $Y_{\text{size\_iso}}$ are refinable parameters related to an isotropic strain and size broadening effects, whereas $D_{\text{strain\_aniso}}$ and $F_{\text{size\_anizo}}$ are analytical functions for the *hkl*-dependent model. ζ is a mixing coefficient for the Lorentzian part of strains. The integral method is finally applied to calculate apparent crystallite size and strains in the sample.

The whole profile matching of the diffraction pattern of HSA β-$AlF_{3-x}(OH)_x$ was resumed using different anisotropic size broadening models. The first to be applied was the needlelike model, suggested by the Williamson−Hall analysis, and it was not successful. Satisfactory refinement was reached when using a platelet-shaped model with the short dimension along the *a* axis ($cR_p = 7.8\%$, $cR_{wp} = 9.7\%$, $\chi^2 = 1.5\%$). The final fit is displayed in Figure 10. This result is perfectly compatible with the Williamson−Hall plot because it defines the largest values for the domain size along the [00*l*], [0*k*0], and [0*kl*] directions. The calculated limit dimensions of the platelet crystallites are 8 nm along the *a* axis and 34 nm in the *b*, *c* plane. The average particle size was 15 nm. The microstrains, for their part, were refined within an isotropic model and the calculated average value is $\epsilon = 2.2 \times 10^{-3}$.

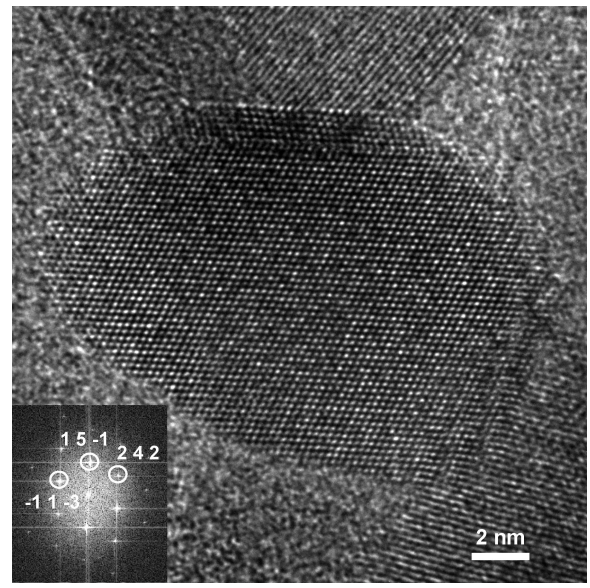

Figure 11. HRTEM image of an HSA β-$AlF_{3-x}(OH)_x$ particle with [−723] zone axis. The corresponding Fourier transform is given in the inset.

3.2.1.3. Transmission Electron Microscopy. High-resolution transmission microscopy experiments were performed on the HSA material, and Figure 11illustrates a HRTEM image of a particle typically observed during HRTEM investigation. The corresponding Fourier transform performed on the particle is shown on the inset of the Figure

(27) Rodriguez-Carvajal, J.; Roisnel, T. Line broadening analysis using Fullprof: determination of microstructural properties. *Proceedings if the 8th European Powder Diffraction Conference*, Uppsala, Sweden, May 23−26, 2002; Trans Tech Publication: Zurich, Switzerland, 2002.
(28) Thompson, P.; Cox, D. E.; Hastings, J. B. *J. Appl. Crystallogr.* **1987**, *20*, 79.

Table 3. Rietveld Refinement Results

sample	cell parameters (Å)	B_{iso} (Å^2)	cR_p (%)	cR_{wp} (%)	R_{Bragg} (%)	χ^2 (%)
HSA	6.9681(2) 12.0360(3) 7.1434(1)	Al^{3+}: 0.79(3); F^-:0.83(3)	11	13.2	4.1	2.96
LSA	6.9494(4) 12.0352(6) 7.1328(8)	Al^{3+}: 0.62(3); F^-:1.25(4)	22.6	24.2	8.8	3.85

Table 4. Comparison of Crystallographic Data of HSA and LSA β-AlF$_{3-x}$(OH)$_x$ with Those of β-AlF$_3$

interatomic distances (Å), bond angles (deg)	HSA-AlF$_{3-x}$(OH)$_x$	LSA-AlF$_{3-x}$(OH)$_x$	β-AlF$_3$
Al2−F1	2 × 1.857(12)	2 × 1.83(3)	2 × 1.800(1)
Al1/Al2−F2	4 × 1.77(3)/2 × 1.82(2)	4 × 1.81(8)/2 × 1.78(9)	4 × 1.801(1)/2 × 1.800(1)
Al1−F3	2 × 1.789(5)	2 × 1.787(6)	2 × 1.796(1)
Al2−F4	2 × 1.804(8)	2 × 1.803(9)	2 × 1.798(1)
Al2−F1−Al2	139.4(5)	143.7(12)	148.7
Al1−F2−Al1	151.9(11)	151.0(4)	148.3
Al1−F3−Al1	173.1(2)	172.3(3)	166.4
Al2−F4−Al2	163.8(4)	162.9(4)	165.5

11, and the zone axis particle has been indexed as [−723]. Because of the high *h* values and low *k* and *l* ones, this zone axis can be assimilated to [*h*00] type. This is consistent with the model used for X-ray diffraction analysis, i.e., a platelet model perpendicular to the a direction. Finally, one should have to point out that the particle size that can be associated to a (0*kl*) plane is in the range of that determined by refinement, i.e., 13–18 nm.

3.2.2. Probing the Anionic Environment by Rietveld Refinement and NMR Spectroscopy: OH/F Ordering. As previously quoted, the β phase adopts the *Cmcm* space group,[3c] in which Al atoms occupy two crystallographic sites Al1 and Al2, in the 4b and 8d Wyckoff positions, respectively. In addition to the different multiplicity, Al1 and Al2 also differ on the type of anionic environment. Al1 is surrounded by four F2 and two F4, whereas Al2 is surrounded by two F3, two F1, and two F2, which link both aluminum atoms. F3 and F4 fluorine atoms form the four-membered rings, which are related to the building unit presents in α-AlF$_3$, whereas F1 and F2 atoms described the six-membered rings.

Crystalline structures of HSA and LSA β-AlF$_{3-x}$(OH)$_x$ were refined by the Rietveld method. Some refinement results are summarized in Table 3.

Interatomic Al−X (X = OH, F) distances found in aluminum fluorides differ from those in hydroxyfluorides phases: 1.797 and 1.842 Å in α-AlF$_3$ and pyrochlore AlF$_{1.5}$(OH)$_{1.5}$ phases, respectively.[3a,3b]

In an attempt to localize the hydroxyl groups inside peculiar crystallographic sites of the HTB framework, some refined interatomic distances and angles of HSA and LSA β-AlF$_{3-x}$(OH)$_x$ are displayed in Table 4 and are compared with those of the free-hydroxyl compound β-AlF$_3$. Atomic positions are available in the Supporting Information. In both samples, the two F3 and F4 anionic crystallographic sites present interatomic distances in the range of those found in β-AlF$_3$. These sites can thus be considered as fully fluorinated. On the contrary, the large estimated standard deviations observed for interatomic distances relative to F1 and F2 sites show that the structures should present a heterogeneity of distances, which depends on the nature of the anion occupying these sites. The long Al−F1 distance found in the case of HSA β-AlF$_{3-x}$(OH)$_x$ should account for the location of OH groups in this site (Table 4). Therefore, in both samples, sites F1 and F2 can thus be considered as partially hydroxylated. As explained previously, the presence of hydroxyl groups tend to favor small Al−X−Al angles. In both HSA and LSA β-AlF$_{3-x}$(OH)$_x$, the Al2−F1−Al2 angle (Table 4) is smaller than those found in hydroxyl-free β-AlF$_3$, confirming the presence of OH groups in this site. On the contrary, the Al1−F2−Al2 angle is larger than that found in β-AlF$_3$. This can be explained considering that the strain induced by the small Al2−F1−Al2 angle should be compensated by the relaxation of the Al1−F2−Al2 angle, because a decrease in both angles should lead to the destabilization of the structure. Nevertheless, the F2 site should probably contain fewer OH species than the F1 one.

To probe the F/OH anionic repartition and the cationic disorder, we have used ^{19}F and ^{27}Al MAS NMR spectroscopies for both LSA and HSA samples.

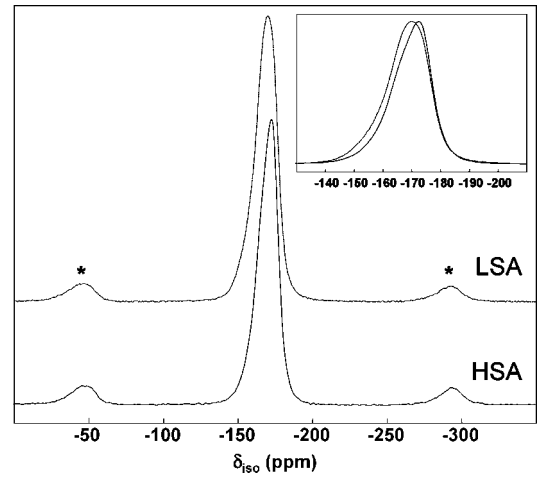

Figure 12. ^{19}F MAS NMR spectra of LSA and HSA at 34 kHz. The star symbols indicate the spinning sidebands.

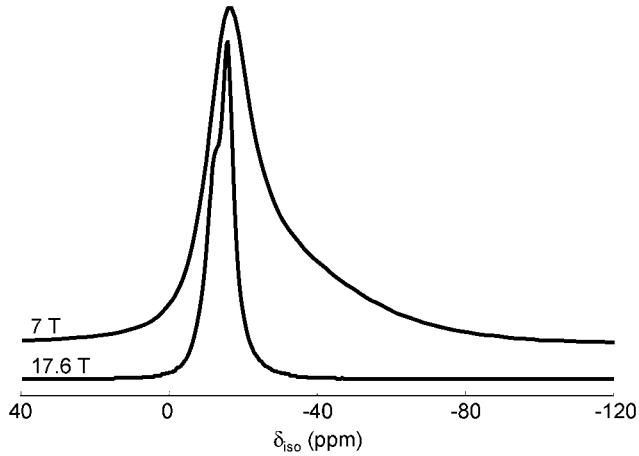

Figure 13. Central transition of the[27] Al NMR spectra of the LSA sample recorded at 7 and 17.6 T.

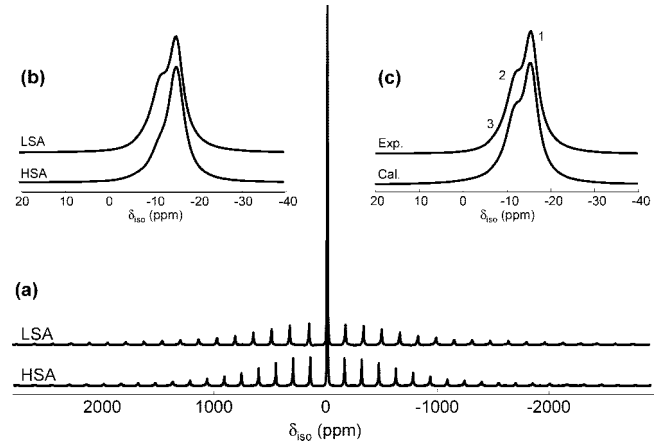

Figure 14. (a) Experimental[27] Al NMR spectra of LSA and HSA, recorded at 17.6 T, at spinning rates of 32 and 30 kHz, respectively. (b) Central transition of both compounds. The reconstruction of the central transition of the LSA sample using three contributions is presented in (c).

^{19}F MAS NMR spectra of LSA and HSA, displayed in Figure 12, show one broad peak. Despite the existence of four different fluorine sites for each sample, the spectra were reconstructed using three contributions whose characteristics are gathered in the Supporting Information. The widths of the resonances (2–6 kHz) mirror the chemical shift distribution related to the disorder around fluorine atoms in these compounds. The lowest δ_{iso} values may be related to fluorine atoms in AlF_6^{3-} octahedra (δ_{iso} (^{19}F in α- and β-AlF_3) = −172[29]). As already observed,[25,29–36] ^{19}F chemical shifts of octahedral aluminum environments with oxygen and fluorine in the first coordination sphere increase with the oxygen content. Despite identical chemical formula for the two compounds, it can be noticed that the δ_{iso} values increase from HSA to LSA sample (Figure 12), which may indicate a more important OH/F ratio in the LSA sample.

^{27}Al MAS NMR spectra of HSA and LSA materials recorded at 7 and 17.6 T are shown in Figure 13. The full spinning sideband manifold is featureless (Figure 14), indicating a distribution of quadrupolar coupling constants (QCCs) supported by the characteristic tail of the central transition of the 7 T spectra (Figure 13). The high magnetic field reduces the influence of the quadrupolar interaction contribution to the spectrum, allowing resolution of ^{27}Al resonances with close δ_{iso} values. Deconvolution of both spectra shown in Figure 14c for the LSA sample and in the Supporting Information for the HSA sample is achieved with three Gaussian lines (see Experimental Section) whose features are gathered in Table 5. The chemical shifts range from −15.5 to −7.7 ppm, characteristic of a 6-fold coordinated aluminum ion. It can be reminded that pure aluminum fluorides, α- and β-AlF_3, exhibit resonances at −16 and −15 ppm, respectively.[29,37] The appearance of peaks at higher chemical shifts is assigned to the occurrence of oxygen in the vicinity of Al^{3+} ions.[25,29,30,32–36] For LSA and HSA β-$AlF_{3-x}(OH)_x$, the $\nu_{Q\eta}$ values are higher than that of β-AlF_3 (132 kHz).[29] Moreover, the $\nu_{Q\eta}$ values increase with the number of OH groups in the vicinity of Al^{3+} ions (Table 5), in agreement with a more disordered environment. One can notice larger $\nu_{Q\eta}$ values for HSA. The higher surface area may give rise to more distorted $AlF_{6-x}(OH)_x$ octahedra.

As shown in Figure 14 and Table 5, the peaks at higher chemical shifts have a higher relative intensity in the LSA sample than in the HSA sample, in contradiction with the proposed identical chemical formula. This discrepancy is ascribed to the difficulty to accurately determine the OH/F ratio in those compounds. To quantify the various possible $AlF_{6-x}(OH)_x$ environments, we considered three compositions that remain within the uncertainty on compositions given by chemical analyses: $AlF_{2.6}(OH)_{0.4}$, $AlF_{2.5}(OH)_{0.5}$, and $AlF_{2.4}(OH)_{0.6}$. On the basis of a random F/OH distribution occurring on F1 and F2 sites, the various possible environments are $AlF_2F'_{4-x}(OH)_x$ with F = F3 or F4 and F′ = F1 and/or F2 (Figure 1) whose probabilities of occurrence are given for the three compositions in Table 6 taking into account a binomial law. If we assume that AlF_6 and $AlF_5(OH)$ species give rise to the main peak observed at −15.5 ppm, the chemical composition of the HSA material would be $AlF_{2.6}(OH)_{0.4}$. This sample contains 82% AlF_6 and $AlF_5(OH)$, 16% $AlF_4(OH)_2$, and 2% $AlF_3(OH)_3$ species. On the other hand, for LSA compound, the chemical composition $AlF_{2.4}(OH)_{0.6}$ gives the best agreement with the ^{27}Al NMR line intensities (Table 5).

(29) Chupas, P. J.; Ciraolo, M. F.; Hanson, J. C.; Grey, C. P. *J. Am. Chem. Soc.* **2001**, *123*, 1694.
(31) Simon, N.; Guillou, N.; Loiseau, T.; Taulelle, F.; Férey, G. *J. Solid State Chem.* **1999**, *147*, 92.
(32) Fischer, L.; Harlé, V.; Kasztelan, S.; d'Espinose de la Caillerie, J.-B. *Solid State Nucl. Magn. Reson.* **2000**, *16*, 85.
(33) Dumas, E.; Taulelle, F.; Férey, G. *Solid State Sci.* **2001**, *3*, 613.
(34) Zhou, B.; Sherriff, B. L.; Taulelle, F.; Wu, G. *Can. Mineral.* **2003**, *1*, 891.
(35) Chupas, P. J.; Grey, C. P. *J. Catal.* **2004**, *224*, 69.
(36) Kemnitz, E.; Groβ, U.; Rüdiger, St.; Scholz, G.; Heidemann, D.; Troyanov, S. I.; Morosov, I. V.; Lemée-Cailleau, M.-H. *Solid State Sci.* **2006**, *8*, 1443.
(37) Silly, G.; Legein, C. Buzaré, J.-Y.; Calvayrac, F. *Solid State Nucl. Magn. Reson.* **2004**, *25*, 241.
(30) Taulelle, F.; Pruski, M.; Amoureux, J. P.; Lang, D.; Bailly, A.; Huguenard, C.; Haouas, M.; Gérardin, C.; Loiseau, T.; Férey, G. *J. Am. Chem. Soc.* **1999**, *121*, 12148.
(38) Zhou, B.; Sherriff, B. L.; Hartman, J. S.; Wu, G. *Am. Mineral.* **2007**, *92*, 34.
(39) Scheurell, K.; Scholz, G.; Kemnitz, E. *J. Solid. State Chem.* **2007**, *180*, 749.

Table 5. Line Label, Isotropic Chemical Shift δ_{iso}, Quadrupolar Product $\nu_{Q\eta}$ (kHz), and Relative Line Intensity (%) Deduced from the Reconstruction of the^{27} Al MAS NMR Spectra (see Experimental Section) of the LSA and HSA Samples, and Assignment of the^{27} Al NMR Lines

	LSA			HSA		
line	1	2	3	1	2	3
δ_{iso} (ppm)	−15.5	−11.7	−7.7	−15.5	−11.7	−9.5
$\nu_{Q\eta}$	250	530	840	280	610	990
relative intensity	64	33	3	82	16	2
assignment	AlF_6 and $AlF_5(OH)$	$AlF_4(OH)_2$	$AlF_3(OH)_3$	AlF_6 and $AlF_5(OH)$	$AlF_4(OH)_2$	$AlF_3(OH)_3$

Table 6. Probability of Occurrence of the $AlF_{6-x}(OH)_x$ species, Based on a OH/F Distribution on F1 and F2 sites, OH Content Being Equal in Both Al1 and Al2 sites

chemical composition	P_F[a]	AlF_6 (%)	$AlF_5(OH)$ (%)	$AlF_4(OH)_2$ (%)	$AlF_3(OH)_3$ (%)	$AlF_2(OH)_4$ (%)[b]
$AlF_{2.6}(OH)_{0.4}$	0.8	41	41	15	3	N
$AlF_{2.5}(OH)_{0.5}$	0.75	32	42	21	5	N
$AlF_{2.4}(OH)_{0.6}$	0.7	24	41	26	8	1

[a] P_F, probability of having a fluorine atom on F1/F2 sites. [b] N, negligible.

This result supports the assumption deduced from the ^{19}F spectra for a higher OH/F ratio in the LSA sample. The higher number of OH groups in LSA β-$AlF_{3-x}(OH)_x$ may explain the poor agreement factor ($R_{Bragg} = 8.8\%$), the large estimated standard deviations observed for Al−F1/F2 distances as well as the high thermal parameter (B_{iso}, Table 3) found for the anionic sites. The ^{27}Al NMR study thus confirms the localization and the statistic distribution of the OH groups in F1 and F2 sites.

Conclusion

The synthesis of aluminum hydroxyfluorides derived from β-AlF_3 has been achieved using microwave-assisted synthesis. The choice of the aluminum precursor, the solvents, and the HF/Al molar ratio are essential in order to get nanosized β-$AlF_{3-x}(OH)_x$. As far as the aluminum precursor is concerned, a secondary reaction occurring during the microwave-assisted synthesis has been identified and involves the reduction of nitrate into ammonium groups coupled with the oxidation of isopropanol. The HF content has been proved to be decisive on the nature of the final allotropic forms. Three various structures can be stabilized corresponding to pyrochlore, HTB, and α-ReO_3 networks, which will be detailed in forthcoming papers. This opens a new pathway for the preparation of aluminum-based fluorides exhibiting high surface area, which in the case of the HTB phase has been monitored as a function of the water/isopropanol volume ratio. X-ray diffraction analysis using the Rietveld method has revealed a platelet shape for the prepared crystallites. NMR spectroscopy has proved to be a powerful tool to probe and quantify the various $AlF_{6-x}(OH)_x$ environments. Furthermore, this technique supports the localization and the statistic distribution of the OH groups in F1 and F2 sites and allows stating more precisely the chemical compositions. The presence of OH groups inside the HTB network seems to strongly perturb the framework as revealed by the difficulty to get accurate Al−X distances. Finally, FTIR spectroscopy has shown the presence of strong Lewis acid sites by NH_3 adsorption. The acidic properties of the nanosized β-$AlF_{3-x}(OH)_x$ are currently studied by adsorption of probe molecules (pyridine, CO, ^{36}Cl radiotracers) and will be discussed in a forthcoming paper.[40]

Acknowledgment. We thank the EU for financial support through the 6th Framework Programme (FUNFLUOS, Contract NMP3-CT-2004-5005575). Lydia Raison is gratefully acknowledged for performing EMPA analysis.

Supporting Information Available: Atomic positions of LSA and HSA; ^{19}F MAS NMR experimental and calculated spectra of LSA and HSA; ^{19}F NMR spectrum reconstruction parameters; and experimental and calculated central line of the ^{27}Al MAS NMR spectra of LSA and HSA (PDF). This material is available free of charge via the Internet at http://pubs.acs.org.

CM702603B

(40) Dambournet, D.; Vimont, A.; Leclerc, H.; Lavalley, J. C.; Daturi, M.; Durand, E.; Winfield, J. M.; Tressaud, A.; Demourgues, A. Submitted.

Nano-structured aluminium hydroxyfluorides derived from β-AlF_3

D. Dambournet, A. Demourgues, C. Martineau, S. Pechev, J. Lhoste, J. Majimel, A. Vimont, J.-C. Lavalley, C. Legein, J.-Y. Buzaré, F. Fayon and A. Tressaud.

Supporting information

Table of contents

Table 1. Atomic positions, thermal displacements and reliability factors ($Å^2$) of LSA and HSA β-$AlF_{3-x}(OH)_x$ from powder X-ray Rietveld analysis

Atoms	Site	x	y	z	Biso
HSA cR_p=11%, cR_{wp}=13.2%, R_{Bragg}=4.1%					
Al1	4b	0	1/2	0	0.79(3)
Al2	8d	1/4	1/4	0	0.79(3)
F1	8f	0	0.200(3)	0.532(4)	0.83(3)
F2	16h	0.323(4)	0.105(2)	0.995(5)	0.83(3)
F3	4c	0	0.509(7)	1/4	0.83(3)
F4	8g	0.217(9)	0.241(3)	1/4	0.83(3)
LSA cR_p=22.6%, cR_{wp}=24.2%, R_{Bragg}=8.8%					
Al1	4b	0	1/2	0	0.62(3)
Al2	8d	1/4	1/4	0	0.62(3)
F1	8f	0	0.203(7)	0.51(1)	1.25(4)
F2	16h	0.32(1)	0.108(8)	0.98(1)	1.25(4)
F3	4c	0	0.510(8)	1/4	1.25(4)
F4	8g	0.22(1)	0.236(4)	1/4	1.25(4)

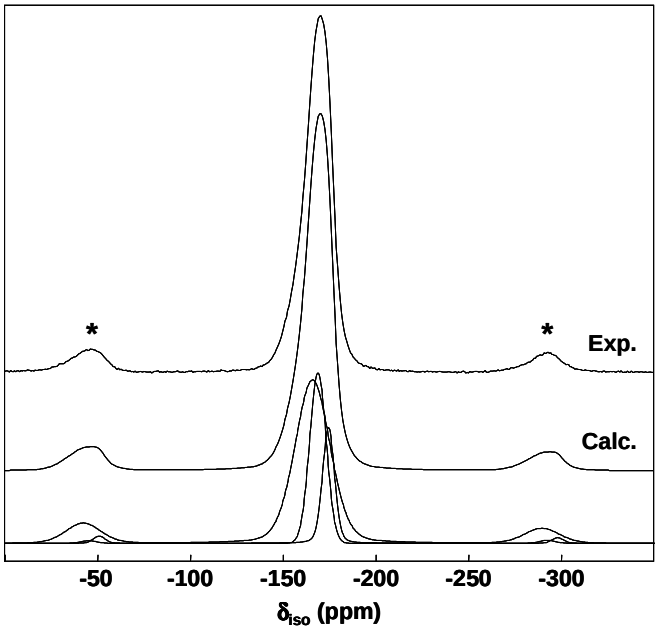

Figure 1. ^{19}F MAS NMR experimental and calculated spectra of LSA at 34 kHz. The star symbols indicate the spinning sidebands. The three individual contributions to the reconstructed spectrum are shown.

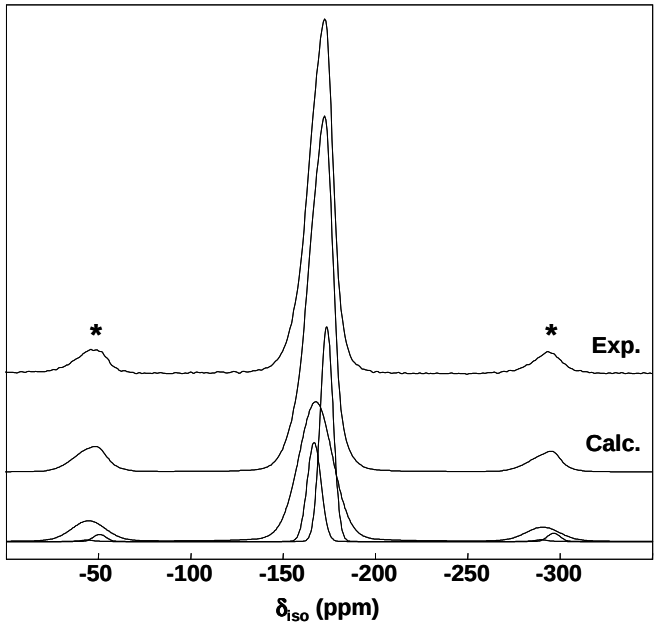

Figure 2. ^{19}F MAS NMR experimental and calculated spectra of HSA at 34 kHz. The star symbols indicate the spinning sidebands. The three individual contributions to the reconstructed spectrum are shown.

Table 2. Samples and Isotropic Chemical Shifts (ppm), Line Widths (ppm) and Relative Intensities (%) as deduced from ^{19}F NMR spectrum simulations.

Sample	δ_{iso}	Width	Intensity
LSA	-174.4	7.6	14
	-168.7	10.5	24
	-165.8	22.2	62
HSA	-173.5	8.2	28
	-167.6	21.6	59
	-166.7	8.8	13

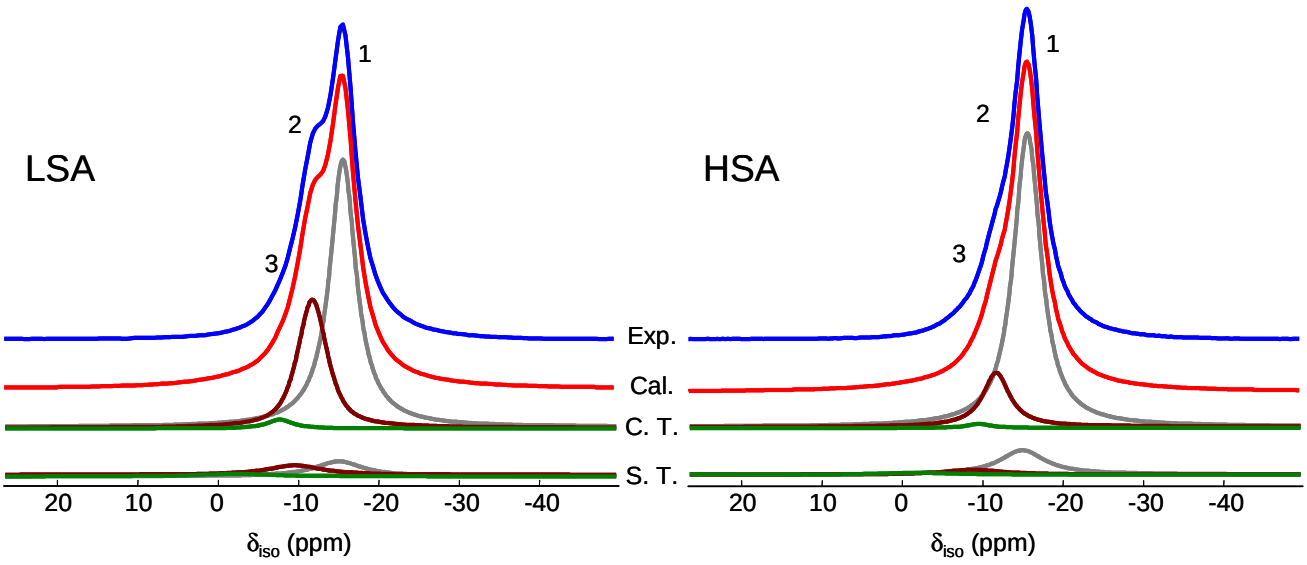

Figure 3. Experimental and calculated central line of the ^{27}Al MAS NMR spectra of LSA and HSA. The deconvolution, achieved using three contributions, takes into account the N = 0 band of both the satellite transitions <3/2> (S. T.) and the central transition <1/2> (C. T.).

2.2 Structure et propriétés acides de l'hydroxyfluorure d'aluminium de type pyrochlore à grande surface spécifique

Publication: *Structural investigations and acidic properties of high surface area pyrochlore aluminium hydroxyfluoride, accepted in Journal of Materials Chemistry*

Dans la première partie de chapitre, nous avons mis en évidence les conditions expérimentales permettant d'obtenir un hydroxyfluorure d'aluminium à structure de type bronze hexagonal de tungstène. Dans cette continuité, nous reportons ici la synthèse de l'hydroxyfluorure présentant une structure de type pyrochlore. Dans un premier temps, la stratégie adoptée pour optimiser la surface spécifique est suivie par une caractérisation structurale. Comme précédemment, la spectroscopie RMN-MAS ^{19}F et ^{27}Al et la méthode de Rietveld seront largement utilisées. La spectroscopie infrarouge à transformée de Fourier (FTIR) viendra compléter l'étude structurale en apportant des informations sur les différentes conformations de l'eau structurale et les groupements hydroxyles de structure. Enfin, les propriétés acides de ce matériau ont été étudiées par adsorption de différentes molécules sondes.

Journal of Materials Chemistry

RSCPublishing

Journals Journal of Materials Chemistry Advance Articles DOI: 10.1039/b718856k

J. Mater. Chem., 2008 | DOI: 10.1039/b718856k | Paper

Structural investigations and acidic properties of high surface area pyrochlore aluminium hydroxyfluoride†

D. Dambournet [a], A. Demourgues *[a], C. Martineau [b], E. Durand [a], J. Majimel [a], A. Vimont [c], H. Leclerc [c], J.-C. Lavalley [c], M. Daturi [c], C. Legein [b], J.-Y. Buzaré [bd], F. Fayon [e] and A. Tressaud [a]

[a]*Institut de Chimie de la Matière Condensée de Bordeaux - CNRS, Université Bordeaux 1. 87, Avenue du Dr. A. Schweitzer, 33608 Pessac cedex, France. E-mail: demourg@icmcb-bordeaux.cnrs.fr; Fax: +33 (0)5 4000 2650; Tel: +33 (0)5 4000 2655*

[b]*Laboratoire des Oxydes et Fluorures, CNRS UMR 6010, IRIM2F, CNRS FR 2575, Université du Maine, Avenue Olivier Messiaen, 72085 Le Mans Cedex 9, France*

[c]*Laboratoire Catalyse et Spectrochimie, ENSICAEN, Université de Caen, CNRS, 6 Bd Maréchal Juin, F-14050 Caen Cedex, France*

[d]*Laboratoire de Physique de l'Etat Condensé, CNRS UMR 6087, IRIM2F, CNRS FR 2575, Université du Maine, Avenue Olivier Messiaen, 72085 Le Mans Cedex 9, France*

[e]*Centre de Recherche sur les Matériaux à Haute Température, CNRS UPR 4212, 1D Avenue Recherche Scientifique, 45071 Orléans Cedex 2, France*

Received 6th December 2007 , Accepted 12th February 2008

First published on the web 25th March 2008

High surface area aluminium hydroxyfluoride exhibiting the pyrochlore-type structure has been synthesized using microwave hydrothermal process. The optimization of the crystallite size and surface area of the material has been performed by varying some synthesis parameters, *i.e.* the nature of the aluminium precursor, the choice of solvents and the addition of a small amount of ether. The as-prepared solid contains nanosized particles as calculated by XRD (average particle size: 12 nm) leading to a surface area around 140 $m^2\ g^{-1}$. These results have been confirmed by TEM observations. The framework is built of $AlF_{6-x}(OH)_x$ species which have been characterized and quantified by high field ^{27}Al NMR. A random distribution of F atoms and OH groups is evidenced to occur on the 48f sites. Inside the channels, water molecules interact with the framework by hydrogen bonding either with fluoride ions or OH groups present in their vicinity. The use of probe molecules has shown that the pyrochlore exhibits a Lewis acidity lying between that of γ-Al_2O_3 and that of the strong Lewis acid β-AlF_3 adopting the hexagonal tungsten bronze form. Surface OH groups have been characterized by IR spectroscopy and exhibit weak Brønsted acidity.

Introduction

Microwave-assisted synthesis has been recently applied to the preparation of high surface area aluminium hydroxyfluorides derived from β-AlF_3[1]
(hexagonal tungsten bronze type structure: HTB). In this study, the variation of the synthesis parameters has enabled monitoring both the surface area and the chemical composition. Furthermore, the [HF]/[Al] precursor molar ratio has been proved to play a decisive role in the stabilization of the final form. It is well-known that the chemical composition strongly governs the intrinsic properties of a solid. The control of the OH : F molar ratio enables various structural features to be obtained with different acidic properties which could play a key role in acid catalysis. Aluminium-based fluorides and hydroxyfluorides are indeed interesting materials in numerous catalytic reactions such as halogen exchange reactions,[2] alkylation reactions[3] or Friedel–Crafts acylation.[4]

In order to modify the Lewis/Brønsted acidic properties of the Al-F systems, the present work is focused

on the synthesis and characterization of the hydroxyfluoride phase $AlF_{3-x}(OH)_x$ exhibiting the cubic pyrochlore framework. This compound exists in both hydrated and anhydrous forms whose structures have been solved by Fourquet *et al.*[5] The network consists of corner sharing $Al(F,OH)_6$ octahedra forming a three-dimensional channel system (Fig. 1), where structural water molecules are located inside the tunnels. The phase was first prepared according to the method described by Cowley and Scott.[6] In this route, solutions containing aluminium fluoride and aluminium sulfate react at basic pH by addition of ammonia. The corresponding reaction is given by the equation:

$$Al_2(SO_4)_3 + 2\ AlF_3 + 6\ NH_4OH + H_2O \rightleftharpoons 2\ Al_2[(OH)_{0.5}F_{0.5}]_6.H_2O + 3\ (NH_4)_2SO_4$$

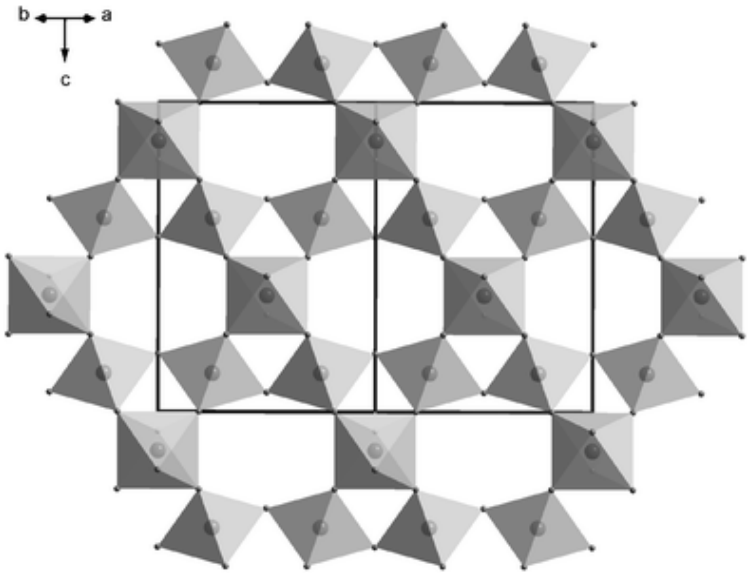

Fig. 1 The pyrochlore network: view along the [110] direction.

A simple method was reported by Hess *et al.*[7] which consists of reacting aluminium acetate $[Al(CH_3COO)_2OH]$ in an aqueous HF solution. However, the resulting material exhibits a low surface area (~15 $m^2\ g^{-1}$). Furthermore, pyrochlore has been obtained by fluorination of γ-Al_2O_3 using pure F_2 gas at room temperature.[8]

Contrary to other Al-based fluoride forms which require the degradation of a precursor, the pyrochlore phase can be easily obtained. Hydroxyl groups are assumed to play a key role in this stabilization. The occurrence of hydroxyl groups has been proved to favour small Al–X–Al (X = F, OH) angles[1,9] typically found in the pyrochlore-type structure and directly related to chemical bonding polarization and enhancement of Al–Al interactions. The stabilization of a hydroxyl-rich aluminium fluoride thus ensures tuning of the acidic properties as compared to aluminium fluorides.

The present work focuses on the characterization of the cubic pyrochlore phase with high surface area prepared by microwave-assisted synthesis. In a first step, the structural features of the prepared material have been thoroughly investigated using X-ray powder diffraction, chemical and thermal analyses, TEM, FTIR and ^1H, ^{19}F and ^{27}Al NMR spectroscopies. Finally, the surface acidic properties have been investigated through the use of FTIR spectra of adsorbed probe molecules.

Experimental

Preparation of the high surface area pyrochlore phase

Syntheses were performed using a MARS-5 Microwave Digestion System (CEM Corp.) which enables control of both the temperature and pressure. First, a precursor solution was prepared as follows: 20 mmol of Al(III) isopropoxide (Sigma-Aldrich: 97%) was added to 17 ml of isopropanol (98%, Sigma-Aldrich). An [HF]/[Al] precursor molar ratio equal to 2 was then prepared using an aqueous solution of HF (Panreac, 40%). Finally, 5 ml of ether and 17 ml of distilled water were added to the mixture. The solution was placed in a closed Teflon container for microwave hydrothermal synthesis (XP-1500 plus model). In the first step, a

temperature of 473 K was rapidly reached by keeping the microwave power irradiation at 300 W (100%). Thereafter, the temperature was kept at 433 K for one hour. Powder was recovered after microwave-assisted drying performed under primary vacuum and argon flow at 363 K for 20 min. The sample was washed with a large amount of ethanol under nitrogen pressure. Finally, the powder was outgassed at 573 K (5 $Kmin^{-1}$) for four hours under vacuum.

Elemental analysis

Fluorine and aluminium contents were quantified using two methods: (i) electron probe micro-analysis (Castaing microprobe CECAMA SX 630 apparatus by Wavelength Dispersive Spectrometry) and chemical elemental analysis at the CNRS Central Service of Analysis, *i.e.* F^- titration with specific electrode and Al^{3+} determination by Inductively Coupled Plasma Mass Spectrometry (ICPMS).

Thermogravimetric analysis

The thermal behaviour was studied by simultaneously coupled TA-MS measurements. A NETZSCH thermoanalyzer STA 409 C, equipped with a BALZERS QMG 421, was used to record the thermoanalytical curves (T, DTA, TG, DTG) together with the ionic current (IC) curves in the multiple ion detection (MID) mode. A constant purge gas flow of 70 ml min^{-1} nitrogen (MESSER-GRIESHEIM 5.0) and a constant heating rate of 10 K min^{-1} were applied.

X-Ray diffraction analysis

A PANalytical X'Pert Pro diffractometer in a Bragg–Brentano geometry (θ–2θ) with a graphite-monochromated Cu Kα radiation (Kα1 = 1.54051 Å) was used for recording the powder diffraction patterns. The investigated 2θ range was 10–110°, with steps of 0.017°. Refinements were carried using the FULLPROF program.[10]

Surface area measurements

The specific surface areas were measured at 77 K using an ASAP 2000 instrument from Micromeritics. A mass of around 200 mg of the sample was evacuated overnight at 573 K under 0.1 Pa prior to each measurement. Estimated standard deviations (e.s.d.) have been calculated for surface areas larger than 30 m^2 g^{-1} and are equal to 5 m^2 g^{-1}.

Transmission electron microscopy

Transmission Electron Microscopy (TEM) was performed on a TECNAI F20 equipment with a field emissive gun, operating at 200 kV and with a point resolution of 0.24 nm. TEM samples were prepared by dispersing a few milligrams of powder in ethanol. The solution was then dipped for ten minutes into an ultrasonic bath in order to disagglomerate powder particles. One drop of the solution was finally deposited on a Formvar/Carbon copper grid.

FTIR spectroscopy

Infrared transmission spectra were recorded on self-supported discs (2 cm^2, ~20 mg) which were placed into an infrared quartz cell (KBr windows) connected to a vacuum line. Samples were activated under vacuum at 573 K overnight. The IR spectrometer was a Nicolet Nexus apparatus equipped with an extended KBr beam splitter and a mercury cadmium telluride (MCT) detector (resolution: 4 cm^{-1}). Probe molecules were introduced into the cell *via* the vacuum line. After activation, the acidity of the materials was studied by IR spectroscopy, using adsorbed pyridine and CD_3CN as spectroscopic probe molecules. Pyridine and CD_3CN (Aldrich, 99+% grade) were dried on molecular sieves prior to their use. These probes were introduced at equilibrium pressure (133 Pa) and the adsorbed probe molecule was evacuated under vacuum at increasing temperatures.

NMR spectroscopy

^{27}Al (I = 5/2) Magic Angle Spinning (MAS) NMR spectra were recorded using a 2.5 mm CP MAS probe at a

spinning speed of 30 kHz on an Avance 750 Bruker spectrometer (B_0 = 17.6 T) operating at a ^{27}Al Larmor frequency of 195.5 MHz. A short pulse length of 1 μs was used to ensure quantitative excitation of the whole spin system. The recycle delay was set to 1 s and 4096 fids were accumulated. The ^{27}Al spectra was referenced to a 1 M aqueous solution of $Al(NO_3)_3$. A two-dimensional one pulse[11–13] (TOP) spectrum was constructed by stacking sub-spectra shifted by the spinning frequency from the 1D MAS NMR spectra. A Multiple Quantum-MAS[14,15] (MQ-MAS) spectrum was recorded using the three-pulse *z*-filter experiment.[16] Pulse duration to create the triple quantum and the conversion were respectively taken to 4 and 2 μs. The selective pulse duration after the *z*-filter was 5.5 μs. The experiment was synchronised with the spinning rate (30 kHz). Signal acquisition was done using the STATES procedure.[17] A two-dimensional Fourier transformation followed by a shearing transformation[18] gave a pure absorption two-dimensional spectrum. Quantitative reconstruction[19–22] of the central lines of the conventional ^{27}Al 1D NMR spectra was achieved taking into account the $N = 0$ spinning sideband of the satellite transitions ⟨3/2⟩ and the $N = 0$ spinning sideband of the central transition ⟨1/2⟩ which completely overlap. For each ^{27}Al NMR site, the isotropic chemical shift δ_{iso} and the quadrupolar product $\nu_Q\eta$ were calculated by comparison of the centre of gravity $\delta_{cs}^{\langle 3/2\rangle}$ of the Al satellite sidebands with that of the central transition $\delta_{cs}^{\langle 1/2\rangle}$, through the following equation:

$$\delta_{CS}^{\langle m\rangle} = \delta_{iso} - \nu_{Q\eta}^2 \frac{\left[I(I+1) - 3 - 9m(m-1)\right]}{30\nu_0^2} 10^6$$

where $I = 5/2$ in the case of ^{27}Al, ν_0 = 195.5 MHz (for the 17.6 T spectrometer) and

$$\nu_{Q\eta} = \nu_Q \sqrt{1 + \frac{\eta_Q^2}{3}}$$

.[21]

The ^{19}F and ^{1}H Hahn echo MAS NMR spectra were acquired on an Avance 300 Bruker spectrometer (B_0 = 7 T), using a 2.5 mm ^{19}F optimized CP MAS probe, operating at a Larmor frequency of 282.2 MHz and 300 MHz for ^{19}F and ^{1}H, respectively. The 90° pulse durations were set to 4 μs (RF field 60 kHz) and 2.5 μs (RF field 100 kHz) for ^{19}F and ^{1}H, respectively, with an inter-pulse delay equal to one rotor period. The recycle delays were taken to 10 s and 1 s for ^{19}F and ^{1}H, respectively. The ^{19}F chemical shifts were referenced to $CFCl_3$ at 0 ppm. The ^{1}H chemical shifts were referenced to ^{1}H in TMS at 0 ppm. The spectra were reconstructed using DMFIT software.[23]

Results and discussion

Structural features of the aluminium hydroxyfluoride with the pyrochlore-type structure

Strategy for preparing a high surface area material. As already reported, the [HF]/[Al] molar ratio was proved to play a key role in the stabilization of the final aluminium hydroxyfluoride form. The pyrochlore-type structure was obtained using an [HF]/[Al] precursor molar ratio equal to 2 in a water–isopropanol solution. In the course of obtaining nanosized particles, the effect of the synthesis parameters on the surface area was investigated. The various conditions used and the corresponding measured surface areas are summarized in Table 1.

Table 1
Synthesis conditions and surface area of pyrochlore phases obtained by microwave-assisted synthesis performed at 160 °C for 1 h. The starting [HF]/[Al] molar ratio is equal to 2

Al^{3+} precursor	Solvents used and volume ratio	Surface area/m^2 g^{-1}
Nitrate	Isopropanol–Water: 1 : 1	6
Isopropoxyde	Isopropanol–Water: 1 : 1	77
Isopropoxyde	Isopropanol–Water–Ether: 1 : 1 : 0.3	137

Powder X-ray diffraction patterns of the as-prepared samples are presented in Fig. 2. At first, the use of nitrate as aluminium precursors leads to a very well crystallized material as proved by the corresponding powder X-ray diffraction pattern (Fig. 2a). Consequently, the specific surface area is very low, *i.e.* 6 $m^2\ g^{-1}$. The effect of the nature of the aluminium precursor has then been investigated using isopropoxyde. The surface area largely increases from 6 to 77 $m^2\ g^{-1}$. The effect of isopropoxide was therefore suggested to reduce the crystallization growth by limiting the kinetics of fluorination. Steric hindrance induced by the size of the precursor should limit the strong reactivity of fluorine.

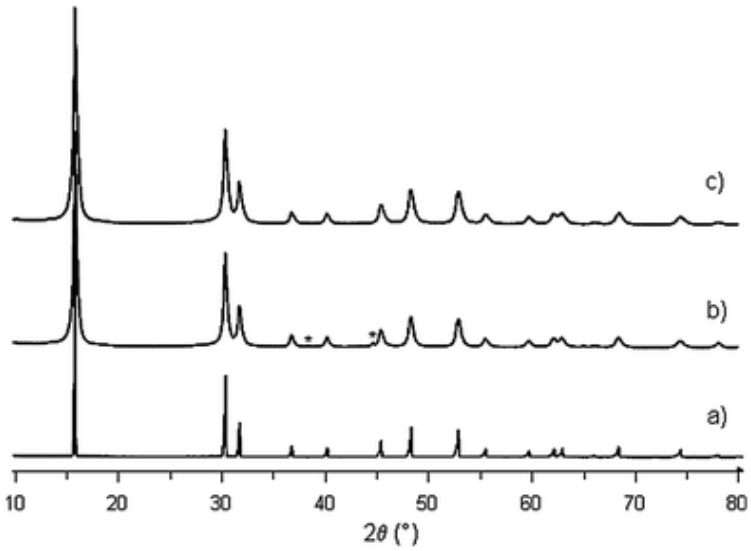

Fig. 2 X-Ray powder diffraction patterns of the pyrochlore phases prepared using (a) aluminium nitrate, $S = 6\ m^2\ g^{-1}$, (b) aluminium isopropoxyde, $S = 77\ m^2\ g^{-1}$ and (c) aluminium isopropoxide with the addition of a small amount ether, $S = 137\ m^2\ g^{-1}$ (asterisks denote sample holder).

After having highlighted the effect of the nature of the aluminium precursor on the morphology, the solvents used during the synthesis process have been considered in a second time. Recently, a non aqueous sol–gel fluorination procedure has been developed by Kemnitz *et al.*[24] for the synthesis of high surface X-ray amorphous aluminium alkoxy-fluorides. In this study, the use of aqueous hydrofluoric acid was replaced by dissolving gaseous anhydrous HF in an organic solvent, *i.e.* ether or alcohol. The use of ether appears particularly interesting since the protonation of Et_2O by HF led to the formation of oxonium ions in anhydrous HF.[25]
Such ionic species should probably exist in the present medium containing a large content of organics and then should limit the fluoride ions' reactivity, *i.e.* the crystallization growth. Following these considerations, a small amount of ether was therefore introduced into the synthesis mixture, resulting in a jump of the surface area from 77 to 137 $m^2\ g^{-1}$ (Table 1). The obtained material is mesoporous exhibiting a type IV isotherm.

Structural investigations. *Chemical composition and thermal analysis.* The two different elemental analysis methods both led to a final F/Al molar ratio equal to 1.8 (±0.1). NMR spectroscopy has been previously used to accurately determine the chemical composition of β-$AlF_{3-x}(OH)_x$.[1] The same approach will be used and presented later. The content of the hydroxyl groups was deduced from the electro-neutrality principle leading to the corresponding chemical formula: $AlF_{1.8}(OH)_{1.2}{\cdot}nH_2O$. Thermogravimetric measurements were coupled with a mass spectrometer in order to follow the dehydration process (Fig. 3). Three events can be noticed at 473, 613 and 693 K, through the ionic curve of the $m/z = 18$ (H_2O^+ fragment). Their origin will be specified in the investigation of the infrared spectra of non-activated and activated samples (see below).

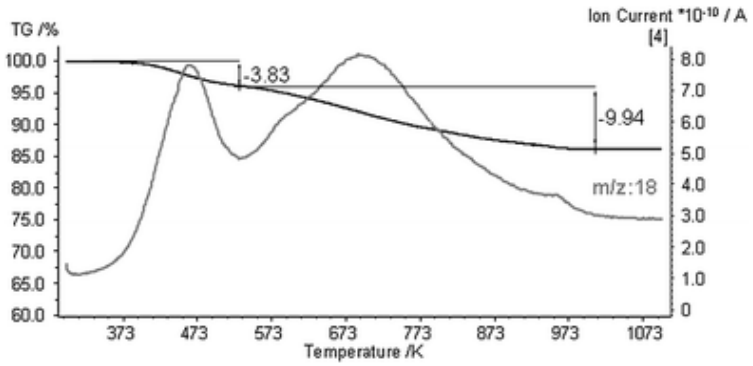

Fig. 3 Thermal analysis of the pyrochlore $AlF_{1.8}(OH)_{1.2}{\cdot}nH_2O$ and mass spectrometry analysis (m/z =18).

X-Ray powder diffraction.

The pyrochlore-type structure of the high surface area sample was confirmed by X-ray diffraction analysis by comparison with the JCPDS-ICDD file No. 78-2259. Due to constrains induced by the nanometric size of the particles, the structural features of the sample were investigated through Rietveld refinement (Fig. 4).

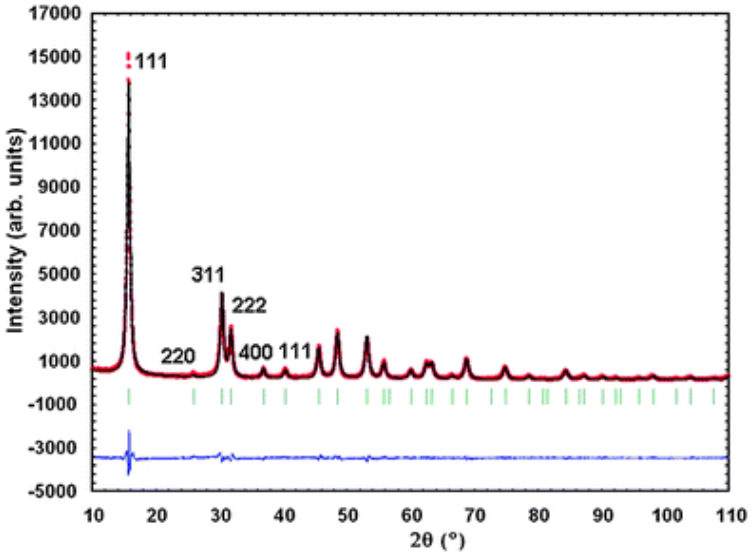

Fig. 4 Rietveld refinements of the experimental X-ray powder diffraction pattern of the pyrochlore phase $AlF_{1.8}(OH)_{1.2}{\cdot}0.3H_2O$ (dotted curve) compared to the Rietveld-refined profile and the difference curve (below). The vertical bars correspond to the positions of the Bragg reflections.

Profile matching was performed using the Thompson–Cox–Hastings function[26] which takes into account the microstructural properties (coherent domains and micro-strains $\Delta d/d$) of the solid. In spite of a dehydration step performed at 573 K for 4 h, a better Rietveld convergence was reached by introducing into the calculation the presence of structural water (O_w) in the tunnels. The refinement of the corresponding occupancy rate led to 0.3 H_2O. The pyrochlore $AlF_{1.8}(OH)_{1.2}{\cdot}0.3\ H_2O$ crystallizes in the cubic symmetry ($Fd\bar{3}m$ space group, Z = 1), with a = 9.7309(1) Å. Final agreement factors are good with cR_p = 8%, cR_{wp} = 9.2% and R_{Bragg} = 1.9%. The corresponding crystallographic data are summarized in Table 2.

Table 2 Crystallographic data of the refined pyrochlore phase $AlF_{1.8}(OH)_{1.2}{\cdot}0.3H_2O$ (O_w is oxygen belonging to water molecules)

Atom	Site	x	y	z	B_{iso}/Å^2	Occupancy (%)
Al	16c	0	0	0	0.78(2)	100

Atom	Site	x	y	z	B_{iso}/Å^2	Occupancy (%)
F	48f	0.3124(2)	0.125	0.125	1.12(2)	100
O_w	8b	0.375	0.375	0.375	3.18(8)	58.0(3)

Structural data ($Fd\bar{3}m$)		Reliability factors
Al–(O,F) distance	1.824(1) Å	cR_p = 8%
O_w–(O,F) distance	3.042 Å	
Unit cell constant	9.7309(1) Å	cR_{wp} = 9.2%
Al–F–Al angle	141.12(6)°	R_{Bragg} = 1.9%

The calculated average size particle equals 12 nm and the average micro-strain ($\Delta d/d$) value is $\langle \varepsilon \rangle = 2.7 \times 10^{-3}$. The transmission electron micrograph displayed in Fig. 5. A shows that the solid consists of agglomerates built of nanoparticles. The HRTEM image (Fig 5B) illustrates an isolated nano-crystallite in good agreement with XRD data analysis (crystallite size and inter-reticular distances). One can notice the occurrence of an amorphous zone located at the outer edge of the crystallite arising from either partial decomposition induced by the dehydration step or by evolution of the particle under the electron beam.

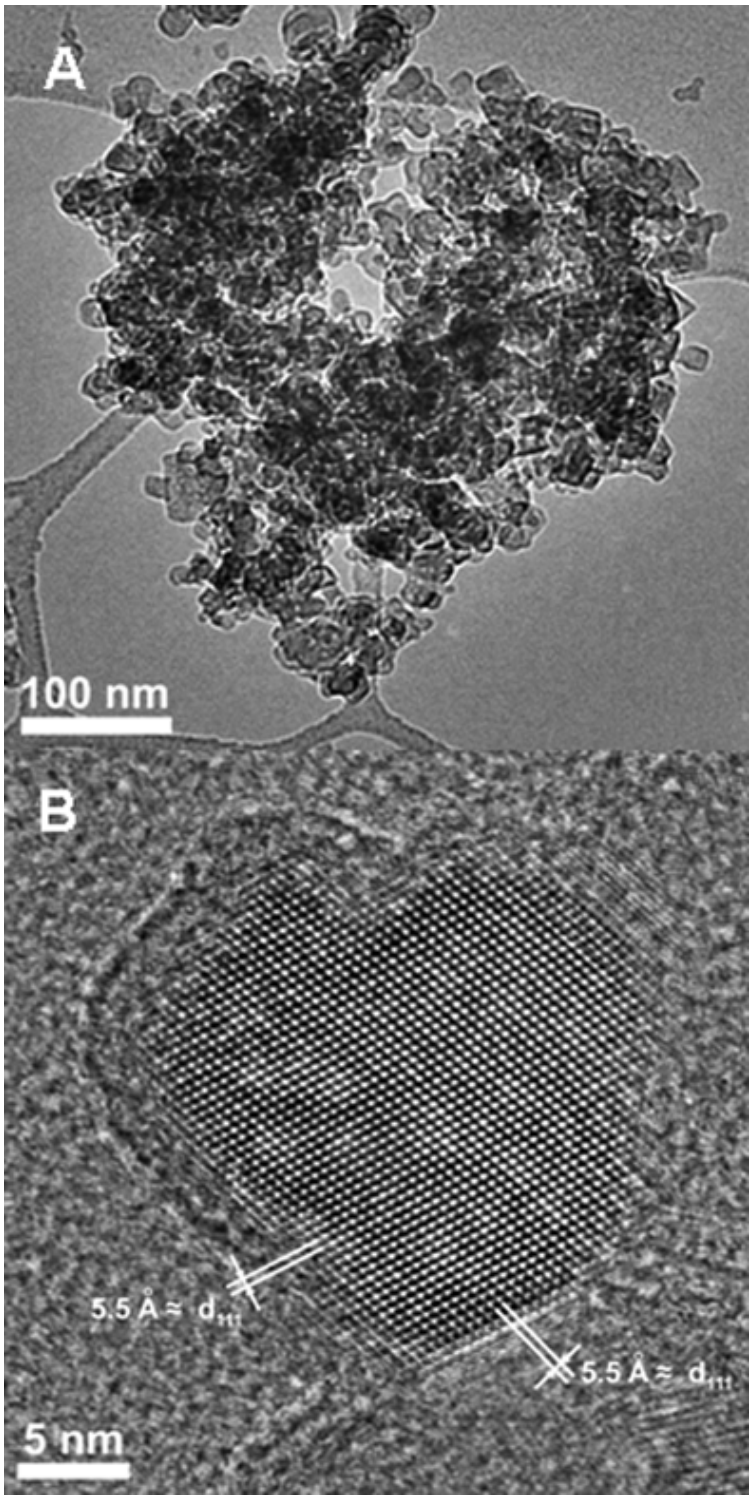

Fig. 5 Transmission electron micrograph of agglomerate particles (A) and HRTEM of isolated crystallite (B).

Characterization of OH groups and structural water. Hydroxyl groups as well as structural water were characterized using FTIR and ^{1}H MAS NMR spectroscopies. First, IR spectra were recorded under air and after activation overnight at 573 K. The corresponding IR spectra are displayed in Fig. 6. Most bands are sensitive to the activation step. At first, the broad band detected between 2800 and 3500 cm^{-1} accounts for the presence of hydrogen bonds which disappear after activation. The occurrence of bands at wavenumbers higher than 5200 cm^{-1} (inset A) unambiguously reveals the presence of water through the combination $\nu + \delta$ (H_2O) mode. The bending mode of water species is located around 1600–1650 cm^{-1}. Two bands are observed for this mode at 1605 and 1645 cm^{-1}
and the corresponding combination bands are detected at 5241 and 5275 cm^{-1}, respectively. Each $\delta(H_2O)$

band indicates the occurrence of one type of water configuration. According to Burneau *et al.*,[27] the highest component at 1645 cm^{-1} and the lowest one at 1605 cm^{-1} are ascribed to water molecules which are donors and acceptors of hydrogen bonds, respectively.

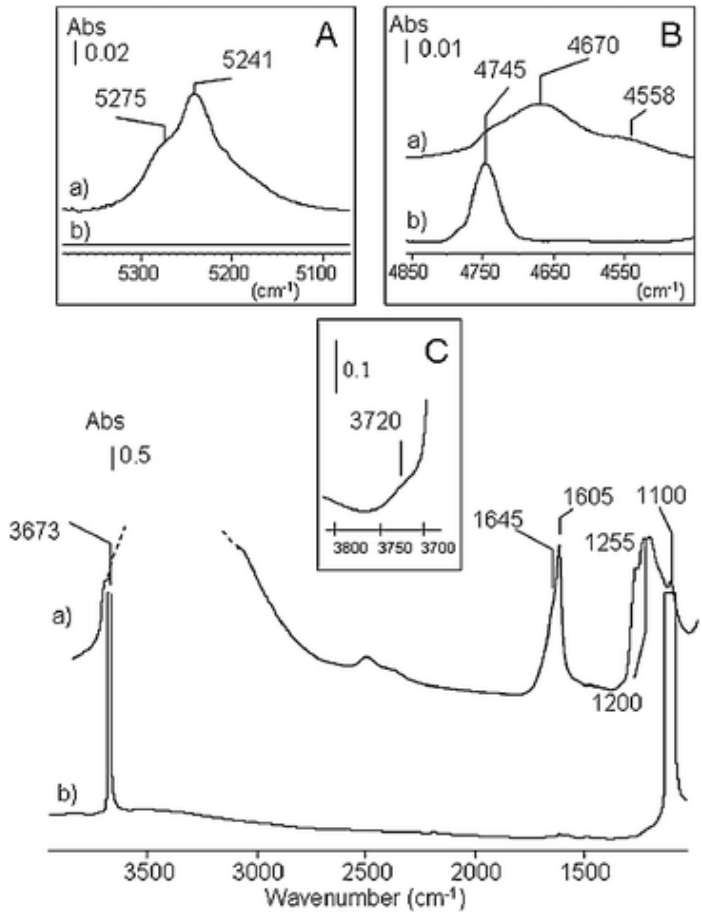

Fig. 6 IR spectra of the pyrochlore phase recorded (a) under air and (b) after activation at 573 K.

These water configurations can be rationalized on the basis of the anionic environments of these water molecules. The negative charge on fluoride ions (compared with that on the free electron pairs of oxygen in the water molecule) is more likely to form species A (scheme 1) in which F plays the role of a hydrogen acceptor and water is the donor, whereas species B is expected when acidic hydroxyl groups interact with water. These water molecules are incorporated into the channel of the solid during the synthesis step and are not located on the outer surface of the material. It is likely that such water molecules can interact with several sites of the framework.

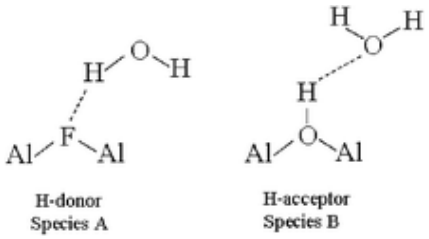

Scheme 1 Possible configurations of water molecules.

After activation, two very intense bands are clearly observed at 1100 and 3673 cm^{-1} with a shoulder at 3720 cm^{-1} (Fig. 6, inset C). According to Vimont *et al.*,[28] the two bands at lower wavenumbers can be ascribed to the deformation δ(OH) and stretching ν(OH) modes of isolated bridged Al–OH groups, respectively. The corresponding combination band is detected at 4745 cm^{-1}. However, under air three bands are detected in this range, *i.e.* at 4558, 4670 and 4745 cm^{-1} (Fig. 6, inset B). After activation, the band at 4745 cm^{-1}

increases whereas the two others disappear. Therefore, it can be deduced that a part of the bridged Al–OH group does not interact with water in the non-activated solid; this assumption is confirmed by the presence of a weak band at 1100 cm^{-1} (Fig. 6a). The bands at 4558 and 4670 cm^{-1} account for perturbed OH groups, *i.e.* by water molecules or neighbouring OH groups. Moreover, activation also leads to the disappearance of two bands at 1200 and 1255 cm^{-1} whereas the δ(OH) at 1100 cm^{-1} increases significantly. Perturbed hydroxyl groups are therefore characterized by δ(OH) at 1200 and 1255 cm^{-1} and ν + δ(OH) at 4558 and 4670 cm^{-1}. Since the disappearance of the perturbed δ
(OH) bands occurs simultaneously with the disappearance of water, it confirms that OH groups are H-bonded with water. This structural water desorption requires a relatively high temperature because of the diffusion limitation which explains the weak desorption peak at about 613 K. The low temperature peak (473 K) rather corresponds to water desorption from the outer surface of pyrochlore. The final event located at 693 K is ascribed to the dehydroxylation process (Fig. 3).

The ^{1}H MAS NMR spectrum of pyrochlore $AlF_{1.8}(OH)_{1.2}\cdot 0.3H_2O$ is displayed in Fig. 7.

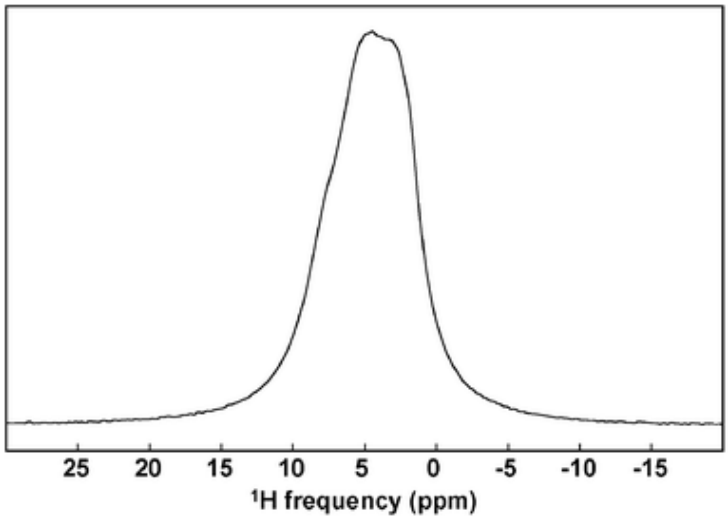

Fig. 7 ^{1}H MAS NMR spectrum of pyrochlore $AlF_{1.8}(OH)_{1.2}\cdot 0.3H_2O$ at 34 kHz.

According to the chemical formula of the compound, two contributions of 67% (^{1}H from hydroxyl groups) and 33% (^{1}H from water) are expected. However the spectrum is not resolved enough for them to be distinguished. The isotropic chemical shifts range from 0 to 10 ppm, which are in agreement with structural water (4–6 ppm) and OH groups where hydrogen atoms are involved in H-bonds. This supports the results from IR spectra in which the occurrence of hydrogen bonds is revealed through the broad band located at 2800–3500 cm^{-1}, as well as perturbed bands. ^{1}H chemical shifts of oxygen-bonded hydrogen depend linearly on the O–H···O distance, a pointer of the H-bond strength, following the relation:[29]

$$d(O\cdots O)\ (\mathrm{pm}) = \frac{79.05 - \delta_{iso}\ (\mathrm{ppm})}{0.255}$$

The O,F···O_w distance determined by Rietveld analysis, *i.e.* 3.042 Å, gives a δ_{iso} value of 1.5 ppm. The large δ_{iso} range (0–10 ppm) may indicate a distribution of O···O_w distances correlated to the distribution of O and F atoms on the 48f site. Moreover, the average O···O_w distance seems shorter than the one determined from Rietveld analysis. The ν(OH) band of isolated hydroxyl groups observed in the IR spectrum at 3673 cm^{-1} can be ascribed to non H-bonded hydroxyl groups and be related to the low frequency part of the ^{1}H NMR spectrum.

Aluminium and fluorine environments: ^{27}Al and ^{19}F NMR spectroscopy. In order to probe the F/OH anionic repartition and the cationic disorder, ^{19}F and ^{27}Al MAS NMR spectroscopies have been used.

The ^{19}F MAS NMR spectrum of pyrochlore $AlF_{1.8}(OH)_{1.2}\cdot 0.3\ H_2O$, displayed in Fig. 8, shows one broad peak which can be reconstructed with a single line at $\delta_{iso} = -161.2$ ppm.

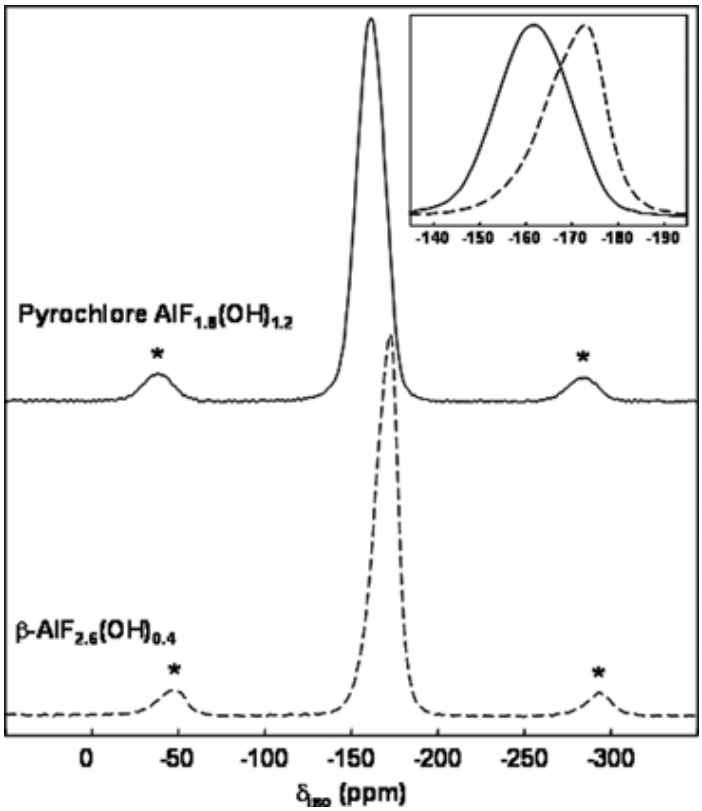

Fig. 8 ^{19}F MAS NMR spectra of pyrochlore $AlF_{1.8}(OH)_{1.2}\cdot 0.3H_2O$ and β-$AlF_{2.6}(OH)_{0.4}$ at 34 kHz. The asterisks indicate the spinning sidebands.

The width of the resonance (5.3 kHz) mirrors the chemical shift distribution related to the disorder around fluorine atoms in this compound. As illustrated in Fig. 8 in which the spectrum of β-$AlF_{2.6}(OH)_{0.4}$[1] is also displayed, and as already observed,[9,30–37] ^{19}F chemical shifts of octahedral aluminium environments with oxygen and fluorine in the first coordination sphere increase with oxygen content.

The central transition of the ^{27}Al MAS NMR spectrum of the pyrochlore $AlF_{1.8}(OH)_{1.2}\cdot 0.3\ H_2O$ recorded at 17.6 T is shown in Fig. 9a. Resonances are located in three distinct regions: −20 to 0 ppm and tiny amounts at 20–40 ppm and 50–70 ppm (Table 3).

Table 3 Line label, isotropic chemical shift δ_{iso}, quadrupolar product $\nu_Q\eta$, relative line intensity and $^{[6]}Al$ relative intensity deduced from the reconstruction of the ^{27}Al MAS NMR spectrum (see Experimental Section) of the pyrochlore $AlF_{1.8}(OH)_{1.2}\cdot 0.3H_2O$. Assignment of the ^{27}Al NMR lines

Line	δ_{iso}[a] (±0.5)/ppm	$\nu_Q\eta$ (±5)/kHz	Line intensity (±0.5)/%	$^{[6]}Al$ relative intensity (%)	Assignment
1	−12.5	345	46.4	47.3	AlF_6, $AlF_5(OH)$ and $AlF_4(OH)_2$
2	−8.7	540	32.7	33.4	$AlF_3(OH)_3$
3	−4.2	625	15.2	15.5	$AlF_2(OH)_4$
4	1.8	505	3.8	3.9	$AlF(OH)_5$
a	30.9		0.6	—	$^{[5]}Al$
b	56.1		1.3	—	$^{[4]}Al$
c	64.6		1.3	—	$^{[4]}Al$

[a] For $^{[4]}Al$ and $^{[5]}Al$ NMR lines: peak maxima.

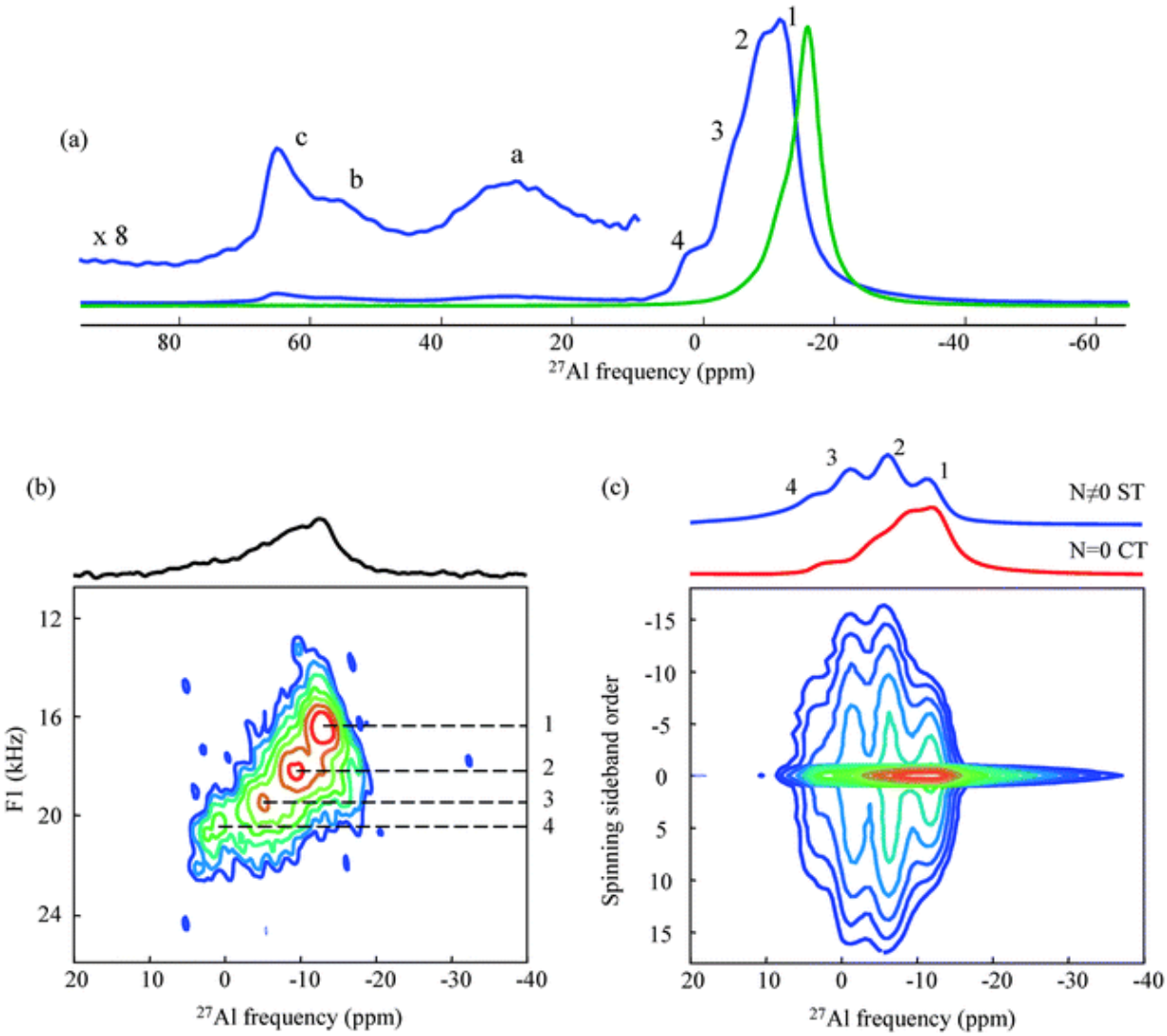

Fig. 9 (a) Central transition of the one pulse ^{27}Al MAS (30 kHz) spectrum of the HTB $AlF_{2.6}(OH)_{0.4}$ (in green) and one pulse ^{27}Al MAS (30 kHz) spectrum of the pyrochlore $AlF_{1.8}(OH)_{1.2}\cdot 0.3H_2O$ (in blue) with an extension of the high frequency sites. (b) 3Q-MAS spectrum. (c) 2D TOP spectrum. The $N = 0$ cross-section shows the central transition spectrum and the $N \neq 0$ sum is the satellite transition spectrum showing enhanced resolution.

An important and well-known feature of ^{27}Al solid-state NMR is the dependence of the isotropic chemical shift on local Al coordination: AlO_4 (~80 to 45 ppm), AlO_5 (~52 to 14 ppm) and AlO_6 (~20 to −20 ppm).[38,39] Therefore lines b and c can be assigned to 4-fold coordinated aluminium: $^{[4]}$Al. The occurrence of fluorine in the vicinity of aluminium shifts the δ_{iso} to lower values.[1,9,30,32–37,40,41] Line c may be thus assigned to AlO_4 species, line b to $AlO_{4-x}F_x$ species and line a to 5-fold coordinated Al site: $^{[5]}$Al. The presence of these species suggests that the pyrochlore has begun to decompose during the outgassing step. It should be noted that the broadening of lines a, b and c characterizes disordered sites. These lines have been reconstructed using Gaussian profiles on the full projection of the TOP spectrum (see ESI†) in order to get an estimation of the proportion of $^{[4]}$ and $^{[5]}$Al (Table 3). This very small amount of decomposition products may be amorphous which explains why they were not detected by X-ray powder diffraction.

The main resonance (−20 to 0 ppm) is obviously assigned to a 6-fold coordinated Al site: $^{[6]}$Al. The full spinning sideband manifold is featureless, indicating a distribution of quadrupolar coupling constants (QCCs) supported by the characteristic tail of the central transition of the 7 T spectrum (see ESI†). The high magnetic field reduces the influence of the quadrupolar interaction contribution to the spectrum, improving

the resolution of the ^{27}Al resonances with close δ_{iso} values. Four contributions are distinguished (Fig. 9a) on the main resonance of the central transition. A better resolution of these poorly resolved contributions could be obtained by ^{27}Al 3Q-MAS experiment. The two-dimensional MQ-MAS spectrum correlates an isotropic dimension (F1 vertical axis) to the usual MAS dimension (horizontal axis). The spectrum (Fig. 9b) evidences four lines. Another way to increase resolution and avoid a too long experimental time is to construct a TOP (two-dimensional one pulse) spectrum[11–13]
from a conventional 1D MAS spectrum. The TOP spectrum evidences the well-known narrowing of the inner satellite transition line width:[42–44] when the components are not well resolved on the $N = 0$ cross-section, the projection over the satellite transitions ($N \neq 0$) shows a much better resolution of the four contributions (Fig. 9c). In the present case, the 3Q-MAS experiment does not improve the resolution compared to the TOP procedure. Deconvolution of the 1D MAS NMR spectra shown on ESI† is achieved with four Gaussian lines (see Experimental Section) whose features are gathered in Table 3. The chemical shifts range from −12.5 to 1.8 ppm. It can be reminded that pure aluminium fluorides, α- and β-AlF_3, exhibit resonances at −16 and −15 ppm, respectively,[34,45] and those of β-$AlF_{2.6}(OH)_{0.4}$ (Fig. 9a) range from −15.5 to −9.5 ppm.[1] The higher chemical shift values in the pyrochlore $AlF_{1.8}(OH)_{1.2}\cdot 0.3\ H_2O$ are in agreement with a higher OH/Al ratio. In order to assign the ^{27}Al NMR lines and to quantify the various possible $AlF_{6-x}(OH)_x$ environments, we have considered three compositions that remain within the average compositions given by chemical analyses: $AlF_{1.7}(OH)_{1.3}\cdot nH_2O$, $AlF_{1.8}(OH)_{1.2}\cdot nH_2O$ and $AlF_{1.9}(OH)_{1.1}\cdot nH_2O$. Based on a random F/OH distribution occurring in the 48f sites, the occurrence probabilities of the possible environments are given for the three compositions in Table 4.

Table 4 Occurrence probabilities of the $AlF_{6-x}(OH)_x$ species (%) based on an OH/F distribution in 48f sites

Chemical composition	$AlF_{1.7}(OH)_{1.3}$	$AlF_{1.8}(OH)_{1.2}$	$AlF_{1.9}(OH)_{1.1}$
AlF_6	3.3	4.7	6.5
$AlF_5(OH)$	15.2	18.7	22.4
$AlF_4(OH)_2$	29.0	31.1	32.4
$AlF_3(OH)_3$	29.6	27.6	25.0
$AlF_2(OH)_4$	17.0	13.8	10.9
$AlF(OH)_5$	5.2	3.7	2.5
$Al(OH)_6$	0.7	0.4	0.2

The best agreement between experimental relative line intensities and calculated probabilities is obtained with the chemical composition $AlF_{1.7}(OH)_{1.3}\cdot 0.3\ H_2O$, assuming that AlF_6, $AlF_5(OH)$ and $AlF_4(OH)_2$ species give rise to the main peak observed at $\delta_{iso} = -12.5$ ppm and assigning the three remaining lines at $\delta_{iso} = -8.7$, −4.2 and 1.8 ppm to $AlF_3(OH)_3$, $AlF_2(OH)_4$ and $AlF(OH)_5$ species, respectively (Table 3). This result appears to confirm the statistical repartition of the fluoride and hydroxyl anions in the 48f site and is in good agreement with the analytical data and X-ray diffraction refinement data. It should be noted that in the HTB phases, the δ_{iso} values of AlF_6 and $AlF_5(OH)$ (−15.5 ppm), $AlF_4(OH)_2$ (−11.7 ppm) and $AlF_3(OH)_3$ (−7.7 and −9.5 ppm depending on the sample) species[1] are close to those found for similar species in pyrochlore. The $\nu_Q\eta$ values range from 345 to 625 kHz (Table 3) and are close to those encountered in β-$AlF_{2.6}(OH)_{0.4}$.[1]

Investigation of the pyrochlore acidic properties

FTIR spectroscopy was used to probe the acidic surface properties using adsorption and temperature desorption of probe molecules. The choice of probe molecule depends on the nature of the acidity present at the surface of the material.[46] Pyridine and CD_3CN allow one to access both type of acidity (Lewis and Brønsted) and therefore were used in the present study.

Adsorption of CD_3CN. Fig. 10 presents the IR spectra of CD_3CN adsorbed on the surface of the

pyrochlore previously activated at 573 K.

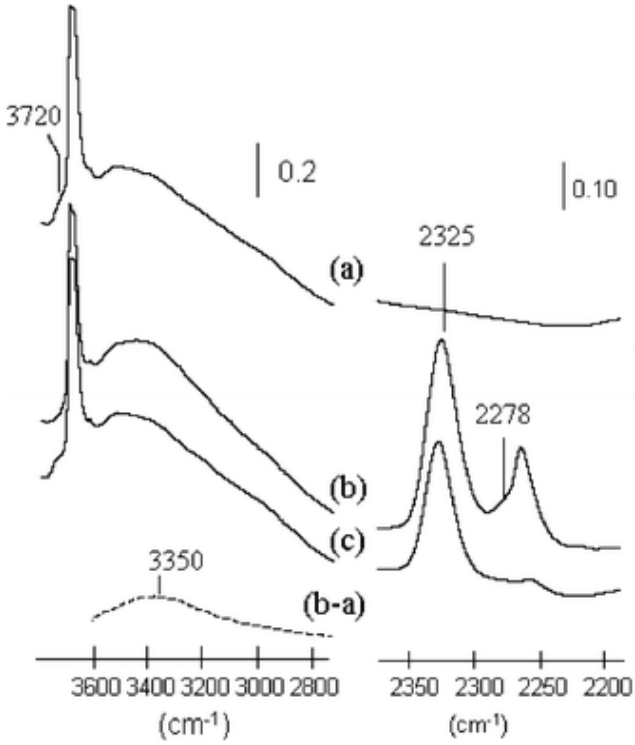

Fig. 10 IR spectra of CD_3CN adsorbed on the pyrochlore surface previously activated at 573 K (a), after introduction of an equilibrium pressure of CD_3CN (665 Pa) (b) and then evacuation under secondary vacuum at room temperature (c).

The use of such a molecule enables us to get information on the strength of Lewis acid sites through the position of the ν(C≡N) band which is generally located in the 2300–2350 cm^{-1} range.[47] At lower wavenumbers, a band around 2265 cm^{-1}
is due to physisorbed species whereas hydrogen-bonded species are characterized by the ν(CN) band at 2278 cm^{-1}. The latter is clearly observed in the spectrum recorded under an equilibrium pressure of CD_3CN (665 Pa) (Fig. 10b) but disappears after evacuation at room temperature. Such H-bonded species formation involves surface hydroxyl groups since their formation occurs at the expense of the OH groups characterized by the ν(OH) band at 3720 cm^{-1}. By contrast, no shoulder at wavenumbers higher than 1100 cm^{-1} is noted, showing that structural OH groups are not affected by the CD_3CN adsorption.

As reported in the case of the HTB form β-$AlF_{3-x}(OH)_x$,[1,28] the ν(OH) band of structural OH groups (3673 cm^{-1}) is located at a lower wavenumber than the one of surface OH groups (3720 cm^{-1}), due to confinement effects. The Brønsted acidity of the perturbed OH groups can be estimated through the wavenumber of the perturbed ν(OH) band (Fig. 10 spectra a and b) at 3350 cm^{-1} [Δν(OH) shift is equal to 370 cm^{-1}: 3720 – 3350]. Such a shift is similar to that reported for silanol groups of silicalite,[48] showing that pyrochlore compounds present some low acidic surface OH groups. However, this does not exclude the presence of a low number of stronger Brønsted acid sites since the perturbed ν(OH) band at 3350 cm^{-1} is quite broad.

The wavenumber of the ν(CN) band ascribed to coordinated CD_3CN sites at 2325 cm^{-1} is indicative of the strength of the Lewis acid sites, *i.e.*
the higher the wavenumber, the higher the strength of the Lewis acidity. For comparison, this band is observed under the same experimental conditions at 2320 cm^{-1} on γ-Al_2O_3[49] and 2329 cm^{-1} on β-$AlF_{2.6}OH)_{0.4}$.[50]
This shows that the Lewis acidity displayed by the pyrochlore is intermediate between that of γ-Al_2O_3 (strong) and β-AlF_3 (very strong).

Adsorption of pyridine. Fig. 11
presents the subtracted spectra recorded after introduction of pyridine into the cell (133 Pa) followed by

evacuation at increasing temperatures. After pyridine evacuation at room temperature, a weak ν8a band at 1600 cm^{-1}
characterizes the formation of H-bonded species which are desorbed by evacuation at 373 K. A very weak band is also observed at 1540 cm^{-1}, a wavenumber characteristic of pyridinium species revealing the occurrence of a very small number of strong Brønsted acid sites. As in the case of CD_3CN adsorption, the δ (OH) band at 1100 cm^{-1}
is not affected by pyridine introduction, showing that structural OH groups are not accessible to this probe. By contrast, the 3720 cm^{-1}
band is totally perturbed after pyridine evacuation at room temperature and is only partially recovered after outgassing at higher temperature. This shows that surface OH groups are involved in both H-bonded and protonated pyridinium species. However, pyridine coordination can also perturb OH groups in the neighbourhood by indirect interaction as shown on silica–alumina samples[51] which explains that the 3720 cm^{-1} band is not completely restored after pyridine evacuation at 573 K.

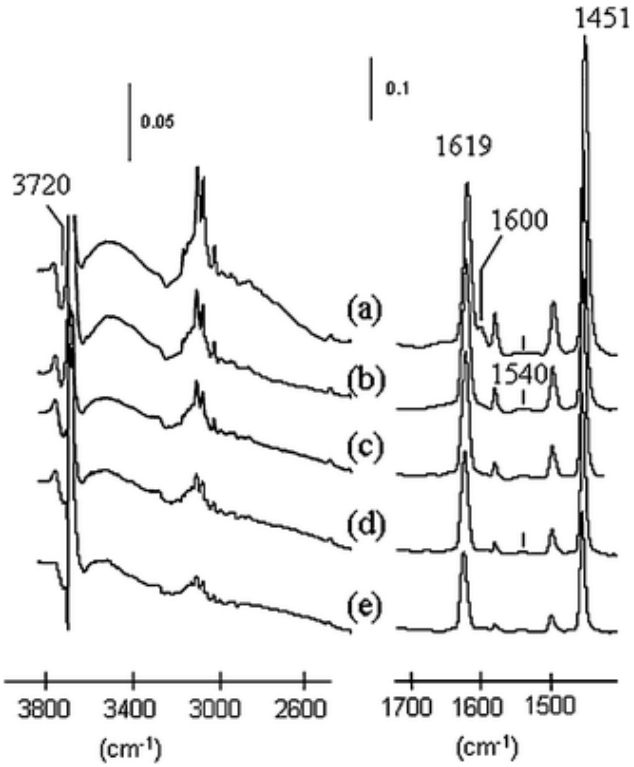

Fig. 11 IR difference spectra (blank subtracted) of adsorbed pyridine after activation at 573K. IR spectra recorded after thermodesorption at (a) room temperature, (b) 373K, (c) 423K, (d) 473K and (e) 573K.

The ν8a and ν19b frequencies of coordinated species observed at 1619 and 1452 cm^{-1} respectively (Fig. 11a) characterize the strength of the Lewis acid sites. Their wavenumber is higher than those reported for γ -alumina (1612 and 1449 cm^{-1} after pyridine evacuation at rt) and slightly lower than those observed for β -AlF_3 (1620 and 1454 cm^{-1}), a more fluorinated material[28] in good agreement with the results obtained with CD_3CN adsorption.

Conclusions

This work shows that the microwave-assisted route is a suitable technique for the achievement of high surface area metal-based fluorides. One of the key parameters is the low [HF]/[Al] precursor molar ratio which allows stabilization of the pyrochlore forms of aluminium hydroxyfluoride, whereas higher molar ratios led to the synthesis of HTB and distorted-ReO_3 forms. The use of aluminium alkoxyde and the addition of a small amount of ether have enabled the preparation of nanosized materials.

^{1}H, ^{19}F and ^{27}Al NMR studies evidence a disorder which is correlated to the distribution of O and F atoms on the 48f site. ^{19}F and ^{27}Al NMR spectra confirm the more important hydroxyl content in the

pyrochlore than in HTB phases in agreement with the proposed chemical formula. ^{27}Al high field NMR enables the quantification of the various $AlF_{6-x}(OH)_x$ environments and supports the random distribution of the F atoms and of the OH groups in 48f sites.

FTIR and NMR spectroscopies have been used to get more insight into the channel environment where hydrogen bonds have been evidenced. Two different zeolitic water configurations have been observed depending on the nature of the anionic framework environment: the water molecules being H-donor and H-acceptor with fluoride ions and hydroxyl groups in their vicinity, respectively.

The use of CD_3CN and pyridine as probe molecules shows that pyrochlore exhibits Lewis and Brønsted acid sites stronger than those of alumina, confirming the influence of fluorine content on the acid properties of Al hydroxyl fluorides. IR spectroscopy allows us to distinguish the hydroxyl groups present on the outer surface (3720 cm^{-1}) from those located inside the channels (3673 cm^{-1}). Due to steric hindrance, these latter are not accessible to the probe molecules, whereas those present on the outer surface generate weak and strong Brønsted acid sites. The use of CO as a probe molecule will be further used to get more insight into the Brønsted acidity.

Acknowledgements

The EU is thanked for financial support through the 6th Framework Programme (FUNFLUOS, Contract No. NMP3-CT-2004-5005575).

References

1 D. Dambournet, A. Demourgues, C. Martineau, S. Pechev, J. Lhoste, J. Majimel, A. Vimont, J.-C. Lavalley, C. Legein, J.-Y. Buzaré, F. Fayon and A. Tressaud, *Chem. Mater.*, 2008, **20**, 1459 [Links].

2 E. Kemnitz and D. H. Menz, *Prog. Solid State Chem.*, 1998, **26**, 97 [Links].

3 L. M. Rodriguez, J. Alcaraz, M. Hernadez, Y. Ben Taarid and M. Vrinat, *Applied Catalysis A: General*, 1998, **169**, 15; L. M. Rodriguez, J. Alcaraz, M. Hernadez, M. Dufaux, Y. Ben Taarid and M. Vrinat, *Applied Catalysis A: General*, 1999, **189**, 53; M. Moreno-Bravo, M. Hernandez-Luna, J. Alcaraz-Cienfuegos and A. Rosas-Aburto, *Applied Catalysis A: General*, 2003, **249**, 35; M. Moreno, A. Rosas, J. Alcaraz, M. Hernandez, S. Toppi and P. Da Costa, *Applied Catalysis A: General*, 2003, **251**, 369.

4 C. G. Krespan and V. A. Petrov, *Chem. Rev.*, 1996, **96**, 3269 [Links].

5 J. L. Fourquet, M. Riviere, A. Le Bail and M. Nygrens, *Eur. J. Solid State Inorg. Chem.*, 1988, **25**, 535 [Links].

6 J. M. Cowley and T. R. Scott, *J. Am. Chem. Soc.*, 1978, **70**, 105.

7 A. Hess, E. Kemnitz, A. Lippitz, W. E. S. Unger and D. H. Menz, *J. Catalysis*, 1994, **148**, 270.

8 J. M. Saniger, N. A. Sanchez and J. O. Flores, *J. Fluorine Chem.*, 1998, **117**, 88.

9 P. J. Chupas, D. R. Corbin, V. N. M. Rao, J. C. Hanson and C. P. Grey, *J. Phys. Chem. B*, 2003, **107**, 8327 [Links].

10 J. Rodríguez-Carvajal, *Physica B*, 1993, **192**, 55 [Links].

11 B. Blümich, P. Blumler and J. Jansen, *Solid State Nucl. Magn. Reson.*, 1992, **1**, 111 [Links].

12 P. Blumler, B. Blümich and J. Jansen, *Solid State Nucl. Magn. Reson.*, 1994, **3**, 237 [Links].

13 D. Massiot, J. Hiet, N. Pellerin, F. Fayon, M. Deschamps, S. Steuernagel and P. J. Grandinetti, *J. Magn. Reson.*, 2006, **181**, 310 [Links].

14 L. Frydman and J. S. Hardwood, *J. Am. Chem. Soc.*, 1995, **117**, 5367 [Links].

15 A. Medek, J. S. Hardwood and L. Frydman, *J. Am. Chem. Soc.*, 1995, **117**, 12779 [Links].

16 J. P. Amoureux, C. Fernandez and S. Steuernagel, *J. Magn. Reson.*, 1996, **123**, 116 [Links].

17 D. States, R. Haberkorn and D. Ruben, *J. Magn. Reson.*, 1982, **48**, 286 [Links].

18 R. Ernst, G. Bodenhausen, A. Wolkaun, *Principle of Nuclear Magnetic Resonance in One and Two Dimensions.*, Oxford University Press: New York, 1987.

19 D. Massiot, C. Bessada, J. P. Coutures and F. Taulelle, *J. Magn. Reson.*, 1990, **90**, 231 [Links].

20 L. B. Alemany, D. Massiot, B. L. Sherriff, M. E. Smith and F. Taulelle, *Chem. Phys. Lett.*, 1991, **177**, 301 [Links].

21 D. Massiot, D. Müller, Th. Hübert, M. Schneider, A. P. M. Kentgens, B. Coté, J. P. Coutures and W. Gessner, *Solid State Nucl. Magn. Reson.*, 1995, **5**, 175 [Links].

22 J. F. Stebbins, S. Kroeker, S. K. Lee and T. J. Kiczenski, *J. Non-Cryst. Solids*, 2000, **275**, 1 [Links].

23 D. Massiot, F. Fayon, M. Capron, I. King, S. Le Calvé, B. Alonso, J.-O. Durand, B. Bujoli, Z. Gan and G. Hoatson, *Magn. Reson. Chem.*, 2002, **40**, 70 [Links].

24 E. Kemnitz, U. Groß, S. Rudiger and C. S. Shekar, *Angew. Chem., Int. Ed.*, 2003, **42**, 4251 [Links].

25 L. Quarterman, H. H. Hyman and J. J. Katz, *J. Phys. Chem.*, 1961, **65**, 90 [Links].

26 P. Thompson, D. E. Cox and J. B. Hastings, *J. Appl. Crystallogr.*, 1987, **20**, 79 [Links].

27 A. Burneau, O. Barrès, J. P. Gallas and J. C. Lavalley, *Langmuir*, 1990, **6**, 1364 [Links].

28 A. Vimont, J. C. Lavalley, L. Francke, A. Demourgues, A. Tressaud and M. Daturi, *J. Phys. Chem. B*, 2004, **108**, 3246 [Links].

29 H. Eckert, J. P. Yesinowski, L. A. Silver and E. M. Stolper, *J. Phys. Chem.*, 1988, **92**, 2055 [Links].

30 F. Taulelle, M. Pruski, J. P. Amoureux, D. Lang, A. Bailly, C. Huguenard, M. Haouas, C. Gérardin, T. Loiseau and G. Férey, *J. Am. Chem. Soc.*, 1999, **121**, 12148 [Links].

31 N. Simon, N. Guillou, T. Loiseau, F. Taulelle and G. Férey, *J. Solid State Chem.*, 1999, **147**, 92 [Links].

32 L. Fischer, V. Harlé, S. Kasztelan and J.-B. d'Espinose de la Caillerie, *Solid State Nucl. Magn. Reson.*, 2000, **16**, 85 [Links].

33 E. Dumas, F. Taulelle and G. Férey, *Solid State Sci.*, 2001, **3**, 613 [Links].

34 P. J. Chupas, M. F. Ciraolo, J. C. Hanson and C. P. Grey, *J. Am. Chem. Soc.*, 2001, **123**, 1694 [Links].

35 B. Zhou, B. L. Sherriff, F. Taulelle and G. Wu, *Can. Mineral.*, 2003, **1**, 891 [Links].

36 P. J. Chupas and C. P. Grey, *J. Catal.*, 2004, **224**, 69 [Links].

37 E. Kemnitz, U. Groß, St. Rüdiger, G. Scholz, D. Heidemann, S. I. Troyanov, I. V. Morosov and M.-H. Lemée-Cailleau, *Solid State Sci.*, 2006, **8**, 1443 [Links].

38 M. E. Smith, *Appl. Magn. Reson.*, 1993, **4**, 1 [Links].

39 S. R. Jansen, H. T. Hintzen, R. Metselaar, J. W. de Haan, L. J. M. van de Ven, A. P. M. Kentgens and G. H. Nachtegaal, *J. Phys. Chem. B*, 1998, **102**, 5969 [Links].

40 B. Zhou, B. L. Sherriff, J. S. Hartman and G. Wu, *Am. Mineral.*, 2007, **92**, 34 [Links].

41 K. Scheurell, G. Scholz and E. Kemnitz, *J. Solid State Chem.*, 2007, **180**, 749 [Links].

42 A. Samoson, *Chem. Phys. Lett.*, 1985, **119**, 29 [Links].

43 C. Jäger, *J. Magn. Reson.*, 1992, **92**, 353.

44 D. Massiot, D. Müller, T. Hubert, M. Schneider, A. P. M. Kentgens, B. Cote, J. -P. Coutures and W. Gessner, *Solid State Nucl. Magn. Reson.*, 1995, **5**, 175 [Links].

45 G. Silly, C. Legein, J.-Y. Buzaré and F. Calvayrac, *Solid State Nucl. Magn. Reson.*, 2004, **25**, 241 [Links].

46 E. Payen, J. Grimblot, J. C. Lavalley, M. Daturi, F. Maugé, Application of Vibrational Spectroscopy in the Characterization of Oxides and Sulfides Catalysts, in *Handbook of Vibrational Spectroscopy*, Vol. 4, Ed. J. M. Chalmers and P. R. Griffith, Wiley, 2002.

47 H. Knozinger and H. Krietenbrink, *J. Chem. Soc., Faraday Trans.*, 1975, **71**, 2421; F. Thibault-Starzyk, A. Travert, J. Saussey and J.-C. Lavalley, *Topics in Catal.*, 1998, **6**, 111.

48 C. Paze, S. Bordiga, G. Spoto, C. Lambert and A. Zecchina, *J. Chem. Soc., Faraday Trans.*, 1998, **94**, 309 [Links].

49 A. Vimont, J. C. Lavalley, A. Sahibed-Dine, C. Otero Arean, M. Rodriguez Delgado and M. Daturi, *J. Phys. Chem. B*, 2005, **109**, 9656 [Links].

50 D. Dambournet, A. Vimont, H. Leclerc, J.-C. Lavalley, M. Daturi, A. Demourgues, A. Tressaud, M. Nickkho-Amiry, J. M. Winfield, In preparation.

51 A. Janin, M. Maache, J. C. Lavalley, J. F. Joly, F. Raatz and N. Szydlowski, *Zeolites*, 1991, **11**, 391 [Links].

Supplementary Material (ESI) for Journal of Materials Chemistry

Supplementary information

Structural investigations and acidic properties of high surface area pyrochlore aluminium hydroxyfluoride

D. Dambournet, A. Demourgues, C. Martineau, E. Durand, J. Majimel, A. Vimont, H. Leclerc, J.-C. Lavalley, M. Daturi, C. Legein, J.-Y. Buzaré, F. Fayon and A. Tressaud

Table of contents

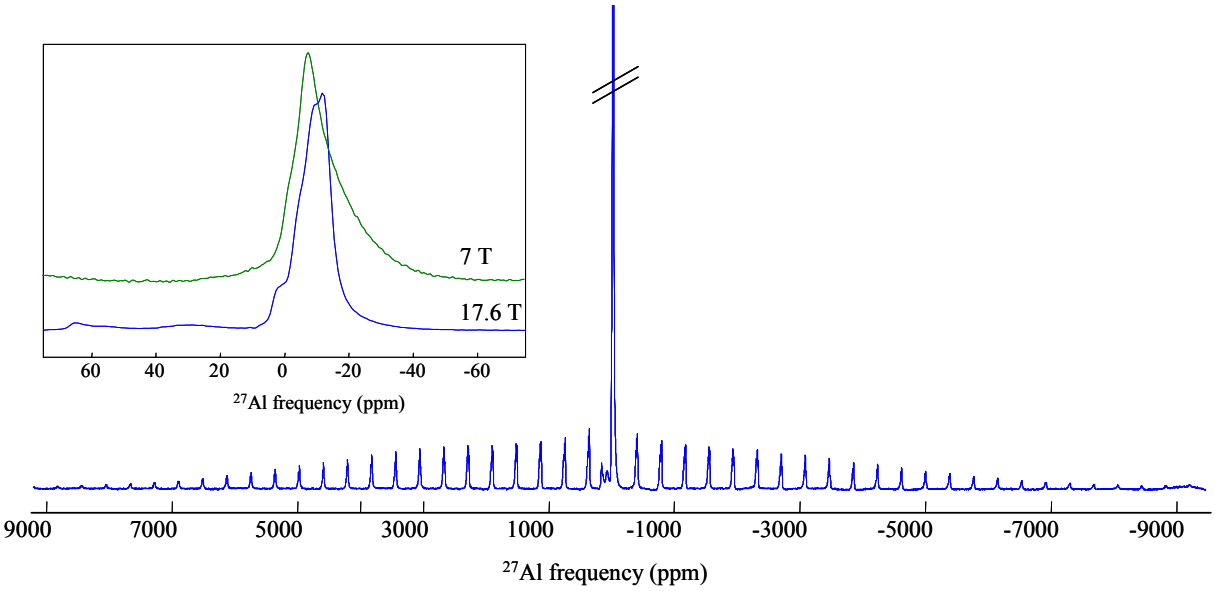

Figure S1. ^{27}Al MAS (30 kHz) one pulse spectrum of the pyrochlore $AlF_{1.8}(OH)_{1.2}.0.3H_2O$ recorded at 17.6 T. The central transitions of the spectra recorded at 17.6 and 7 T are presented in the inset.

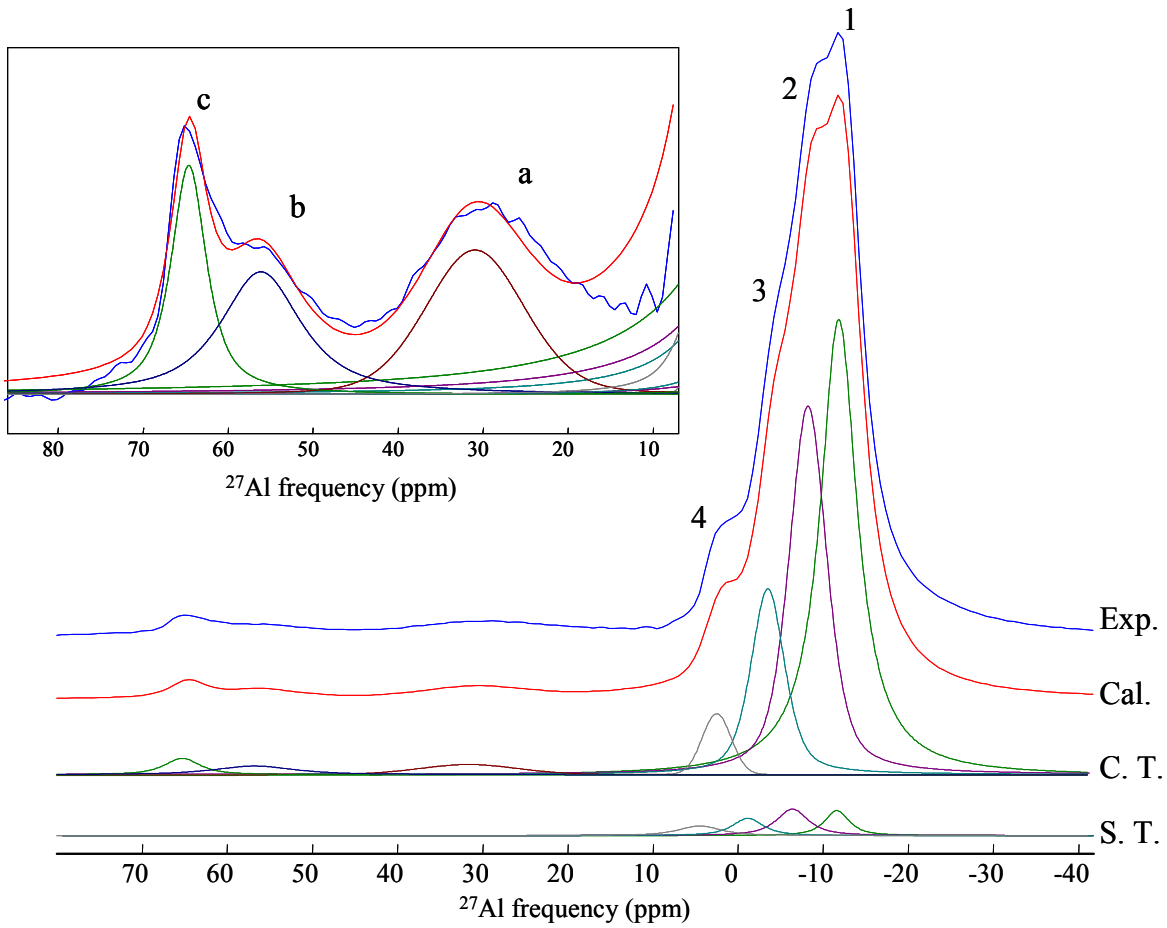

Figure S2. Experimental (blue) and calculated (red) central line of the ^{27}Al MAS NMR spectrum of the pyrochlore $AlF_{1.8}(OH)_{1.2}.0.3H_2O$. The deconvolution, achieved using four contributions, takes into account the N = 0 band of both the satellite transitions <3/2> (S. T.) and the central transition <1/2> (C. T.). Resonances a, b and c were reconstructed using Gaussian lines to extract isotropic chemical shifts.

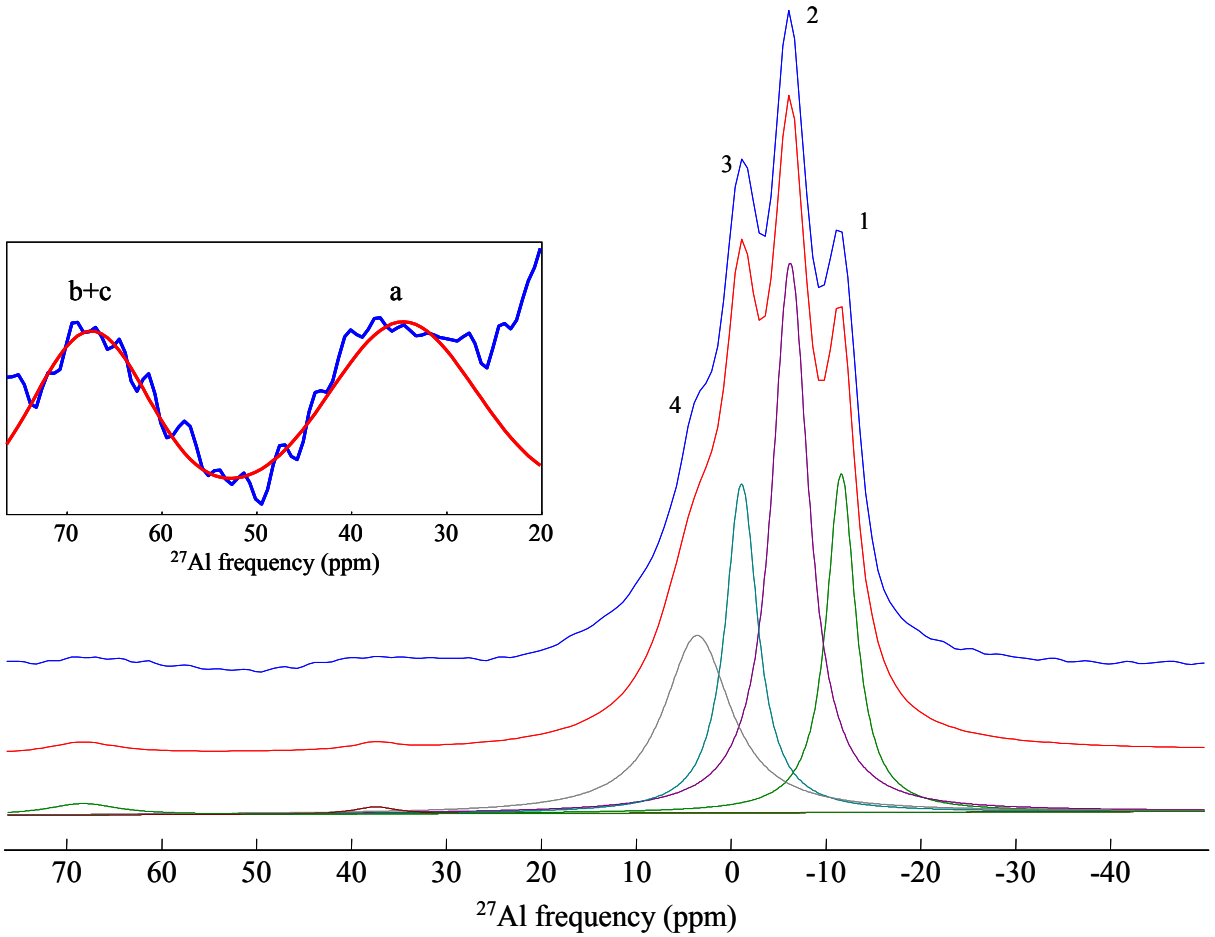

Figure S3. Experimental (blue) and calculated (red) full projection of the TOP reconstruction of the ^{27}Al MAS NMR spectrum of the pyrochlore $AlF_{1.8}(OH)_{1.2}.0.3H_2O$. The deconvolution is achieved using Gaussian contributions.

2.3 Un nouveau fluorure d'aluminium hydraté à lacunes cationiques.

Publication: *A new aluminium fluoride hydrate with cationic vacancies: structure, thermal stability and acidic properties, submitted to Journal of the American Chemical Society*

Contrairement aux deux premières parties qui traitent de types structuraux bien connus de la littérature, nous reportons ici la synthèse et la caractérisation d'une nouvelle variété de fluorure d'aluminium hydraté présentant une structure cubique dérivée de ReO_3. Dans un premier temps, nous rappelons les différents paramètres clés qui nous ont permis d'obtenir des différentes variétés présentées dans ce manuscrit. Puis nous présentons la caractérisation structurale de cette nouvelle variété qui a nécessité la combinaison de plusieurs techniques. La méthode de Rietveld a permis de mettre en évidence la présence de lacunes cationiques générées par la présence de molécules d'eau jouant le rôle de ligand. Ces entités ont été caractérisée par analyse thermique et infrarouge à transformée de Fourier. La présence de molécules d'eau associées aux lacunes cationiques confère au solide des propriétés acides au sens de Lewis et de Brønsted tout à fait particulières.

A new aluminum fluoride hydrate with cationic vacancies: structure, thermal stability and acidic properties

Damien Dambournet,[#] Alain Demourgues,[#] Charlotte Martineau,[†] Etienne Durand,[#] Jérôme Majimel,[#] Christophe Legein,[†] Jean-Yves Buzaré,[‡] Franck Fayon,[§,/] Marco Daturi[+] and Alain Tressaud[#]*

Institut de Chimie de la Matière Condensée de Bordeaux-CNRS, Université Bordeaux 1. 87, Avenue du Dr. A. Schweitzer, 33608 Pessac cedex, France.

† Laboratoire des Oxydes et Fluorures, CNRS UMR 6010, IRIM2F, CNRS FR 2575, Université du Maine, Avenue Olivier Messiaen, 72085 Le Mans Cedex 9, France.

‡ Laboratoire de Physique de l'Etat Condensé, CNRS UMR 6087, IRIM2F, CNRS FR 2575, Université du Maine, Avenue Olivier Messiaen, 72085 Le Mans Cedex 9, France.

§ Conditions Extrêmes et Matériaux : Haute Température et Irradiation, UPR CNRS 3079, 1D Avenue de la Recherche Scientifique, 45071 Orléans Cedex 2, France.

[+] Laboratoire Catalyse et Spectrochimie, UMR 6506, CNRS-ENSICAEN-Université de CAEN, Boulevard du Maréchal Juin, F-14050 Caen Cedex, France.

ABSTRACT. A new aluminum fluoride hydrate was synthesized by microwave hydrothermal process. The structure derives from the ReO_3 type structure, *i.e.* the high temperature structure of α-AlF_3. The cubic symmetry adopted by this compound arises from water molecules, stabilized as ligand surrounding Al^{3+} cations which induces cationic vacancies as revealed by Rietveld refinement. The following chemical formula $Al_{0.82}\square_{0.18}F_{2.46}(H_2O)_{0.54}$ is supported by chemical analysis and TGA measurements. This represents the first example of aluminum vacancy compound in the Al-based fluorides chemistry. High field ^{27}Al NMR spectroscopy enabled identification and quantification of the following species: AlF_6 and $AlF_{6-x}(H_2O)_x$ with x=1, 2, 3 and showed that vacancies are mainly surrounded by water molecules but also by a low content of fluoride ions as also evidenced by ^{19}F NMR. Hydrogen bonding network, which takes place in the vicinity of the cationic vacancies was characterized by FTIR and ^{1}H NMR spectroscopies. A 2:1 complex X···H-O-H···X where X is a proton acceptor, which is related to a shift of the $\nu_{sym}(OH)$ and $\nu_{asym}(OH)$, was detected. This complex appears to be stable up to 773 K. The phase transition into the rhombohedral form occurs at around 573 K but at such a temperature a large amount of water molecules associated to cationic vacancies still remained thanks to the 2:1 complex. The acidic properties have been revealed by pyridine and CO probe molecules. At 573 K, the solid exhibits both strong Lewis and Brønsted acidities with an equivalent number of sites providing bifunctionality. The strong acidic behavior highlights the effect of water molecules/cationic vacancies on the surface structure. Whereas the Lewis strength acidity progressively decreases with dehydration, Brønsted acidity remains strong even at 773 K.

KEYWORDS. Aluminum fluoride hydrate, cubic form, ^{1}H, ^{19}F and high field ^{27}Al solid state NMR, hydrogen bonds, 2:1 water complex, strong Lewis/Brønsted acidities.

Introduction. The chemistry of aluminum-fluorine system is very rich through the existence of several allotropic forms of AlF_3: α, β, η, θ, κ-AlF_3,[1] but for a long time these compounds could not be prepared as nanomaterials. The extreme reactivity of fluorine element prevented the stabilization of nano-particles using conventional "chimie douce" routes. Recently, microwave-assisted synthesis has allowed obtaining nano-sized crystallized aluminum hydroxy-fluoride.[2,3] Tuning the OH/F molar ratio has been proved to be a decisive tool to get the required compositions and structures. Some aluminum fluorides are known to be strong Lewis acids.[4,5] The presence of OH groups in these materials enables to balance the Brønsted/Lewis acidic behavior. Water molecules can also be considered to act as potential strong Brønsted acid sites as revealed for instance in the case of alumino-silicates.[6] In order to be suitable for catalytic applications, anion species and water should be thermally stable. The occurrence of both acidities can be suitable for peculiar reactions involving a Brønsted/Lewis acid synergy, as reported for instance in zeolite-promoted hydrocarbons reactions.[7] Such a synergetic effect has been evidenced by ab-initio calculations to occur with HF and AlF_3. The synergy between both catalysts enables a drastic lowering of the activation barrier of the formamide synthesis.[8]

Aluminum fluoride hydrates have been used as precursors to prepare various forms of AlF_3. For instance, the decompositions of α- and β-$AlF_3.3H_2O$ that occur at rather low temperatures (<623K), lead to the metastable β-AlF_3 form and the thermodynamically stable one α-AlF_3, respectively.[4] The most known among the aluminum fluoride hydrates, *i.e.* $AlF_3.9H_2O$, α and β-$AlF_3.3H_2O$, have been recently reinvestigated using X-ray/neutron diffractions and Nuclear Magnetic Resonance (NMR) spectroscopy.[9] These structures are built either from isolated octahedra for the first two compounds ($AlF_3.9H_2O$, α-$AlF_3.3H_2O$) or 1D chains of corner-bridging $AlF_{6-x}(H_2O)_x$ octahedra for the third one (β-$AlF_3.3H_2O$) with hydrogen network giving rise to a low thermal stability.

The α-form of aluminum trifluoride has received extended attention over the years. This structure adopts a distorted ReO_3-type structure and undergoes a first-order phase transition at around 723 K into the cubic ReO_3 form.[1a] The phase transition has been studied using molecular dynamics simulations and the anion polarization has been established as the driving force of the tilting AlF_6 octahedra.[10] Fluorination of γ-Al_2O_3 with $CHClF_2$ led to a catalytically active phase[11] which has been identified as the cubic α-AlF_3 form, highlighting potential application as catalyst. Concomitantly, ab initio calculations performed on the

(0001) surface of the rhombohedral form of α-AlF_3 show that potential Lewis acid sites are masked by two fluoride ions leading to poor Lewis acidity.[12,13] However, Lewis acid centres have been evidenced to occur on clean α-AlF_3 (01-12) surface.[14] Nevertheless, the conditions to avoid hydroxylation which provokes the inaccessibility of these centres have been concluded to be unrealistic.[14] Additionally, molecular dynamic simulation performed on cubic α-AlF_3 nano-particles showed the occurrence of potential strong Lewis acid sites.[15] The rhombohedral form α-AlF_3 therefore appears as a weak Lewis catalyst whereas a small perturbation of the network, *i.e.* cubic symmetry, seems to lead to a completely different surface structure generating Lewis acidity.

The present work reports the synthesis and the characterization of a new aluminum fluoride hydrate exhibiting the ReO_3-type structure. Powder Rietveld refinement, high resolution transmission electron microscopy (HRTEM), BET measurement, ^1H, ^{19}F and ^{27}Al magic angle spinning (MAS) NMR investigations, thermogravimetric analysis coupled with mass spectrometry (TGA-MS) and Fourier transform infra-red (FTIR) analysis with and without the adsorption of probe molecules (pyridine, CO) have been used to characterize the structural features and acidic properties of this compound.

Experimental procedures.

1. Synthesis procedure. Synthesis was performed using a MARS-5 Microwave Digestion System oven (CEM Corp.). A precursor solution was first prepared as follows: 25 mmol of Al(III) chloride hexahydrated ($AlCl_3.6H_2O$, Sigma-Aldrich: 99%) was added to a solution containing 10 ml of isopropanol (Isopropanol Sigma-Aldrich 98%) and 10 ml of distilled water. An aqueous HF solution (Panreac 40%) was added to the mixture in proportions ensuring an [HF]/[Al] molar ratio equal to 3.5. The solution was placed in a closed Teflon container (XP-1500 plus model) and submitted to microwave heating for 1h to a temperature of 413 K (17 $K.min^{-1}$). After microwave-assisted drying performed for 30 minutes under primary vacuum and argon flow at 373 K a powdered sample was recovered. The sample was washed with a large amount of ethanol under nitrogen flow.

2. Characterizations.

Elemental analysis. The final [F]/[Al] molar ratio was measured by electron probe micro-analysis (EPMA) using a Castaing microprobe CECAMA SX 630 apparatus equipped with Wavelength Dispersive Spectrometry.

X-ray diffraction analysis: The compounds were characterized by X-ray powder diffraction (XRPD) using a Philips PW 1050 diffractometer in a Bragg-Brentano geometry with Cu Kα radiation ($K\alpha_1$=1.54059 Å and $K\alpha_2$=1.54441 Å). The intensity data were collected

at room temperature over a 2θ range of 5-110° with 0.02° steps and integration time of 10 s. The whole pattern profile matching and the Rietveld structural refinement were performed with the FULLPROF program.[16]

Surface area measurement. Prior to adsorption, around 200 mg of the powdered sample were evacuated overnight at 573 K under 0.1 Pa. N_2 adsorption isotherms were performed at 77 K using an ASAP 2000 instrument from Micromeritics. The specific surface area S_{BET} was calculated from BET results applied in the P/P° [0.03 – 0.25] range.

Transmission electron microscopy. Transmission Electron Microscopy (TEM) was performed on a TECNAI F20 equipment with a field emissive gun (operating at 200 kV and with a point resolution of 0.24 nm). The Gatan Digital Micrograph® software was used to calculate the Fast Fourier Transforms (FFT) of HRTEM. TEM samples were prepared by dissolving few milligrams of powder in ethanol. The solution was then dipped ten minutes into an ultrasonic bath so as to disagglomerate the powder particles. One drop of the solution was finally deposited on a Formvar/Carbon copper grid.

FTIR spectroscopy. Infrared transmission spectra were recorded on self-supporting wafers (2 cm^2, 20 mg) which were placed into an infrared quartz cell (KBr windows) connected to a vacuum line. Samples were activated under vacuum at 573 K overnight. Spectra were recorded with a resolution of 4 cm^{-1}. The IR spectrometer was a Nicolet Nexus apparatus equipped with an extended KBr beam splitter and a mercury cadmium telluride (MCT) detector. Probe molecules were introduced into the cell via the vacuum line. After activation, the acidity of the materials was studied using adsorption of pyridine and CO (at 100K).

NMR spectroscopy.

The ^{19}F and ^{1}H Hahn echo Magic Angle Spinning (MAS) NMR spectra were acquired on an Avance 300 Bruker spectrometer (B_0 = 7 T), using a 2.5 mm ^{19}F optimized CP MAS probe, operating at a Larmor frequency of 282.2 MHz and 300.1 MHz for ^{19}F and ^{1}H, respectively. The 90° pulse durations were set to 4 μs (RF field 60 kHz) and 2.5 μs (RF field 100 kHz) for ^{19}F and ^{1}H, respectively, with an inter-pulse delay equal to one rotor period. The recycle delays were taken to 10 s and 1 s for ^{19}F and ^{1}H, respectively. The ^{19}F chemical shifts were referenced to $CFCl_3$ at 0 ppm. The ^{1}H chemical shifts were referenced to ^{1}H in TMS at 0 ppm. These spectra were reconstructed using DMFIT software.[17]

^{27}Al (I = 5/2) MAS NMR spectrum was recorded using a 2.5 mm CP MAS probe on an Avance 750 Bruker spectrometer (B_0 = 17.6 T) and an Avance 300 Bruker spectrometer (B_0 = 7 T) operating at a ^{27}Al Larmor frequency of 195.5 and 78.2 MHz, respectively. A short pulse length of 1 μs was used to ensure quantitative excitation of the whole spin system. The recycle

delay was set to 1 s. ^{27}Al spectra were referenced to 1 M aqueous solution of $Al(NO_3)_3$. Quantitative reconstructions[18-21] of the main resonance of the ^{27}Al NMR spectra were achieved taking into account the N = 0 spinning sideband of the satellite transitions <3/2> and the N = 0 spinning sideband of the central transition <1/2> which completely overlap. For each ^{27}Al NMR site, the isotropic chemical shift δ_{iso} and the quadrupolar product $\nu_{Q\eta}$ were calculated by comparison of the centre of gravity $\delta_{cs}^{<3/2>}$ of the Al satellite sideband with that of the central transition $\delta_{cs}^{<1/2>}$, through the following equation: $\delta_{cs}^{<m>} = \delta_{iso} - \nu_{Q\eta}^2 \frac{[I(I+1) - 3 - 9m(m-1)]}{30\nu_0^2}.10^6$, where I = 5/2 in the case of ^{27}Al, ν_0 = 195.5 MHz (for the 17.6 T spectrometer) and $\nu_{Q\eta} = \nu_Q \sqrt{1 + \frac{\eta_Q^2}{3}}$.[20] A two-dimensional one pulse[22-24] (TOP) spectrum was constructed by stacking sub-spectra shifted by the spinning frequency from the 1D MAS NMR spectra.

Thermogravimetric analysis. The thermal behaviour was studied by simultaneously coupled TA-MS measurements. A NETZSCH thermoanalyzer STA 409 C, equipped with a BALZERS QMG 421, was used to record the thermoanalytical curves (T, DTA, TG, DTG) together with the ionic current (IC) curves in the multiple ion detection (MID) mode. A constant purge gas flow of 70 ml/min nitrogen (MESSER-GRIESHEIM 5.0) and a constant heating rate of 10 K/min were applied.

Results and discussion.

1. Microwave-assisted synthesis and determination of the chemical composition

Microwave-assisted synthesis was recently proved to be an efficient way to obtain nanosized crystallized aluminum fluorides. This method enables the achievement of high surface area aluminum hydroxyfluorides exhibiting either the pyrochlore-type[3] (137 $m^2.g^{-1}$) or the metastable hexagonal tungsten bronze-type which is alternatively named β or HTB[2] (82 $m^2.g^{-1}$). During these investigations, it has been demonstrated that some key parameters play a decisive role in the stabilization of the final structure and in getting high surface area materials. Among them, the R=[HF]/[Al] molar ratio was proved to be a relevant parameter in the stabilization of the final form. Using nitrate ($Al(NO_3)_3$) as aluminum precursor, three domains could be distinguished: R=2, R=3 and R>3. For R=2 and R=3, the pyrochlore-type structure and a derived form of β-AlF_3 were obtained, respectively. Higher [HF] contents, *i.e.*

R>3, led to a mixture containing β-AlF_3, rhombohedral and cubic form of Al-based fluoride. The influence of the aluminum precursor on the stabilized structures was also found to be decisive. For R=3, aluminum chloride as precursor led to a mixture of β-AlF_3 and α-AlF_3, whereas Al nitrate, by being reduced into ammonium ions during the microwave-assisted synthesis, enabled the stabilization of the metastable phase β-AlF_3.

Chloride precursor appears however interesting when a solution with high [HF]/[Al] molar ratio is added to a water/isopropanol mixture. The hydrothermal microwave heat treatment of the resulting mixture enables to prepare a powder which can be indexed with the ICDD-JSPDS file N°72-1117 referred as $AlF_3.H_2O$. It should be noted that the procedure should be carefully followed to get phase purity. The structure of this material was solved by Chandross[25] using a cubic lattice (Pm-3m) and a unit cell parameter, a=3.610Å, which is closely related to that of the high temperature phase[11] of the thermodynamically stable phase α-AlF_3 (R-3c). In this paper, the water molecules were located in the centre of the cube with AlF_6 octahedra at the corners. Nevertheless, the poor agreement factor reported by the author, *i.e.* 16.4%, revealed an unrealistic structural model. In such conditions, we decided to reinvestigate the structure of this material, as it will be described in the next section.

The chemical composition of the compound was determined prior to the structure investigation. EPMA gave a F/Al molar ratio close to 3. The occurrence of a very small amount of OH groups can not be excluded. Thermogravimetric analysis coupled with a mass spectrometer was performed up to 1073 K and a weight loss of 13.8% was measured. The weight loss was mainly ascribed to the release of water through the ionic curve m/z = 18, characterizing H_2O^+ fragments. The presence of structural water was further confirmed by FTIR spectroscopy, as it will be discussed later. When aged in moist air, the material undergoes a partial decomposition with the detection by XRD of trace of the pyrochlore phase.

2. Structural investigation

2.1. Rietveld Refinement

Rietveld refinement was first performed using the high temperature α-AlF_3 structure (Pm-3m a=3.60 Å)[11] where Al^{3+} ions are placed at the corner of the cube (0, 0, 0), and F^- ions are on the edge (½, 0, 0). A poor agreement factor R_{Bragg} = 18.8% was obtained for such a model (Figure 1A). In a fisrt step, the presence of water on the centre (½, ½, ½) of the cube have been tested but no residual electron density in this atomic position have been found and the Bragg factor remains high around 18%. In a second step, we introduced water molecule in the first coordination sphere of the Al^{3+} ions.

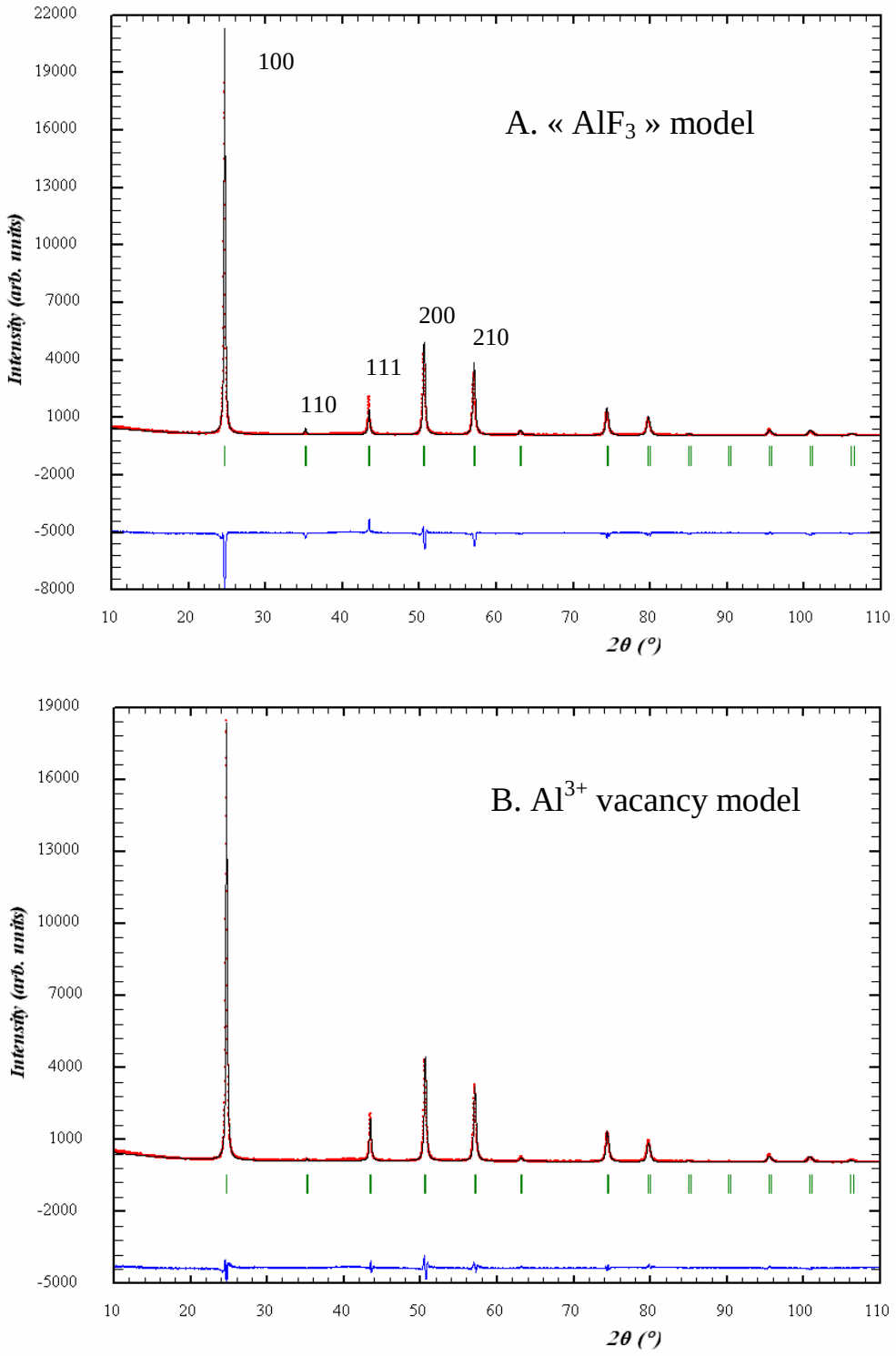

Figure 1. Rietveld plot obtained using: A. α-AlF_3 cubic model, B. model with cation vacancies. Experimental X-ray diffraction powder pattern (red curve) compared to the Rietveld-refined profile (black curve) and the difference curve (blue curve). The vertical bars correspond to the positions of the Bragg reflections.

The resulting octahedra element can then be written as $[AlF_{6-x}(H_2O)_x]^{x-3}$, in which water is considered as neutral; the lack of electron density upon the octahedra should be balanced by the occurrence of cation vacancies. Rietveld refinement was therefore performed based on this new structural model where the cation vacancies are correlated with the occurrence of H_2O molecules substituting F^- ions. The anionic site (3a) is statistically occupied either by F^- ions or H_2O molecules (Table 1).

Crystal symmetry: cubic

Space group: Pm-3m; Z = 1

A. "AlF_3" model

Atoms (Wyckoff position)	(x, y, z)	B_{iso} (Å^2)	Occupancy	Reliability Factors (%)
Al^{3+} (1a)	0, 0, 0	0.7(3)	1	χ^2: 7.37 cR_p: 27.5 cR_{wp}: 26.6 R_{Bragg}: 18.8
F^- (3d)	1/2, 0, 0	2.1(5)	1	

B. Al^{3+} vacancies model

Atoms (Wyckoff position)	(x, y, z)	B_{iso} (Å^2)	Occupancy	Reliability Factors (%)
Al^{3+} (1a)	0, 0, 0	0.6(3)	0.816(18)	χ^2: 3.37 cR_p: 17.8 cR_{wp}: 18.0 R_{Bragg}: 4.3
F^- (3d)	1/2, 0, 0	2.1(4)	0.820(6)	
H_2O (3d)	1/2, 0, 0	2.1(4)	0.178(6)	

a = 3.6067(1) Å

Al-F: 1.8034(1) Å

F-F: 2.5503(1) Å

Table 1. X-ray refinement data

A relation which can be summarized by the following chemical formula: $Al_{1-x}\square_xF_{3-3x}(H_2O)_{3x}$ was used in the Rietveld refinement to ensure the electroneutrality of the model. The corresponding model strongly improved the Rietveld refinement to a better agreement factor R_{Bragg} equal to 4.3% (Figure 1B). One should have to notice the disorder for the F/H_2O site revealed by the high Debye-Weller factor (Table 1). This disorder can be explained by the occupancy of the same crystallographic site by F^- ions and H_2O molecules and the occurrence of Al^{3+} vacancies. Table 1 summarizes the refinement results obtained using the stoechiometric and Al^{3+} vacancy models.

On the basis of the refinement and chemical analysis, the corresponding formula could be established: $Al_{0.82}\square_{0.18}F_{2.46}(H_2O)_{0.54}$. This represents the first example of aluminum vacancy compound in the Al-based fluoride chemistry. Several density measurements have been performed but because of the water departure, these data are not exploitable. Thermogravimetric analysis was in rather fair agreement with the above chemical formula, *i.e.* the experimental weight loss deduced from thermogravimetric analysis is equal to 13.8%. vs. 12.4% calculated from Rietveld refinement with the above formula. The difference can arise from standard deviation from Rietveld refinement and/or from the release of HF molecules resulting from the reaction of water with the fluoride network.

The cubic symmetry of the structure was confirmed by the Fast Fourier Transforms (FFT) of HRTEM images displayed on Figure 2 (Inset). It can be noted that the cubic symmetry is additionally reflected by the shape of the particles (Figure 2).

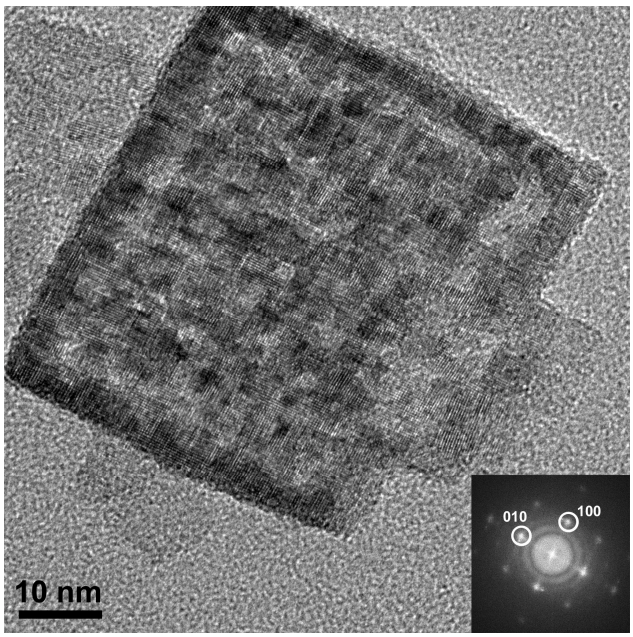

Figure 2. HRTEM micrograph of a particle of cubic aluminum fluoride hydrate. Inset: digital diffractogram of the nanoparticle revealing a [001] zone axis.

X-ray diffraction line broadening analysis was used to get more insight into the microstructure with the calculation of the micro-strains (Δd/d) and crystallite size. By using the global profile refinement, the microstructural features (coherent domains and micro-strains) were extracted from the additional line broadening of the Bragg peaks. Instrumental contribution was established by the XRD pattern of standard LaB_6 powder. Isotropic contributions were considered for both coherent domains and micro-strains. The calculated average size particle is 50 nm, which is in agreement with HRTEM observation (Figure 2) and the calculated micro-strains value is $\Delta d/d = 2.10^{-3}$. It should be noted that some micro-distortions have been observed on HRTEM images confirming the results of XRD analysis. The occurrence of water molecules inside the network could be at the origin of such a microdistorsion.

2.2. Evolution of the structural features upon annealing

As previously mentioned, during the TG analysis the thermodesorption process of water has been followed using mass spectrometry (Figure 3).

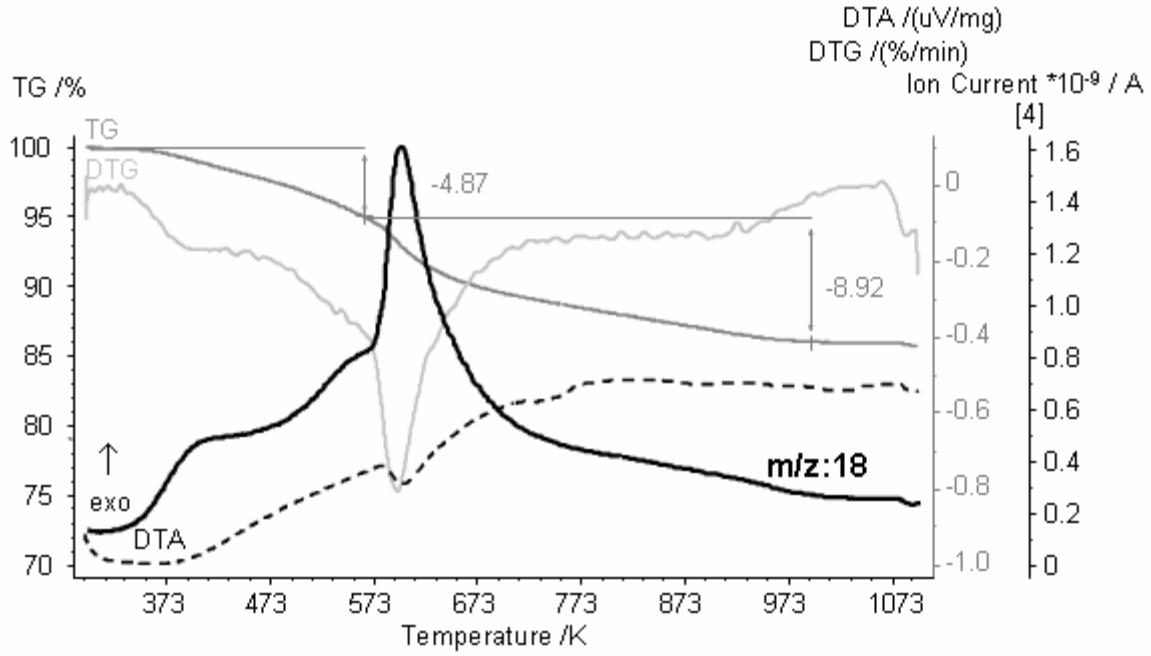

Figure 3. Thermogravimetric (DTG, DTA) analyses and mass spectrometry curve of m/z=18 (H_2O^+ fragment) performed on the cubic aluminum fluoride hydrate.

The ionic curve m/z=18 (H_2O^+) shows three events located at 413, 563 and 588 K. The first one can be ascribed to the departure of water molecules. The second event is very weak and can be ascribed to structural water which appears less stable than those for which the departure occurs at 588 K. This last one is very intense but seems thereafter to continue over a

large range of temperatures, *i.e.* up to 973 K. It should be noted that a weak endothermic effect concomitant with the third event is detected on the DTA curve close to 588 K.

The effect of the dehydration upon the structure has been studied by annealing $Al_{0.82}\square_{0.18}F_{2.46}(H_2O)_{0.54}$ at various temperatures, *i.e.* from 373 to 773 K. Samples were annealed under Ar flow (10 ml.min^{-1}) for 24 hours. The corresponding room temperature powder XRD patterns of annealed samples are displayed in Figure 4.

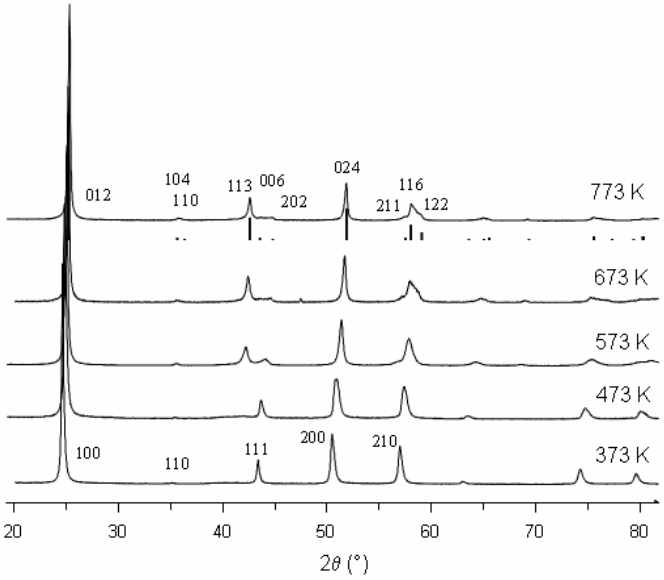

Figure 4. Evolution of the powder XRD patterns (room temperature) of cubic aluminum fluoride hydrate after annealing at various temperatures. Vertical bars represent the XRD peaks positions of α-AlF_3 (R-3c) from ICDD-JCPDS file N°44-0231.

The cubic form appears to be stable up to 473 K with a smaller unit-cell constant probably associated to water departure and the reduction of cation vacancy rate. After annealing at higher temperatures, some X-ray diffraction lines split revealing a lower symmetry. At 573 K, the cubic phase undergoes a rhombohedral distortion which is associated in the DTA curve with the small endothermic phenomenon. The Bragg peaks corresponding to the rhombohedral form of α-AlF_3 have been included in Figure 4, accounting for the symmetry change.

2.3. Hydrogen bonding network characterization

FTIR spectroscopy has been further used to study the stability of water molecules. Additionally, this technique enables to probe the conformation of water molecules and to check the occurrence of hydrogen bonding inside the structure. The inter-anionic distance obtained from Rietveld refinement is 2.55 Å, a value which should lead to strong hydrogen bonding.[26,27] Due to the large amount of water in the sample, the IR spectrum presents a high signal to noise. For sake of clarity, the sample was annealed in situ at various temperatures up

to 773 K in order to reduce such a background. IR spectra of $Al_{0.82}\square_{0.18}F_{2.46}(H_2O)_{0.54}$ after annealing at 573, 673 and 773 K are displayed in Figure 5.

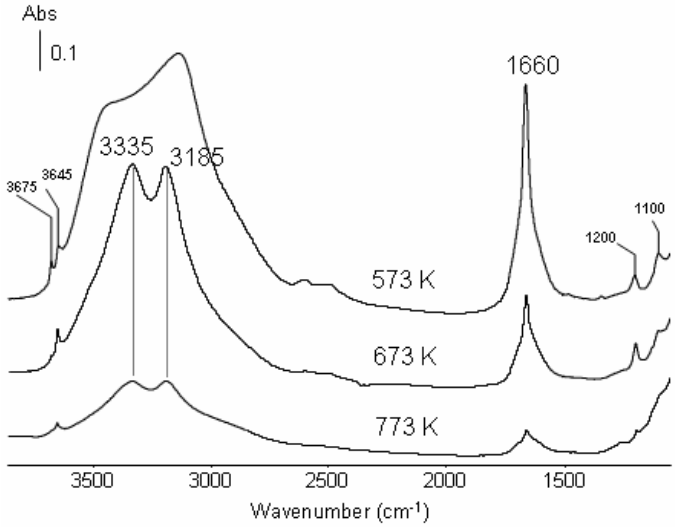

Figure 5. IR spectra of cubic aluminum fluoride hydrate recorded after in-situ annealing at various temperatures.

The spectra reveal two types of contributions located in the 2800-3700 cm^{-1} and 1600-1700 cm^{-1} ranges which are ascribed to the stretching and deformation modes of water molecules, respectively. The large envelop detected in the 2800-3700 cm^{-1} range confirms the occurrence of hydrogen bonding inside the structure. The stability of structural water molecules is clearly evidenced since the stretching and deformation modes of H_2O are still detected at 773 K. The two contributions decrease significantly during the annealing process. At 573 K, in the 2800-3500 cm^{-1} region (water molecules linked by hydrogen bonding), two bands can be clearly distinguished at 3185 and 3335 cm^{-1}.

Without any interaction, water molecule is built of "free OH bonds" which exhibit two OH stretching modes, $\nu_{sym}(OH)$ and $\nu_{asym}(OH)$ vibrating at 3616 and 3708 cm^{-1}, respectively.[28] The shifts of these two frequencies depend on the energy of the hydrogen bonding interaction, *i.e.* the stronger the hydrogen bonding, the larger the shift toward low wavenumbers.[28] The position of the two perturbed $\nu(OH)$ thus accounts for moderate hydrogen bonding. The shift from the "free OH bond" is almost similar for both $\nu_{sym}(OH)$ and $\nu_{asym}(OH)$ suggesting similar hydrogen bonding strength interactions. The corresponding complex is called a 2:1 complex[29] and can be written as X···H-O-H···X where X is a poton acceptor. Water molecules can act as both hydrogen donor and hydrogen acceptor with F^- ions and neighbouring water molecules, respectively. A complex hydrogen network is therefore assumed to occur.

Additionally, the deformation mode of water molecules $\delta(H_2O)$ is detected at 1660 cm^{-1} which corresponds to a shift of 60 cm^{-1} as compared to water in an inert solvent and accounts for water molecules involved in hydrogen bonding[30,31] confirming the above observations. Some very weak bands which can be ascribed to hydroxyl groups are also detected. Such bands are indeed observed at 1100-1200 and 3645-3675 cm^{-1} (Figure 5) and may account for the deformation and stretching mode of hydroxyl groups,[32] respectively. Traces of hydroxyl groups can thus be considered, even at high temperatures.

^1H solid-state NMR was used to confirm the existence and the strength of hydrogen bonds in the hydrate form. Two ^1H resonances with δ_{iso}=5.0 and 8.0 ppm are readily apparent in the ^1H MAS NMR spectrum of $Al_{0.82}\square_{0.18}F_{2.46}(H_2O)_{0.54}$ (Figure 6 and Table 2).

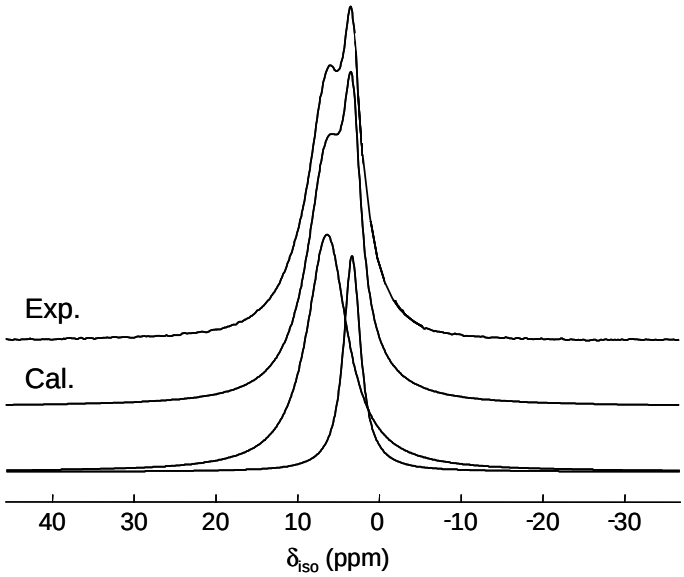

Figure 6. Experimental and calculated ^1H MAS (30 kHz) NMR spectra of $Al_{0.82}\square_{0.18}F_{2.46}(H_2O)_{0.54}$. The two individual contributions to the reconstructed spectrum are shown.

The proton is increasingly deshielded with increasing hydrogen bond strength, which leads to ^1H downfield shifts. The two resonances can then be assigned to non or weak H-bonded and moderate H-bonded[26,27] protons, respectively. ^1H downfield shifts can be correlated with the length of the hydrogen bond.[26,33] It has been shown that ^1H chemical shifts of oxygen-bonded hydrogen linearly depend on the O-H···O distance, through the following relation: $d(O...O)\ (pm) = \frac{79.05\ -\ \delta_{iso}(ppm)}{0.255}$.[33] This relation allows an estimation of the O…O distance for H_2O molecules involving H-bonded hydrogen atoms, *i.e.* 2.79 Å. The O…O distance estimated from this empirical relation and experimental ^1H isotropic chemical shift is typical of hydrogen bonds with water molecules (mean O…O distance equal to 2.825 Å)[27] and is

significantly larger than the O/F···O/F distance determined by Rietveld analysis (2.55 Å, Table 1) indicating that H_2O molecules are only in average located on the 3d sites, in agreement with the disorder outlined above for the F/H_2O site. Finally, from both ^{1}H NMR and IR studies, hydrogen bonds appear moderate in $Al_{0.82}\square_{0.18}F_{2.46}(H_2O)_{0.54}$ following the classification of Jeffrey.[26]

Line	δ_{iso} (±0.2)	Width (±0.2)	Intensity (±1)
1	5.0	2.5	27
2	8.0	6.0	73

Table 2. Isotropic Chemical Shift δ_{iso} (ppm), Line Width (ppm) and Relative Intensity (%) as deduced from the reconstruction of the ^{1}H NMR Spectrum of $Al_{0.82}\square_{0.18}F_{2.46}(H_2O)_{0.54}$.

The ^{1}H MAS NMR spectrum of the sample annealed at 773 K (shown in SI) exhibits a single broad resonance at 5.0 ppm in agreement with the disappearance of the hydrogen bond network, supported by IR study showing the occurrence of residual H_2O molecules in the sample annealed at 773 K.

2.4. Local environments of Al^{3+} ions, cationic vacancies, F^- ions and H_2O molecules

^{19}F and ^{27}Al high field solid-state NMR was used to probe the local environments of F^- and Al^{3+} ions. Two compounds have been considered, *i.e.* the hydrate form and the compound annealed at 773 K.

^{19}F MAS NMR spectra of the hydrate form and the annealed compound are displayed in Figure 7.

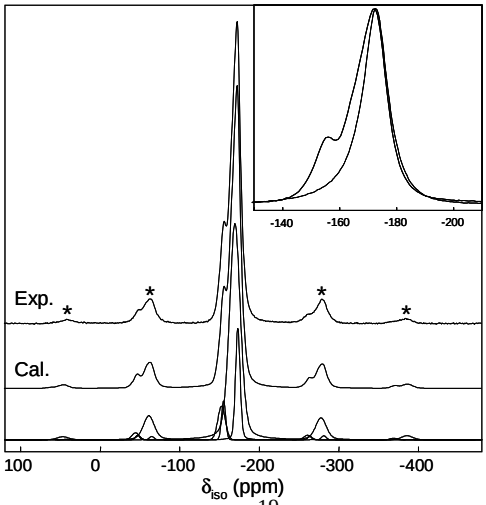

Figure 7. Experimental and calculated ^{19}F MAS (30 kHz) NMR spectra of $Al_{0.82}\square_{0.18}F_{2.46}(H_2O)_{0.54}$. The star symbols indicate the spinning sidebands. The four individual contributions to the reconstructed spectrum are shown. Experimental ^{19}F MAS (30 kHz) NMR spectra of $Al_{0.82}\square_{0.18}F_{2.46}(H_2O)_{0.54}$ and compound obtained after annealed at 773 K during 24 h under Ar (dash line) are presented in the inset.

The hydrate compound spectrum shows two major contributions reconstructed using four signals (Table 3).

Line	δ_{iso} (±0.5)	Width (±0.5)	Intensity (±0.5)
1	-173.0	6.7	13.4
2	-169.4	16.0	74.3
3	-155.2	6.1	4.4
4	-152.5	11.0	7.9

Table 3. Isotropic Chemical Shifts δ_{iso} (ppm), Line Widths (ppm) and Relative Intensities (%) as deduced from the reconstruction of the ^{19}F NMR Spectrum of $Al_{0.82}\square_{0.18}F_{2.46}(H_2O)_{0.54}$.

The lowest δ_{iso} value (line 1, -173 ppm) may be related to bridging fluorine atoms in AlF_6 octahedra (δ_{iso} (^{19}F in α- and β-AlF_3) = -172 ppm[11]). ^{19}F chemical shifts of octahedral aluminum environments with oxygen and fluorine in the first coordination sphere increase with the oxygen content.[2,3,9,11,34-40] The isotropic chemical shift of line 2 is similar to those observed in aluminum hydroxy-fluoride derived from β-AlF_3[2] and pyrochlore[3] without cationic vacancy. Line 2 is then assigned to bridging fluorine atoms in $AlF_{6-x}(H_2O)_x$ octahedra. Lines 3 and 4, at higher isotropic chemical shifts, are attributed to non-bridging fluorine atoms in $AlF_{6-x}(H_2O)_x$ octahedra, *i. e.* fluorine atoms between an aluminum atom and a vacancy. This is in agreement with chemical shift values observed in aluminum fluoride hydrate built from isolated aluminum octahedra, $AlF_3,9H_2O$ and α-$AlF_3,3H_2O$ (δ_{iso}= -149.5 and -147.9 ppm, respectively).[9] These contributions disappear during the annealing process (Inset Figure 7), thus confirming the previous assignment. The ^{19}F MAS NMR spectrum of the sample annealed at 773 K is reconstructed with three resonances (shown in SI). The lowest δ_{iso} values may be related to bridging fluorine atoms in AlF_6^{3-} octahedra and the highest δ_{iso} value may be related to bridging fluorine atoms in $AlF_{6-x}(H_2O)_x$ octahedra. This confirms the occurrence of residual H_2O molecules in the sample annealed at 773 K.

The characteristic tail of the central transition of the 7 T ^{27}Al MAS NMR spectrum (see SI) and the featureless full spinning sideband manifold of the 7 T and 17.6 T ^{27}Al NMR spectra of $Al_{0.82}\square_{0.18}F_{2.46}(H_2O)_{0.54}$ indicate a distribution of quadrupolar coupling constants. This is in agreement with a distribution of aluminum environments due to the occupancy of the 3d sites by both F^- ions and H_2O molecules, the disorder of the F/H_2O site and the occurrence of cationic vacancies. The central transition of the ^{27}Al MAS NMR spectra of the hydrate form and the annealed compound recorded at 17.6 T are displayed in Figure 8a.

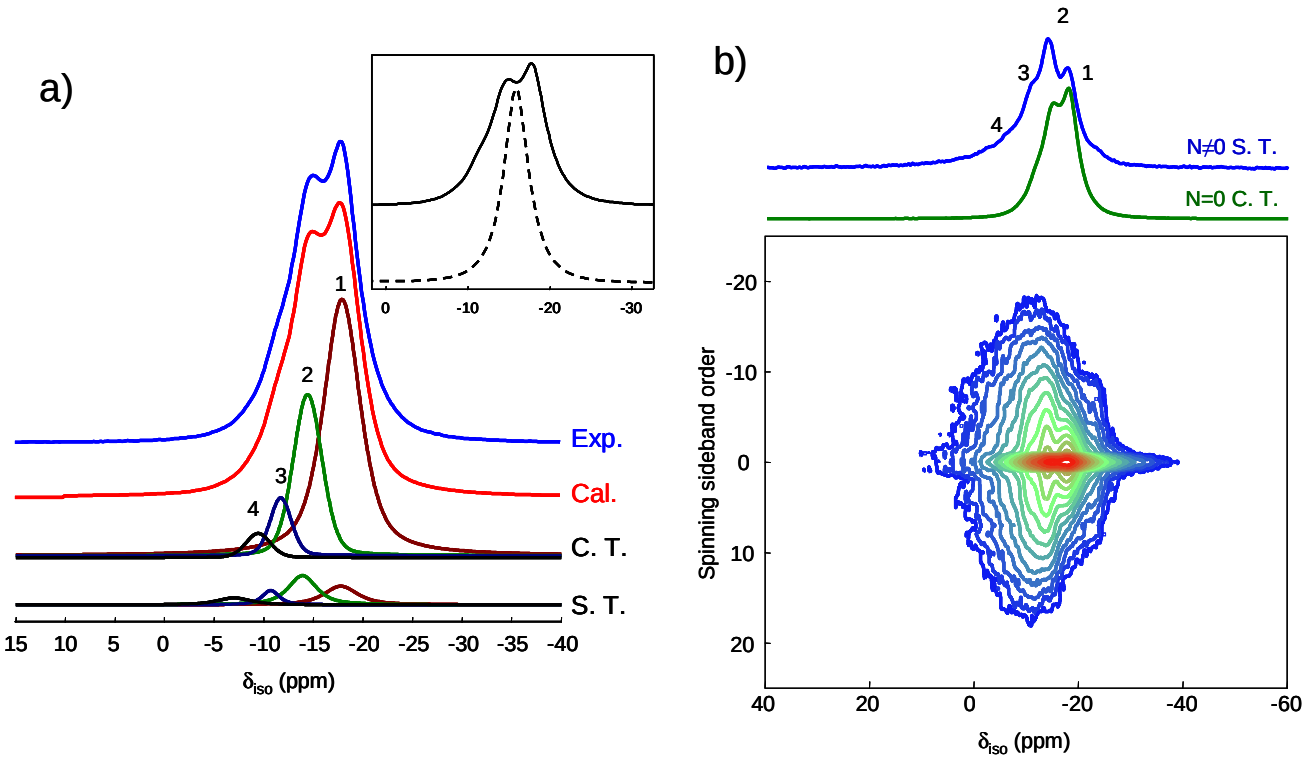

Figure 8. (a) Experimental and calculated central transitions of the ^{27}Al MAS (30 kHz) NMR spectrum of $Al_{0.82}\square_{0.18}F_{2.46}(H_2O)_{0.54}$ recorded at 17.6 T. The fitting, achieved using four contributions, takes into account the N = 0 band of both the satellite transitions (S. T.) <3/2> and the central transition (C. T.) <1/2>. Experimental central transitions of the ^{27}Al MAS (34 kHz) NMR spectrum of $Al_{0.82}\square_{0.18}F_{2.46}(H_2O)_{0.54}$ and compound obtained after annealed at 773 K during 24 h under Ar (dash line) are presented in the inset. (b) 2D TOP spectrum of $Al_{0.82}\square_{0.18}F_{2.46}(H_2O)_{0.54}$. The N = 0 cross-section shows the central transition spectrum and the N ≠ 0 sum is the satellite transition spectrum showing enhanced resolution.

Several contributions are distinguished for $Al_{0.82}\square_{0.18}F_{2.46}(H_2O)_{0.54}$. A way to increase resolution is to construct a two-dimensional one pulse TOP[22-24] spectrum from a conventional 1D MAS spectrum. The TOP spectrum evidences the narrowing of the inner satellite transition line width and allows distinguishing four contributions (Figure 8b). Then, the ^{27}Al MAS NMR spectrum of the hydrate form has been reconstructed using four signals located at: -17.9, -14.4, -11.7 and -9.4 ppm (Figure 8a, Table 4). ^{27}Al isotropic chemical shift is sensitive to the anionic environment. The occurrence of fluorine in the vicinity of aluminum shifts the δ_{iso} to lower values.[2,3,9,11,34,35,37-42] In previous studies, lines with δ_{iso} ranging from -16 to 2 ppm were assigned to the different $AlF_{6-x}(OH)_x$ species existing in β-$AlF_{2.6}(OH)_{0.4}$ (x<4)[2] and pyrochlore $AlF_{1.7}(OH)_{1.3}.0.3H_2O$ (x<6)[3], δ_{iso} value increasing with x. By analogy, $AlF_{6-x}(H_2O)_x$ species are expected to occur in $Al_{0.82}\square_{0.18}F_{2.46}(H_2O)_{0.54}$. The two lowest chemical shifts can be assigned to $AlF_4(H_2O)_2$ (-11.7 ppm) and $AlF_3(H_2O)_3$ (-9.4 ppm). These species are assumed to be metastable since these configurations led to strong electron deficiencies.

Line	δ_{iso} (±0.5)	$\nu_{Q\eta}$ (±10)	Intensity (±0.5)	Assignment	Amount of F^- and H_2O	
					F^-	H_2O
1	-17.9	120	59.1	AlF_6	1.773	0
2	-14.4	250	28.7	$AlF_5(H_2O)$	0.717	0.143
3	-11.7	360	7.8	$AlF_4(H_2O)_2$	0.156	0.078
4	-9.4	560	4.4	$AlF_3(H_2O)_3$	0.066	0.066
						$AlF_{2.71}(H_2O)_{0.29}$

Table 4. Line Label, Isotropic Chemical Shift δ_{iso} (ppm), Quadrupolar Product $\nu_{Q\eta}$ (kHz), Relative Line Intensity (%) as deduced from the reconstruction of the ^{27}Al MAS NMR spectrum of $Al_{0.82}\square_{0.18}F_{2.46}(H_2O)_{0.54}$, Line Assignment and Amount of F^- Ions and H_2O Molecules around Aluminum ions.

It can be reminded that ageing the sample led to the appearance of the pyrochlore type-structure as an impurity. Such a structure mostly contains $AlF_3(OH)_3$ species.[3] It can be assumed that the water molecules contained in $AlF_4(H_2O)_2$ and $AlF_3(H_2O)_3$ species can be dissociated giving rise to hydroxyl-fluorinated species, thus forming the pyrochlore type-structure. The resonances at δ_{iso}=-14.4 and -17.9 ppm are assigned to $AlF_5(H_2O)$ and AlF_6, respectively. The disorder around Al^{3+} ions is clearly evidenced by the $\nu_{Q\eta}$ values of the four resonances which are different from zero when the 1a site symmetry is $m\bar{3}m$. One can notice that the $\nu_{Q\eta}$ value of line 1, assigned to AlF_6 species, is higher than that of α-AlF_3 (32 kHz)[43] and is of the same order of magnitude than that of β-AlF_3 (132 kHz).[11] The $\nu_{Q\eta}$ values increase from line 1 to 4, *i. e.* with the amount of H_2O molecules around Al^{3+} ions. The proportions of the $AlF_{6-x}(H_2O)_x$ species differ from their probability of occurrence calculated based on a random H_2O/F distribution on 3d sites (Table 5) because of the presence of Al^{3+} vacancies stabilized in the ReO_3 network.

AlF_6	$AlF_5(H_2O)$	$AlF_4(H_2O)_2$	$AlF_3(H_2O)_3$	$AlF_2(H_2O)_4$	$AlF(H_2O)_5$	$Al(H_2O)_6$
30.4	40.0	22.0	6.4	1.1	0.1	/

Table 5. Probability of occurrence of the $AlF_{6-x}(H_2O)_x$ species based on a random H_2O/F distribution on 3d sites.

Proportions of F^- ions and H_2O molecules around Al^{3+} ions can be determined from experimental ^{27}Al NMR line intensities (Table 4) and lead to the formula: $AlF_{2.71}(H_2O)_{0.29.}$ Taking into account the occupancy of Al^{3+} ion on the 1a site, *i.e.* the amount of cationic vacancy and the compound formula, $Al_{0.82}\square_{0.18}F_{2.46}(H_2O)_{0.54}$, *i.e.* the amount of F^- ions and

H_2O molecules, we obtain the following formula: $Al_{0.82}F_{2.22}(H_2O)_{0.24}\square_{0.18}F_{0.24}(H_2O)_{0.30}$ which gives independent insights of both the Al^{3+} ions and vacancies environments. This indicates that F^- ions prefer sitting between two Al^{3+} ions rather than between one Al^{3+} ion and one vacancy. However, around 10% of F^- ions still sit in the vicinity of a vacancy, which is in agreement with the proportion of non-bridging F^- ions in $AlF_{6-x}(H_2O)_x$ octahedra determined from ^{19}F NMR (~12%, Table 2). The occurrence of water molecule between two Al^{3+} ions can be excluded because of unrealistic electronic configuration. The larger amount of H_2O molecules around cationic vacancies than around Al^{3+} ions reinforces this assumption. Moreover, some water molecules are located between two vacancies, in agreement with the high vacancies content, *i.e.* 18%. These water molecules are stabilized by hydrogen bonding. The departure of such water molecules matches with the second weak departure observed in the IC curve m/z=18 occurring at 563 K (Figure 3).

Finally, the annealing process at 773 K leads to a compound in which the ^{27}Al resonances at δ_{iso} = -9.4 and -11.7 ppm have disappeared confirming the previous assignments of the hydrated species. For this compound, a single ^{27}Al NMR signal is detected (Figure 8a and SI), reconstructed (see SI) using the following parameters: δ_{iso} = -15.9 (±0.2) ppm and $\nu_{Q\eta}$ = 140 (±20) kHz. The δ_{iso} value is intermediate between those assigned to AlF_6 and $AlF_5(H_2O)$ species in $Al_{0.82}\square_{0.18}F_{2.46}(H_2O)_{0.54}$ before annealing and close to the δ_{iso} value of the line assigned to AlF_6 and $AlF_5(OH)$ species in β-$AlF_{2.6}(OH)_{0.4}$.[2] The quadrupolar product $\nu_{Q\eta}$ value is significantly larger than that in α-AlF_3 ($\nu_{Q\eta}$ = 32 kHz).[43] This may be related to a larger disorder around Al^{3+} ions in $Al_{0.82}\square_{0.18}F_{2.46}(H_2O)_{0.54}$ after annealing at 773 K than in α-AlF_3. Finally the ^{27}Al NMR parameters confirm the IR and ^1H and ^{19}F NMR observations, *i. e.*, the occurrence of residual H_2O molecules in the sample annealed at 773 K.

Based on the above results, a representation of the structure of $Al_{0.82}\square_{0.18}F_{2.46}(H_2O)_{0.54}$ can be proposed with a view of the cubic unit cell with the occurrence of one vacancy where a 2:1 (X···H-O-H···X) complex occurs (Figure 9A) and a view of a super cell showing two vacancies located side by side with an isolated water molecule in between (Figure 9B).

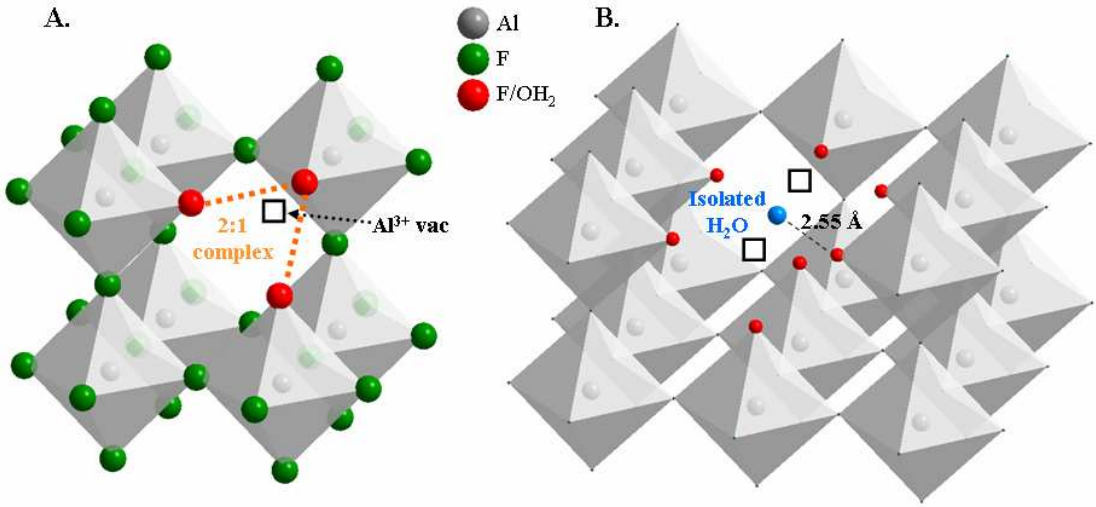

Figure 9. Schematic representation of the structure. (A) View of the cubic unit cell with the occurrence of one Al^{3+} vacancy with a 2:1 complex. (B) View of the structure with the occurrence of two vacancies located side by side with an isolated water molecule in between**.**

3. Acidic properties

The acidic properties of this new aluminum fluoride hydrate have been characterized by adsorption of probe molecules (CO and pyridine) followed by FTIR spectroscopy. The use of two different probes enables a better description of the surface properties. As a weak base, CO enables the detection of Brønsted and Lewis acidities and the adsorption of small doses enables the detection of the strongest sites.[44] Pyridine molecule is a strong base and is commonly used to probe Lewis acidity and characterize strong Brønsted acidic sites.

Prior to the characterization of the surface, the material is activated to remove surface impurities. The activation is carried out at 573 K under vacuum which is a convenient temperature for the characterization of the surface of aluminum fluorides.[32] In addition, the specific surface area of the sample annealed overnight at 573 K is 61 $m^2.g^{-1}$ suitable for FTIR characterization. The material is then characterized using pyridine molecule and CO adsorption performed at low temperature (100 K). In a second step, the surface is further activated successively at 673 and 773 K to investigate by using CO adsorption the effect of the dehydration on the acidic properties.

Activation at 573 K. After activation at 573 K, 133 Pa of pyridine are adsorbed at room temperature. Physisorbed species were removed by evacuation under secondary vacuum at RT. The spectrum showing the vibration modes (1400-1700 cm^{-1}) of coordinated pyridine molecule is displayed in Figure 10.

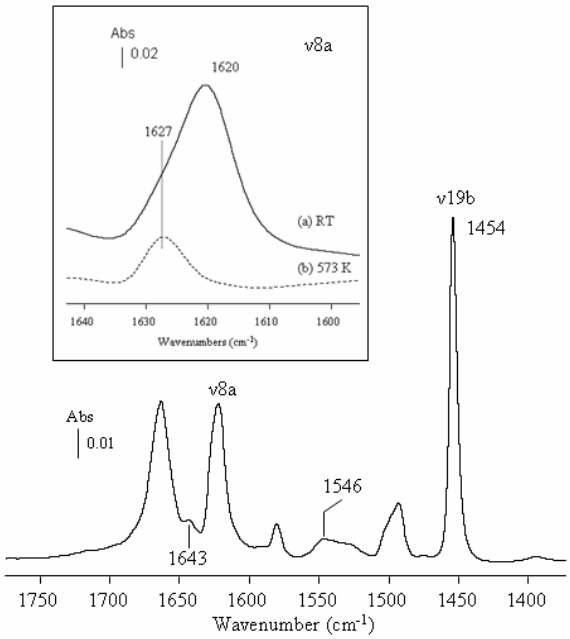

Figure 10. IR difference spectrum of adsorbed pyridine (133 Pa) after activation at 573 K and recorded after evacuation at room temperature. Inset: extension on the ν8a vibration mode from IR spectra recorded at (a) RT and (b) after thermodesorption at 573 K.

Note that the band located at 1660 cm^{-1} is ascribed to the bending mode of water molecule which is slightly shifted after pyridine adsorption. Both Lewis and Brønsted acidities are detected. The protonation of pyridine molecule is clearly evidenced by the bands observed at 1546 and 1643 cm^{-1}, ascribed to pyridinium species. The bands detected at 1620 and 1454 cm^{-1} are related to the ν8a and ν19b modes of coordinated pyridine which characterize the Lewis acidity. Their position accounts for the strength of the Lewis acidity, *i.e.* the higher the wavenumber, the stronger the acidity. Same values have been reported for β-AlF_3.[32] However, the ν8a band which is more sensitive to the Lewis strength presents a shoulder (Inset Figure 10) detected at higher wavenumber, *i.e.* 1627 cm^{-1}, revealing Lewis strength heterogeneity, the higher component characterizing strong Lewis acid sites. The strength of such a site has been ascertained by thermodesorption at 573 K (Inset, b) Figure 10) showing the disappearance of the lowest component at 1620 cm^{-1} whereas the contribution at 1627 cm^{-1} remains.

The concentration of Lewis acid sites per nm^2 has been estimated by integrating the ν19b area band and yields 1.55 sites per nm^2. Such a value is higher than that reported for β-AlF_3 (1.2-1.3 sites/nm^2)[32] certainly due to the denser packed stacking structure displayed by the ReO_3 type network as compared to the HTB (or β-) type structure which exhibits channel system.

To gain insight into the acidic properties of the solid, CO adsorption has been performed at about 100 K after activation at 573 K. The IR difference spectra of adsorbed CO are displayed

in Figure 11. The use of such a molecule enables to discriminate the nature and the acidic strength heterogeneity through CO stretching vibration. Different regions can be distinguished: (i) ν(CO) > 2180 cm^{-1} which accounts for Lewis acid sites, (ii) a broad band appearing at 2180 cm^{-1} (spectrum a), shifting downward to 2173 cm^{-1} for saturated spectrum (h), (iii) after CO saturation, a band at around 2160 cm^{-1} is detected and can be ascribed either to Brønsted or weak Lewis acid sites. Finally, physisorbed species are detected for ν(CO) < 2150 cm^{-1}. In order to gain insight into the variety of the acidic sites, a reconstruction of the saturated CO spectrum (curve h) has been performed (Inset A, figure 10). The region relative to Lewis acid sites, *i.e.* ν(CO) > 2180 cm^{-1}, reveals four contributions for which the higher the ν(CO) positions, the stronger the Lewis acidity. The bands located at ν(CO)>2200 cm^{-1} account for strong Lewis acidic sites, *i.e.* 2205, 2215 and 2225 cm^{-1}, whereas the band ν(CO) detected at 2195 cm^{-1} is related to medium[45] acidic sites. The surface reactivity of α- and β-AlF_3 has been rationalize by ab initio method highlighting the occurrence of five-fold coordinated Al^{3+} ions.[13] The strength of these centres depends on their accessibility. α-AlF_3 presents a low Lewis acidity whereas the β-AlF_3 surface exhibits strong Lewis acid sites.[13]

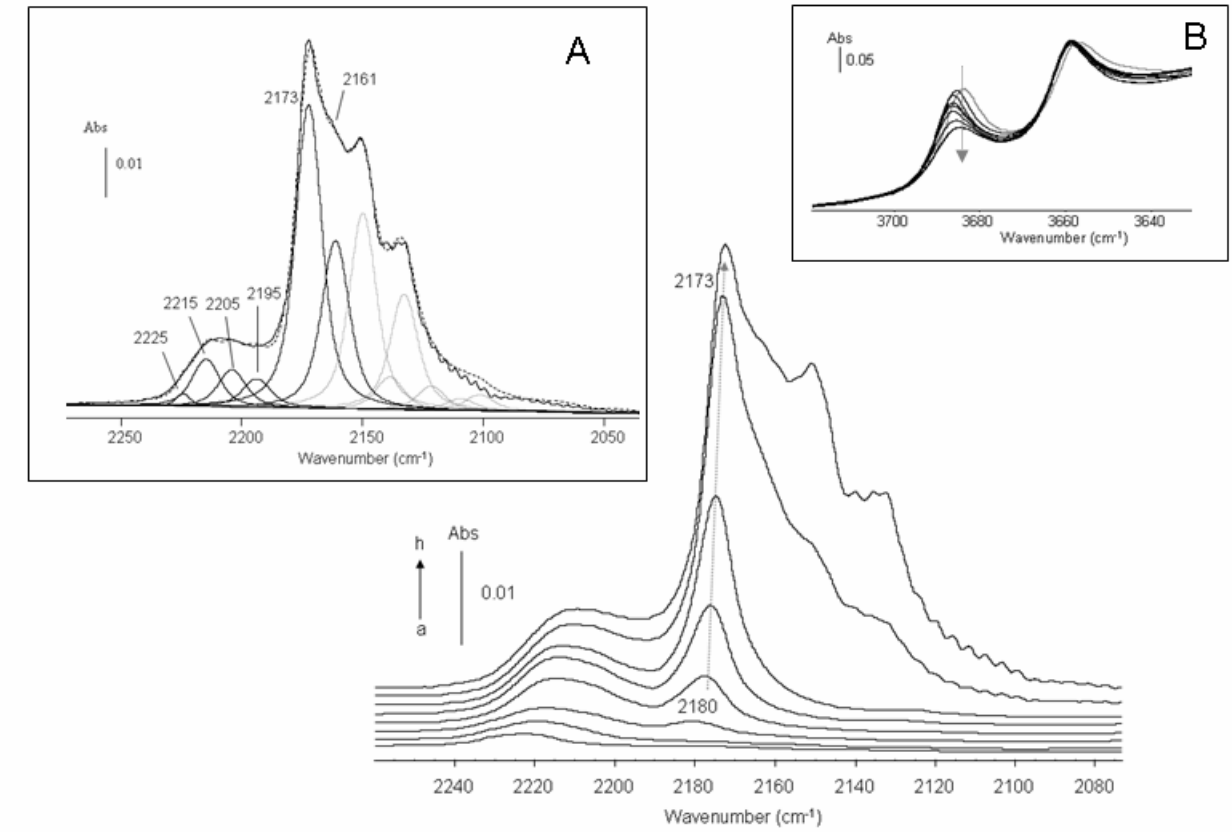

Figure 11. IR difference spectra of adsorbed CO on aluminum fluoride hydrate activated at 573 K overnight (increasing CO doses from spectrum a to spectrum h; the latter being at equilibrium pressure). Inset A: Deconvolution of spectrum h. Inset B: Evolution of the ν(OH) range during CO addition.

The bands located at ν(CO)>2190 cm^{-1} have been suggested to arise from acidic five-fold coordinated Al^{3+} ions.[46] By analogy, it can be suggested that aluminum fluoride hydrate exhibits Lewis acidic centres similar to those displayed by β-AlF_3 surface. The heterogeneity of the Lewis acidic strength displayed by the solid can be correlated to the geometry, *i.e.* the accessibility of the Lewis site but also to a variation of the anionic environment of the Lewis centre affecting the Lewis acidic strength.

In the low frequency region, a band appears at 2180 cm^{-1}, which is shifted downward to 2173 cm^{-1} for saturated spectra. The assignment of this band is not straightforward because this ν(CO) range accounts either for Lewis or Brønsted acidity. The appearance of such a band is however correlated to the perturbation of the ν(OH) at 3675 cm^{-1} (Figure 11, Inset B) which reveals the Brønsted nature of this site. This band at 3675 cm^{-1} can be ascribed either to surface hydroxyl group or to "free" O-H group from a water molecule oriented toward the surface. Due a high intensity of the bands relative to water molecules (Figure 5), the detection of the perturbed ν(OH) bands is not straightforward. Additionally, the low temperature required for CO experiments leads to a slight shift of the ν(OH) band reinforcing the difficulty to accurately interpret the IR difference spectra. The Brønsted nature of this band (2180-2173 cm^{-1}) is consistent with the previous detection of pyridinium species (Figure 10) which account for very strong Brønsted acidity.

Effect of dehydration upon the acidic properties. IR spectra of saturated CO adsorbed after annealing treatment performed at 573, 673 and 773 K are displayed on Figure 12.

The dehydration process induces a drastic change of the surface structure as revealed by the evolution ν(CO) position. At first, the bands located at ν(CO)>2200 cm^{-1} decrease upon annealing. This is going with an increase of the bands lying between 2180-2195 cm^{-1} related to medium Lewis acidic sites. Additionally, the band located at around 2160-2165 cm^{-1} strongly increases upon annealing which evidences the Lewis origin of this band. Thermal treatments clearly converts the strong Lewis acid sites (ν(CO)>2200 cm^{-1}) into medium (2180-2200 cm^{-1}) and weak (2160-2165 cm^{-1}) ones.

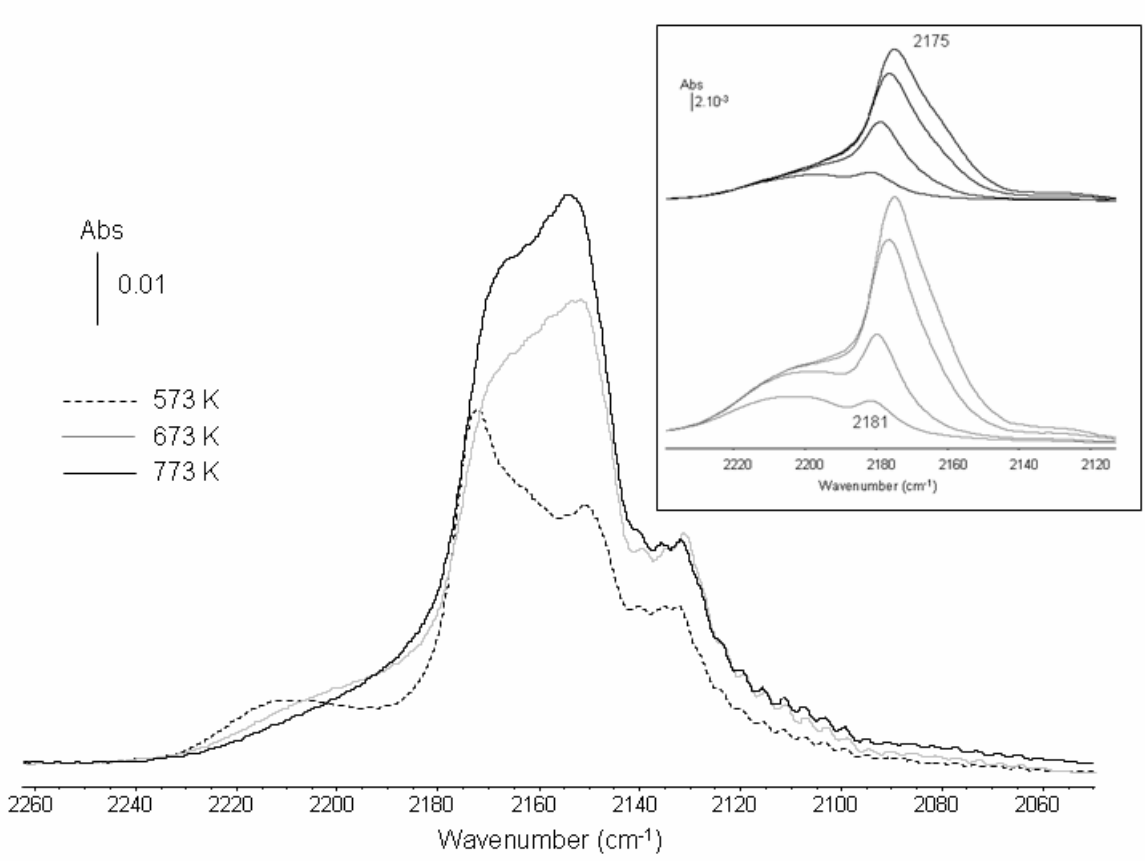

Figure 12. IR difference spectra of adsorbed CO on aluminum fluoride hydrate activated at various temperatures overnight. Inset: Details analysis for samples activated at 673 (down) and 773 K (top) after successive (4) additions of CO doses.

The Brønsted contribution previously described is still present even after such annealing treatments. A detailed analysis using small amounts of CO reveals that ν(CO) lying between 2181 and 2175 cm^{-1} are present after annealing treatment at 673 and 773 K (Inset Figure 12). The amount of Brønsted sites decreases upon annealing as revealed by the ν(CO) intensities. The nature of the Brønsted acidity is still unclear but one can remind that water molecules can act as a very strong Brønsted site.[6] The ν(CO) positions as well as the detection of pyridinum species account for the presence of strong Brønsted acid sites in favour of water molecules contribution. Moreover, OH groups are unlikely to be stable up to 773 K.

The study of the effect of annealing treatment upon the acidic properties allows a better view of the surface structure. The acidic behaviors depend on the temperature of activation which is correlated to the remaining water/cationic vacancies. After annealing at 573 K (common procedure), the structure contains a large amount of water molecules in addition to cationic vacancies since, as revealed by thermal analysis, (Figure 3) the main dehydration event started above 573 K. In this configuration, the surface material contains strong Lewis acid sites which are similar to those modeled in β-AlF_3. Strong Brønsted acid sites are also

displayed by the surface which can be ascribed to water molecules. The relative contribution between Lewis and Brønsted acidity has been established by integration of each band and using an extension coefficient equal to 2.1 and 2.7 $cm.\mu mol^{-1}$ for $\nu(CO)>2200\ cm^{-1}$ and $\nu(CO)<2200\ cm^{-1}$, respectively. The estimation leads to 0.544 Lewis acid sites and 0.504 Brønsted site per nm^2. The difference between the number of Lewis acid sites estimated by pyridine and CO is ascribed to the strongest basicity displays by pyridine molecule. Finally, the surface exhibits an equivalent number of Brønsted and Lewis acid sites which defined this new material as bifunctional.

Since dehydration led to the conversion of the strong Lewis acid sites into weaker ones, it can be assumed that the occurrence of water molecules and cationic vacancies perturbed the surface structure generating accessible and strong Lewis acidic sites. After the annealing treatment at 773 K, the solid is closely related to the rhombohedral form of α-AlF_3 (Figure 4). CO adsorption performed after such a treatment revealed the occurrence of weak and medium Lewis acidity in agreement with the modeled acidic behavior for the (0001) α-AlF_3 surface. Such a result also confirms the role of the water molecules and cationic vacancies on the occurrence of strong Lewis acid sites. Finally, another remarkable point is the strong Brønsted acidity that remains even after annealing at 773 K.

Conclusion.

A new aluminum fluoride hydrate was prepared using microwave-assisted synthesis. The acidification of the medium using high HF contents favors the stabilization of water molecules in the first coordination sphere of the cation, as opposed to OH groups previously described in the pyrochlore and HTB compounds. The variation of the charge density upon the octahedra induced by the substitution of F^- ions by H_2O molecules is balanced by the occurrence of cationic vacancies, as revealed by the Rietveld refinement. This is the first example of aluminum vacancy compound in the Al-based fluorides system. ^{19}F NMR investigations confirm the occurrence of cationic vacancies through the identification of bridging and non-bridging F^- ions. $AlF_{6-x}(H_2O)_x$ species containing various number of water molecules were quantified using high field ^{27}Al NMR spectroscopy. This quantification led to the following formula: $Al_{0.82}F_{2.22}(H_2O)_{0.24}\square_{0.18}F_{0.24}(H_2O)_{0.30}$ which gives independent insights of both the Al^{3+} ions and vacancies environments and shows the occurrence of unusual H_2O molecules surrounded by two cationic vacancies. Hydrogen-bond interactions contribute to stabilize the cationic vacancies. FTIR spectroscopy enables the characterization of a 2:1 complex (X···H-O-H···X where X is a proton acceptor) formed by water molecules, which is stable up to 773

K. The cubic symmetry is transformed upon annealing into a rhombohedral form at around 573 K, *i.e.* after the departure of isolated water molecules.

The investigation of the acidic properties evidences various acidic behaviours depending on the activation temperature. At 573 K, both strong Lewis and Brønsted acidic sites are present at the surface. Such a configuration can be used for reactions involving the synergy between Lewis/Brønsted acidities. By contrast with the modeled α-AlF_3 phase, the strong Lewis acidity occurring at this temperature has been rationalized by the presence of water/Al^{3+} vacancy inducing a peculiar surface structure. Further dehydration leads to a conversion of strong Lewis acid sites into weaker ones and the obtained surface structure resembles to that modeled for the (001) surface of α-AlF_3. The various acidic behaviors displayed by the aluminum fluoride hydrate thus open the possibility to target a large range of catalytic reactions.

ACKNOWLEDGMENT. The EU is acknowledged for financial support through the 6th Framework Program (FUNFLUOS, Contract No. NMP3-CT-2004-5005575). Lydia Raison is gratefully acknowledged for performing EMPA analysis.

Supporting Information Available. ^{1}H MAS (30 kHz) NMR spectrum, ^{19}F MAS (30 kHz) NMR experimental and calculated spectra of $Al_{0.82}\square_{0.18}F_{2.46}(H_2O)_{0.54}$ after annealing at 773 K during 24 h under Ar, Isotropic chemical shifts δ_{iso} (ppm), line widths (ppm) and relative intensities (%) as deduced from the reconstruction of the ^{19}F NMR spectrum of $Al_{0.82}\square_{0.18}F_{2.46}(H_2O)_{0.54}$ after annealing at 773 K during 24h under Ar, ^{27}Al MAS (30 kHz) one pulse NMR spectrum recorded at 17.6 T of (a) $Al_{0.82}\square_{0.18}F_{2.46}(H_2O)_{0.54}$ and (b) $Al_{0.82}\square_{0.18}F_{2.46}(H_2O)_{0.54}$ after annealing at 773 K during 24 h under Ar, ^{27}Al MAS (25 kHz) one pulse NMR spectrum of $Al_{0.82}\square_{0.18}F_{2.46}(H_2O)_{0.54}$ recorded at 7 T, Experimental and calculated central transitions of the ^{27}Al MAS (30 kHz) NMR spectrum recorded at 17.6 T of $Al_{0.82}\square_{0.18}F_{2.46}(H_2O)_{0.54}$ after annealing at 773 K during 24 h under Ar.

References.

(1) a) Daniel, P.; Bulou, A.; Rousseau, M.; Nouet, J.; Fourquet, J.-L.; Leblanc, M.; Burriel, R. *J. Phys.: Condens. Matter* **1990**, *2*, 5663. b) Fourquet, J.-L.; Rivière, M.; Le Bail, A. *Eur. J. Solid State Inorg. Chem.* **1988**, *25*, 535. c) Le Bail, A.; Jacoboni, C.; Leblanc, M.; De Pape, R.; Duroy, H.; Fourquet, J.-L. *J. Solid State Chem.* **1988**, *77*, 96. d) Herron, N.; Thorn, D. L.; Harlow, R. L.; Jones, G. A.; Parise, J. B.; Fernandez-Baca, J. A.; Vogt, T. *Chem. Mater.* **1995**, *7*, 75. e) Le Bail, A.; Fourquet, J.-L.; Bentrup, U. *J. Solid State Chem.* **1992**, *199*, 151. f) Ravez, J.; Mogus-Milankovic, A.; Chaminade, J.-P.; Hagenmuller, P. *Mat. Res. Bull.* **1984**, *19*, 1311.

(2) Dambournet, D.; Demourgues, A.; Martineau, C.; Pechev, S.; Lhoste, J.; Majimel, J.; Vimont, A.; Lavalley, J.-C.; Legein, C.; Buzaré, J.-Y.; Fayon, F.; Tressaud, A. *Chem. Mater.* **2008**, *20*, 1459.

(3) Dambournet, D.; Demourgues, A.; Martineau, C.; Durand , E.; Majimel, J.; Vimont, A.; Leclerc, H.; Lavalley, J.-C.; Daturi, M.; Legein, C.; Buzaré, J.-Y.; Fayon, F.; Tressaud, A. *J. Mater. Chem.*, DOI: 10.1039/B718856K.

(4) Kemnitz, E.; Menz., D. H. *Prog. Solid State Chem.* **1998**, *26*, 97.

(5) Herron, N.; Farneth, W. E. *Adv Mater*. **1996**, *12*, 8.

(6) Garrone, E.; Onida, B.; Bonelli, B.; Busco, C.; Ugliengo, P. *J. Phys. Chem. B.* **2006**, *110*, 19087.

(7) Li, S.; Zheng, A.; Su, Y.; Zhang, H.; Chen, L.; Yang, J.; Ye, C.; Deng. F. *J. Am. Chem. Soc.* **2007**, *129*, 11171.

(8) Rimola, A.; Tosoni, S.; Sodupe, M.; Ugliengo, P. *Chem. Phys. Lett.* **2005**, *408*, 295.

(9) Kemnitz, E.; Groß, U.; Rüdiger, St.; Scholz, G.; Heidemann, D.; Troyanov, S. I.; Morosov, I. V.; Lemée-Cailleau, M.-H. *Solid State Sci.* **2006**, *8*, 1443.

(10) Chaudhuri, S.; Chupas, P. J.; Wilson, M.; Madden, P.; Grey, C. P. *J. Phys. Chem. B.* **2004**, *108*, 3437.

(11) Chupas, P. J.; Ciraolo, M. F.; Hanson, J. C.; Grey, C. P. *J. Am. Chem. Soc.* **2001**, *123*, 1694.

(12) Wander, A.; Searle, B. G.; Bailey, C. L.; Harrison, N. M. *J. Phys. Chem. B.* **2005**, *109*, 22935.

(13) Wander, A.; Bailey, C. L.; Mukhopadhyay, S.; Searle, B. G.; Harrison, N. M. *J. Mater. Chem.* **2006**, *16*, 1906-1910.

(14) Mukhopadhyay, S.; Bailey, C. L.; Wander, A.; Searle, B. G.; Muryn, C.A.; Schroeder, S. L. M.; Lindsay, R.; Weiher, N.; Harrison, N. M. *Surf Sci*. **2007**, *601*, 4433.

(15) Chaudhuri, S.; Chupas, P.; Morgan, B. J.; Madden, P. A.; Grey, C. P. *Phys. Chem. Chem. Phys.* **2006**, *8*, 5045.

(16) Rodríguez-Carvajal, J. *Physica B.* **1993**, *192*, 55.

(17) Massiot, D.; Fayon, F.; Capron, M.; King, I.; Le Calvé, S.; Alonso, B.; Durand, J.-O.; Bujoli, B.; Gan, Z.; Hoatson, G. *Magn. Reson. Chem.* **2002**, *40*, 70

(18) Massiot, D.; Bessada, C.; Coutures, J. P.; Taulelle, F. *J. Magn. Reson*. **1990**, *90*, 231.

(19) Alemany, L. B.; Massiot, D.; Sherriff, B. L.; Smith, M. E.; Taulelle, F. *Chem. Phys. Lett.* **1991**, *177*, 301.

(20) Massiot, D.; Müller, D.; Hübert, Th.; Schneider, M.; Kentgens, A. P. M.; Coté, B.; Coutures, J. P.; Gessner, W. *Solid State Nucl. Magn. Reson.* **1995**, *5*, 175.

(21) Stebbins, J. F.; Kroeker, S.; Lee, S. K.; Kiczenski, T. J. *J. Non-Cryst. Solids.* **2000**, *275*, 1-6.

(22) Blümich, B.; Blumler, P.; Jansen, J. *Solid State Nucl. Magn. Reson.*, **1992**, *1*, 111.

(23) Blumler, P.; Blümich, B.; Jansen, J. *Solid State Nucl. Magn. Reson.*, **1994**, *3*, 237.

(24) Massiot, D.; Hiet, J.; Pellerin, N.; Fayon, F.; Deschamps, M.; Steuernagel, S.; Grandinetti, P. J. *J. Magn. Reson.*, **2006**, *181*, 310.

(25) Chandross, R. *Acta Crystallogr*. **1964**, *17*, 1477.

(26) Jeffrey, G. A., An Introduction to Hydrogen Bonding, Oxford University Press, Oxford, **1997**.

(27) Steiner, T. *Angew. Chem. Int. Ed.* **2002**, *41*, 48.

(28) Scatena, L. F.; Brown, M. G.; Richmond, G. L. *Science* **2001**, *292*, 908.

(29) Bricknell, B. C.; Ford, T. A.; Letcher, T. M. *Spectrochimica Acta Part A*. **1997**, *53*, 299.

(30) Burneau, A. *J. Mol. Liq.* **1990**, *46*, 99.
(31) Burneau, A.; Corset, J. *J. Chim. Phys.* **1972**, *69*, 171.
(32) Vimont, A. ; Lavalley, J. C. ; Francke, L. ; Demourgues, A. ; Tressaud, A. ; Daturi, M. *J. Phys. Chem. B* **2004**, *108*, 3246.
(33) Eckert, H.; Yesinowski, J. P.; Silver, L. A.; Stolper, E. M. *J. Phys. Chem.*, 1988, ***92***, 2055.
(34) Chupas, P. J.; Corbin, D. R.; Rao, V. N. M.; Hanson, J. C.; Grey, C. P. *J. Phys. Chem. B.* **2003**, *107*, 8327.
(35) Taulelle, F.; Pruski, M.; Amoureux, J. P.; Lang, D.; Bailly, A.; Huguenard, C.; Haouas, M.; Gérardin, C.; Loiseau, T.; Férey, G. *J. Am. Chem. Soc.* **1999**, *121*, 12148.
(36) Simon, N.; Guillou, N.; Loiseau, T.; Taulelle, F.; Férey, G. *J. Solid State Chem.* **1999**, *147*, 92.
(37) Fischer, L.; Harlé, V.; Kasztelan, S.; d'Espinose de la Caillerie, J.-B. *Solid State Nucl. Magn. Reson.* **2000**, *16*, 85.
(38) Dumas, E.; Taulelle, F.; Férey, G. *Solid State Sci.* **2001**, *3*, 613.
(39) Zhou, B.; Sherriff, B. L.; Taulelle, F.; Wu, G. *Can. Mineral.* **2003**, *1*, 891.
(40) Chupas, P. J.; Grey, C. P. *J. Catal.* **2004**, *224*, 69.
(41) Zhou, B.; Sherriff, B. L.; Hartman, J. S.; Wu, G. *Am. Miner.* **2007**, *92*, 34.
(42) Scheurell, K.; Scholz, G.; Kemnitz, E. *J. Solid. State Chem.* **2007,** *180*, 749.
(43) Silly, G.; Legein, C.; Buzaré, J.-Y.; Calvayrac, F. *Solid State Nucl. Magn. Reson.* **2004**, *25*, 241.
(44) Hadjiivanov, K. I.; Vayssilov, G. N. *Adv. Catal*. **2002**, *47*, 307.
(45) Morterra, C.; Cerrato, G.; Cuzzato, P.; Masiero, A.; Padovan, M. *J. Chem. Soc., Faraday Transactions*. **1992**, *88*, 2239.
(46) Krahl, T.; Vimont, A.; Eltanamy, G.; Daturi, M.; Kemnitz, E. *J. Phys. Chem. C*. **2007**, *111*, 18317.

A new aluminium fluoride hydrate with cationic vacancies: structure, thermal stability and acidic properties

D.Dambournet, A.Demourgues, C.Martineau, E.Durand, J. Majimel, C. Legein, J.-Y. Buzaré, F. Fayon, M. Daturi and A. Tressaud

Supporting information

Table of contents

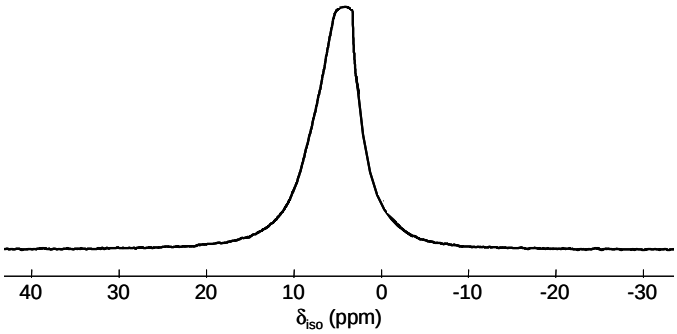

Figure 1. ^{1}H MAS (30 kHz) NMR spectrum of $Al_{0.82}\square_{0.18}F_{2.46}(H_2O)_{0.54}$ after annealing at 773 K during 24 h under Ar.

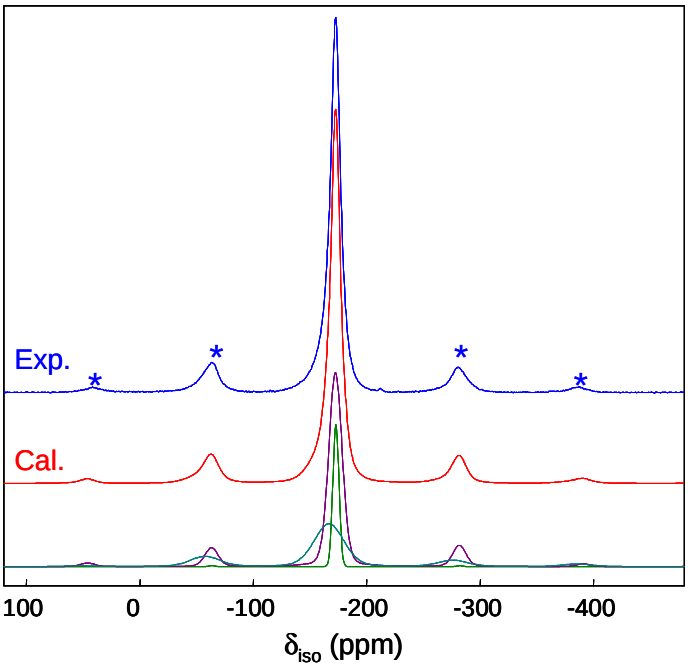

Figure 2. Experimental and calculated ^{19}F MAS (30 kHz) NMR spectra of $Al_{0.82}\square_{0.18}F_{2.46}(H_2O)_{0.54}$ after annealing at 773 K during 24 h under Ar. The star symbols indicate the spinning sidebands. The three individual contributions to the reconstructed spectrum are shown.

Table 1. Isotropic chemical shift δ_{iso} (ppm), line width (ppm) and relative intensity (%) as deduced from the reconstruction of the ^{19}F NMR spectrum of $Al_{0.82}\square_{0.18}F_{2.46}(H_2O)_{0.54}$ after annealing at 773 K during 24h under Ar.

Line	δ_{iso} (±0.5)	Width (±0.5)	Intensity (±0.5)
1	-172.9	6.3	13.7
2	-172.5	13.9	54.8
3	-166.8	30.9	31.5

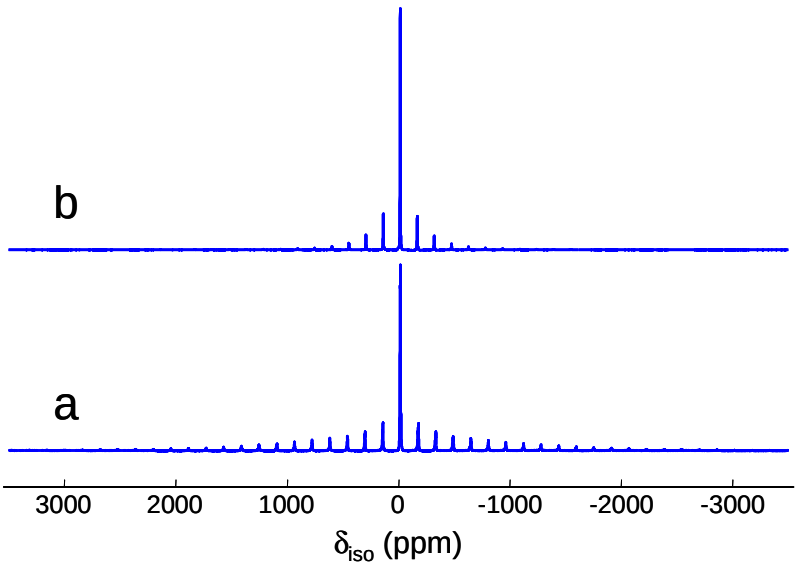

Figure 3. ^{27}Al MAS (30 kHz) one pulse NMR spectrum recorded at 17.6 T of (a) $Al_{0.82}\square_{0.18}F_{2.46}(H_2O)_{0.54}$ and (b) $Al_{0.82}\square_{0.18}F_{2.46}(H_2O)_{0.54}$ after annealing at 773 K during 24 h under Ar.

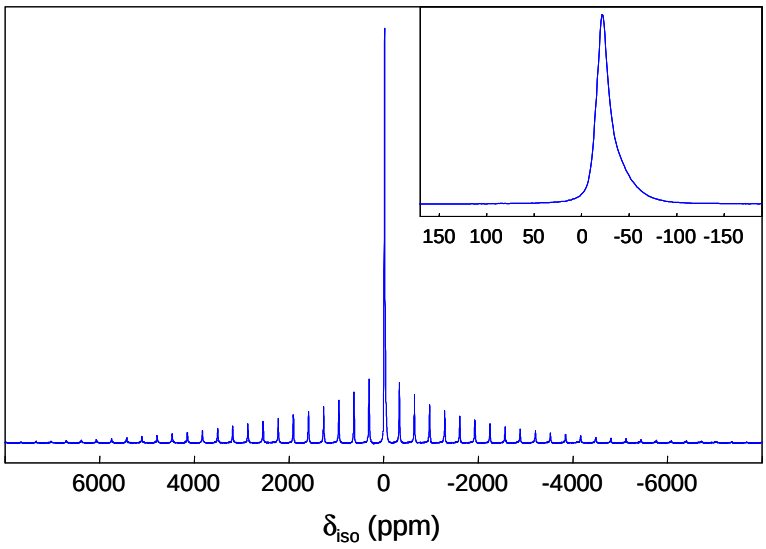

Figure 4. ^{27}Al MAS (25 kHz) one pulse NMR spectrum of $Al_{0.82}\square_{0.18}F_{2.46}(H_2O)_{0.54}$ recorded at 7 T. Central transition is presented in the inset.

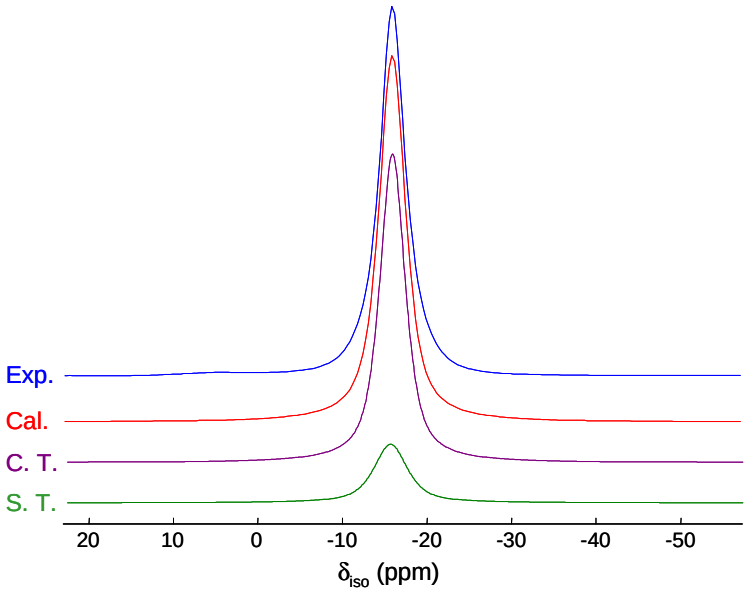

Figure 5. Experimental and calculated central transitions of the ^{27}Al MAS (30 kHz) NMR spectrum recorded at 17.6 T of $Al_{0.82}\square_{0.18}F_{2.46}(H_2O)_{0.54}$ after annealing at 773 K during 24 h under Ar. The fitting takes into account the N = 0 band of both the satellite transitions (S. T.) <3/2> and the central transition (C. T.) <1/2> and leads to the following parameters: δ_{iso}=-16 (±0.5) ppm and $\nu_{Q\eta}$=140 (±20) kHz.

2.4 Combinaison d'une synthèse sol-gel et d'un traitement thermique assisté par micro-ondes: nouvelle voie d'obtention de matériaux fluorés à haute surface spécifique

Publication: *Coupling sol-gel synthesis and microwave-assisted technique: a new route from amorphous to crystallized high surface area aluminium fluoride, accepted in Chemistry – A European Journal*

Cette étude présente la combinaison originale de deux techniques : un traitement hydrothermal assisté par micro-ondes d'un alkoxy-fluorure d'aluminium en milieu organique obtenu par une méthode sol-gel. Nous avons ainsi étudié l'influence de la température de traitement sur les propriétés (structurale et texture) des matériaux ainsi synthétisés. Un traitement sous fluor gazeux à basse température permet l'obtention d'un matériau à très grande surface spécifique. Les propriétés acides de ce dernier seront comparées à celles des différents matériaux obtenus lors de ces travaux.

Coupling sol-gel synthesis and microwave-assisted technique: a new route from amorphous to crystallized high surface area aluminium fluoride

Damien Dambournet,[#] Gehan Eltanamy,[‡] Alexandre Vimont,[+] Jean-Claude Lavalley,[+] Jean-Michel Goupil,[+] Alain Demourgues,[#] Etienne Durand,[#] Jérôme Majimel,[#] Stephan Rudiger,[‡] Erhard Kemnitz,[‡] John M. Winfield [§] and Alain Tressaud [#].*

[#] Institut de Chimie de la Matière Condensée de Bordeaux-CNRS, Université Bordeaux 1. 87, Avenue du Dr. A. Schweitzer, 33608 Pessac cedex, France

[+] Laboratoire Catalyse et Spectrochimie, UMR 6506, CNRS-ENSICAEN-Université de CAEN, Boulevard du Maréchal Juin, F-14050 Caen Cedex, France

[‡] Institut für Chemie, Humboldt-Universität zu Berlin, Brook-Taylor-Strasse 2, D-12489 Berlin, Germany

[§] Department of Chemistry, University of Glasgow, Glasgow G12 8QQ, Scotland, UK.

*Corresponding authors: tressaud@icmcb-bordeaux.cnrs.fr

Abstract

Non aqueous sol-gel fluoride has been subject to microwave hydrothermal process. The final material depends on the temperature heat treatment used. Three types of materials have been prepared: (i) for low temperature heat treatment, *i.e.* 90°C, X-ray amorphous alkoxy-fluoride has been obtained, (ii) for the highest temperature used, *i.e.* 200°C, the metastable form β-AlF_3 has been obtained with a very large surface area of 125 $m^2.g^{-1}$. The mechanism of the amorphous ⇔ crystallized transformation has been rationalized by the occurrence of a decomposition reaction of the gel fluoride induced by the microwave irradiation. (iii) Finally, at intermediate temperature, *i.e.* 180°C, a multi-component material mixture exhibiting a huge surface area of 525 $m^2.g^{-1}$ has been obtained and further investigated after mild post-treatment fluorination using F_2-gas. The resulting aluminium-based fluorides still possess a high surface area of 330 $m^2.g^{-1}$. HRTEM revealed that the solid is built from large particles, *i.e.* 50 nm, identified as α-AlF_3 and small ones of about 10 nm and less related to an unidentified phase. This new high surface area material exhibits strong Lewis acidity as revealed by pyridine adsorption and catalytic tests. By comparison to other materials, it has been shown that whatever the composition/structure of the Al based fluorides materials, the number of strong Lewis acid site was related to the surface area highlighting the role of surface reconstruction occurring at a nanoscopic scale on the formation of the strongest Lewis acid sites.

Keywords: Non aqueous sol gel fluoride, microwave hydrothermal process, solid Lewis acid, nano-sized material, high surface area, F_2-gas fluorination.

Introduction

A non aqueous sol-gel process has been reported by Kemnitz *et al*[1] for the preparation of X-ray amorphous metal fluorides having high surface area and exhibiting very strong Lewis acidity. In a first step, an incomplete reaction between a metal alkoxide and hydrofluoric acid takes place in an organic solvent: $M(OR)_3 + x\ HF \rightarrow MF_x(OR)_{3-x} + x\ ROH$. Whereas the formation of M-F bond is thermodynamically favoured when compared to M-OR bond, the formation of a gel limits the OR/F substitution. After drying this gel under heating up to 70°C, a powdered metal alkoxyfluoride, named dry gel, with the general formula $MF_x(OR)_{3-x}.yROH$ can be obtained. In a second step, a fluorination post-treatment, using gaseous CFC_s or anhydrous HF, is further performed to replace the remaining alkoxy-groups by fluoride anions and get pure high surface aluminium fluoride (HS-AlF_3).

At every step, those parameters which could have an influence on the properties of HS-AlF_3 have been fully investigated regarding the surface area and the reactivity properties of the final solid.[2] Concerning the liquid phase fluorination step, the authors have pointed out minor effect on the final solid properties of parameters such as the sol-gel synthesis temperature, the concentration and even the nature of the alkoxide.

On the other hand, due to the peculiar heating mode[3] resulting from the interaction between mater and the electric field component, microwave-assisted synthesis has been proved to be a new promising technique.[4] Recently, this microwave-assisted hydrothermal route has been successively applied for the synthesis of nanosized crystallized aluminium hydroxyfluorides.[5]

The present work deals with the transformation under microwave heating of a fluoride gel obtained through the sol-gel process previously described. The influence of the temperature heat treatment on the final product will be discussed. In addition, the morphology and some catalytic properties of a high surface aluminium fluoride obtained by fluorination of the dry gel using F_2-gas will be reported.

---

[1] Kemnitz, E.; Groß, U.; Rudiger, S.; Shekar, C. S. *Angew. Chem. Int. Ed.* **2003**, *42*, 4251.
[2] Rudiger, S.; Eltanany, G.; Groß, U.; Kemnitz. E. *J Sol-Gel Sci Techn*. **2007**, *41*, 299.
[3] Kappe, C. O. *Angew. Chem. Int. Ed.* **2004**, *43*, 6250.
[4] Adam, D. *Nature.* **2003**, *421*, 571.
[5] Dambournet, D.; Demourgues, A.; Martineau, C.; Pechev, S.; Lhoste, J.; Majimel, J.; Vimont, A.; Lavalley, J-C. ; Legein, C.; Buzaré, J-Y.; Fayon, F.; Tressaud, A. *Chem Mat (accepted).*

Experimental

1. Synthesis procedure

A wet gel obtained by reacting aluminium isopropoxide dissolved in isopropanol with an anhydrous HF/ether mixture in the following molar concentration ratio: $C_{HF}/C_{Al} = 3$ was used as the starting precursor. Fifty mL of this gel were enclosed in a PTFE container for a one hour duration microwave hydrothermal process. Syntheses were conducted inside a Microwave Digestion System (MARS 5, CEM Corporation). The temperature was monitored via an optical fiber and was regulated by percent increments of the microwave power (300W, 2.45 GHz frequency). The internal pressure was measured by a pressure sensor. Four different temperatures were used: 90, 130, 180 and 200°C. After heat treatment and back to room temperature, the gel was dried using a second microwave irradiation. The drying step was performed using a specific device by which solvents were evaporated through primary vacuum and argon flow. The obtained dry gel was finally outgassed at 200°C for 4h under primary vacuum.

2. Characterizations

X-ray diffraction analysis: Powder X-ray diffraction patterns were recorded on a Philips PW1820, PANalytical X'Pert diffractometer in a Bragg–Brentano geometry (θ-2θ), using Cu-Kα1/α2 radiation (λ=1.54051Å).

Textural measurements: N_2 adsorption isotherms were recorded at 77 K using an ASAP 2000 instrument from Micromeritics. The powder sample of mass around 200 mg was evacuated overnight at 473 K under 0.1 Pa, prior to N_2-adsorption. The total pore volume V_{pore} was calculated from the volume of nitrogen adsorbed at relative pressure P/P° = 0.99. The apparent specific surface area S_{BET} was calculated from the BET method applied in the P/P° [0.03 – 0.25] range. Pore size distribution was obtained taking the Barrett-Joyner-Halenda (BJH) algorithm using the adsorption branch. In Table 2, the mesopore size was taken as the value at the "top"of the (dV / d log D) plot, where D is the pore diameter.

Fluorination post-treatment: The sample was placed in a Ni crucible and was outgassed at 80°C for 1h. Undiluted F_2-gas was introduced with a flow of 10 $mL.min^{-1}$. The temperature was increased to 225°C and kept for 5h at this temperature. At the end of the experiment, unreacted F_2-gas was eliminated from the oven by an N_2 flow and reacted on a soda lime.

T.E.M: High Resolution Transmission Electron Microscopy (HRTEM) was performed on TECNAI F20 equipment with a field emissive gun, operating at 200 kV and with a point resolution of 0.24 nm. TEM samples were prepared by dispersing a few milligrams of powder

in isopropanol. The dispersion was then dipped ten minutes into an ultrasonic bath in order to disagglomerate the powder particles. One drop was finally deposited on a Formvar/carbon copper grid.

FTIR spectroscopy: Approximately 20 mg of powder was pressed into a self-supported disc (2 cm^2 area). Transmission IR spectra were recorded in the 500-5600 cm^{-1} range with a 4 cm^{-1} resolution on a Nicolet Nexus spectrometer. The cell was connected to a vacuum line for evacuation and activation steps. Samples were activated at 300°C for 4 hours under vacuum.

After activation, the acidity of the material was studied by IR spectroscopy, using adsorbed pyridine as spectroscopic probe molecules. Pyridine (Aldrich, 99+% grade) was dried on molecular sieves prior to use. Introduction of pyridine was performed at equilibrium pressure (133 Pa) and then evacuated under vacuum to remove physisorbed species and at increasing temperatures.

Catalytic tests: Dismutation of $CHClF_2$ was performed in a continuous-flow fixed-bed reactor. A mixture of $CHClF_2$:N_2 (5:20 ml min^{-1}) was passed through the sample. The temperature was increased step-wise, held at each respective temperature for 20 min. After reaching 99% conversion, the reactor was cooled down to 50°C.

The isomerisation of 1, 2-dibromohexafluoropropane $CBrF_2CBrFCF_3$ was tested at room temperature. Inside a glove box, 20 mg of sample was placed in a flask equipped with a magnetic stirrer. The flask was then sealed with a rubber septum cap. About 300 µL of $CBrF_2CBrFCF_3$ was added via the septum using a µL syringe and the mixture was stirred at ambient temperature for 2 h. The yield of the target product was deduced by ^{19}F NMR spectroscopy (solvent: $CDCl_3$).

Elemental analysis: Fluorine and aluminium contents were quantified by the Service Central of Analysis (SCA-CNRS Vernaison: F titration with specific electrode and Al by ICPMS). Carbon content was determined by the combustion method using a LECO CHNS-932 apparatus.

Results and discussions

1. Microwave-assisted synthesis

1.1. Synthesis features and characterization of the dry gel

During the microwave experiment, the synthesis temperature was tuned at four levels: 90, 130, 180 and 200°C. Table 1 summarizes the internal pressure measured during the heat treatment; the state of the gel observed after the corresponding treatment is also noted. Based on these observations, it appears clearly that the synthesis temperature is a crucial parameter. At 200°C a liquid is obtained after reaction while a very high internal pressure is measured during the synthesis.

Heating temperature (°C)	Chamber pressure (bars)	Appearance after treatment	Final F/Al molar ratio of the dry gel	Weight loss (%) of the dry gel at 200°C
90	< 1	Gel	1.5	50
130	4-5	Clear sol	1.7	42
180	16-18	Clear sol	2 (C: 12wt%)	26
200	48-51	Liquid	2.7 (C: 0.1wt%)	5

Table 1: Experimental parameters of the microwave process. The reported chamber pressure was measured before the end of the heat treatment. The appearance of gel was noted after cooling down to room temperature.

After the final microwave-assisted drying, the obtained solid depends on the synthesis temperature. From the powder X-ray diffraction patterns displayed on Figure 1, three steps can be distinguished. At 90 and 130°C, X-ray amorphous materials are obtained. At 180°C the crystallization has started, as revealed by two well defined X-ray lines at approximatively $2\theta = 25$ and 51° which are related to the main lines of the thermodynamically stable α-AlF_3 phase.[6] Several additional broad X-ray peaks located at 4.7 and 3.1 Å and marked by asteriks on Figure 1, have been detected but no satisfactory indexing could be found using the JCPDS data files. A derived-rutile aluminium oxy-fluoride has been reported[7] and the main X-ray peak of this phase is close to the peak detected at 3.1Å. These peaks present large full width at half maximum (FWHM) as compared to those of the α-AlF_3, suggesting that this unknown

[6] Daniel, P. ; Bulou, A. ; Rousseau, M. ; Nouet, J. ; Fourquet, J.L. ; Leblanc, M. ; Burriel, R. *J. Phys.: Condens. Matter* 2. **1990,** 5663.
[7] Kutoglu. A. *Z. Kristallogr*. **1992**, *199*, 197.

phase consists of smaller particles. Finally, when the reaction temperature is 200°C, a very well crystallized aluminium fluoride is formed which exhibits the hexagonal tungsten bronze type structure, *i.e.* β-AlF_3.[8]

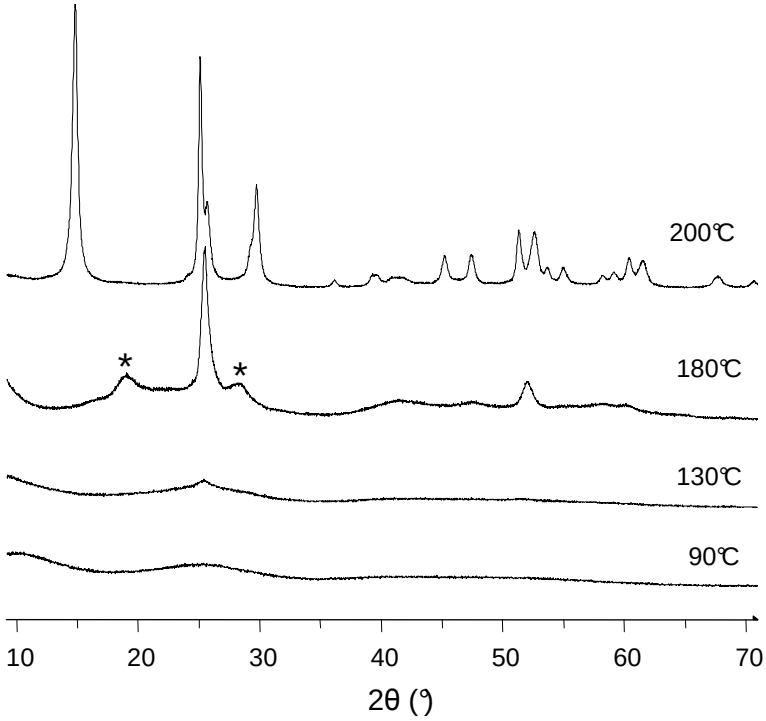

Figure 1: X-ray diffraction powder patterns of samples obtained after microwave irradiation at various temperatures. (* unknown phase)

This evolution of the crystalline features can be related to the increase of the F/Al molar ratio, as displayed in Table 1. A slight increase of the fluorine content from 1.5 to 1.7 is observed when heat treatment temperature is increased from 90 to 130°C. Treatments at higher temperature improve largely the fluorine content. Moreover, the F/Al molar ratio increases sharply from 2 to 2.7 when the temperature is increased from 180 to 200°C. In addition, the content of organic moieties can be basically quantified by measuring the weight loss after outgassing at 200°C under dynamic vacuum (table 1). A general trend can be raised: the higher the fluorine content, the lower the weight loss and the lower the organics content. For dry gels obtained at high temperatures, *i.e.* 180 and 200°C, the carbon contents were measured to be 12.7 and under 0.1 wt%, respectively. Such results imply the formation of intermediate alkoxy-fluorides with the already reported general formula: AlF_3-

[8] Le Bail, A. ; Jacoboni, C. ; Leblanc, M. ; De Pape, R. ; Duroy, H. ; Fourquet, J.L. *J. Solid State Chem.* **1988**, *77*, 96.

$_x(OiPr)_x.y.iPrOH$[9] when the synthesis was conducted below 200°C. The 0.1wt% C content clearly evidences that the phase obtained at 200°C is no more an alkoxy-fluoride but is more likely an oxy- or hydroxy-fluoride.

Concerning the textural properties of the obtained dry gels, the nitrogen adsorption-desorption isotherms, as well as the derived pore size distribution are collected in **Figure 2. A)**. BET specific surface area, total pore volume and mesopore size are listed in **Table 2**.

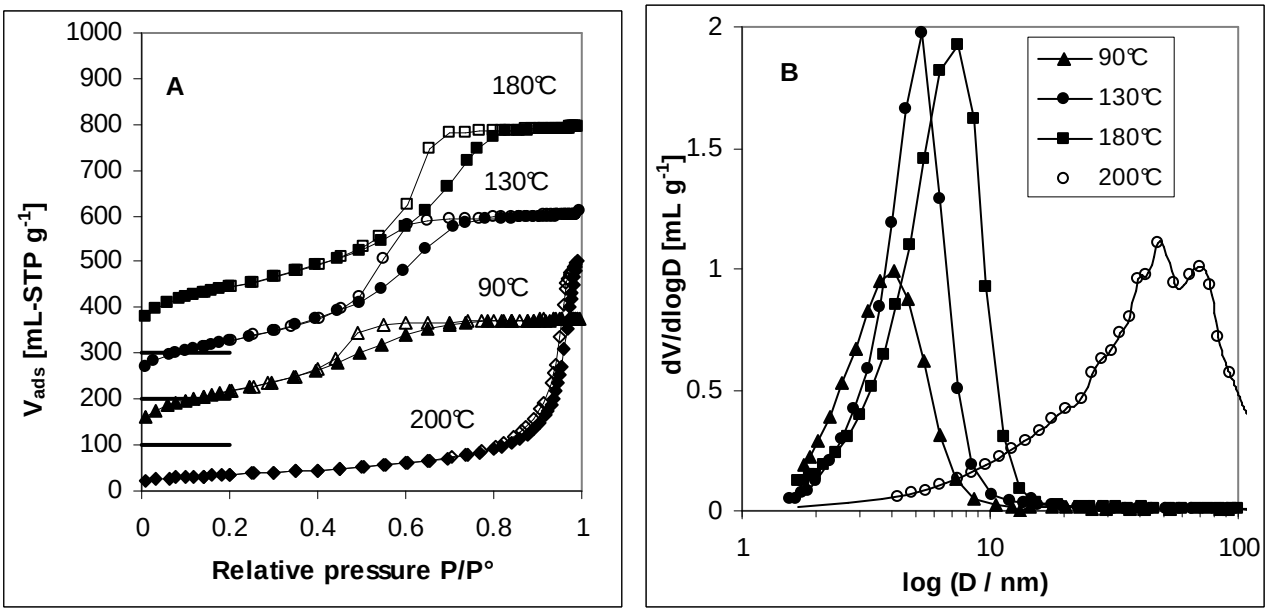

Figure 2: A) N_2 adsorption isotherms of materials prepared at various temperatures. Full symbols correspond to the adsorption branch and empty symbols to the desorption branch. For the sake of readability the isotherms are shifted upwards for n×100 mL g^{-1}. B) Pore size distribution.

Heating temperature (°C)	V_{pore} [mLg^{-1}]	S_{BET} [m^2g^{-1}]	Pore size [nm]
90	0.43	426	4.1
130	0.62	468	5.3
180	0.76	524	7.4
200	0.77	126	≈ 50

Table 2: Porosity measurements by N_2 isotherm results

The most salient observation is the very large surface area of the obtained materials. As far as the textural properties are concerned, a clear distinction can be made between the sample prepared at 200°C and those obtained at lower temperatures. Samples prepared below 200°C are mesoporous materials exhibiting a type IV isotherm with a well defined plateau and a H2-type (IUPAC) hysteresis loop. When the treatment temperature is raised from 90°C up to

[9] Ruediger, S. ; Groß, U. ; Feist, M.; Prescott, H. A. ; Chandra Shekar, S. ; Troyanov S. I.; Kemnitz, E. *J. Mater. Chem.* **2005**, *15*, 588.

180°C, the total pore volume increases from 0.43 to 0.76 $mL \cdot g^{-1}$ whereas the surface area only increases from 425 to 525 $m^2\ g^{-1}$. This is ascribed to an enlarging of the width of mesopores which is directly evidenced by a shift of the hysteresis loop toward higher relative pressures. The mesoporous network could be described by a distribution of mesopores centred at increasing width, from 3.7 to 6.3 nm (Figure 2. B).

The sample prepared at 200°C exhibits also a type IV isotherm but with a very different shape and a H1-type loop observed at high relative pressures (above ≈ 0.95). So, it can be observed on Figure 2. B that this material exhibits a very broad distribution of wide pores. The decrease of the surface area down to 125 $m^2\ g^{-1}$ while a high pore volume is preserved (0.77 mLg^{-1}) is consistent with the completion of a crystallization process in agreement with the very well crystallized state of this material.

1.2. From amorphous to crystallized materials: proposed mechanisms

Based on the above results, it appears that the temperature at which the microwave treatment is performed is the main factor which drives the nature of the final product. However, the temperature factor seems to induce a complex mechanism involving the different constituents of the mixture and this point will be discussed in the following.

At 90 and 130°C, the fluorination of the alkoxide remains very low and the resulting aluminium alkoxy-fluoride is X-ray amorphous due to the presence of a large amount of organic moieties which limit the coherence length of the crystallites. At these temperatures, the dry gel should exhibit the topology of the original gel which consists of an $Al(F,OR)_3$ network. An increase of the synthesis temperature up to 180°C favours the formation of higher fluorinated species, as revealed by the increase of the F/Al molar ratio up to 2 **(**Table 1**)**. This increase of the fluorine content is simultaneous with the appearance of crystallized domains, most of them being the α-AlF_3. The appearance of this phase within an amorphous matrix reveals the inhomogeneity of the activated gel mixture. Such inhomogeneities have also been demonstrated by ^{27}Al NMR spectroscopy on the dry gel prepared with a low C_{HF}/C_{Al} molar ratio (R=2). Aluminium species with various anionic environments[2], *i.e.* fluorinated species located at -10 ppm and oxygenated species at 14 ppm, are highlighted. Regarding the low FWHM for the X-ray peaks of the α-AlF_3 phase obtained at 180°C (Fig 1), it is clear that this phase consists of large particles as compared to the other constituents. The other constituents of this sample should be considered as an $AlF_{3-x}(OiPr)_x$ and/or an Al

oxyfluoride phase with very small particle size giving rise to the extremely high surface area, *i.e.* 525 m^2 g^{-1}.

The crystallization process begins between 130 and 180°C and induces an increase of the kinetics of fluorination and surprisingly an increase of the surface area. It can be suggested that the densification of α-AlF_3 particles implies a migration of matter which results in a high improvement of the porous volume associated with an only slight increase of the surface area. Finally, the sample obtained at 200°C preserves a high pore volume (0.77 mL g^{-1}) but the surface area is decreased by a factor of 4.2, *i.e.* from 525 to 125 m^2 g^{-1}. This drastic decrease of the surface area is consistent with the completion of a full crystallization process which is also unambiguously highlighted by several factors: (i) the appearance of the β-AlF_3 phase revealed by the XRD pattern (Figure 1), (ii) the strong increase of the fluorine content (Table 1), (iii) the disappearance of organic moieties revealed by the very low carbon content (C% = 0.1wt%) and (iv) a strong increase of the internal pressure, *i.e.* from 20 to 50 bars. The two last features suggest that between 180 and 200°C, the decomposition of the organic constituents takes place thanks to the high energy brought to the system. It has already been reported that microwave irradiation is able to induce side reactions: decomposition of organics molecules[10], redox processes[5], and decomposition of ionic liquids.[11] The reaction mixture also contained some ether molecules as solvent which are considered as inert under microwave irradiation since they are non polar. Therefore, it can be assumed that ether molecules are not decomposed under microwave irradiation. Additionally, during microwave synthesis of oxides, K. J. Rao *et al*[12] reported the formation of ether molecules by condensation of alcohol molecules. Moreover, MS-coupled DTA/TG-investigations on the dry aluminium alkoxyfluoride clearly evidenced the formation of ether and water as result of Lewis-acid (Al^{3+}) induced alcohol condensation.[9] Hence, it is likely to consider that such mechanism occurs here too: $2R\text{-}OH \rightarrow R\text{-}O\text{-}R + H_2O$. The released water can thus favour the hydrolysis of the alkoxy-fluoride species as follows: $AlF_{3-x}(OiPr)_x + xH_2O \rightarrow AlF_{3-x}(OH)_x +$ xiPrOH. The kinetics of fluorination can thus be improved by the decrease of steric hindrance induced by alkoxy ligands. Taking into account the already mentioned MS-coupled thermal investigations[9], an alternative reaction path can be discussed. In this investigation, most of the solvated isopropanol molecules were desorbed between 100 and 150°C; then the formation of propene as well as a very small amount of ether was detected between 175 and 225°C.

[10] Kubrakova, I. V. ; Khamizov, R. Kh. *Russ. Chem. Bull. Intern*. **2005**, *54*, 1413.
[11] Jacob, D.S.; Bitton, L.; Grinblat, J.; Felner, I.; Koltypin, Y.; Gedanken, A. *Chem. Mater.* **2006**, *18*, 3162.
[12] Rao, K.J.; Mahesh, K. ; Kumar, S. *Bull, Mater, Sci.* **2005**, *28*, 19.

Consequently, in this temperature range a fluorinating gas must be provided to complete the fluorination. This conclusion is in full agreement with the synthesis experience. By analogy with the thermal decomposition mechanism of the aluminium alkoxy-fluoride, the process inducing the transformation of an amorphous phase into crystallized fluorides using microwave heating can be described as follows: (i) the increase of the synthesis temperature up to 180°C favours the fluorination of the already formed aluminium alkoxy-fluorides; thermal motions induced by the microwave irradiation increases the reactivity of fluoride anions toward the alkoxy group substitution, (ii) at temperatures above 180°C, breaking of the Al-OiPr bonds can be considered to occur. In this scheme, bonds are cleaved forming propene and OH groups, as previously reported[9]: Al-O-CH(CH_3)$_2$ → Al-OH + CH_2=CH-CH_3. This scheme is in good agreement with the drastic increase of the internal pressure occurring between heat treatments performed at 180 and 200°C. Additionally, after cooling down to room temperature, an internal pressure still remains inside the vessel, suggesting the presence of a gas phase.

Another remarkable point is that the decomposition of solvent molecules occurring between 180 and 200°C induces a dissolution/recrystallization process leading to the metastable phase β-AlF_3 and the disappearance of the thermodynamically stable phase α-AlF_3. This reaction could be compared with the synthesis of nano-structured aluminium hydroxy-fluorides using microwave irradiation of an alcoholic solution containing nitrate as aluminium precursor.[5] During such a synthesis an exothermic phenomenon occurs involving the reduction of nitrate precursor into ammonium species coupled with the oxidation of isopropanol. In this case also, the synthesis of the metastable beta phase implies a side reaction which finally, through drastic variation of the thermodynamic state (P, T), provides the requested energy for the stabilization of such a metastable β-form.

2. High surface AlF_3 and acidic properties

2.1. Post fluorination-treatment using F_2-gas

It has been shown above that the microwave-assisted sol-gel synthesis leads to fluoride materials exhibiting high surface area (above 500 $m^2.g^{-1}$). However such a material still contains large amounts of organic moieties since the carbon content is still around 12wt% after microwave treatment at 180°C (Table 1). In order to remove these species while retaining the high surface area, a low-temperature fluorination was performed using gaseous

F_2. The sample obtained at 180°C was selected because of its highest surface area of 525 m^2 g^{-1}. In order to avoid a full crystallization process, a medium temperature, *i.e.* 225°C, was chosen for the fluorination.

This post fluorinated sample still exhibits a high surface area 330 $m^2 \cdot g^{-1}$, providing a suitable material for catalytic ability. All carbon was removed showing that the post fluorination-treatment enables the complete removal of organic moieties. No significant change was observed by X-ray diffraction analysis except for the detection of a peak located at 9.4 Å and noted with a sign "+" in Figure 3. The broad peaks located at around 4.7 and 3.1 Å are still present (asterisks on Figure 3). It should be noted that these three peaks can be indexed as multiple of reticular planes with d=9.4 Å.

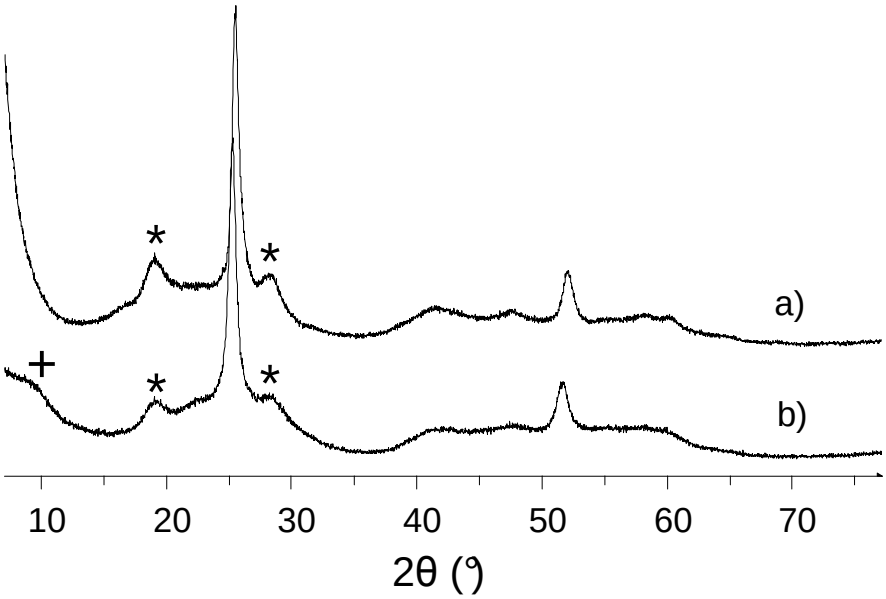

Figure 3: X-ray diffraction powder pattern of samples microwave treated at 180°C a) and after fluorination with undiluted F_2-gas at 225°C b). (* unknown phase, + shoulder at 9.4Å)

Figure 4 displays some T.E.M images of the F_2-treated sample. The solid consists of agglomerates built from large and small particles denoted (1) and (2) on Figure 4.A. Some of these large particles (50 nm) are displayed in Fig 4.B. A zoom on a particle with a rodlike structure, *i.e.* 50 nm in length, shows interplanar distances of approximately 3.5-3.7Å (insert Fig 4.B) which correspond to (012) inter-reticular distances of α-AlF_3. These large particles can therefore be ascribed to α-AlF_3 in agreement with the narrow FWHM of their X-ray peaks. The second type of particles consisting of small crystallized domains of about 10 nm or less, are shown in Figure 4.C These domains present some interplanar distances of about 3 Å (Inset, Fig 4.C). Such a distance is very close to the X-ray peak detected at 3.1 Å, which, in

turn, is considered to characterize this phase. According to the high surface area of the solid, it is clear that these small particles, *i.e.* around 10 nm should be preponderant in the material.

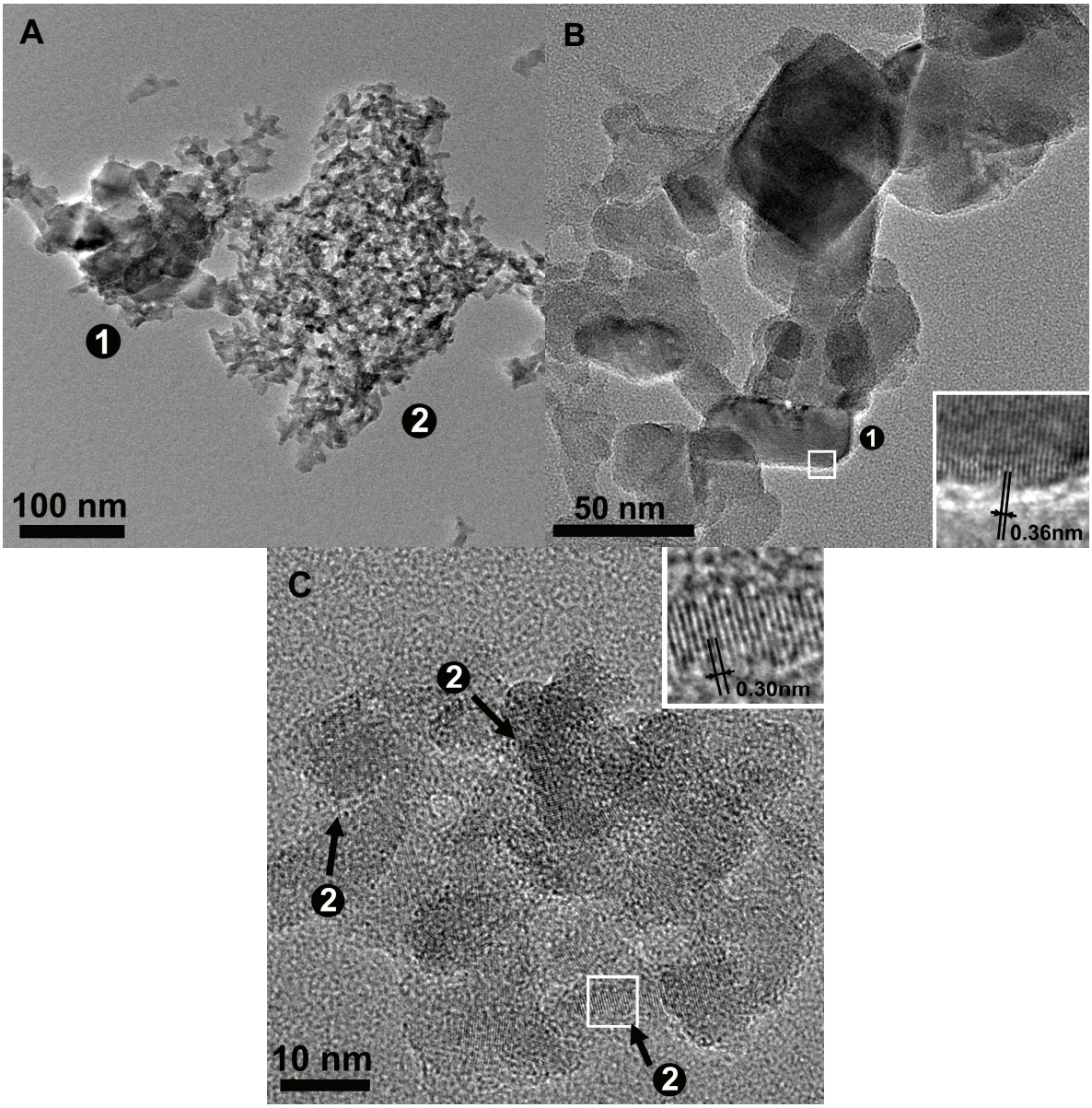

Figure 4: Transmission electron micrographs A) and HRTEM images B) C) of high surface aluminium fluoride.

2.2. Surface acidic properties

The surface acidic properties of this new high surface aluminium fluoride (330 m^2g^{-1}) have been investigated by catalytic tests and adsorption of pyridine using FTIR spectroscopy.

First, catalytic tests were performed regarding the catalytic activity upon the $CHClF_2$ dismutation reaction. According to the data given in Table 3, full catalytic activity of $CHClF_2$ dismutation proceeds after an activation period at 200°C. This inductive period is required to

remove water molecules adsorbed onto the surface. Once the catalyst is active, the dismutation reaction proceeds to completion even at 50°C showing high catalytic properties.
The isomerisation of 1, 2-dibromohexafluoropropane has been also tested. This reaction is a good indicator of the presence of very strong Lewis acid sites since it takes place only in presence of the strongest Lewis acids (amorphous HS-AlF_3, SbF_5, ACF). The rate of conversion is found to be 18% and accounts for the presence of strong Lewis acid sites.

$CHClF_2$ dismutation							1,2-DBP Isomerization
T(°C)	100°C	150°C	200°C	150°C	100°C	50°C	
Conversion rate (%)	2	2	97-98	~ 100	~ 100	~ 100	18

Table 3: Catalytic activities of post-fluorinated high surface AlF_3 (330 $m^2.g^{-1}$) sample toward the dismutation reaction of $CHClF_2$ and the isomerisation of 1, 2-dibromohexafluoropropane.

The type of surface acidic sites (Lewis or Brønsted) and their number have been determined using pyridine (Py) adsorption at room temperature. The high-surface AlF_3 sample has been outgassed at 300°C prior to pyridine adsorption at room temperature. The spectrum obtained after introduction of 1 torr of pyridine and followed by evacuation at room temperature is shown in Figure 5**.** The 1400-1800 cm^{-1} range displayed is typical of the vibration modes of coordinated pyridine. Only Lewis acid sites are detected since no band due to pyridine protonation (Brønsted acid site) has been detected. Pyridinium species are indeed characterized by bands occurring around 1540 and 1640 cm^{-1}.
The wavenumber of the two bands at 1619 and 1453 cm^{-1} (ν8a and ν19b modes of coordinated Py species) accounts for the strength of the Lewis acid sites[13], *i.e.* the higher the wavenumber, the stronger the Lewis acidity. They are closed to those previously reported for β-AlF_3 compound[14] and higher than those characterizing the Lewis acidity of alumina[15] (1614 and 1448 cm^{-1}).

[13] Busca, G. *Phys. Chem. Chem. Phys*. **1999**, *1*, 723.
[14] Vimont, A. ; Lavalley, J. C. ; Francke, L. ; Demourgues, A. ; Tressaud, A. ; Daturi, M. *J. Phys. Chem. B.* **2004**, *108*, 3246-3255.
[15] Vimont, A.; Lavalley, J. C.; Sahibed-Dine, A.; Otero Arean, C.; Rodriguez Delgado, M.; Daturi, M. *J. Phys. Chem. B.* **2005,** *109*, 9656.

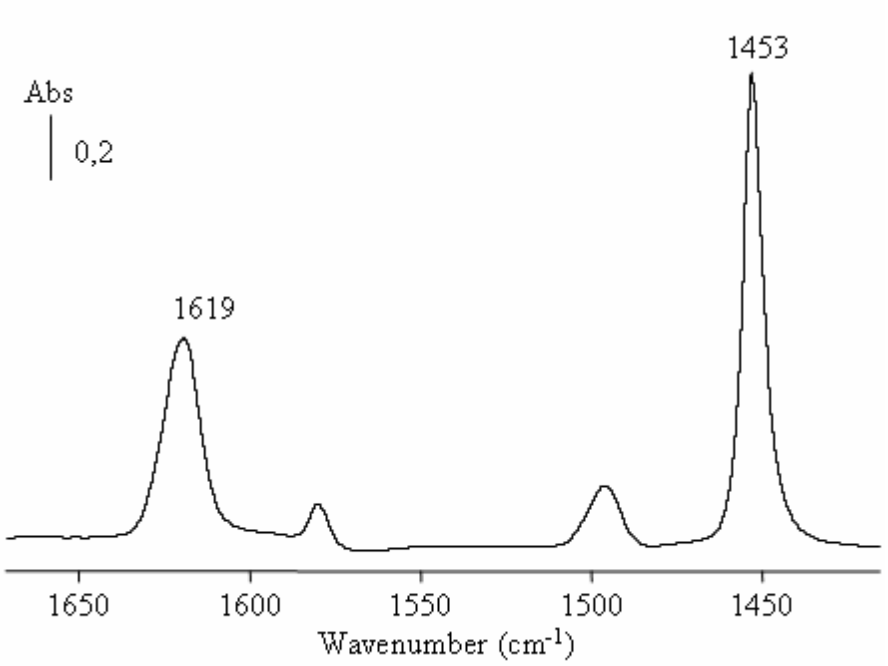

Figure 5: IR spectrum recorded after introduction of 1 torr of pyridine at room temperature on high surface AlF_3 after outgassed at 300°C followed by evacuation at room temperature.

Pyridine desorption at higher temperature increases the ν8a and ν19b wavenumbers (Table 4). This phenomenon can be explained either by the site heterogeneity, the weakest sites being liberated first or by the pyridine inductive effects which depend on the amount of adsorbed pyridine. The concentration of Lewis acid sites, estimated from the integrated area of the ν19b band, assuming a molar absorption coefficient value of 1.8 cm μmol^{-1},[14] is equal to about 615 $\mu mol.g^{-1}$, *i.e.* 1.1 site.nm^{-2}.

It was important to compare the strength and the number of strong Lewis acid sites determined for this high surface area AlF_3 sample to those measured for other divided AlF_3 materials. Table 4 reports the strength and the amount of the Lewis acid sites determined as reported above from the wavenumber and the intensity of the ν19b band after pyridine desorption at RT, 200 and 300°C. The quoted AlF_3 materials are (i) the post-fluorinated sample exhibiting a high surface area (330 $m^2.g^{-1}$) and therefore denoted HS-AlF_3, (ii) two HTB samples with different surface areas[14,5] (20 and 82 $m^2.g^{-1}$) denoted LS (low surface) and HS (high surface) β-AlF_3, respectively, (iii) an hydroxyfluoride exhibiting the pyrochlore type-structure[16] (130 $m^2.g^{-1}$) and (iv) a derived form of α-AlF_3 (61 $m^2.g^{-1}$).[17]

[16] Dambournet, D.; Demourgues, A. ; Martineau, C.; Durand , E. ; Majimel, J.; Vimont, A.; Leclerc, H. ; Lavalley, J-C.; Daturi, M.; Legein, C.; Buzaré, J-Y.; Fayon, F. ; Tressaud, A. *Submitted*.
[17] Dambournet, D.; Demourgues, A. ; Martineau, C.; Durand , E. ; Majimel, J.; Vimont, A.; Lavalley, J-C.; Legein, C.; Buzaré, J-Y.; Fayon, F. ; Tressaud, A. *Submitted*.

		Samples					
	Outgassing temperature	HS AlF_3 (330 $m^2.g^{-1}$)	LS β-AlF_3 (20 $m^2.g^{-1}$)	HS β-AlF_3 (82 $m^2.g^{-1}$)	Pyrochlore (130 $m^2.g^{-1}$)	α-AlF_3 (61 $m^2.g^{-1}$)	γ-Alumina (290 $m^2.g^{-1}$)
ν19b band wavenumbers	RT 200°C 300°C	1453 1455.5 1456	1454 1455 1456.5	1453.5 1455 1457	1451.5 1454.5 1456	1453 1455 1456	1448 1454 1455
Site numbers (µmol.g^{-1})	RT 200°C 300°C	615 283 203	35 20 10	200 100 43	336 137 77	158 63 32	480 110 40
Site numbers (per nm^2)	RT 200°C 300°C	1.1 0.5 0.35	1.3 0.75 0.35	1.45 0.75 0.3	1.45 0.6 0.35	1.55 0.6 0.3	1.0 0.25 0.1

Table 4: Strength and concentration of Lewis acid sites detected by pyridine adsorption on fluorinated materials and alumina. F-samples and alumina are pre-treated under vacuum at 300 and 500°C, respectively.

As far as the AlF_3 samples are concerned, the ν19b wavenumber after pyridine outgassing at RT is slightly lower in the case of the pyrochlore sample. This can be related to the low fluorine content (F/Al=1.8) of this material by comparison to the other compounds (F/Al>2.5). The inductive effect of fluoride ions is also evidenced regarding the ν19b wavenumber of γ-Al_2O_3 which possesses weaker Lewis acid sites compared to fluorinated materials.

After pyridine desorption at 300°C, the ν19b band wavenumber of the residual adsorbed species is almost similar whatever the sample, showing that the Lewis acid sites present similar strength. This point should be regarded carefully and specified by adsorption of other probes like CO which enables the discrimination between Lewis sites with different acid strengths.

The thermodesorption performed at 300°C characterizes the strongest Lewis acid sites. The ratio between the number of sites measured after thermodesorption at 300°C and those measured after evacuation at RT enables the quantification of the proportion of the strong Lewis acid sites exhibited by each solid. The highest proportion of strong Lewis acid is found on the HS-AlF_3 material with 33% of the Lewis acid sites being strong. This result suggests the occurrence on HS-AlF_3 surface of more homogeneous Lewis acid sites as compared to the

other materials. In agreement with the promoting effect of fluoride ions, γ-alumina possesses the lowest fraction of strong Lewis acid sites, *i.e.* 8.3% of the total number of sites.

The most interesting result presented in Table 4 is relative to the concentration of Lewis acid sites per gram of material. They are much higher on HS-AlF_3 whatever the considered temperature of pyridine evacuation. Figure 6 clearly evidences that the number of Lewis acid sites is correlated to the specific area.

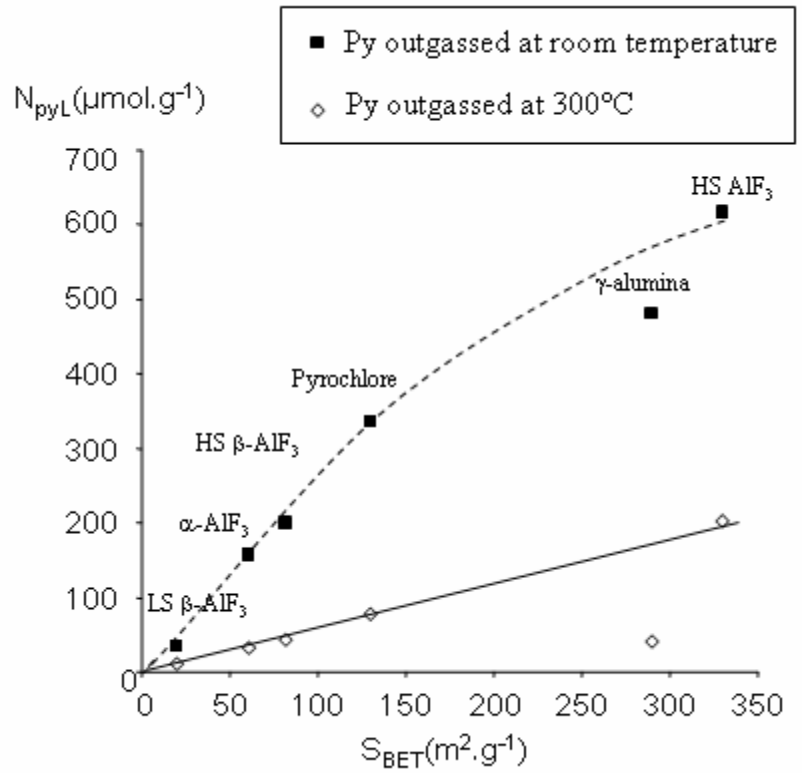

Figure 6: Dependence of the concentration of Lewis acid sites detected by pyridine adsorption on the specific area.

This is the first time that such a correlation is pointed out. This result underlines the interest of probe molecules adsorption/desorption experiments for characterizing the amount and strength of Lewis acidic sites in highly divided fluorine-based materials. Finally, it is worthwhile interesting to note that the number of the strongest Lewis acid sites (Py outgassed at 300°C) does not depend on the origin of the AlF_3 samples as illustrated in the case of the pyrochlore sample. The latter indeed exhibits a large number of Lewis acid sites after thermodesorption at 300°C. This fact can be rationalized by considering finite size effect. The increase of the surface area is basically related to a decrease of the particle sizes. Chaudhuri *et al*[18] have clearly shown that a decrease of the particle size was on going with an increase of

[18] Chaudhuri, S.; Chupas, P.; Morgan, B. J.; Madden, P. A.; Grey, C. P. *Phys. Chem. Chem. Phys.* **2006**, *8*, 5045.

the number of under-coordinated Al^{3+} ions, *i.e.* potential strong Lewis acid sites. Surface reconstruction taking into account the nanometric scale led to five and even four-fold coordinated Al^{3+} ions which should be regarded as very strong Lewis acid sites. This is consistent with our results where the number of strong Lewis acid sites is related to the surface area, *i.e.* to the particle sizes.

Conclusion and key points

This work was based on the combination of two synthesis methods in which non-aqueous sol-gel fluoride material was further subjected to microwave irradiation. The crystallized state of the final material depends on the microwave temperature treatment. An amorphous product is achieved at 90°C and a crystallized phase exhibiting the HTB type structure at 200°C. The mechanism of the amorphous ⇔ crystallized transformation of the gel under microwave irradiation was discussed. It has been suggested that the decomposition of the gel induces the crystallization process of the HTB phase.

In addition to a high surface area β-AlF_3, *i.e.* 125 m^2 g^{-1}, a multi-component material mixture exhibiting a huge surface area of 525 m^2 g^{-1} has been prepared. The later material contains residual organic moieties which have been completely removed by low-temperature fluorination using F_2-gas. This technique allows preserving a surface area as high as 330 m^2 g^{-1}. From HRTEM experiments the latter material is built of two types of nano-particles: 50 nm crystallites ascribed to α-AlF_3 and of smaller particles of about 10 nm related to an unidentified phase.

This work also confirmed that the microwave-assisted synthesis is a suitable route to achieve high surface area materials. This method is a fast and simple procedure which could be easily applied for the synthesis of other high surface metal fluorides. It opens a promising way to develop more divided materials and stabilize novel phases. Since the interaction between microwave and the mixture is a decisive step on the final stabilized material, further work should be performed using the incorporation of different organic solvents such as butanol or ionic liquids to tune the reactivity and the behaviour of the mixture under microwave irradiation. The ability of solvents to generate heat under microwave irradiation could be one way to obtain both new aluminium based-fluorides framework as well as highly divided materials.

FTIR spectroscopy evidences for the first time on Al-based fluorides materials, that the number of strong Lewis acid sites is primarily related to the surface area, whatever the structure/composition of the compound. This result highlights the role of surface reconstruction occurring at a nanoscopic scale leading to the formation of the strongest Lewis acid sites.

Acknowledgement

The EU is gratefully acknowledged for financial support through the 6th Framework Programme (FUNFLUOS, Contract No. NMP3-CT-2004-5005575).

Chapitre 3

Propriétés acides et comportement thermique de l'hydroxyfluorure de type HTB

Dans le chapitre précédent, parmi les diverses phases stabilisés, nous avons reporté la synthèse et la caractérisation structurale d'un hydroxyfluorure d'aluminium adoptant la structure HTB. En raison de l'importance de ce type de matériau à des fins catalytiques, ce chapitre se propose de compléter l'étude relative à cette phase en caractérisant d'une part ses propriétés acides et d'autre part son comportement thermique.

3.1 Etude des propriétés acides de l'hydroxyfluorure de type HTB par adsorption de molécules sondes : spectroscopie infrarouge FTIR et radiotraceurs chlorés

Publication: *The use of multiple probe molecules for the study of the acidic properties of aluminium hydroxyfluorides: FTIR and ^{36}Cl radiotracer studies, submitted to Physical Chemistry Chemical Physics*

Cette étude relative à la caractérisation des propriétés acides (Lewis/Brønsted) de la phase β-$AlF_{2.6}(OH)_{0.4}$ comporte deux parties. Dans un premier temps, l'acidité de surface sera étudiée par l'adsorption de diverses molécules sondes détectée par FTIR. Cette méthode, très performante, a permis de dresser une image détaillée de la surface. Une discussion relative à l'utilisation de diverses molécules sondes a été entreprise. Dans une deuxième partie, une technique non conventionnelle utilisant l'adsorption de marqueurs radioactifs chlorés sera présentée.

The use of multiple probe molecules for the study of the acid-base properties of aluminium hydroxyfluoride having the hexagonal tungsten bronze structure: FTIR and [^{36}Cl] radiotracer studies

Damien Dambournet,[#] Hervé Leclerc,[+] Alexandre Vimont,[+] Jean-Claude Lavalley,[+] Mahmood Nickkho-Amiry,[§] John M. Winfield,[§] Marco Daturi,[+]*

[#] Institut de Chimie de la Matière Condensée de Bordeaux-CNRS, Université Bordeaux 1. 87, Avenue du Dr. A. Schweitzer, 33608 Pessac cedex, France

[+] Laboratoire Catalyse et Spectrochimie, UMR 6506, CNRS-ENSICAEN-Université de CAEN, Boulevard du Maréchal Juin, F-14050 Caen Cedex, France

[§] Department of Chemistry, University of Glasgow, Glasgow G12 8QQ, Scotland, UK.

Corresponding authors: johnwin@chem.gla.ac.uk

Abstract

The combination of several probe molecules has enabled the construction of a detailed picture for the surface of the aluminium hydroxyl fluoride, $AlF_{2.6}(OH)_{0.4}$, which has the hexagonal tungsten bronze (HTB) structure. Using pyridine as a probe leads to features at 1628 cm^{-1}, ascribed to very strong Lewis acid sites, and at 1620-1623 cm^{-1}, which is the result of several different types of Lewis sites. This heterogeneity is indicated also from CO adsorption at 100 K; the presence of five different types of Lewis site is deduced and is suggested to arise from the hydroxylated environment. Brønsted acid sites of medium strength are indicated by adsorption of lutidine and CO. Adsorption of lutidine occurs at OH groups, which are exposed at the surface, and CO reveals that these OH groups have a single environment that can be correlated with their specific location inside the bulk assuming that the surface OH group may reflect the bulk OH periodicity. A correlation between the data obtained from CO and pyridine molecules has been established using co-adsorption experiments, which also highlight the inductive effect induced by pyridine. Adsorption of the strong Brønsted acid, anhydrous hydrogen chloride, detected by monitoring the β^- emission of [^{36}Cl]-HCl at the surface, indicates that surface hydroxyl groups can behave also as a Brønsted base and that H_2O---HCl interactions, either within the hexagonal channels or at the surface are possible. Finally, the formation of strongly bound H^{36}Cl as a result of the room temperature dehydrochlorination of [^{36}Cl]-labelled *tert*-butyl chloride provides additional evidence that HTB-$AlF_{2.6}(OH)_{0.4}$ can behave as a Lewis acid.

Keywords: Lewis and Brønsted acidity, hexagonal tungsten bronze (HTB), aluminium hydroxyl fluoride, FTIR probe, chlorine-36.

1. Introduction

The development of new routes toward high surface area materials emphasises the importance of the surface compared with the bulk. It is necessary therefore to combine crystal and surface characterization for a detailed understanding of the reactivity of a nanostructured solid. Infrared spectroscopy of adsorbed probe molecules is one of the most powerful techniques used to investigate solid surfaces.[1] The choice of the spectroscopic molecular probes allows specific properties exhibited by a material to be investigated. Very often a combination of several probe molecules enables a detailed characterisation and for a better comprehension of experimental results. Pyridine, carbon monoxide or ammonia are the most widely known probe molecules for acidity characterisation but in contrast to aluminium oxide-based materials, relatively few studies of surface characterization of aluminium-based fluorides using such molecules have been made.[2,3,4]

Recent investigations of the chemical reactivities of aluminium-based fluoride surfaces have made use of a monitoring technique based on radio-labelled probe molecules. A [^{36}Cl] radiotracer approach[5,6] has been used to probe the surface properties of the metastable β-aluminium trifluoride phase, which adopts the hexagonal tungsten bronze (HTB) structure.[7] Because of the highly sensitive nature of the radiotracer technique, room temperature adsorption of H^{36}Cl at the β-AlF_3 surface can be detected and desorption of H^{36}Cl (which is accompanied by loss of H_2O) followed.[5] At higher temperature, replacement of surface hydroxyl groups by Al-^{36}Cl bonds can be detected and surface hydroxyl site densities estimated.[6] [^{36}Cl]-Labelled *tert*-butyl chloride, Bu^{t}Cl, can be used to investigate Lewis surface acidity. The ability of Lewis acidic oxides to catalyse the dehydrochlorination of various hydrochlorocarbons, reactions normally carried out at elevated temperatures, is well established.[8,9,10,11] In the investigations of metal fluorides that have employed [^{36}Cl] labelling,

[1] Busca, G. *Phys. Chem. Chem. Phys*. **1999**, *1*, 723.
[2] Morterra, C.; Cerrato, G.; Cuzzato, P.; Masiero, A.; Padovan, M. *J. Chem. Soc. Faraday Trans.* **1992**, *88*, 2239.
[3] Vimont, A. ; Lavalley, J. C. ; Francke, L. ; Demourgues, A. ; Tressaud, A. ; Daturi, M. *J. Phys. Chem. B*. **2004**, *108*, 3246.
[4] Krahl, T.; Vimont, A.; Eltanamy, G.; Daturi, M.; Kemnitz, E. *J. Phys. Chem. C*. **2007**, 111(49), 18317.
[5] Barclay, C. H.; Borzorgzadeh, H.; Kemnitz, E.; Nickkho-Amiry, M.; Ross, D. E. M.; Skapin, T.; Thomson, J.; Webb, G.; Winfield, J. M. *J. Chem. Soc., Dalton Trans.* **2002**, 40.
[6] Berndt, H.; Bozorg Zadeh, H.; Kemnitz, E.; Nickkho-Amiry, M.; Pohl, M.; Skapin, T.; Winfield, J. M. *J. Mater. Chem.* **2002**, *12*, 3499.
[7] Le Bail, A. ; Jacoboni, C. ; Leblanc, M. ; De Pape, R. ; Duroy, H. ; Fourquet, J.L. *J. Solid State Chem.* **1988**, *77*, 96.
[8] Ballinger, T. H.; Yates, Jr., J. T. *J. Phys. Chem.* **1992**, *96*, 1417.
[9] Ballinger, T. H.; Smith, R. S.; Colson, S. D.; Yates, Jr., J. T. *Langmuir*. **1992**, *8*, 2473.

reactions have been performed normally at ambient temperature, making use of the great sensitivity of the isotopic tracer method. For example, strong Lewis acidic fluorides such as aluminium chlorofluoride, $AlCl_xF_{3-x}$, x = 0.05 – 0.3,[12,13] and high surface area aluminium trifluoride, HS-AlF_3,[14,15,16] have been shown to be able to catalyse the dehydrochlorination of Bu^{t}Cl at room temperature. When [^{36}Cl]-labelled Bu^{t}Cl is used, the H^{36}Cl evolved can be detected on the surface and its subsequent fate determined.[17,18]

Microwave-assisted synthesis is a promising route to obtain nanosized crystallized aluminium based-fluorides. One of the products recently reported[19] is an aluminium hydroxyfluoride, whose stoichiometry is $AlF_{2.6}(OH)_{0.4}$ and which adopts the hexagonal tungsten bronze type-structure.[7] Its surface area is 82 $m^2\ g^{-1}$, which is far higher than found for materials prepared by conventional routes. In a previous study,[19] line broadening analysis/Rietveld refinement and high field ^{27}Al NMR spectroscopy enabled an accurate knowledge of the local and long-range structure to be obtained. According to the Rietveld refinement, hydroxyl groups are situated in peculiar anion crystallographic sites, *i.e.* 8f (F1) and 16h (F2) Wyckoff positions, located inside the hexagonal channels of the HTB structure. These conclusions are confirmed by high field ^{27}Al NMR, which also enables the identification and the quantification of $AlF_{6-x}(OH)_x$ species. The solid is built of 82% of AlF_6 and $AlF_5(OH)$, 16% of $AlF_4(OH)_2$ and 2 % of $AlF_3(OH)_3$ species.[19]

FTIR experiments, performed as part of the study,[19] indicated the occurrence of two kinds of OH groups through the use of NH_3 adsorption: outer surface OH groups characterized by a ν(OH) band at 3677 cm^{-1} and bulk hydroxyls partly substituting F^- anions inside the channels, characterized by a ν(OH) band at 3669 cm^{-1}. However, the conformation of the surface OH groups located on the outer surface or at the entrance of a channel could not be determined.

---

[10] Pistarino, C.; Finocchio, E.; Romezzano, G.; Brichese, F.; di Felice, R.; Busca, G.; Baldi, M. *Ind. Eng. Chem. Res.* **2000**, *39*, 2752.
[11] Pistarino, C.; Finnochio, E.; Larrubia, M.A.; Serra, B.; Braggio, S.; Busca, G.; Baldi, M. *Ind. Eng. Chem. Res*. **2001**, *40*, 3262.
[12] Krahl, T.; Stösser, R.; Kemnitz, E.; Scholz, G.; Feist, M.; Silly, G.; Buzaré, J.-Y. *Inorg. Chem*. **2003**, *42*, 6474.
[13] Krahl, T.; Kemnitz, E. *J. Fluor Chem*. **2006**, *127*, 663.
[14] Kemnitz, E.; Groβ, U.; Rüdiger, St.; Shakar, C. S. *Angew. Chem., Int. Ed.* **2003**, *42*, 4251.
[15] Rüdiger, St.; Groβ, U.; Feist, M.; Prescott, H. A.;. Shakar, C. S.; Troyanov, S. I.; Kemnitz, E. *J. Mater. Chem.* **2005**, *15*, 588.
[16] Rüdiger, St.; Groβ, U.; Kemnitz, E. *J. Fluorine Chem.* **2007**, *128*, 353.
[17] Nickkho-Amiry, M.; Winfield, J. M. *J. Fluorine Chem*. **2007**, *128*, 344.
[18] Nickkho-Amiry, M.; Eltanany, G.; Wuttke, St.; Rüdiger, St.; Kemnitz, E.; Winfield, J. M.; *J. Fluorine Chem*, **2008**, in press.
[19] Dambournet, D.; Demourgues, A.; Martineau, C.; Pechev, S.; Lhoste, J.; Majimel, J.; Vimont, A.; Lavalley, J-C. ; Legein, C.; Buzaré, J-Y.; Fayon, F.; Tressaud, A. *Chem Mater*. **2008**, *20*, 1459.

In the present work the acidic character of the surface has been investigated in detail by FTIR spectroscopy using several basic probe molecules. Acid-base reactions that involve the surface have been examined by the [^{36}Cl] method outlined above in order to make comparisons with other recently investigated aluminium fluorides of high surface areas. This multi-probe approach using pyridine, lutidine (2,6-dimethylpyridine), carbon monoxide and anhydrous hydrogen chloride, the latter being used either directly or *via* the precursor *tert*-butyl chloride, has allowed a detailed picture of this material, which exhibits both Lewis and Brønsted acidities and Brønsted basicity.

2. Experimental section

2.1 Sample preparation

The compound β-$AlF_{2.6}(OH)_{0.4}$ has been prepared as described elsewhere.[19] A solution containing water/isopropanol as solvents, aluminium nitrate as the precursor and an aqueous solution of HF (molar ratio [HF] : [Al] equal to 3) was treated under microwave irradiation at 433 K for two hours in a closed Teflon® container. The sample was washed under a pressure of dinitrogen with a large quantity of ethanol then outgassed at 573 K for 4h under vacuum. A powdered solid with $AlF_{2.6}(OH)_{0.4}$,xH_2O (x = 0.1-0.2) composition was obtained. The remaining water was removed: (i) in FTIR experiments, by in situ activation at 573 K and (ii) in [^{36}Cl] radiotracer experiments, by a further annealing treatment performed at 573 K for 12h. Note that both hydrated and anhydrous solids have been investigated with [^{36}Cl]-labelled probes.

2.2 FTIR spectroscopy

Samples were pressed (10^9 Pa) into self supported discs (2 cm^2 area, 7-10 mg cm^{-2}). They were placed in a quartz cell equipped with CaF_2 windows. A movable quartz sample holder permitted to adjust the pellet in the infrared beam for spectra acquisition and to displace it into a furnace at the top of the cell for thermal treatments. The cell was connected to a vacuum line for evacuation, calcination steps ($P_{residual}$ = 10^{-3}-10^{-4} Pa) and for the introduction of probe molecules (in gas or vapour phase) into the infrared cell. Spectra were recorded at room temperature. In CO adsorption experiments, the temperature of the pellet was decreased to about 100 K by cooling the sample holder with liquid N_2 after quenching the sample from the thermal treatment temperature. The addition of accurately known increments of probe molecules in the cell (a typical increment corresponded to 100 µmol of probe per gram of

material) was possible via a calibrated volume (1.75 cm^3) connected to a pressure gauge for the control of the probe pressure (1-10^4 Pa range). The probe pressure inside the IR cell was monitored by another pressure gauge (1-10^3 Pa range). Transmission IR spectra were recorded in the 5600–500 cm^{-1} range, at 4 cm^{-1} resolution, on a Nicolet Nexus spectrometer equipped with an extended KBr beam splitting device and a mercury cadmium telluride (MCT) cryodetector. Prior to the adsorption of probe molecules, the sample was activated at 573 K overnight.

2.3 [^{36}Cl] radiotracer experiments

Anhydrous hydrogen chloride labelled with [^{36}Cl] was synthesised by a modification of a previously reported method.[20] A standard solution was prepared from a commercial sample of aqueous $Na^{36}Cl$ and concentrated HCl (10 cm^3). An aliquot, diluted further with conc. aqueous HCl (to 10 cm^{-3} using 1 to 5 cm^{-3} of the standard), was allowed to react with H_2SO_4 (98%) dropwise at room temperature. Purification was by low temperature trap to trap distillation over P_4O_{10}, with the final distillation conducted *in vacuo*. The radio-labelled product was stored in stainless steel or Monel over $P_4O_{10.}$ *Tert*-butyl chloride labelled with [^{36}Cl] was prepared by a literature method[21] modified for [^{36}Cl] use.[5] A mixture of 2-methylpropan-2-ol (1.66 g, 23.0 mmol) and an aliquot (up to 10 cm^3) of the standard aqueous $H^{36}Cl$ solution was allowed to react at room temperature for 2 h with intermittent shaking. The organic layer was washed, firstly with aqueous $NaHCO_3$, then with water. It was dried over $CaSO_4$ followed by activated 3A sieves *in vacuo*.

The procedure for monitoring $H^{36}Cl$ adsorption at β-AlF_3 through multiple exposures of $H^{36}Cl$ to the solid at room temperature has been described ,[5] as have the principles that underlie the application of the Geiger-Müller direct monitoring method to the study of room temperature dehydrochlorination of [^{36}Cl]-labelled Bu^tCl.[17] A sample of HTB-aluminium hydroxyl-fluoride to be studied was dropped into the Pyrex counting cell *in vacuo* via a Pyrex ampoule, which could be attached vertically to a Pyrex vacuum system *via* a standard joint and an high vacuum PTFE/Pyrex stopcock (J. Young). Prior to use, the flamed out ampoule was loaded with the solid sample in a glove box. After it was added to the cell, the sample (normally 250 – 500 mg) was spread as thinly as possible along the base of a moveable Pyrex boat. This could be positioned, using a magnet and soft iron bar encased in the boat handle, directly below one of the G.-M. counters. This arrangement and procedure enabled the requirement

[20] L. Rowley, G. Webb, J. M. Winfield and A. McCulloch, *Appl. Catal.*, 1989, **52**, 69.
[21] Vogel, A. I. *Textbook of Practical Organic Chemistry'*, 4th ed., Longman, London, **1978**, 383.

for an infinitely thin layer of solid to be located directly below one counter to be approximately fulfilled. The solid and the cell were thoroughly outgassed, then a measured pressure of [^{36}Cl]-labelled anhydrous HCl or Bu^{t}Cl was expanded into the cell from a calibrated, gas-handling manifold. The cell was isolated from the remainder of the vacuum manifold and was allowed to equilibrate for 15 min. Counts from each G.-M. counter were recorded simultaneously on two scaler-timers for 500 s. The vapour was removed from the cell and the sequence of admission of gas, equilibration and counting, repeated. Usually eight or nine aliquots were used for each experiment. After removal of the last aliquot, the counts were recorded from both counters. The cell was left evacuated over a period of at least 18 h, usually with intermittent pumping before additional counts were recorded. Background counts were obtained before and after each experiment. Counters were replaced when contamination became significant. Prior to using a new batch of labelled HCl or Bu^{t}Cl, the intercalibration factor of the two counters was re-determined. Details of the intercalibration counting procedure are given elsewhere.[17]

3. Results and discussion

3.1 FTIR spectroscopy

3.1.1 Pyridine adsorption. Pyridine (py) is commonly used as probe molecule for the infrared characterisation of the acidity of particulate solids. Discrimination among different types of acid, for example Lewis and Brønsted acids, is in principle, possible and determination of their concentrations at the accessible surface can often be achieved. The ν_{8a} mode of the coordinated molecule, located in the 1590-1630 cm^{-1} range, is indicative of the strength of the Lewis acidic sites, the higher the position, the higher is the acidic strength. The relative strengths of the acid sites are commonly determined by thermodesorption of coordinated py. The ν_{19b} vibrational mode (1440-1460 cm^{-1}) is indicative of the number of acid sites; the integrated intensity of the band is proportional to the surface density of sites *via* the molar absorption coefficient. The occurrence of strong Brønsted acid sites is indicated by the presence of bands assigned to protonated pyridine for $\nu > 1630$ cm^{-1} and more specifically in the 1540-1560 cm^{-1} range.

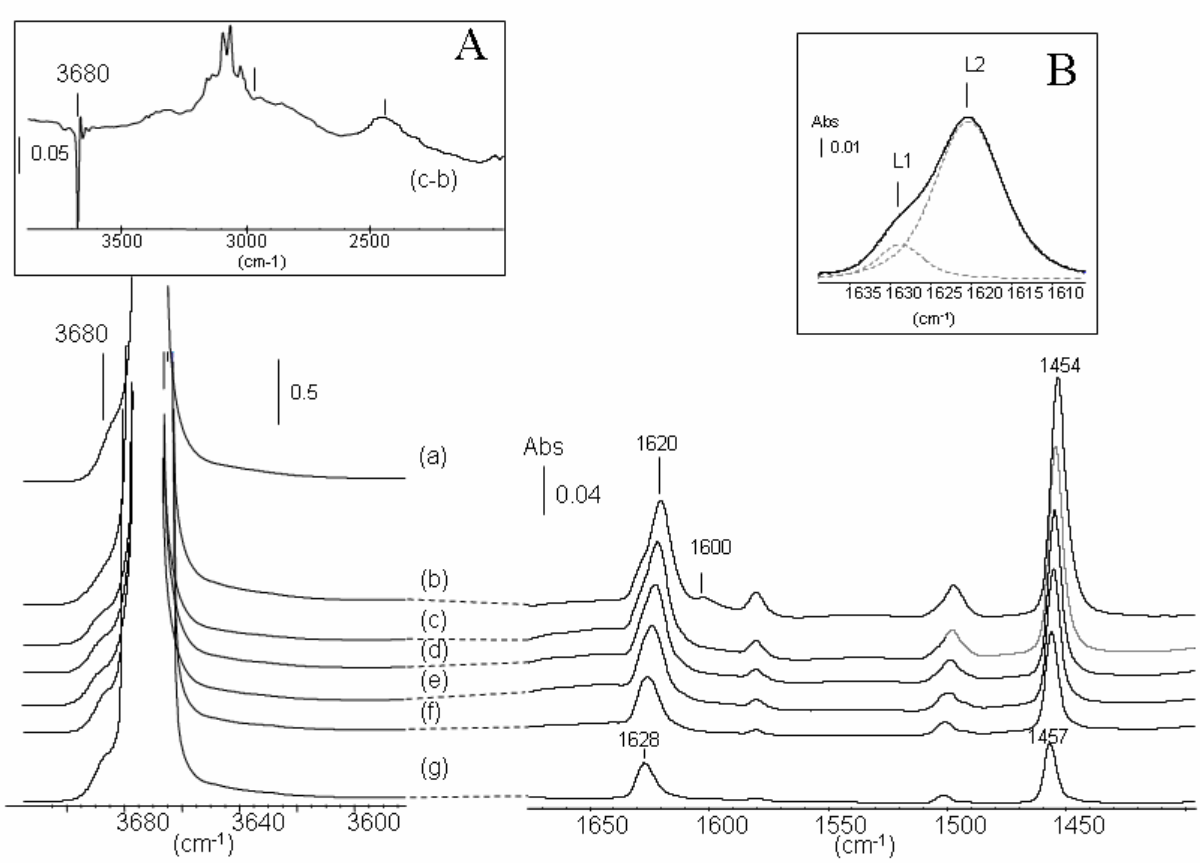

Fig. 1 IR spectra of β-$AlF_{2.6}(OH)_{0.4}$ after activation at 573K before (a) and after introduction of an equilibrium pressure (133 Pa) of pyridine (b-g) .(b) evacuation at room temperature under vacuum and thermodesorption at (c) 323, (d) 423, (e) 473, (f) 523 and (g) 573 K. Inset A: difference IR spectra after introduction of an equilibrium pressure (133 Pa) of pyridine followed by evacuation at r.t. Insert B: deconvolution (dotted lines) of the ν_{8a} vibrational mode (at room temperature).

Spectra of the activated sample present a main band at 3665 cm^{-1} and a shoulder at *ca.* 3680 cm^{-1} (Fig. 1-a). This latter is strongly affected by pyridine adsorption followed by an evacuation at room temperature (Fig. 1-b) but is partially restored after evacuation at 323 K (Fig. 1-c). No band ascribed to pyridinium species has been detected, but its absence does not mean that Brønsted acidity is absent, since protonation of pyridine requires strongly acidic OH groups. Subtracted spectrum (c-b) presented inset A indicates that the intensity of the 3680 cm^{-1} band decreases to the expense of two new broad bands centred at about 3000 and 2500 cm^{-1}. In absence of characteristic band of pyridinium species, these latter are assigned to ν(OH) band strongly downward shifted by a hydrogen bond interaction between the OH groups and adsorbed pyridine. The ν_{8a} band at 1600 cm^{-1} observed in the spectrum of the sample outgassed at room temperature (Fig. 1-b) is thus assigned to Py H-bonded species in interaction with Al-OH groups, characterised in the spectrum of freshly activated sample by a ν(OH) band at 3680 cm^{-1}. This result is consistent with the acidic character of this hydroxyl

group, previously reported on the same sample using ammonia as probe molecule. However, due to its small size, such a probe does not ascertain only the presence of surface OH groups but also can enter cavities. The occurrence of accessible surface OH groups has been therefore checked by the use of a bulkier molecule, lutidine (2,6-dimethylpyridine), which is more sensitive to the weak Brønsted acid due to its higher basicity .[22,23] The results will be presented in the next section.

The evolution of the vibrational modes of coordinated pyridine on β-$AlF_{2.6}(OH)_{0.4}$ (previously activated at 573 K) during thermodesorption is shown in Fig. 1 (spectra b to g). The bands at 1580 and 1500 cm^{-1} are not specific to a given adsorption mode. On the contrary, the ν_{8a} vibrational mode, diagnostic for Lewis acidity, gives rise to a weak band at 1600 cm^{-1} and an intense envelope at higher wavenumber, for which two components can be distinguished. The band at lower frequencies is due to H-bonded py species, as confirmed by the spectral position and by the low stability to thermodesorption. As presented in the inset of Fig. 1, deconvolution of the high wavenumber ν_{8a} envelope leads to two features, at 1628 cm^{-1} (L1) and 1620 cm^{-1} (L2). Their positions indicate the relative strengths of the sites they represent, the higher (L1) being associated with a stronger Lewis acidity. Thermodesorption confirms this point: spectra recorded after outgassing from room temperature to 573 K show that the intensity of the component situated at lower wavenumber is affected by the desorption process whereas this is not the case for the component situated at 1628 cm^{-1}. The adsorbed py molecules associated with the higher wavenumber are the more stable toward thermal desorption, which indicates a stronger interaction with the coordination site, *i.e.* a greater acidity as compared with those generating the L2 component. This is highlighted by the evolution of the integrated areas of both ν_{8a} components during the thermodesorption (Fig. 2 left). The higher wavenumber component is almost insensitive to the temperature (only small variations due to the decrease of the lateral interaction between adsorbed species with the surface concentration can be detected), whereas the lower one decreases progressively.

In addition, the position of the L2 component shifts from 1620 to 1623 cm^{-1} during the thermodesorption. This shift is commonly observed during py adsorption experiments and is assigned either to the heterogeneity of the Lewis acid sites or to an electronic effect induced by pyridine adsorption.[1] As shown below, this problem can be resolved by the use of different probe molecules.

[22] Payen, E.; Grimblot, J.; Lavalley, J.C.; Daturi, M.; Maugé, F. Application of Vibrational Spectroscopy in the Characterization of Oxides and Sulfides Catalysts, in "*Handbook of Vibrational Spectroscopy*", *Vol. 4*, Ed. J.M. Chalmers and P.R. Griffith, Wiley, **2002**.

[23] Morterra, C. ; Cerrato, G. ; Meligrana, G. *Langmuir*. **2001**, *17*, 7053.

In the case of conventionally prepared β-AlF_3, Vimont *et al*[3] found one band at 1620 cm^{-1}, which progressively shifts up to 1627 cm^{-1} at 573 K. The higher component was assumed to be present also at room temperature but was masked by the more intense component. In the present case, the higher component (1628 cm^{-1}) of the py adduct is already visible in the band envelope recorded at room temperature, being partially hidden only by a larger fraction of Lewis sites related to the L2 component (1620 cm^{-1}). The larger surface area exhibited by β-$AlF_{2.6}(OH)_{0.4}$ as compared with conventionally prepared β-AlF_3 enables such sites to be detected. Additionally, the wavenumber of the L1 component (1628 cm^{-1}) has not been reported previously for a solid acid.[24] The assignment of such a band is not trivial. Morterra *et al*[2] reported, for an aluminium hydroxyfluoride series, one band at 1620 cm^{-1}, which was ascribed to py coordinated at coordinatively unsaturated Al^{3+} ions in a tetrahedral environment. From computational studies, Wander *et al.*[25,26] have shown that four-fold coordinated aluminium atoms are not stable and recombine to give five-fold coordinated aluminium sites. A similar situation is assumed to occur on the β-$AlF_{2.6}(OH)_{0.4}$ surface. Additionally, Wander *et al.* have shown the occurrence of two different terminations on the (100) surface. Two different five-fold coordinated Al^{III} geometries are therefore predicted and should give rise to different Lewis acidities depending on the Al^{3+} electronic state and the accessibility of these centres. Generally, it is accepted that the lower is the Al^{3+} coordination, the stronger the Lewis acidity. Conversely, for alumina, it has been proposed that some of the five-fold coordinated Al^{3+} was more acidic than a four-fold one.[27] Such a point of view highlights the importance of the accessibility of the Lewis centre, as well as the necessity to undertake deep and multitechnique investigations to ascertain the origin and the strength of a surface site.

The number of coordinated pyridine can be estimated from the integrated intensity of the ν_{19b} band, using a molar adsorption coefficient value of 1.8 cm μmol^{-1}. The number of L2 coordinated pyridine has been determined considering the py spectra recorded in the 323 K - 573 K temperature range. Since only L2 py coordinated species are sensitive to the thermodesorption procedure in the 293 – 573 K, the absorption coefficient of the ν_{8a} band of the L2 species can be determined by plotting the integrated intensity of the ν_{8a} band at 1620

[24] Busca, G. *Chem. Rev*. **2007**, *107*, 11.
[25] Wander, A.; Bailey, C. L.; Searle, B. G.; Mukhopadhyay , S.; Harrison, N.M. *Phys. Chem. Chem. Phys*. **2005**, *7*, 3989.
[26] Wander, A.; Bailey, C. L.; Mukhopadhyay, S.; Searle, B. G.; Harrison, N. M. *J. Mater. Chem*. **2006**, *16*, 1906.
[27] Digne, M. ; Sautet, P. ; Raybaud, P. ; Euzen, P. ; Toulhoat, H. *Journal of Catalysis.* **2004**, *226*, 54.

cm^{-1} versus that of the ν_{19b} band (Fig. 2, right part). The straight line indicates that the molar absorption coefficient of the ν_{8a} band is nearly constant whatever the temperature imposed. The slope of the line is equal to 1 showing that the molar adsorption coefficients of the ν_{8a} and ν_{19b} band of pyL1 species are the same. From the intensity of these bands, we deduced that the total number of py coordinate species at room temperature is about 1.45 per nm^2 and that of L2 species about 1.2 entities per nm^2. This result shows that the strong Lewis acid sites responsible for the pyL1 species formation (1628 cm^{-1}) are much less abundant that the weaker ones responsible for the pyL2 adduct. We should stress that a position for the ν_{8a} vibration mode such as that found for the L1 component (1628 cm^{-1}) of adsorbed py has never been detected before on solids, to our knowledge, highlighting the occurrence of very strong Lewis acid sites on the materials investigated during the present study.

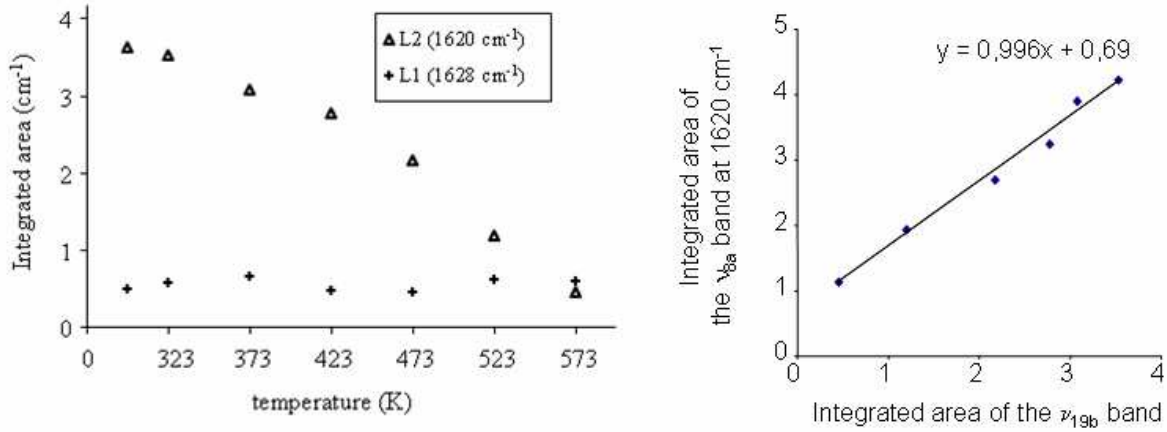

Fig. 2 Integrated areas of the different components of the ν_{8a} (1620-1628 cm^{-1}) vibrational mode of coordinated pyridine during the thermodesorption (left side). Integrated area of the ν_{8a} band of coordinated pyL2 species (1620 cm^{-1}) vs. the integrated area of the ν_{19b} band of coordinated py species (right side).

3.1.2 Lutidine adsorption. The IR spectrum of adsorbed lutidine on β-$AlF_{2.6}(OH)_{0.4}$ displayed in Fig. 3, shows three types of species, physisorbed (1580 cm^{-1} band), coordinated (ν_{8a} at ~1615 cm^{-1} and ν_{8b} at 1590 cm^{-1}) and lutidinium species (ν_{8a} at 1652 cm^{-1} and ν_{8b} at ~1630 cm^{-1}). The formation of the latter indicates the presence of surface Brønsted acid sites. In agreement with this finding, subtracted spectra in the 3000-3800 cm^{-1} range show a decrease of the 3680 cm^{-1} band intensity (Fig 3. inset). According to the data reported by Oliviero *et al*[28], the wavenumber detected for lutidinium species (ν_{8a} mode) accounts for medium Brønsted acidic sites. Despite the steric hindrance induced by the methyl groups of

[28] Oliviero, L.; Vimont, A.; Lavalley, J-C.; Sarria, F-R.; Gaillard, M.; Maugé, F. *Phys Chem Chem Phys*. **2005**, *7*, 1861.

lutidine, it appears that accessible acidic OH groups are present at the surface of β-$AlF_{2.6}(OH)_{0.4}$. The steric hindrance induced by the two methyl groups results in a weaker Lewis complex.[23] This is confirmed by the IR spectra obtained after thermodesorption where the feature arising from the Lewis adduct decreases as a result of the annealing treatment.

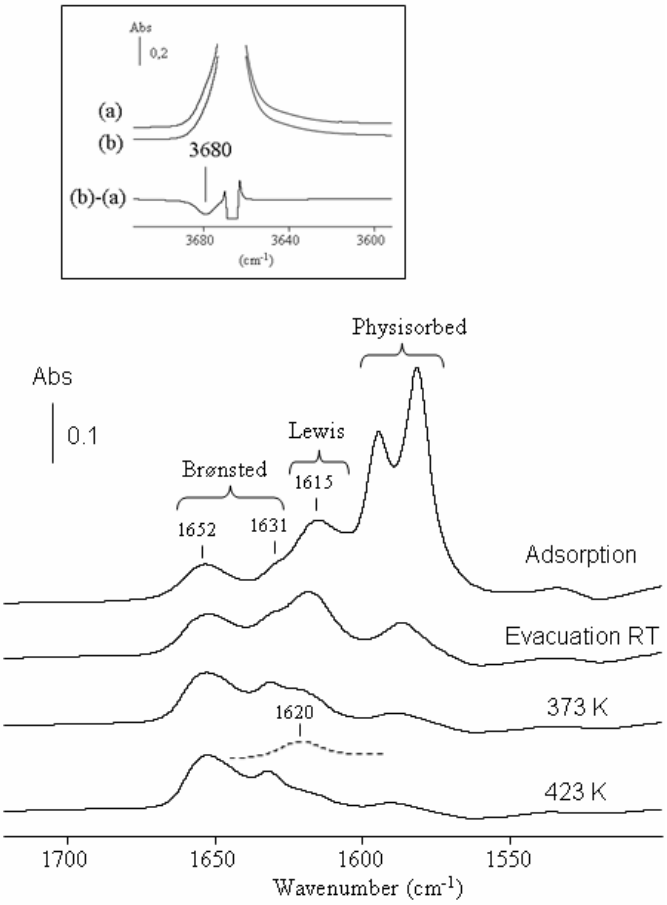

Fig. 3 Difference IR spectra of coordinated lutidine on β-$AlF_{2.6}(OH)_{0.4}$ after adsorption of 133 Pa at equilibrium pressure, followed by desorption under vacuum at room temperature and 423 K. Inset: spectra in the ν(OH) region of the sample activated at 573 K (a) and after adsorption of lutidine (b). The dotted curve is the difference curve between desorption obtained at 373 and 473 K.

The use of 2.6-dimethylpyridine can yield additional information about surface Lewis acidity. In the spectrum recorded under an equilibrium pressure of lutidine, the ν_{8a} vibrational mode at *ca.* 1615 cm^{-1} is indicative of strong Lewis acidity. After outgassing at room temperature, a contribution at *ca.* 1605-1610 cm^{-1} could be present but it is masked by the strong bands at 1615 and 1595 cm^{-1} (this latter is the ν_{8b} band of coordinated species). These features can be related to medium Lewis acid sites. Additionally, some few Lewis acid sites characterized by a band at 1620 cm^{-1}, have been identified by subtraction between the thermodesorption curves performed at 373 and 423 K. For comparison, the strongest Lewis acidic sites displayed by γ-

alumina have been identified through a ν_{8a} band at 1616-1618 cm^{-1} [23,28] and assigned to tetrahedral Al^{3+} coordinatively unsaturated sites.

Lutidine and pyridine are very strong bases and consequently not very sensitive to the heterogeneity of the Lewis acid sites. Pyridine adsorption does not indicate the presence of strong Brønsted sites, but clearly reveals two types of Lewis acid sites. By contrast, lutidine adsorption gives rise to protonated species but hardly detect the Lewis acidity of the sample. In order to clarify these results we have completed the study using CO as probe molecule, a weaker base more sensitive to the heterogeneity and to the strength of the Lewis and Brønsted acid sites.

3.1.3 CO adsorption. In addition to the problem of surface Brønsted acidity characterization, the py adsorption experiments left open the question of the origin of the 1620 cm^{-1} band shift, which could be due either to the heterogeneity of the Lewis acid sites or to the electronic effect induced by py adsorption. Therefore, CO adsorption performed at low temperature (100 K) has been used to get more insight into the acidic properties of β-$AlF_{2.6}(OH)_{0.4}$. This probe molecule is smaller and less basic than pyridine or lutidine, therefore it allows discrimination among Lewis acid sites and enables the detection of Brønsted acid sites presenting various strengths and different accessibility. In a general way, CO addition at 100 K leads to the emergence of three regions that are due to ν(CO), (i) the 2235 – 2180 cm^{-1} region, arising from Lewis acid sites, (ii) the 2180 – 2150 cm^{-1} region, arising from Brønsted acid sites but also weak Lewis acid sites, and (iii) the region < 2150 cm^{-1} due to physisorbed species.[29] The ν(CO) position is a function of acid strength, the higher the wavenumber, the stronger is the acidity. A correlation between the ν(OH) and ν(CO) regions is required to define the nature of the CO interaction, for example *via* coordination or *via* H bonding with hydroxyl groups, to distinguish Brønsted acidity from weak Lewis acidity in the 2150-2180 cm^{-1} range.

Spectra of an activated sample on which successive doses of CO have been adsorbed at 100 K are displayed in Fig. 4. Particular sites present at very low concentrations can be revealed using very small CO doses. Indeed, at low coverage, weak bands are detected in the range 2220-2235 cm^{-1}, which at high coverage give rise to a very weak band located at 2235 cm^{-1} and to a medium band centred at 2215 cm^{-1} (see the deconvolutions in Fig. 4). Simultaneously to the appearance of three low frequency components at *ca.* 2200, 2185 and

[29] Hadjiivanov, K. I.; Vayssilov, G. N. *Adv. Catal*. **2002**, *47*, 307.

2175 cm^{-1}, a band at 3525 cm^{-1} ascribed to perturbed OH groups begins to appear (inset Fig. 4). Finally, at higher coverage, a band at 2166 cm^{-1} can be distinguished as a shoulder.

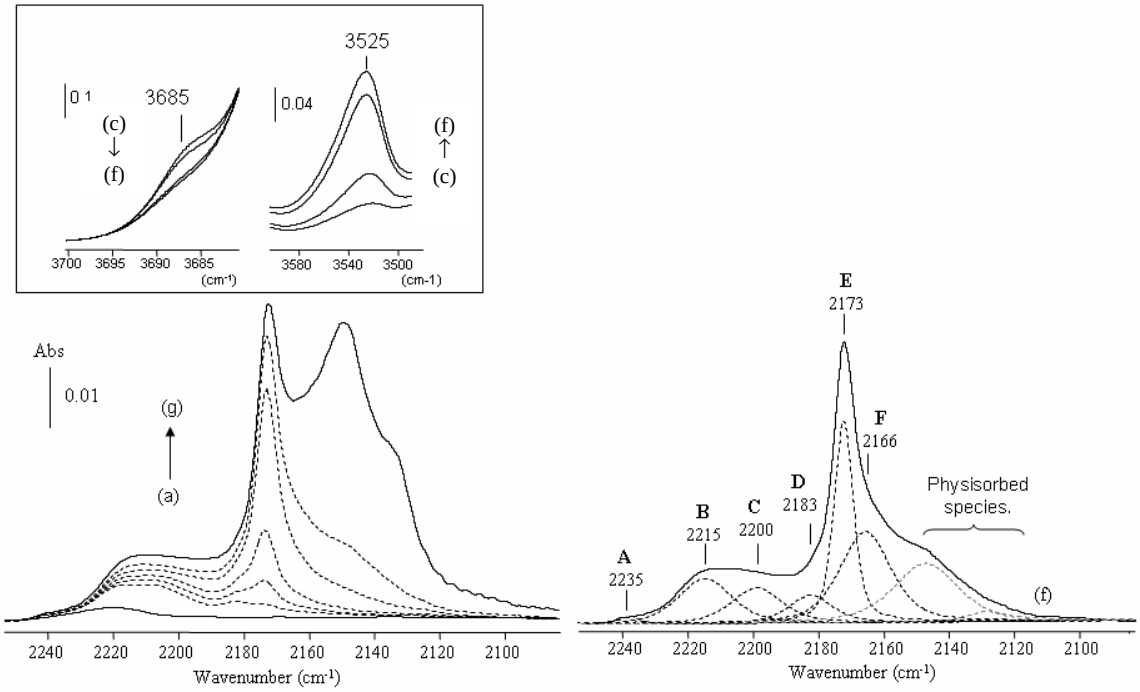

Fig. 4 Left: IR spectra recorded at 100 K after introduction of increasing CO doses at 100 K: 10 µmol g^{-1} (a), 44, 71, 88, 130, 300 µmol g^{-1} (b to f, respectively) then an equilibrium pressure (665 Pa) (g). Right: deconvolution of the ν(CO) band envelope on the spectrum f. Inset: spectral region of the perturbed ν(OH) bands.

Therefore, CO adsorption leads to the occurrence of six types of sites with the following assignments. Site A is a very strong Lewis acid site characterized by a very weak ν(CO) near 2235cm^{-1} (Δν(CO)A ~ 92 cm^{-1}). Site B is a strong Lewis acid site initially identified by a band at 2220 cm^{-1} and progressively shifted to 2215 cm^{-1} for high CO coverage (Δν(CO)B ~ 77-72 cm^{-1}), which indicates that these sites are not isolated, since the ν(CO) shift is due to the inductive effect of the CO molecules: CO adsorption decreases the strength of the neighbouring Lewis centres. Site C is a medium strength Lewis acid site characterized by a band at 2200 cm^{-1} (Δν(CO)C ~ 57 cm^{-1}). Site D is a weak Lewis acid site detected at 2183 cm^{-1} (Δν(CO)D ~ 40 cm^{-1}). Site E identified by ν(CO) at 2173 cm^{-1} (Δν(CO)E ~ 30 cm^{-1}) is due to a Brønsted acid site, since the ν(CO) band intensity concomitantly increases with that of the perturbed ν(OH) band at 3525 cm^{-1} (Fig. 4 inset). The emergence of the perturbed ν(OH) is related to the disappearance of the ν(OH) at 3685 cm^{-1}, as already indicated from lutidine and ammonia[19] experiments. Finally, the assignment of the sites F characterized by a ν(CO) band at 2166 cm^{-1} (Δν(CO)F ~ 23 cm^{-1}) is potentially ambiguous, since bands in this

region may arise from either Lewis or Brønsted acidity. Successive difference spectra clearly show that the emergence of the 2166 cm^{-1} band is not concomitant with the appearance of a perturbed ν(OH) band (Fig.5, spectrum f-e) revealing that the site F is due to a weak Lewis acid site. Table 1 summarizes the results from CO adsorption.

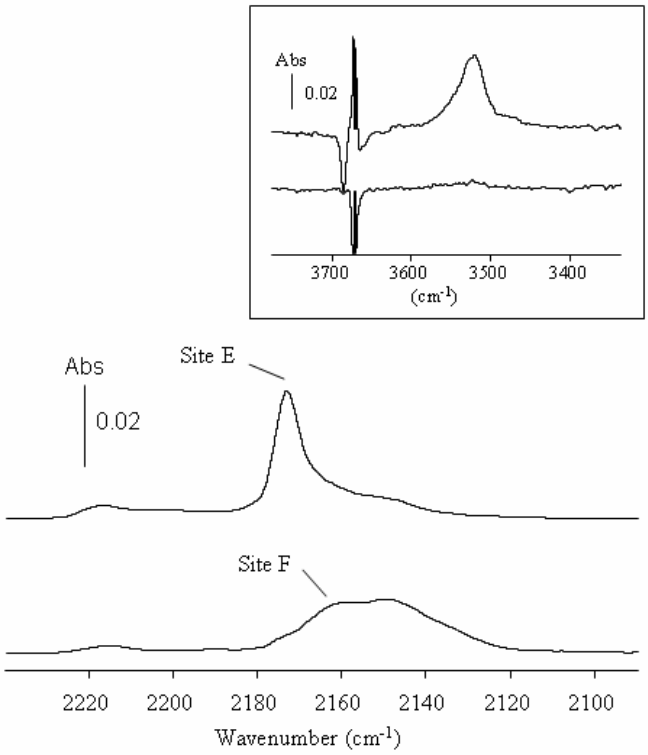

Fig. 5 Successive IR difference spectra of activated β-$AlF_{2.6}(OH)_{0.4}$ after CO adsorption. Inset: corresponding OH region. Spectra d, e and f correspond to those presented in Fig. 4.

Site label	ν(CO) / cm^{-1}	Assignments[a]
A	2235	Very strong LAS
B	2220-2215	Strong LAS
C	2200	Medium LAS
D	2183	Weak LAS
E	2173	Medium BAS
F	2166	Very weak LAS

Table 1. Site labels, ν(CO) bands and corresponding assignments. [a] LAS and BAS are Lewis and Brønsted Acid Site, respectively.

For Brønsted acid sites it is well established that the acid strength acidity can be evaluated from the shift of the ν(OH) vibration perturbed by CO adsorption. The Δν(OH) shift here equals 160 cm^{-1} and corresponds to medium Brønsted acidity. This medium acid strength could explain the discrepancy between the results obtained after lutidine and after pyridine desorption experiments: the acid strength of Al-OH group is strong enough to protonate lutidine but not pyridine,.. In relation with the present result, it has been shown that γ-alumina presents some few OH groups characterized by a Δν(OH) shift e of 155 cm^{-1} after CO adsorption at 100K, which generates lutidinium species but not pyridinium species .[28] It is worthwhile noticing that the Full Width at Half Maximum of the ν(CO) band arising from Brønsted-type adducts appears very small (FWHM ~ 7 cm^{-1}) as compared with the Lewis-type adducts (FWHM ~ 20 cm^{-1}). This can be ascribed to the occurrence of homogeneous Brønsted surface sites having very high symmetry. Such a feature is particularly interesting when the structural OH groups are considered. Bridged hydroxyl groups are localized in peculiar crystallographic sites. The occurrence of homogeneous Brønsted surface sites can be related to the crystal structure, the surface reflecting the bulk periodicity.

3.1.4 Correlation between pyridine and CO adsorptions: a co-adsorption study. The use of CO reveals the range of Lewis acid sites through the detection of five types of Lewis adducts. The origin of the 1620 cm^{-1} band shift of coordinated pyridine mentioned above is therefore due to the heterogeneity of the Lewis acidic sites. However, the correspondence between the various Lewis acid sites found by the two probe molecules is still unknown, especially considering that CO permits a finer mapping of the surface, while pyridine gives a less detailed view of the sites, even modifying the coordination neighbourhoods. To resolve any possible correspondence, Morterra *et* al[30] were the first to use pyridine and CO co-adsorption on η-alumina. In the present study, we have applied this technique on the fluorinated sample.

Pyridine was first introduced and then evacuated at increasing temperature, 323, 423 and 523 K. After each step, a dose of CO was introduced at 100 K and the sample re-evacuated. As shown previously, at these temperatures, only the lowest component of the ν_{8a} mode (1620-1623 cm^{-1}) of the coordinated pyridine is affected. Fig. 6 presents the corresponding IR spectra of co-adsorbed pyridine and CO molecules. After thermodesorption at 323 K (Fig. 6-

[30] Morterra, C.; Coluccia, S.; Garrone, E.; Ghiotti, G. J. Chem. Soc., Faraday Trans. 1. **1979**, *75*, 289.

a), the addition of CO does not show any band located at $\nu > 2180$ cm^{-1}, corresponding to the strongest Lewis acid sites. However, two components related to chemisorbed species can be distinguished between 2155 and 2170 cm^{-1}. These bands are related to the weakest Lewis sites (site F) and the Brønsted acid sites (site E), respectively. During the thermodesorption process, these bands are progressively shifted to higher wavenumber underlining the electronic effect induced by pyridine adsorption. Moreover, pyridine chemisorption is a strongly exothermic process which can produce a perturbation of the original sites probed and, to some extent, a surface reconstruction.

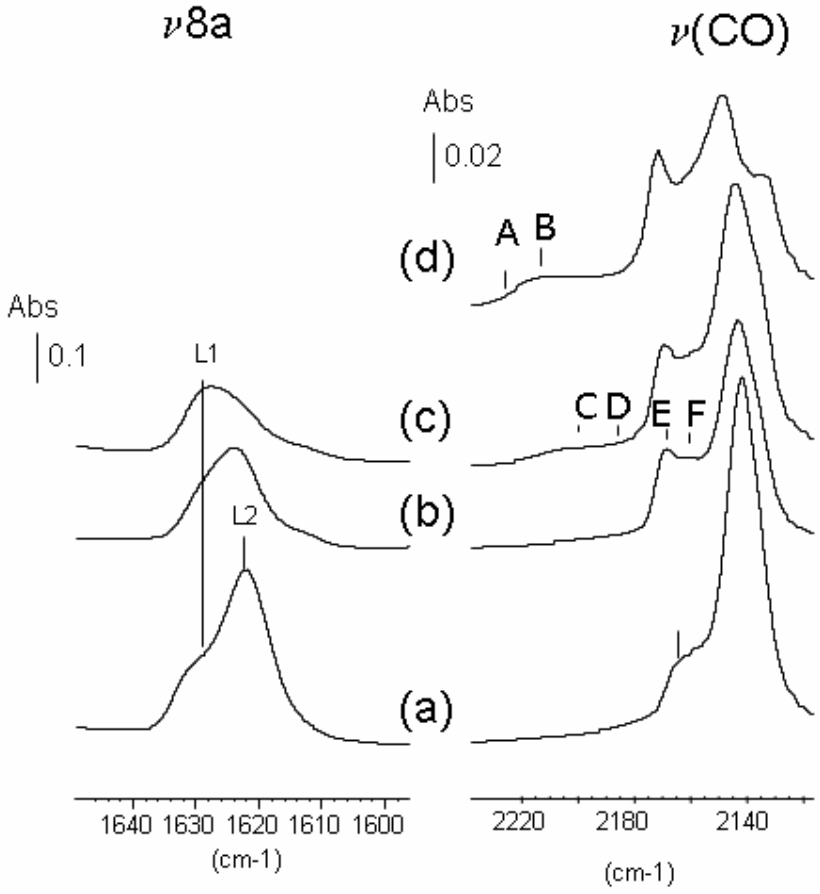

Fig. 6 Left: IR spectra of adsorbed pyridine followed by desorption under vacuum at (a) 323, (b) 423 and (c) 523 K. Right: fitted IR spectra of adsorbed CO after the corresponding successive pyridine desorption steps. Spectrum d corresponds to the ν(CO) range of sample without pyridine treatment.

Thermodesorption at highest temperatures (Fig. 6, spectra b and c) led first to an increase of the E and F components and the appearance of component D. Thereafter, the intensity of D increases and site C appears with a quite weak contribution. The remaining low, L2 pyridine feature observed at 523 K (Fig. 6-c) can be correlated with the unreconstructed band of site C. Consequently sites D and C evidenced by CO adsorption can explain the heterogeneity of the

L2 pyridine band envelope. Therefore, it can be suggested that the highest pyridine (L1) component is related to the sites A and B as revealed by CO adsorption, A being very weak.

3.2 [^{36}Cl] Radiotracer study

Experiments carried out using two different samples, which differed in the quantity of water that still remained in the hexagonal channels, indicated the importance of both Lewis and Brønsted activity in β-$AlF_{2.6}(OH)_{0.4}$ and how the presence of residual water can affect its dehydrochlorination ability. The samples differ only in the nature of the post-synthesis treatment (see Experimental) and are designated as $AlF_{2.6}(OH)_{0.4}.xH_2O$ where x is estimated to be *ca.* 0.12, and $AlF_{2.6}(OH)_{0.4}$ obtained after annealing at 573 K for 16h.

3.2.1 The hydrated sample. The interaction at room temperature between anhydrous HCl and the hydrated HTB solid with the general formula $AlF_{2.6}(OH)_{0.4}.xH_2O$ is substantial enough to be detected using pressure changes in a previously evacuated closed system equipped with a Bourdon gauge.

The exact magnitudes of the HCl uptakes differ and depend on the post synthesis treatments and, although this relationship was not explored in detail, it is clear that the uptake of HCl depends on the water content. By analogy with the behaviour found previously for β-AlF_3,[5] direct interactions between HCl and H_2O are likely to be more important at room temperature than those between HCl and HO-Al groups. These initial observations guided the subsequent experiments that involved [^{36}Cl] labelling.

Three experiments with $AlF_{2.6}(OH)_{0.4}.xH_2O$ were carried out; two involve H^{36}Cl, the other [^{36}Cl]-Bu^{t}Cl. In each case a sequential exposure to the solid of a series of H^{36}Cl or [^{36}Cl]-Bu^{t}Cl aliquots is involved, unchanged [^{36}Cl] vapour being removed by distillation *in vacuo* prior to the exposure of the solid to the next aliquot. Relationships between [^{36}Cl] surface counts and additions of H^{36}Cl or [^{36}Cl]- Bu^{t}Cl made are shown in Fig. 7. The mean [^{36}Cl] count detected from the surface when 9 aliquots (2.4 kPa) of anhydrous H^{36}Cl are successively exposed to a thinly-spread sample of $AlF_{2.6}(OH)_{0.4}.xH_2O$ (Fig. 7(a)) is small and, as a result, is not particularly precisely determined. It is possible to conclude however, that there is a strong interaction between H^{36}Cl and β-$AlF_{2.6}(OH)_{0.4}.xH_2O$. The strength and extent of the interaction result in the retention of essentially all H^{36}Cl, which is adsorbed by the solid. For example, in Fig. 7(a) the [^{36}Cl] surface count determined in the presence of the last aliquot of H^{36}Cl added (count 9) is effectively identical to that determined immediately after

removal of $H^{36}Cl$ vapour (count 10). Count 11 was determined 6 days after $H^{36}Cl$ removal, the cell being maintained under vacuum during this period, and is effectively identical to count 10.

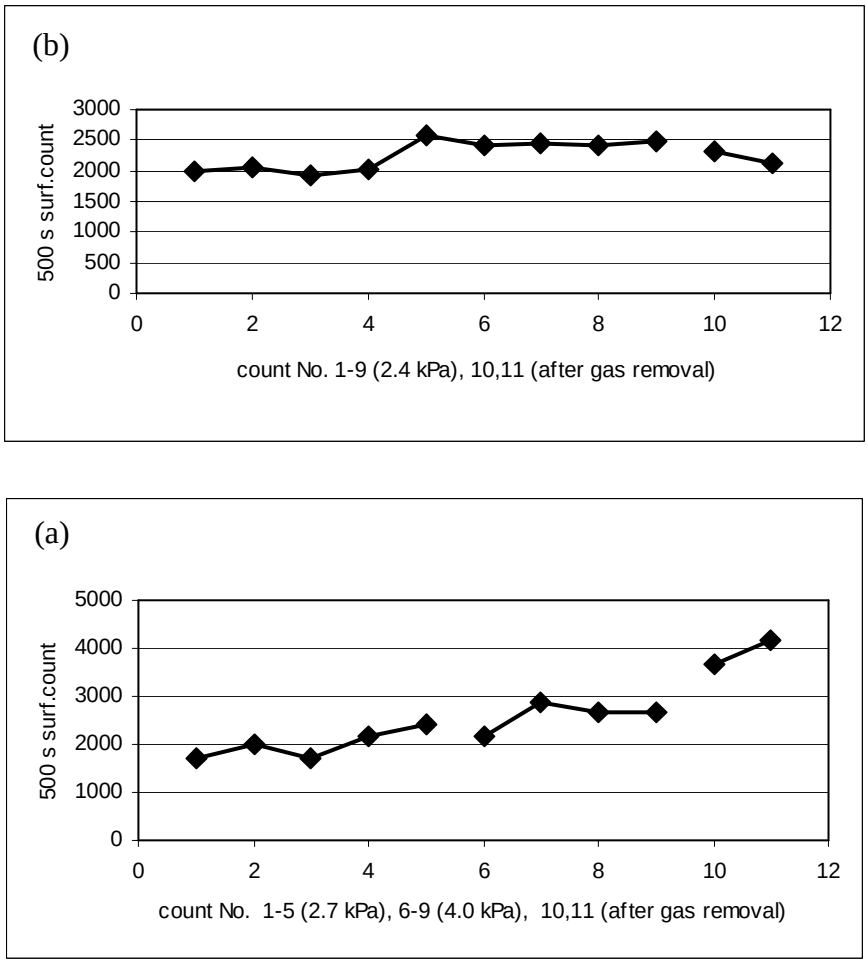

Fig. 7 Surface counts from hydrated β-$AlF_{2.6}(OH)_{0.4}$,xH_2O during exposures to (a) [^{36}Cl]-labelled HCl; relative errors on the individual points are 4.8 – 5.7%; the line break corresponds to the removal of gas; (b) [^{36}Cl]-labelled Bu^{t}Cl; relative errors on the individual points are in the range 6.4 – 10.2%; line breaks correspond to a change in the aliquot pressure from 2.7 to 4.0 kPa then to removal of vapour.

The data in Fig 7(a) are the result of $H^{36}Cl$ exposures that involve relatively small gas pressures. A similar experiment using aliquot gas pressures in the range (4.0 – 6.65 kPa) produced larger surface counts, whose relative errors were 3.0%; the magnitudes of the surface [^{36}Cl] counts were pressure dependent. They increased over the first nine additions but decreased to some extent over the next three. This behaviour is reminiscent of that observed when $H^{36}Cl$ is exposed to β-AlF_3 under similar conditions.[5] By analogy with the latter system, it is suggested that species such as H_2O---HCl could be formed on exposure of HCl on β-$AlF_{2.6}(OH)_{0.4}.xH_2O$. An additional interaction involving Al-OH groups with HCl could be

formulated also. Although the FTIR results using lutidine and CO probes described above indicate Brønsted acidity for Al-OH groups, in the presence of the very strong Brønsted acid, HCl, the interaction is more likely to be one in which HCl behaves as the donor to Al-OH, *i.e.* Cl-H---O(H)-Al. A further possibility is that some replacement of Al-OH groups occurs, according to the process: Al-OH + HCl → Al-Cl + H_2O.[6]

This observed Brønsted activity reflects the potential of the probe species HCl to behave as a strong proton donor. It would be expected that, because of the fluoride environment of these hydroxyl groups, as discussed above, they would exhibit acidic character (*i.e.* behave as proton donors) in most other situations, as has been described above.

Exposure of β-$AlF_{2.6}(OH)_{0.4}.xH_2O$ to a series of [^{36}Cl]-Bu^{t}Cl aliquots at room temperature results in the deposition of a [^{36}Cl]-labelled species on the surface, presumably H^{36}Cl. There is a presumption that dehydrochlorination of Bu^{t}Cl has occurred, although there was no evidence from FTIR spectroscopic examination of the vapour above the solid for any reaction, including hydrolysis of Bu^{t}Cl. Under identical conditions, HCl is evolved slowly to the vapour phase above β-AlF_3,[5] while Bu^{t}Cl is consumed rapidly in the vapour above HS-AlF_3 yielding a mixture of HCl and hydrocarbon species.[18] It appears that dehydrochlorination does occur but only to a small extent and that any HCl formed is retained by the solid. In the [^{36}Cl] experiment shown in Fig. 7(b), the surface count increases to a small extent over the series of aliquot additions 1 to 9. There is however, a marked increase on pumping the solid after removal of the last aliquot of *t*-Bu^{36}Cl. Count 10 was made immediately after removal of weakly adsorbed H^{36}Cl under static vacuum and count 11 was determined on the following day. The behaviour observed can account for by consideration of an important property of the chlorine-36 isotope. Like all β^- emitting isotopes, chlorine-36 is subject to self-absorption and the emitted radiation will not be detectable by a Geiger-Müller counting tube, unless the species, H^{36}Cl in this case, is adsorbed at the exterior surface of the solid. Any H^{36}Cl adsorbed at grain boundaries within the solid or, very plausibly, hydrogen bonded to H_2O or Al-OH groups located within the hexagonal channels of β-$AlF_{2.6}(OH)_{0.4}.xH_2O$, will not be detected. It will be detected only if and when it diffuses to the exterior surface, which process is evidently slow. It appears from this experiment that adsorption within the channels is at least as important as at the exterior surface.

3.2.2 The anhydrous sample. The behaviour of β-$AlF_{2.6}(OH)_{0.4}$ towards H^{36}Cl is shown in Fig. 8. The post-synthesis treatment of this sample was designed to remove loosely bound H_2O, including as much as possible of the water originally located in the hexagonal channels,

and therefore differences in its behaviour compared to that of the previous sample might be expected. In this experiment the specific count rate (count min^{-1} $mmol^{-1}$) of the $H^{36}Cl$ used was far higher than in the experiments described above. This enabled the interaction to be described more precisely than before.

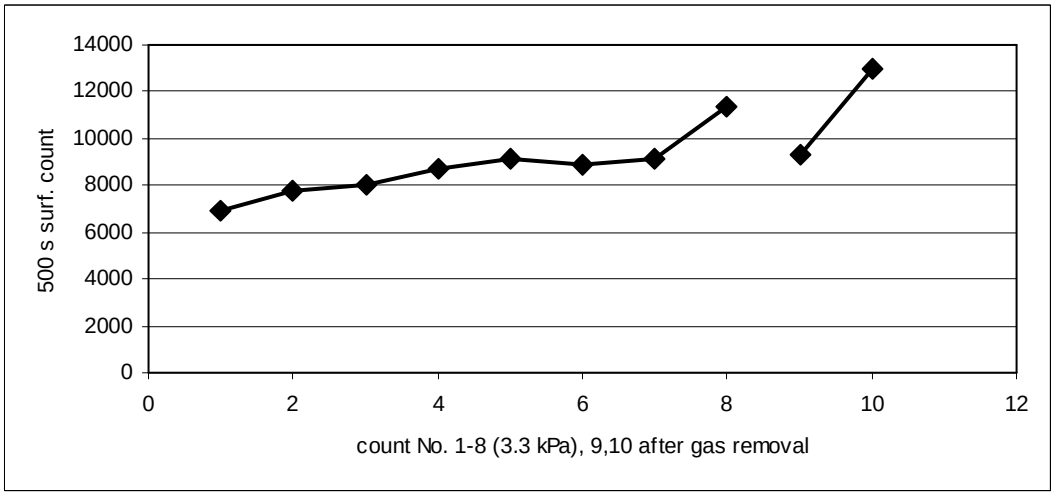

Fig. 8 Surface counts from anhydrous β-$AlF_{2.6}(OH)_{0.4}$ during exposure to $H^{36}Cl$; relative errors on the individual points are in the range 2.5 – 3.9%; the line break corresponds to the removal of gas.

An increase in the surface [^{36}Cl] count is observed with increasing number of $H^{36}Cl$ aliquots, although a plateau region extending over counts 4 - 7 is discernable. The average count in this region is 8987 $(500\ s)^{-1}$ determined with a relative error of ± 2.4%. Thereafter the count increases (count 8), then suffers a small decrease on removal of the last aliquot (count 9) and finally increases to a value greater than count 8 after a period of 24 h *in vacuo*. The observed behaviour indicates that the interaction of $H^{36}Cl$ is progressive with increasing number of aliquots used and that both surface and bulk are involved. In this sample, the interaction apparently involves Al-OH groups both located at the exterior surface and in the hexagonal channels. The evidence for this is similar from the experiment described above. However, the counts are larger enabling them to be determined more precisely and the experiment uses $H^{36}Cl$ directly. As proposed above, the behaviour observed is best rationalised by migration of $H^{36}Cl$ during the storage period *in vacuo*, from hexagonal channels in the HTB-structure, where [^{36}Cl] radiation cannot be detected using Geiger-Müller counting because of self absorption of [^{36}Cl], to sites on the exterior surface where it is detectable.

Contrary to expectation, the activity of β-$AlF_{2.6}(OH)_{0.4}$ with respect to room temperature dehydrochlorination is very low and precise [^{36}Cl] surface counts were not obtained. This highlights the apparent role of H_2O in promoting the room temperature dehydrochlorination

of Bu^tCl. However, a Lewis site is required for the adsorption of Bu^tCl. The HCl liberated by the dehydrochlorination is assumed to migrate to nearby water molecules, where it will be strongly adsorbed. This process evidently drives the dehydrochlorination and H_2O can be considered to be a promoter in this case.

3.3 Comparisons with β-AlF_3 and related aluminium fluorides

Both parts of this study, the detailed mapping of the surface structure by FTIR and the investigation of chemical reactivity using the [^{36}Cl] radiotracer, focus attention on acid-base interactions and reactions. The important elements are coordinatively unsaturated Al^{3+} sites that are responsible for the Lewis acidity, hydroxyl groups present as an integral part of the structure, accessible hydroxyl groups that display Brønsted activity, behaving as Brønsted acids towards lutidine and CO, and probably as bases towards anhydrous HCl. Of importance in addition is the water, originally located in the hexagonal channels of the HTB structure, where in company with the $[NH_4]^+$ cation,[19] it acts as a stabiliser for the metastable β-form. The incomplete removal of H_2O provides a second possible type of Brønsted basic site.
The pertinent spectroscopic data obtained for the β-$AlF_{2.6}(OH)_{0.4}$ surface are summarised in Table 2.

Probe IR bands	Lutidine ν_{8a} ν(cc) cm^{-1}	Pyridine ν_{8a} cm^{-1}	CO ν(CO) cm^{-1}
Bands due to Lewis activity	1615-1620 ~ 1610	1628 1620	2235 2220-2215 2200 2183 2166
Bands due to Brønsted activity	1652, 1631	---	2173 Δν(OH)=155
Proton affinity / kJ mol^{-1} [a]	963	912	598

Table 2. Characterization of the Lewis/Brønsted acidic sites displayed by the β-$AlF_{2.6}(OH)_{0.4}$ surface. [a] Proton affinity of the probe molecule.[22]

What can be designated as strong surface Lewis acidity, by making comparisons with similar work that involves aluminas,[1,24,27,28] is evident from the following spectroscopic features: (i) adsorbed lutidine that has ν_{8a} ~1620 cm^{-1}, (ii) adsorbed pyridine with ν_{8a} ~1628 cm^{-1}, (iii)

adsorbed CO with $\nu_{(CO)}$ ~2235-2210 cm^{-1}. For comparison, highly coordinatively unsaturated Al^{3+} sites on γ-alumina are characterized by adsorbed lutidine with ν_{8a} ~1618 cm^{-1} and adsorbed pyridine with ν_{8a} ~1625 cm^{-1}. Small but significant differences in the band positions found among the adsorbed species can be related to the inductive effect of fluoride ions as already pointed out for aluminium hydroxyl fluoride that exhibits the pyrochlore type.[31]

The second factor that has great influence on the Lewis acidity of β-$AlF_{2.6}(OH)_{0.4}$ is the method used for its synthesis; this results in the formation of very small particles.[19] Using a molecular dynamic simulation,[32] it has been shown that highly coordinatively unsaturated Al^{3+} sites occur on nanoparticles (< 3 nm) of cubic α-AlF_3 where surface reconstruction takes place giving rise to strongly under-coordinated Al^{3+} centres located mainly on the edges and corners of the particles. In a similar fashion, the presence of highly coordinatively unsaturated Al^{3+} sites is suggested to account for the strong Lewis acidity displayed by the high surface area, X-ray amorphous HS-AlF_3.[14-16] For example, the unusual properties of the solid have been rationalised by the occurrence of strong size effect leading to highly unsaturated Al^{3+} characterized by a ν(CO) > 2220 cm^{-1}.[4] Additionally, by comparison with other aluminium fluoride materials, it has been shown that, whatever the composition/structure, the number of strong Lewis acid sites increases with the surface area, *i.e.* with the decrease of the particle size, highlighting the role of surface reconstruction occurring at a nanoscopic scale on the formation of the strongest Lewis acid sites.[33] Such a trend is well evidenced by the behaviour of the β-$AlF_{2.6}(OH)_{0.4}$ surface. The L1 pyridine component situated at 1628 cm^{-1} is already detected at RT whereas in the case of conventionally prepared β-AlF_3,[3] a band at 1627 cm^{-1} is only observed after desorption at 573 K.

A third factor could be correlated with the amount of fluorine saturating the Al^{3+} coordination. The presence of hydroxyl groups as an integral part of the composition, as opposed to being a minor element arising from hydrolysis, is believed to be the main factor responsible for the Lewis heterogeneity of the β-$AlF_{2.6}(OH)_{0.4}$ surface. This heterogeneity is well demonstrated by CO adsorption, leading to the observation of five types of Lewis sites. Other probes lead to similar but not identical results. The use of pyridine leads to two types of Lewis acid sites.

---

[31] Dambournet, D.; Demourgues, A.; Martineau, C.; Durand , E.; Majimel, J.; Vimont, A.; Leclerc, H.; Lavalley, J.-C.; Daturi, M.; Legein, C.; Buzaré, J.-Y.; Fayon, F.; Tressaud, A. *J. Mater. Chem.* **2008**, in press. DOI: 10.1039/B718856K.

[32] Chaudhuri, S.; Chupas, P.; Morgan, B. J.; Madden, P. A.; Grey, C. P. *Phys. Chem. Chem. Phys.* **2006**, 8, 5045.

[33] Dambournet, D.; Eltanamy, G.; Vimont, A.; Lavalley, J-C.; Goupil, J-M.; Demourgues, A.; Durand, E.; Majimel, J.; Rudiger, S.; Kemnitz, E.; Winfield, J. M.; Tressaud, A. *Chemistry – A European Journal.* **2008**, *in press.* D.O.I: chem.200701831.

. One important criterion to enable the detection of various strengths of Lewis acid sites is the frequency range displayed by the Lewis-specific vibrational mode. For instance, the range of the ν(CO) shift is much greater than that of the ν_{8a} mode of pyridine (up to 100 [1] *vs* 35 cm^{-1}). This can explain why pyridine is not able to discriminate site A, its intensity being very low.

Previous investigations on aluminium hydroxyfluoride series[2] suggest that the ν(CO) band detected *ca*. 2195 cm^{-1} (equivalent to site C in the present work) arises from "oxidic islands". It can be deduced therefore that the occurrence of OH groups inside the network induces the Lewis heterogeneity observed. The occurrence of various F/OH anionic environments in the vicinity of Al^{III} is revealed by high resolution ^{27}Al NMR spectroscopy.[19] Although this result is obtained from a bulk technique, it can be suggested that such species can be found in an under-coordinated configuration at the surface of the solid.

It seems likely that, in contrast to the behaviour shown by β-AlF_3,[5] interactions between surface hydroxyl groups and HCl are important, in addition to the H_2O --- HCl interactions postulated to occur in β-AlF_3. This is not too surprising, since in β-AlF_3 hydroxyl groups are present solely as a result of trace hydrolysis, whereas in the hydroxyl fluoride examined here they form an integral part of the HTB structure. There is good evidence that adsorption of HCl occurs within the hexagonal channels of the HTB structures as well as at the exterior surface.

It can be concluded from this and related studies that anhydrous HCl can be adsorbed on aluminium oxides, fluorides and hydroxyfluorides in different ways. It is normally dissociatively adsorbed at aluminas,[34,35,36,37,38,39] although associative adsorption is known.. Associative adsorption is the obvious possibility in binary fluorides and their derivatives, either at coordinatively unsaturated Al^{III} sites as proposed for HS-AlF_3[18] or at hydroxylated or hydrated sites, as in the HTB solids β-$AlF_{2.6}(OH)_{0.4}$, β-$AlF_{2.6}(OH)_{0.4}.xH_2O$ and β-AlF_3[5]. However, given the probability that some of the Lewis acid sites in β-$AlF_{2.6}(OH)_{0.4}$ will have mixed F/OH nearest neighbours, dissociative adsorption of HCl also becomes a possibility.

A direct comparison among β-$AlF_{2.6}(OH)_{0.4}$, β-$AlF_{2.6}(OH)_{0.4}$,xH_2O, β-AlF_3 and amorphous HS-AlF_3 with respect to their reactivity in the promotion of Bu^tCl dehydrochlorination, indicates that HS-AlF_3 is the most effective catalyst for the reaction. In part this will be the

[34] Peri, J. B. *J. Phys. Chem.* **1966**, 70, 1482.
[35] Tanaka, M.; Ogasawa, S. *J. Catal*. **1970**, *16*, 157.
[36] Kytökivi, A.; Lindblad, M.; Root, A. *J. Chem. Soc., Faraday Trans*. **1995**, *91*, 941.
[37] Elam, J. W.; Nelson, C. E.; Tolbert, M. A.; George, S. M. *Surf. Sci.* **2000**, *490*, 64.
[38] Alavi, S.; Sorescu, D. C.; Thomson, D. L. *J. Phys. Chem. B*, **2003**, *107*, 186.
[39] McInroy, A. R.; Lundie, D. T.; Winfield, J. M.; Dudman, C. C.; Jones, P.; Parker, S. F.; Lennon, D. *Catal. Today*, **2006**, *114*, 403.

result of its far greater specific surface area. Although, β-$AlF_{2.6}(OH)_{0.4}$ should be regarded as having Lewis acid character on the basis of the FTIR study, it can be argued that it is the strong interaction between H_2O in β-$AlF_{2.6}(OH)_{0.4}.xH_2O$ and liberated HCl that drives the dehydrochlorination reaction in this case rather than any intrinsic strength of the Lewis acid sites.

Conclusion

Analysis of the surface properties of an aluminium hydroxyfluoride exhibiting the HTB type structure has been performed using two complementary methods. At first, adsorption of probe molecules has been detected by FTIR. The use of the several probe molecules enabled to get precise information depending on the spectroscopic molecule characteristics. A Lewis strength heterogeneity has been detected on the outer surface and depends on the frequency range and the basicity displayed by the probe molecule. Pyridine detects two type of Lewis acid sites, the first one denoted L1 is very strong (ν_{8a} py band at 1628 cm^{-1}) but is present in low concentration on the surface (~0.2 sites per nm^2). The second one denoted L2 has a weaker acid strength (ν_{8a} py band at 1620-1623 cm^{-1}) but is much more abundant (about 1.2 sites per nm^2). CO adsorption and pyridine-CO co-adsorption experiments reveals that both L1 and L2 sites are heterogeneous: L1 and L2 sites are related to two different sites each one, site A and site B, identified by ν(CO) bands at 2235 and 2220 cm^{-1} for L1 , site C and site D chracterized by ν(CO) bands at 2200 and 2183 cm^{-1} for L2. CO adsorption reveals also the presence of weaker Lewis acid sites characterized by a ν(CO) band at 2166 cm^{-1}. The Lewis strength heterogeneity has been suggested to partly arise from the occurrence of various F/OH anionic environments as revealed by high field ^{27}Al NMR. However, the origin of the Lewis acidity is not far straightforward and is currently under investigation using *ab initio* calculations. CO and lutidine desorption experiments confirm the presence of surface OH group (ν(OH) at 3680 cm^{-1}), which generate homogeneous Brønsted acid sites with a medium acid strength (Δν(OH) = 160 cm^{-1}, ν(CO) = 2173 cm^{-1}), able to protonate lutidine but not pyridine. Contrarily to other aluminium-based fluorides, β-$AlF_{2.6}(OH)_{0.4}$ displays a Brønsted behaviour whose characteristics depends on the probing methods. HCl which acts as a proton donor reveals that both OH groups located at the surface and in the channels could act as a Brønsted base. Another remarkable point which has been highlighted by the radiotracer study is the promoting effect of water molecule on the dehydrochlorination reaction of $(CH_3)_3CCl$.

Acknowledgement We thank the EU for financial support through the 6th Framework Programme (FUNFLUOS, Contract No. NMP3-CT-2004-5005575).

3.2 Préparation et caractérisation de nano-particules (fluorure-oxyde d'aluminium) à structure type "core-shell"

Publication: *Preparation and characterization of nano-structured Al-based fluoride/oxide core-shell, to be submitted to Inorganic Chemistry.*

Cette étude décrit le comportement thermique de la phase HTB : β-$AlF_{2.6}(OH)_{0.4}$. Les différentes réactions qui s'opèrent lors de traitements thermiques conduisent à une modification texturale et chimique du matériau conduisant à des nanoparticules de type cœur-couronne à base de fluorure et oxyde d'aluminium.

Preparation and characterization of nano-structured Al-based fluoride/oxide core-shell

Damien Dambournet,[#] Alain Demourgues,[#] Charlotte Martineau,[†] Jérôme Majimel,[#] Michael Feist,[+] Christophe Legein,[†] Jean-Yves Buzaré,[‡] Franck Fayon[§,|] and Alain Tressaud[,#]*

[#] Institut de Chimie de la Matière Condensée de Bordeaux-CNRS, Université Bordeaux 1, 87, Avenue du Dr. A. Schweitzer, 33608 Pessac cedex, France

[†] Laboratoire des Oxydes et Fluorures, CNRS UMR 6010, IRIM2F, CNRS FR 2575, Université du Maine, Avenue Olivier Messiaen, 72085 Le Mans Cedex 9, France

[‡] Laboratoire de Physique de l'Etat Condensé, CNRS UMR 6087, IRIM2F, CNRS FR 2575, Université du Maine, Avenue Olivier Messiaen, 72085 Le Mans Cedex 9, France

[+] Institut für Chemie, Humboldt-Universität zu Berlin, Brook-Taylor-Strasse 2, D-12489 Berlin, Germany

[§] Conditions Extrêmes et Matériaux : Haute Température et Irradiation, UPR CNRS 3079, 1D Avenue de la Recherche Scientifique, 45071 Orléans Cedex 2, France. [|] Université d'Orléans, Faculté des Sciences, Avenue du Parc Floral, 45067 Orléans Cedex 2, France

ABSTRACT.
The investigation of the thermal behavior of β-$AlF_{2.6}OH_{0.4}$ compound which adopts the HTB network shows that this structure is stable up to 873 K. As revealed by a detailed analysis combining HRTEM, XRD, FTIR and ^{19}F and ^{27}Al NMR, the sample annealed at 873 K exhibits an unusual core-shell like structure. The shell which is amorphous contains some AlO_6, AlO_5 and AlO_4 species which have been identified and quantifying by ^{27}Al NMR. Contrarily, the core part of the material is crystallized and has been identified as a phase closely related to the hydroxyl free compound β-AlF_3 in agreement with the dehydroxylation process. The annealing treatment lowers the Lewis acidity but strong Brønsted acid sites have been created as evidenced by pyridine adsorption. These strong Brønsted sites arise from the reaction between water and strongly under-coordinated species formed upon annealing.

KEYWORDS. Thermal stability, Aluminum hydroxyfluoride, HTB, core-shell nanoparticles, ^{19}F and high field ^{27}Al solid state NMR, Lewis/Brønsted acidities.

Introduction.

The numerous studies which have been devoted to aluminum-based fluoride and hydroxyfluoride compounds account for the interest on such materials. Investigations on these materials are mainly related to the development of new synthesis routes,[1,2] catalytic properties[3,4,5] and computational data.[6,7,8] Among the most important criteria to select effective acid catalysts such as surface area, strength, nature or number of acidic sites, the thermal stability of the nanosized solids is a decisive parameter which can be directly correlated to the synthesis route. The number and the nature of trapped molecules by the framework during the synthesis play indeed a key role on the thermal stability of the structure. The metastable form β-AlF_3[9] which exhibits the hexagonal tungsten bronze type structure (HTB) and characterized by channels along the c-axis, clearly illustrates the importance of the synthesis route upon the thermal stability. β-AlF_3 can be prepared in a conventional way by thermal treatment of α-$AlF_3.3H_2O$ or $(NH_4)_3AlF_6$.[10] Prepared from these routes, the final β-AlF_3 collapses into α-AlF_3 and small amounts of alumina at 748-773 K (ex-H_2O) and 973 K (ex-NH_4) , respectively.[9,11] The low thermal stability of the former (ex-hydrate) β-fluoride is ascribed to residual water and OH groups reacting with F^- ions which tend to induce a pyrohydrolysis process. The replacement of Al-F by an Al-O bond leading to the release of HF molecules induces the collapse of the structure. On the contrary, ammonium species are thermally more stable and therefore enable to keep the framework at higher temperature.

The microwave assisted method which has been recently developed to prepare HTB aluminum hydroxyfluoride β-$AlF_{2.6}(OH)_{0.4}$[12] from aluminum nitrate precursor, leads to the presence of both NH_4^+ and H_2O as residual molecules inside the framework. During the microwave hydrothermal process, the nitrate ions are reduced into ammonium species allowing the stabilization of the HTB framework by a template effect. Due to the occurrence of water and ammonium species trapped by the network, the stability of this compound should lie in between the compounds prepared by the two conventional routes. However, the hydroxyl content should induce a different thermal behavior.

This work first investigates the thermal stability of this material. Then, the evolution of the structural features upon annealing treatment before the collapse of the network is investigated. The composition, structural features, size and morphology of the nanoparticles and the acidic properties of the material are further regarded. Such a study has been performed through the use

of several techniques, including X-ray powder diffraction (XRPD), thermogravimetric analysis coupled with mass spectrometry (TGA/MS), high resolution transmission electron microscopy (HRTEM), infrared spectroscopy (FTIR), and ^{19}F and ^{27}Al solid state nuclear magnetic resonance (NMR).

Experimental Section.

1. Preparation of β-$AlF_{2.6}(OH)_{0.4}$. This material was prepared as previously described.[12] A solution containing aluminum nitrate, water and isopropanol as solvents and an aqueous solution of HF (40%), in the following molar proportions [HF]/[Al]=3, was treated by microwave hydrothermal process. The powder, washed under nitrogen with a large amount of ethanol, was outgassed at 573 K under vacuum for 4 hours. The chemical composition was deduced from elemental analysis, FTIR and NMR spectroscopies.

Thermal treatment. The **s**amples were placed in alumina crucibles. The temperature was increased at 10 $K.min^{-1}$ and kept at a defined temperature, up to 923 K, for 4h under vacuum.

2. Characterizations.

X-ray diffraction analysis. Powder diffraction patterns were recorded on a PANalytical X'Pert Pro diffractometer in a Bragg–Brentano geometry (θ-2θ), using graphite-monochromated Cu-Kα radiation ($K_{\alpha 1}$=1.54051Å).

BET measurement. Specific surface areas were measured at 77 K using an ASAP 2000 instrument from Micromeritics. The powdered sample of about 200 mg mass was evacuated overnight at 573 K under 0.1 Pa prior to adsorption.

Transmission electron microscopy. TEM was performed on a TECNAI F20 equipment with a field emissive gun, operating at 200 kV and with a point resolution of 0.24 nm. TEM samples were prepared by dissolving few milligrams of powder in ethanol. The solution was then dipped ten minutes into an ultrasonic bath in order to disagglomerate powder particles. One drop of the solution was finally deposited on a Formvar/carbon copper grid. Finally it could be noted that, in order to have statistically meaningful experiments, many images from several regions of various samples have been recorded and the most characteristic results are presented here.

NMR spectroscopy. Quantitative ^{19}F Hahn echo Magic Angle Spinning (MAS) NMR spectra were acquired on an Avance 300 Bruker spectrometer (B_0 = 7 T), using a 2.5 mm ^{19}F optimised CP MAS probe, operating at a ^{19}F Larmor frequency of 282.2 MHz. The 90° and 180° pulse durations were set to 4 μs (RF field 60 kHz) and 8 μs, respectively, with an inter-pulse delay

equal to one rotor period. The recycle delay was taken to 10 s. The ^{19}F chemical shifts were referenced to $CFCl_3$ at 0 ppm. These spectra were reconstructed using the DMFIT software[13] which allows a full reconstruction of the spectra (including the spinning sidebands) with six adjustable parameters: isotropic chemical shift δ_{iso}, chemical shift anisotropy δ_{aniso}, chemical shift asymmetry parameter η_{CS}, line width, relative line intensity and line shape. In this study, δ_{iso} values, relative line intensities and line widths are the relevant parameters; the other parameters are not discussed at all in the following.

^{27}Al (I = 5/2) MAS NMR spectrum was recorded using a 2.5 mm CP MAS probe at spinning speed 30 kHz on an Avance 750 Bruker spectrometer (B_0 = 17.6 T) operating at a ^{27}Al Larmor frequency of 195.5 MHz. A short pulse length of 1 µs was used to ensure quantitative excitation of the whole spin system. The recycle delay was set to 1 s and 4096 fids were accumulated. ^{27}Al spectra were referenced to 1 M aqueous solution of $Al(NO_3)_3$. Quantitative reconstruction[14-17] of the main resonance of the ^{27}Al NMR spectra was achieved taking into account the N = 0 spinning sideband of the satellite transitions <3/2> and the N = 0 spinning sideband of the central transition <1/2> which completely overlap. For each ^{27}Al NMR site, the isotropic chemical shift δ_{iso} and the quadrupolar product $\nu_{Q\eta}$ were calculated by comparison of the centre of gravity $\delta_{cs}^{<3/2>}$ of the Al satellite sidebands with that of the central transition $\delta_{cs}^{<1/2>}$, through the following equation: $\delta_{cs}^{<m>} = \delta_{iso} - \nu_{Q\eta}^2 \frac{[I(I+1) - 3 - 9m(m-1)]}{30\nu_0^2}.10^6$, where I = 5/2 in the case of ^{27}Al, ν_0 = 195.5 MHz (for the 17.6 T spectrometer) and $\nu_{Q\eta} = \nu_Q \sqrt{1 + \frac{\eta_Q^2}{3}}$.[16] A two-dimensional one pulse[18-20] (TOP) spectrum was constructed, using DMFIT,[13] by stacking sub-spectra shifted by the spinning frequency from the 1D MAS NMR spectra.

FTIR spectroscopy. The IR spectrometer was a Nicolet Nexus apparatus equipped with an extended KBr beam splitter and a mercury cadmium telluride (MCT) detector (resolution: 4 cm^{-1}). Samples were pressed in a self-supported discs (2 cm^2, ~ 20 mg) and placed into an infrared quartz cell (KBr windows) connected to a vacuum line. Samples were activated under vacuum at 573 K overnight. After activation, the acidity of the materials was studied by IR spectroscopy, using adsorbed pyridine as spectroscopic probe molecule. Pyridine (Aldrich, 99% grade, dried on molecular sieves prior to their use) was introduced at equilibrium pressure (133 Pa) into the cell via the vacuum line and evacuated under vacuum at increasing temperatures.

TGA/MS. Thermal analysis was performed using a NETZSCH thermoanalyzer STA 409 C *Skimmer*®. The thermoanalytical curves (T, DTA, TG, DTG) were recorded together with the ion current (IC) curves in the multiple ion detection (MID) mode. A constant purge gas flow of 70 mL/min nitrogen (N_2 5.0, Messer-Griesheim) and a constant heating rate of 10 $K.min^{-1}$ were applied.

Results and discussion

1. Thermal behavior of β-$AlF_{2.6}(OH)_{0.4}$

In a first approach, TGA coupled to a mass spectrometer was performed on β-$AlF_{2.6}(OH)_{0.4}$ (Figure 1)**.**

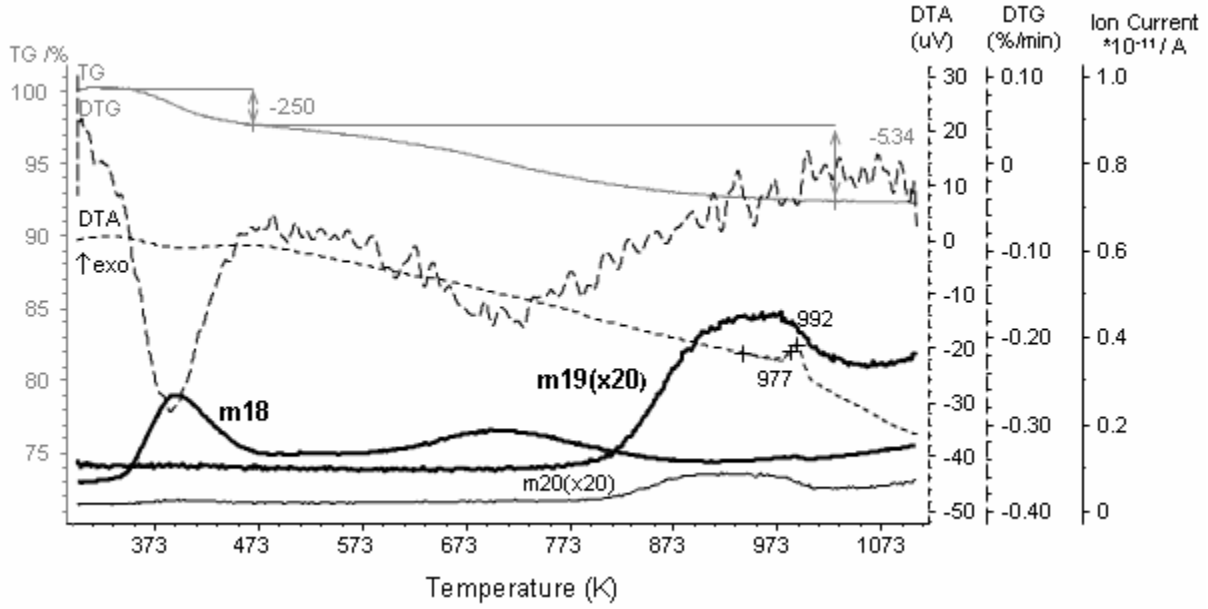

Figure 1. TGA-MS curves of β-$AlF_{2.6}(OH)_{0.4}$ with the IC curves for m/z=18(H_2O^+), 19(F^+), and 20(HF^+). Note the qualitatively different curve shape allowing for the distinction between water and HF.

The DTA curve exhibits a very weak endothermic signal in the dehydration range and an exothermic signal with a peak temperature T_P at 992 K. Two main TG steps with DTG maxima at about 390 and 720 K can be distinguished and have been ascribed to the departure of weakly adsorbed water and the dehydroxylation process, respectively. The IC curves for the mass numbers m/z=18(H_2O^+), 19(F^+), and 20(HF^+) demonstrate that the two steps of water liberation precede the pyrohydrolysis range starting at about 770 K. It is almost completed at 1070 K. The exothermic peak detected at 992 K in the DTA curve is related to the departure of ammonia, as

confirmed by the ionic curve of m/z=17 (NH_3^+ fragment) as it can be seen in Supporting Information (SI). A comparison between intensities of the first departure at 390 K and the third one at 992 K gives the following:

$I_{m17}(390K) : I_{m18}(390K) = 0.97\ 10^{-10}/2.7\ 10^{-10} = 1/2.8$

$I_{m17}(992K) : i_{m18}(992K) = 0.69\ 10^{-10}/1.2\ 10^{-10} = 1/1.8$

Such a result evidences an additional contribution for the m/z=17 ionic curve related to the departure of ammoniac species during the exothermic phenomenon that occurs at 992 K. The interpretation of this DTA effect is not completely clear as it exhibits the typical form of a crystallization peak together with the mentioned weak NH_3 release but other structural data reported here seem to confirm an earlier phase formation of α-AlF_3.

The case of AlF_3 seems to be somewhat peculiar as literature indicates that the phase transition from β-AlF_3 to α-AlF_3 could not always be detected by DTA signals.[9] In order to identify more accurately the stability limit of the HTB network, β-$AlF_{2.6}(OH)_{0.4}$ was annealed at various temperatures in the range where the loss of HF occurs (773-923 K). X-ray diffraction analysis of the annealed samples enables to define the limit of the network stability. The XRPD patterns of β-$AlF_{2.6}(OH)_{0.4}$ before and after annealing at 873 and 923 K are displayed in Figure 2.

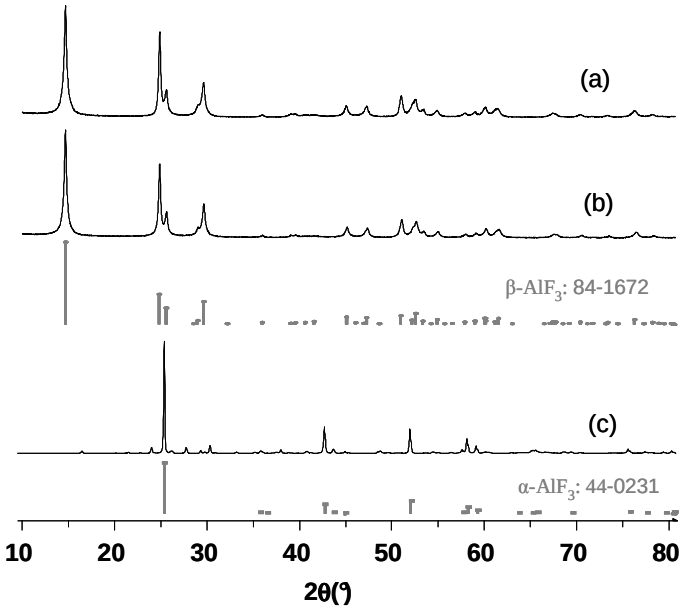

Figure 2. X-ray powder diffraction patterns (room temperature) of (a) starting β-$AlF_{2.6}(OH)_{0.4}$, β-$AlF_{2.6}(OH)_{0.4}$ treated at (b) 873K (β-873) and (c) 923K under vacuum for 4h. JCPDS-ICCD files are noted in grey.

The network is stable up to 873 K. The JCPDS-ICDD file N° 84-1672 relative to β-AlF_3 accounts for the purity of the HTB phase. After the annealing treatment at 923 K, it collapses into the thermodynamically stable phase α-AlF_3 (JCPDS-ICDD file N°44-0231), as well as minor phases which are detected by X-ray diffraction and should correspond to transition alumina in accordance with previous work.[21]

On the basis of the XRPD patterns (Figure 2), the HTB network is stable up to 873 K but at such a temperature, dehydroxylation and pyrohydrolysis reactions have already taken place, since the release of HF starts at around T=773 K, as shown in Figure 1. The structural network should have collapsed after such a thermal treatment. To understand the variation of the structural features upon annealing treatment, the sample treated at 873 K, labeled as β-873, is investigated in the next part.

2. Influence of the annealing treatment on the structural features

XRD and TEM analysis. As already mentioned, XRPD accounts for the phase purity of β-873. Figure 3 displays the profile matching performed on β-873. The cell parameters and volume decrease after annealing and one should have to note that they tend to those found in the hydroxyl-free compound β-AlF_3 [9] (Table 1).

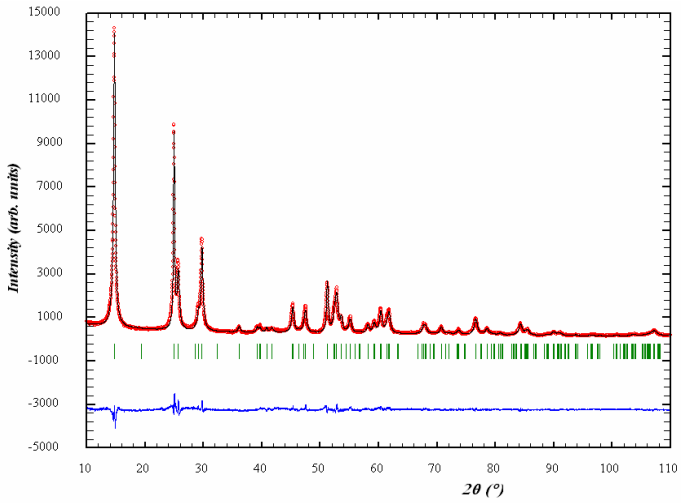

Figure 3. Profile matching of the diffraction pattern of β-873. The vertical bars correspond to the positions of the Bragg reflections.

Sample	Cell parameters : a, b, c (Å)	Cell volume (Å^3)
β-$AlF_{2.6}(OH)_{0.4}$	6.9681(2)	599.1
	12.0360(3)	
	7.1434(1)	
β-873	6.9399(2)	593.8
	12.0010(2)	
	7.12953(7)	
β-AlF_3	6.931(3)	593.4
	12.002(6)	
	7.134(2)	

Table 1. Crystallographic data of β-$AlF_{2.6}(OH)_{0.4}$ before[12] and after annealing at 873K and those of the hydroxyl-free β-AlF_3. [9]

HRTEM was performed on β-873 to study the morphological changes induced by the thermal treatment at the crystallite scale. The first experimental difference between β-$AlF_{2.6}(OH)_{0.4}$[12] and β-873 is the ability of the particles of the latter to be spread on the grid. A great number of isolated particles were indeed observed during TEM experiments. This observation contrasts with the sintering effect often observed in the case of fluoride compounds, thus forming agglomerates. Examples of the observed particles are displayed in Figure 4. Energy-dispersive X-ray spectroscopy (EDX) analysis confirms that the material is composed of aluminum and fluorine. Unfortunately, the detection of oxygen is not possible since already present on the grid. Additionally, energy filtered TEM analysis was not possible since this technique induces an evolution of the particle under the electron beam. HRTEM performed on β-$AlF_{2.6}(OH)_{0.4}$ reveals a high crystalline state of the material.[12] This observation contrasts with the amorphous feature displayed by the annealed particles.

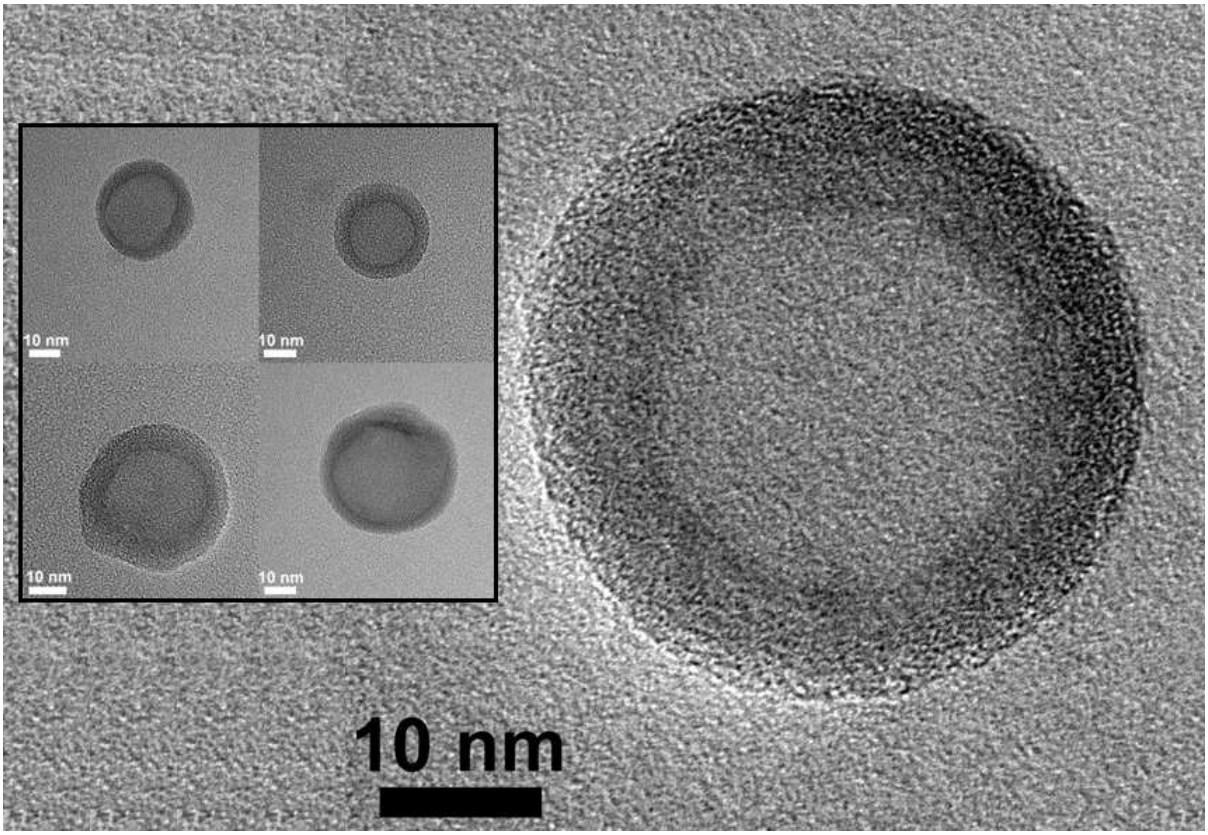

Figure 4. High resolution electron micrograph of β-873 sample. Inset: several other core-shell particles.

The observed particles exhibit an unusual core-shell like morphology; the amorphous component forming a shell hinders the observation of crystallized core detected by XRPD (Figure 2). The amorphization of the outermost surface (shell) of the particle can be explained by the diffusion of species generated by the thermal treatment, *i.e.* H_2O and HF, through the HTB tunnels. The diffusion from the interior to the exterior of the crystallite allows such species to further react with the framework leading to a disorganization of the network. Additionally, the annealing treatment leads to an increase of the particle size, from 13-18nm to 40 nm. Such an increase is going with a decrease of the surface area, *i.e.* from 82 to 46 $m^2.g^{-1}$.

FTIR spectroscopy. The dehydroxylation of β-873 has been ascertained by FTIR spectroscopy. IR spectra of β-$AlF_{2.6}(OH)_{0.4}$ and β-873 recorded after in-situ activation at 573 K are displayed in Figure 5. It can be noted that β-873 exhibits ammonia species (Figure 5, inset B δNH_3~1340cm^{-1}) showing the stability of such species and their role on the exothermic phenomenon observed on the DTA curve at 992 K. The dehydroxylation process is clearly

evidenced by the strong decrease of the band intensity of bridged Al-OH groups located at 3670 and 1130 cm^{-1}, respectively.

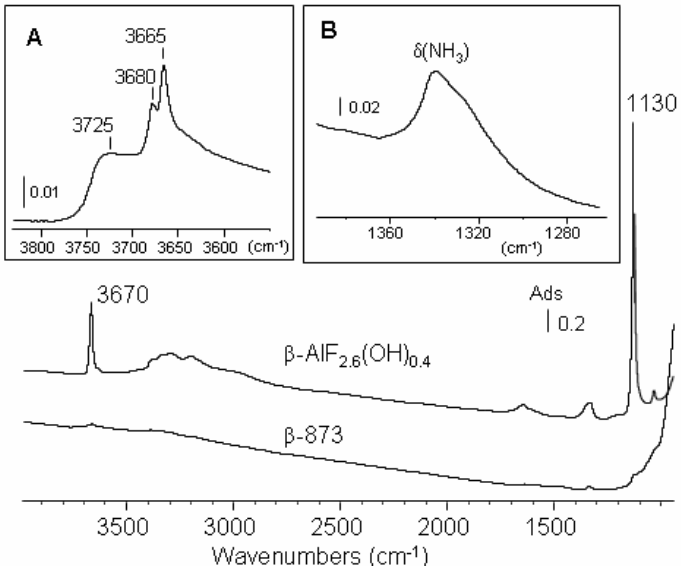

Figure 5. Normalized IR spectra of β-$AlF_{2.6}(OH)_{0.4}$ and β-873 activated in-situ at 573K. Inset A: enlargement of the ν(OH) zone of β-873, Inset B: enlargement of the β-873 spectrum showing the δ(NH_3) band.

Nevertheless, a very weak number of OH groups remains after the annealing treatment since weak ν(OH) bands are detected at 3665, 3680 and 3725 cm^{-1} (Figure 5, inset A). β-$AlF_{2.6}(OH)_{0.4}$ exhibits one ν(OH) at around 3670 cm^{-1} related to bridged Al-OH groups with a shoulder at 3680 cm^{-1} ascribed to surface OH groups.[12] In order to get more insight into the dehydroxylation process, the annealing treatment was reproduced in the FTIR cell, *i.e.* β-$AlF_{2.6}(OH)_{0.4}$ was treated in situ at 873 K (10 $K.min^{-1}$) under vacuum for 4h. The corresponding IR spectrum is displayed in the Figure 7a. Only one weak ν(OH) band was detected at 3665 cm^{-1}. This band accounts for remaining structural bridged OH groups while the origin of the bands at 3680 and 3725 cm^{-1} is not clear. These ν(OH) bands were assumed to arise from surface hydration. The dissociation of surface water can be assumed to occur giving rise to these OH groups. Such hypothesis was confirmed by adsorbing water on the surface (Figure 7 b) and then activating the sample under vacuum at 573K. The corresponding spectrum (Figure 7, inset c) exhibits three ν(OH) bands located at 3667, 3677 and 3730 cm^{-1} which confirms the dissociation of adsorbed water.

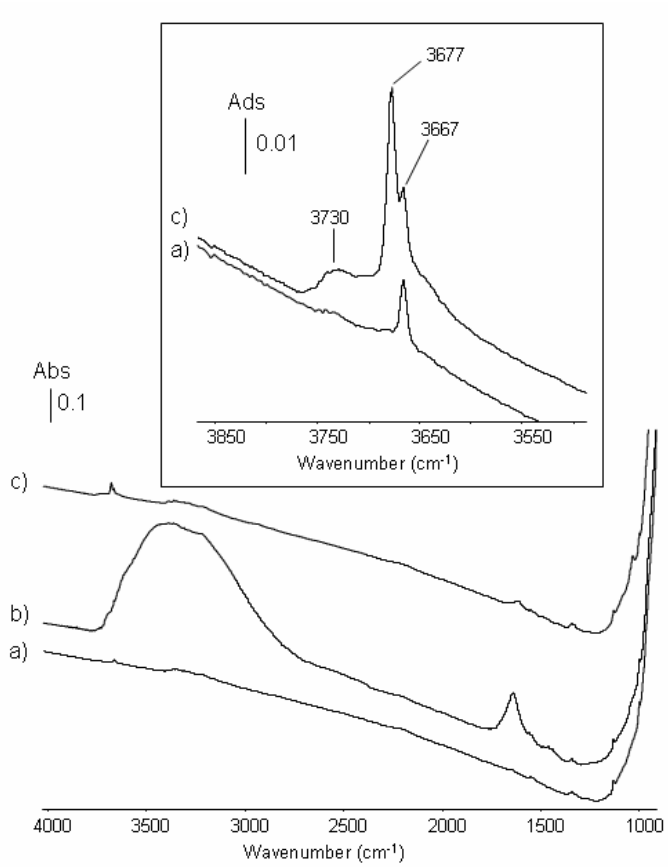

Figure 6. IR spectra of β-$AlF_{2.6}(OH)_{0.4}$ recorded a) after thermal treatment at 873K (10K.min^{-1}) under primary vacuum for 4h, b) after introduction of 1330 Pa H_2O, c) after evacuation at 573K. Inset: ν(OH) region.

NMR spectroscopy. The evolution of the anionic environment of aluminum ions upon annealing was followed using ^{27}Al and ^{19}F MAS NMR spectroscopy. Quantitative proportions of nuclei in both crystalline and disordered part can be extracted from spectrum reconstructions.

^{19}F MAS NMR spectra of β-$AlF_{2.6}(OH)_{0.4}$ and β-873 are displayed on Figure 7. The β-873 one was reconstructed using three contributions whose characteristics are gathered in SI. The lowest δ_{iso} values may be related to fluorine atoms in AlF_6^{3-} octahedra (δ_{iso} (^{19}F in α- and β-AlF_3) = -172 ppm[22]). It is known that ^{19}F chemical shifts of octahedral aluminum environments with oxygen and fluorine in the first coordination sphere increase with the oxygen content.[12,23-31] The annealing treatment clearly induces a narrowing of the resonance peak and a displacement toward lower chemical shift showing the disappearance of hydroxyl species and revealing a more homogeneous fluorinated environment in β-873 for the aluminum ions surrounded by fluorine ions. Such a feature is also evidenced regarding the evolution of the unit cell parameters upon

annealing (Table 1). By comparison, after annealing, the sample is structurally closer to the hydroxyl-free compound, *i.e.* β-AlF_3. Besides, the ^{19}F NMR spectrum shows that some OH groups remain (line at ~ -162 ppm) in agreement with FTIR spectroscopy.

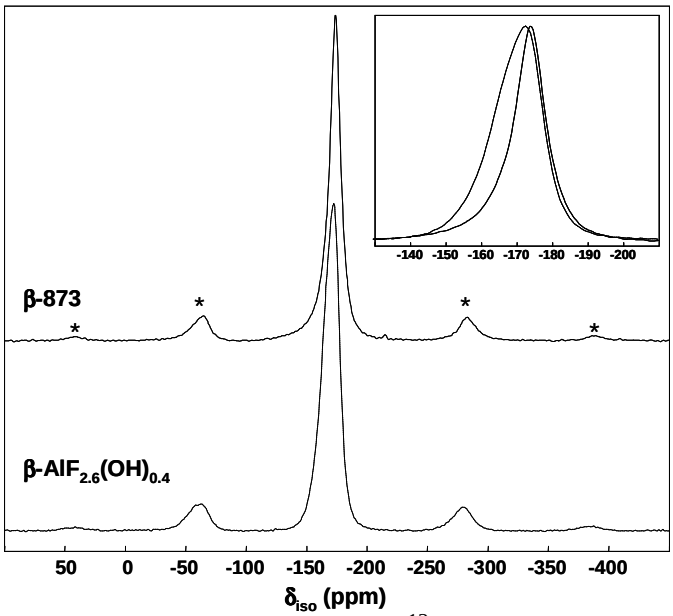

Figure 7. ^{19}F NMR MAS spectra of β-$AlF_{2.6}(OH)_{0.4}$[12] and β-873 at 30 kHz. The star symbols indicate the spinning sidebands.

The central transition of the ^{27}Al MAS NMR spectra of β-873 and β-$AlF_{2.6}(OH)_{0.4}$ recorded at 17.6 T are displayed in Figure 8.

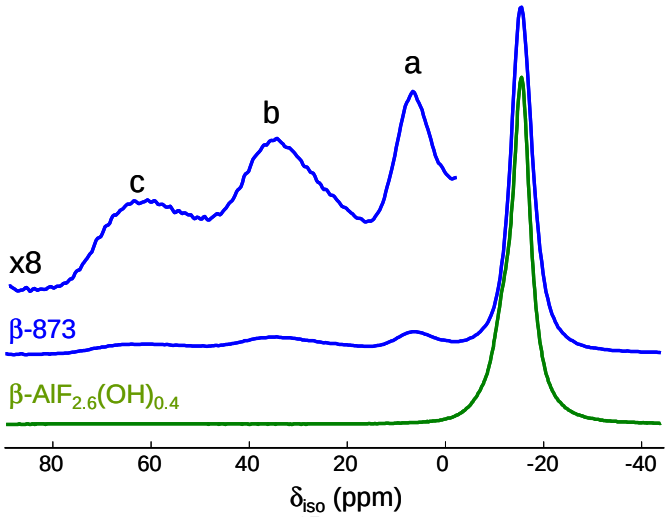

Figure 8. Central transition of the one pulse ^{27}Al MAS (30 kHz) spectrum of β-$AlF_{2.6}(OH)_{0.4}$[12] and one pulse ^{27}Al MAS (30 kHz) spectrum of β-873 with an extension of the high frequency sites.

Contrarily to the featureless full spinning sideband manifold of β-$AlF_{2.6}(OH)_{0.4}$,[12] the main resonance spinning sideband manifold of β-873 shows singularities (see SI) characteristic of less disordered environments. This main resonance was reconstructed with two components at -15.6 and -11.6 ppm (Figure 9 and Table 2) previously ascribed in β-$AlF_{2.6}(OH)_{0.4}$ to AlF_6 and $AlF_5(OH)$ and $AlF_4(OH)_2$ species respectively.[12]

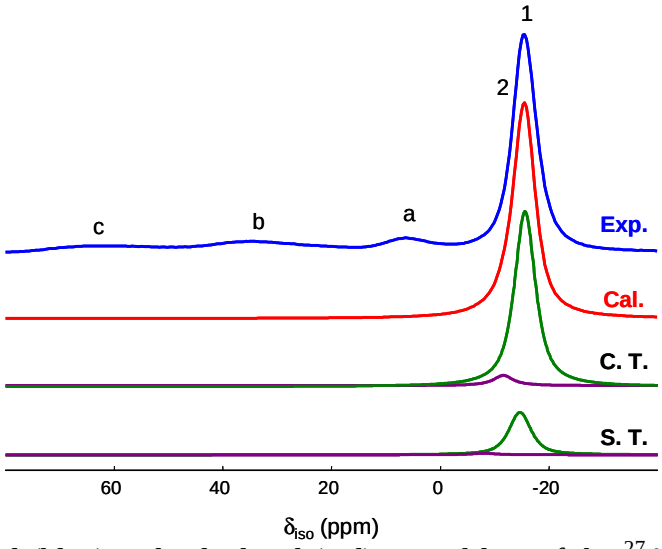

Figure 9. Experimental (blue) and calculated (red) central line of the ^{27}Al MAS NMR spectrum of β-873. The deconvolution, achieved using two contributions, takes into account the N = 0 band of both the satellite transitions <3/2> (S. T.) and the central transition <1/2> (C. T.).

The $\nu_{Q\eta}$ value of line 1 is still higher than the $\nu_{Q\eta}$ value observed in β-AlF_3 (132 kHz),[22] in agreement with OH groups remaining in the vicinity of fluorinated aluminum ions in β-873. The ^{27}Al high field spectrum (17.6 T) evidences also the appearance of resonances located at $\delta_{iso} > 0$ ppm upon annealing treatment (Figure 8). These contributions were reconstructed using Gaussian profiles on the full projection of the TOP spectrum (Figure 10) to get an estimation of the proportion of these new species (Table 2). Lines b and c are broad and have a shape characteristic of disordered ^{27}Al sites. An important feature of ^{27}Al solid-state NMR is the dependence of the isotropic chemical shift on local Al coordination: AlO_4 (~80 to 45 ppm), AlO_5 (~52 to 14 ppm) and AlO_6 (~20 to -20 ppm).[32,33] For instance, the chemical shifts of lines a and c (Table 4) are typical of AlO_6 and AlO_4 sites in γ-Al_2O_3, respectively.[22,23,29,34,35] Then, chemical shifts of lines a, b and c allow their assignment to oxygenated AlO_6, AlO_5 and AlO_4 sites, respectively. ^{27}Al isotropic chemical shift is also sensitive to the anionic environment. The occurrence of fluorine in the vicinity of octahedral aluminium ($AlO_{6-x}F_x$ sites) would shift the ^{27}Al δ_{iso} to lower values and

would induce ^{19}F resonances between ~ -130 and -160 ppm.[22,23,26,29,34] No such resonances being observed (Figure 7), we can thus exclude the existence of $AlO_{6-x}F_x$ sites.

Sample	Line	δ_{iso} (±0.2)	$\nu_{Q\eta}$ (±20)	Relative intensity (±0.5)	Assignments
β-$AlF_{2.6}(OH)_{0.4}$	1	-15.5	280	82	AlF_6-$AlF_5(OH)$
	2	-11.7	610	16	$AlF_4(OH)_2$
	3	-9.5	990	2	$AlF_3(OH)_3$
β-873	1	-15.6	280	82.5	AlF_6-$AlF_5(OH)$
	2	-11.6	670	5.1	$AlF_4(OH)_2$
	a	6.4		2.8	AlO_6
	b	34.0		4.7	AlO_5
	C	62.3		4.9	AlO_4

Table 2. Line labels, isotropic chemical shift δ_{iso} (ppm), quadrupolar product $\nu_{Q\eta}$ (kHz), relative intensity (%) and assignment of the ^{27}Al NMR lines of β-$AlF_{2.6}(OH)_{0.4}$ [12] and β-873.

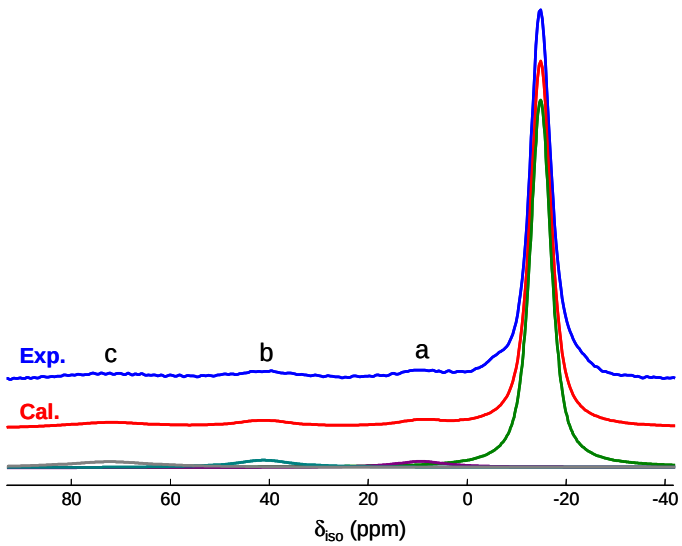

Figure 10. Experimental (blue) and calculated (red) full projection of the TOP reconstruction of the ^{27}Al MAS NMR spectrum of β-873. The deconvolution is achieved using Gaussian contributions.

The appearance of these new Al^{3+} species in β-873 is going with the disappearance of line 3 and the decrease of the relative intensity of line 2 (Table 2) of β-$AlF_{2.6}(OH)_{0.4}$ relative to $AlF_4(OH)_2$ and $AlF_3(OH)_3$ species, respectively.[12] The evolution of the relative intensity of the ^{27}Al NMR lines evidences both dehydroxylation and pyrohydrolysis processes. This result also evidences the lowest stability of hydroxylated species as compared to the fluorinated one's. The new disordered aluminum environments generated after annealing represent about 12% of the aluminum atoms, which is too large to be considered as defects in the HTB structure. Since XRPD analysis shows only lines corresponding to β-AlF_3, it should be deduced that these new components are ill-crystallized phases and build up the amorphous shell revealed by HRTEM. The use of high field ^{27}Al NMR spectroscopy gives here some precise information since it allows identifying and quantifying the amorphous part of the solid. Additionally, it enables a better understanding of the HRTEM observation. Based on the quantification of the amorphous component, the thickness of the shell appears rather weak.

Adsorption of pyridine. The effect of the annealing treatment on the acidic properties has been probed by adsorption and temperature desorption of pyridine as probe molecule followed by FTIR spectroscopy. The IR spectra of coordinated pyridine adsorbed on the surface are displayed in Figure 11. The estimation of the number of pyridine molecules coordinated on Lewis acid sites per nm^2 using the integration of the ν19b band at RT[36] shows that an almost similar number of acid site, *i.e.* 1.4 and 1.2 sites per nm^2, is observed for β-$AlF_{2.6}(OH)_{0.4}$ and β-873, respectively. The strength of the Lewis acidity is regarded through the ν8a vibration mode of coordinated pyridine in the 1600-1630 cm^{-1} range, *i.e.* the higher the position, the stronger the Lewis acidity. At room temperature, the maximum of the ν8a band is detected at 1618 cm^{-1} and shifts toward high wavenumber during thermodesorption and is finally detected at 1625 cm^{-1} after evacuation at 573 K. For β-$AlF_{2.6}(OH)_{0.4}$, these positions are detected at 1620 and 1628 cm^{-1} after evacuation at room temperature and at 573 K, respectively.[37] The annealing process thus leads to the lowering of the Lewis acidity confirming the occurrence of a new surface structure in agreement with HRTEM and NMR. This acidic behaviour is stronger than those of γ-Al_2O_3 and is slightly lower than those displayed by the pyrochlore aluminum hydroxyfluoride $AlF_{1.8}(OH)_{1.2}$.[31] Additionally, the weak band at 1545 cm^{-1} is characteristic of pyridinium species, evidencing the occurrence of some strong Brønsted acid sites. Such a Brønsted acidity reveals that the dissociation of surface water molecules generates acidic surface OH groups. Such a reaction

should occur on very unstable species. The dehydroxylation/pyrohydrolysis process is assumed to generate strongly under-coordinated species which can further react with water creating strong Brønsted acid sites. Some authors have reported the instability of under-coordinated fluorinated Al^{3+} species[38,39] which can dissociate water molecules. One should have to note that such strong Brønsted acidic sites have not been detected on β-$AlF_{2.6}(OH)_{0.4}$,[12] highlighting the peculiar type of surface structure obtained upon annealing.

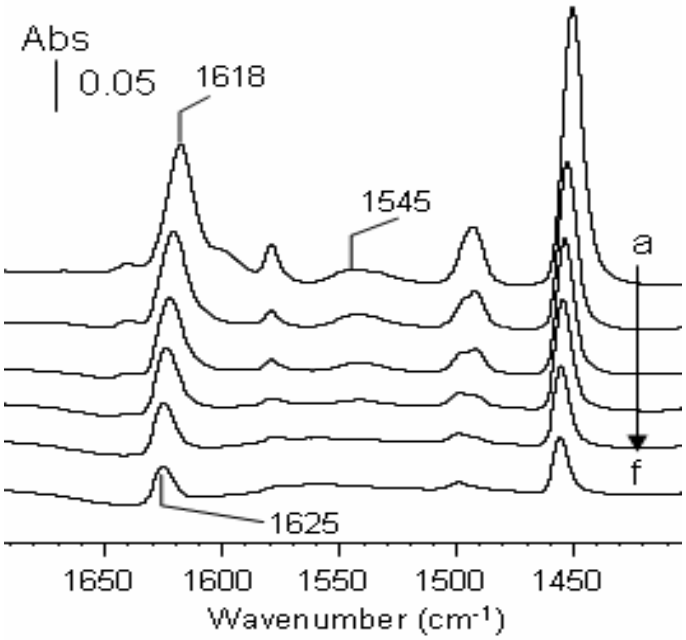

Figure 11. Normalized difference IR spectra of pyridine coordinated on β-873 after introduction of an equilibrium pressure of the probe molecule vapour and followed by a) evacuation at RT under vacuum and thermodesorption at b) 323K, c) 423K, d) 473K, e) 523K and f) 573K.

Conclusion

The thermal behavior of an aluminum hydroxyfluoride, *i.e.* β-$AlF_{2.6}(OH)_{0.4}$, has been thoroughly investigated for the first time using several techniques such as TGA/MS, XRPD, HRTEM, FTIR and ^{19}F and high field ^{27}Al NMR. A detailed thermal analysis reveals both dehydroxylation and pyrohydrolysis reactions and shows that the HTB-type network is stable up to 873 K. The evolution of the structural feature of the material upon annealing was studied before the collapse of the structure. An almost complete transformation of the outermost surface of the nanoparticles, yielding an unusual core-shell like morphology, has been observed. It has been suggested that the diffusion of species liberated by the dehydroxylation/pyrohydrolysis process further react on the outermost part of the particle leading to a disorganization of the

network which therefore appears as X-ray amorphous. Such a shell, observed by HRTEM, hides the crystallized part of the material which has been identified as a closely related β-AlF_3 phase through XRPD and ^{19}F and ^{27}Al NMR. The lowest thermal stability of the hydrolylated species as compared to the fluorinated ones is then confirmed. AlO_6 and under coordinated species (AlO_4 and AlO_5) have been identified and quantified by ^{27}Al NMR and ascribed to the amorphous shell. The newly formed surface exhibits a lower Lewis acidity than β-$AlF_{2.6}(OH)_{0.4}$. However, strong Brønsted acid sites have been revealed by pyridine adsorption and were assumed to arise from the dissociation of water on strongly under-coordinated species located at the surface.

ACKNOWLEDGMENT. The EU is acknowledged for financial support through the 6th Framework Programme (FUNFLUOS, Contract No. NMP3-CT-2004-5005575). M. Daturi, A. Vimont and H. Leclerc are acknowledged for FTIR data and fruitful discussions.

Supporting Information Available. TGA-MS curve of β-$AlF_{2.6}(OH)_{0.4}$ with the IC curves m/z=18 and 17, ^{19}F MAS NMR experimental and calculated spectra of β-873 at 30 kHz, Isotropic Chemical Shifts, Line Widths and Relative Intensities as deduced from ^{19}F NMR spectrum simulation and ^{27}Al MAS one pulse spectrum of β-873 recorded at 17.6 T. This material is available free of charge via the Internet at http://pubs.acs.org.

References.

(1) Kemnitz, E.; Groß, U.; Rudiger, S.; Shekar, C. S. *Angew. Chem. Int. Ed.* **2003**, *42*, 4251.
(2) Delattre, J. L.; Chupas, P. J.; Grey, C. P.; Stacy, A. M. *J. Am. Chem. Soc.* **2001**, 123, 5364.
(3) Kemnitz, E.; Menz., D.H. *Prog. Solid State Chem.* **1998**, *26*, 97.
(4) Rudiger, S.; Eltanany, G.; Groß, U.; Kemnitz, E. *J. Sol-Gel Sci. Techn.* **2007**, 41, 299.
(5) Hajime, E. K. L. Y.; Delattre, J. L.; Stacy, A. M. *Chem. Mater.* **2007**, *19*, 894.
(6) Wander, A.; Bailey, C. L.; Searle, B. G.; Mukhopadhyay, S.; Harrison, N. M. *Phys. Chem. Chem. Phys*. **2005**, *7*, 3989.
(7) Wander, A.; Bailey, C. L.; Mukhopadhyay, S.; Searle, B. G.; Harrison, N. M. *J. Mater. Chem.* **2006**, *16*, 1906.
(8) Chaudhuri, S.; Chupas, P.; Morgan, B. J.; Madden, P. A.; Grey, C. P. *Phys. Chem. Chem. Phys.* **2006**, *8*, 5045.
(9) Le Bail, A.; Jacoboni, C.; Leblanc, M.; De Pape, R.; Duroy, H.; Fourquet, J.-L. *J. Solid State Chem.* **1988**, *77*, 96.
(10) Francke, L.; Durand, E.; Demourgues, A.; Vimont, A.; Daturi, M.; Tressaud, A. *J. Mater. Chem.* **2003**, *13*, 2330.
(11) Hess, A.; Kemnitz, E. *J. Catal.* **1994**, *149*, 449.
(12) Dambournet, D.; Demourgues, A.; Martineau, C.; Pechev, S.; Lhoste, J.; Majimel, J.; Vimont, A.; Lavalley, J.-C.; Legein, C.; Buzaré, J-Y.; Fayon, F.; Tressaud, A. *Chem Mate*r.; 2008; ASAP Article; DOI: 10.1021/cm702603b
(13) Massiot, D.; Fayon, F.; Capron, M.; King, I.; Le Calvé, S.; Alonso, B.; Durand, J.-O.; Bujoli, B.; Gan, Z.; Hoatson, G. *Magn. Reson. Chem.* **2002**, *40*, 70.
(14) Massiot, D.; Bessada, C.; Coutures, J. P.; Taulelle, F. *J. Magn. Reson*. **1990**, *90*, 231.
(15) Alemany, L. B.; Massiot, D.; Sherriff, B. L.; Smith, M. E.; Taulelle, F. *Chem. Phys. Lett.* **1991**, *177*, 301.
(16) Massiot, D.; Müller, D.; Hübert, Th.; Schneider, M.; Kentgens, A.P.M.; Coté, B.; Coutures, J.P.; Gessner, W. *Solid State Nucl. Magn. Reson.* **1995**, *5*, 175.
(17) Stebbins, J. F.; Kroeker, S.; Lee, S. K.; Kiczenski, T. J. *J. Non-Cryst. Solids.* **2000**, *275*, 1.
(18) Blümich, B.; Blumler, P.; Jansen, J. *Solid State Nucl. Magn. Reson.* **1992**, *1*, 111.
(19) Blumler, P.; Blümich, B.; Jansen, J. *Solid State Nucl. Magn. Reson.* **1994**, *3*, 237.
(20) Massiot, D.; Hiet, J.; Pellerin, N.; Fayon, F.; Deschamps, M.; Steuernagel, S.; Grandinetti, P. J. *J. Magn. Reson.* 2006, ***181***, 310.
(21) Menz, D.-H.; Zacharias, A.; Kolditz, L. *J. Therm. Anal.* **1988**, *33*, 811.
(22) Chupas, P. J.; Ciraolo, M. F.; Hanson, J. C.; Grey, C. P. *J. Am. Chem. Soc.* **2001**, *123*, 1694.
(23) Chupas, P. J.; Corbin, D. R.; Rao, V. N. M.; Hanson, J. C.; Grey, C. P. *J. Phys. Chem. B.* **2003**, *107*, 8327.
(24) Taulelle, F.; Pruski, M.; Amoureux, J. P.; Lang, D.; Bailly, A.; Huguenard, C.; Haouas, M.; Gérardin, C.; Loiseau, T.; Férey, G. *J. Am. Chem. Soc.* **1999**, *121*, 12148.
(25) Simon, N.; Guillou, N.; Loiseau, T.; Taulelle, F.; Férey, G. *J. Solid State Chem.* **1999**, *147*, 92.
(26) Fischer, L.; Harlé, V.; Kasztelan, S.; d'Espinose de la Caillerie, J.-B. *Solid State Nucl. Magn. Reson.* **2000**, *16*, 85.
(27) Dumas, E.; Taulelle, F.; Férey, G. *Solid State Sci.* **2001**, *3*, 613.

(28) Zhou, B.; Sherriff, B.L.; Taulelle, F.; Wu, G. *Can. Mineral.* **2003**, *1*, 891.
(29) Chupas, P. J.; Grey, C. P. *J. Catal.* **2004**, *224*, 69.
(30) Kemnitz, E.; Groß, U.; Rüdiger, St.; Scholz, G.; Heidemann, D.; Troyanov, S.I.; Morosov, I.V.; Lemée-Cailleau, M.-H. *Solid State Sci.* **2006**, *8*, 1443.
(31) Dambournet, D.; Demourgues, A.; Martineau, C.; Durand, E.; Majimel, J.; Vimont, A.; Leclerc, H.; Lavalley, J.-C.; Daturi, M.; Legein, C.; Buzaré, J.-Y.; Fayon, F.; Tressaud, A. *J. Mater. Chem.* (In press).
(32) Smith, M. E. *Appl. Magn. Reson.* **1993**, *4*, 1.
(33) Jansen, S. R.; Hintzen, H. T.; Metselaar, R.; de Haan, J. W.; van de Ven, L. J. M.; Kentgens, A. P. M.; Nachtegaal, G. H. *J. Phys. Chem. B* **1998**, *102*, 5969.
(34) Zhang, W.; Sun, M.; Prins, R. *J. Phys. Chem. B* **2002**, *106*, 11805.
(35) Stösser, R.; Scholz, G.; Buzaré, J.-Y.; Silly, G.; Nofz, M.; Schultze, D. *J. Am. Ceram. Soc.* **2005**, *88*, 2913.
(36) Vimont, A.; Lavalley, J. C.; Francke, L.; Demourgues, A.; Tressaud, A.; Daturi, M. *J. Phys. Chem. B* **2004**, *108*, 3246.
(37) Dambournet, D.; Vimont, A.; Leclerc, H.; Lavalley, J.-C.; Daturi, M.; Demourgues, A.; Tressaud, A.; Nickkho-Amiry, M.; Winfield, J. M. *Submitted.*
(38) Grey, C.P.; Corbin, D. R. *J. Phys. Chem.* **1995**, *99*, 16821.
(39) Groß, U.; Müller, D.; Kemnitz, E. *Angew. Chem. Int. Ed.* **2003**, *42*, 2626.

Preparation and characterization of nano-structured Al-based fluoride/oxide core-shell

D. Dambournet, A. Demourgues, C. Martineau, J. Majimel, M. Feist, C. Legein, J.-Y. Buzaré, F. Fayon and A. Tressaud

Supporting information

Table of contents

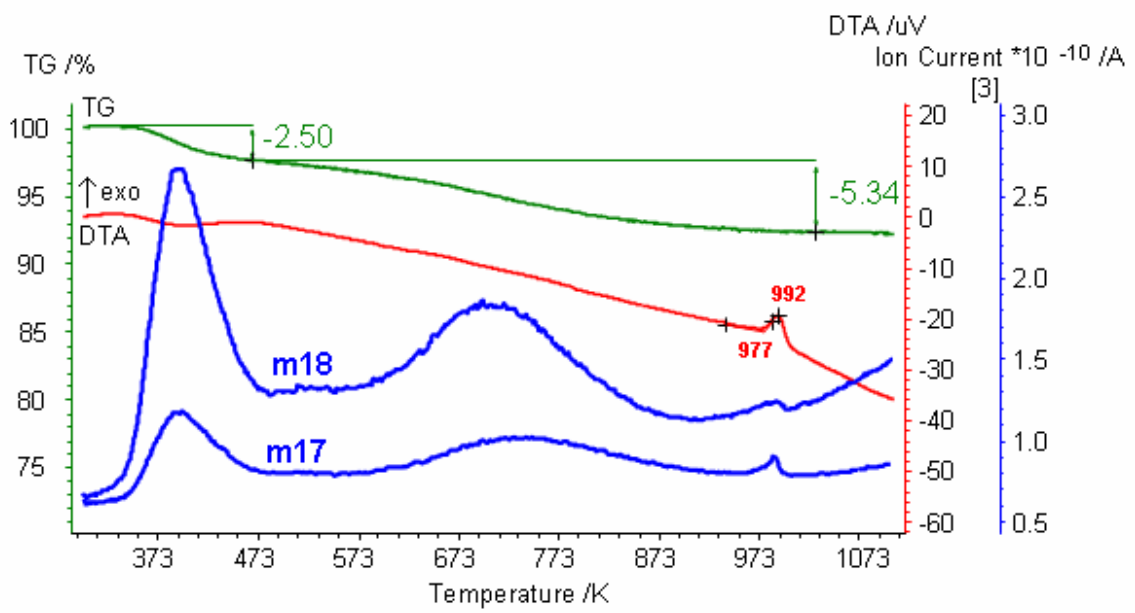

Figure 1. TGA-MS curves of β-$AlF_{2.6}(OH)_{0.4}$ with the IC curves m/z=18(H_2O^+) and 17(OH^+/NH_3^+)

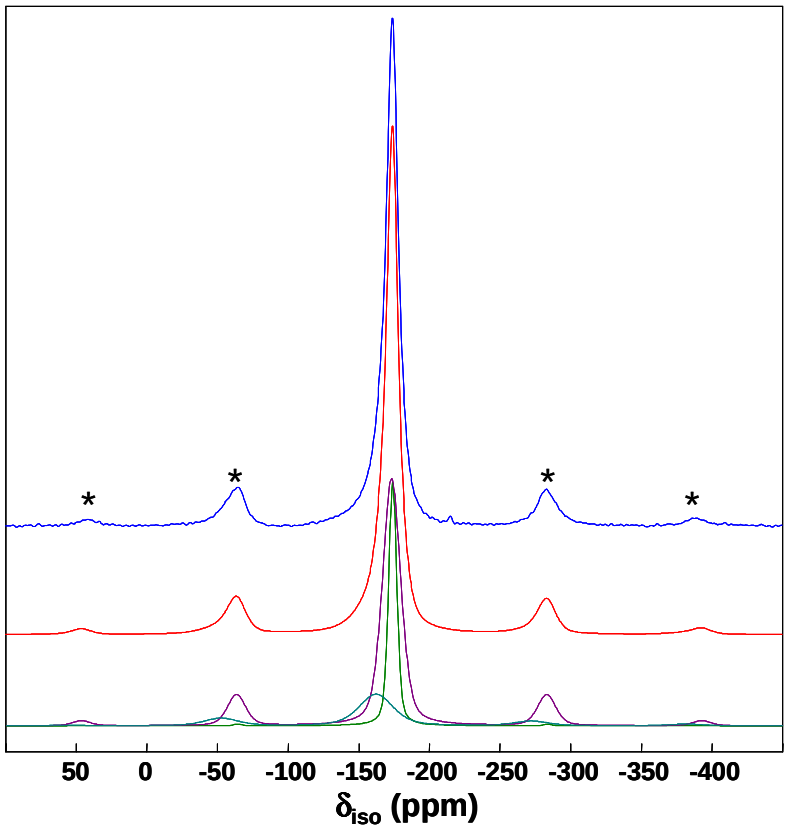

Figure 2. ^{19}F MAS NMR experimental and calculated spectra of β-873 at 30 kHz. The star symbols indicate the spinning sidebands. The three individual contributions to the reconstructed spectrum are shown.

Table 1. Isotropic Chemical Shifts (ppm), Line Widths (ppm) and Relative Intensities (%) as deduced from ^{19}F NMR spectrum simulation.

δ_{iso}	Width	Intensity
-174.1	6.8	21.4
-173.3	15.2	61.4
-162.3	28.6	17.2

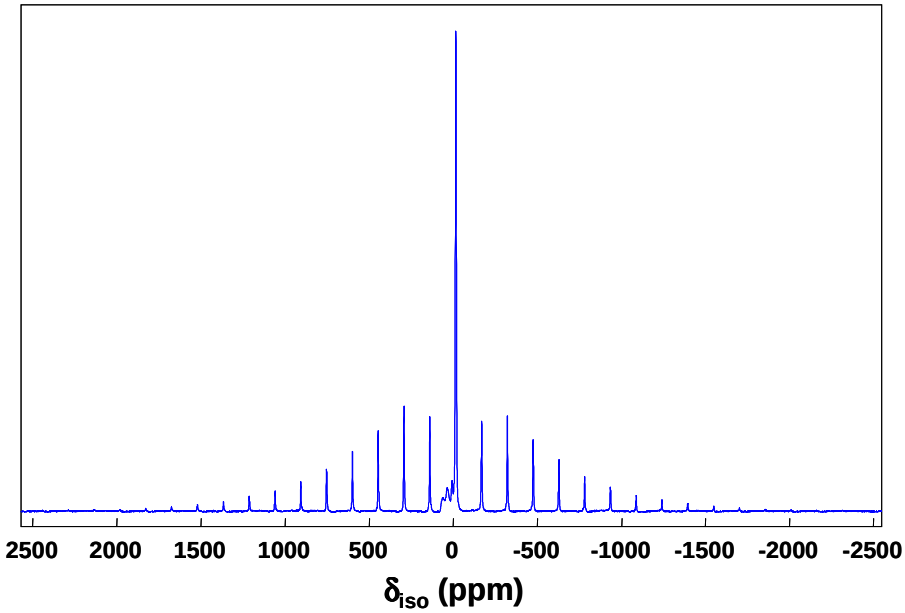

Figure 3. ^{27}Al MAS (30 kHz) one pulse spectrum of β-873 recorded at 17.6 T.

Conclusion générale et perspectives

Conclusion générale et perspectives

Ce travail s'est articulé autour de la synthèse et la caractérisation de fluorures d'aluminium présentant de grande surface spécifique en vue d'accroître la réactivité du solide divisé.

La synthèse mise en œuvre pour atteindre ces objectifs consiste en un procédé hydrothermal assistée par micro-ondes. Plusieurs paramètres ont été optimisés en vue d'obtenir des phases pures qui présentent des particules de taille nanométrique.

Trois types structuraux ont été préparés :

- Un hydroxyfluorure de type bronze de tungstène hexagonal (orthorhombique, GS : Cmcm) de formule $AlF_{2.6}(OH)_{0.4}$ (HTB ou β) et une surface spécifique de 82 $m^2.g^{-1}$.
- Un hydroxyfluorure de type pyrochlore (cubique, GS : Fd-3m) de formule $AlF_{1.8}(OH)_{1.2}$ avec une surface spécifique de 137 $m^2.g^{-1}$.
- Un nouveau fluorure d'aluminium hydraté de structure type ReO_3 (cubique, GS : Pm-3m) présentant des lacunes cationiques de formule $Al_{0.82}\square_{0.18}F_{2.46}(H_2O)_{0.54}$ et une surface spécifique de 61 $m^2.g^{-1}$.

Les paramètres de synthèse qui se sont avérés être décisifs sont les suivants :

<u>La nature du précurseur métallique :</u> celle-ci permet de choisir le type structural. Par exemple, la réduction d'un précurseur nitrate conduit à l'obtention d'une phase HTB pure. Par contre, c'est l'utilisation d'alkoxyde qui permet d'obtenir un composé de type pyrochlore présentant une très grande surface spécifique (137 $m^2.g^{-1}$).

<u>Le rapport molaire HF/Al :</u> il a été clairement démontré que le taux de fluor avait une influence directe sur la variété stabilisée. En outre, l'introduction d'une grande quantité de HF en milieu chlorure ($AlCl_3$) mène à une forte acidification du milieu qui permet de stabiliser les molécules d'eau en tant que ligand au détriment des groupements hydroxyles.

<u>Le solvant :</u> dans la synthèse de la phase β-$AlF_{2.6}(OH)_{0.4}$, la variation du taux de solvant a permis de limiter la croissance cristalline, l'isopropanol contribuant à réduire cette dernière. L'ajout d'une faible quantité d'éther, formant un complexe avec le fluor, a quant à lui contribué à obtenir une phase pyrochlore possédant une grande surface spécifique.

Les trois variétés obtenues ont fait l'objet d'une étude structurale par la méthode de Rietveld. Celle-ci a permis de mettre en avant différents points clés qui sont :

Dans le cas de la phase HTB, deux des quatre sites cristallographiques (F1 et F2) ont été identifiés comme étant partiellement hydroxylés. C'est l'étude fine des distances inter-atomiques et angles de liaisons qui ont permis de trancher en faveur de cette hypothèse.
Dans la phase hydratée de type ReO_3, l'existence de lacunes cationiques a été pour la première fois mise en évidence dans un fluorure hydraté.
La diffraction des rayons X sur poudre a permis parallèlement une étude microstructurale (micro-contraintes et domaines de cohérence) du solide. La taille moyenne de ces domaines est de nanométrique : 12 nm pour le pyrochlore, 15 nm pour le HTB et 50 nm pour la phase lacunaire hydraté de type ReO_3. Dans le cas du HTB, cette analyse a mis en évidence une anisotropie liée à la forme des particules. Un affinement satisfaisant du profil des raies de diffraction n'est en effet rendu possible que par l'introduction d'un modèle plaquettaire confirmé par l'observation microscopique. Les petites et grandes dimensions des cristallites ont été établies respectivement selon l'axe a et le plan bc avec des valeurs de 8 et 34 nm.
La résonance magnétique nucléaire a permis une meilleure description de l'arrangement structural des réseaux par l'identification et la quantification des espèces octaédriques de type ($AlF_{6-x}O_x$) formant le squelette de la structure. Cette technique a également permis d'établir avec plus de précision les compositions chimiques des phases. Les déplacements chimiques obtenus pour les noyaux ^{19}F et ^{27}Al dans ces composés constituant ainsi de nouvelles références dans la caractérisation de matériaux fluorés.
Le couplage de la voie sol-gel non-aqueuse utilisée pour préparer des AlF_3 amorphe et la synthèse assistée par micro-ondes a ouvert des perspectives non seulement dans l'obtention de matériaux très divisés mais aussi dans la préparation de nouvelles compositions. Cette étude a permis de mettre l'accent sur l'importance de l'interaction entre le sol-gel initial et l'irradiation micro-ondes sur la nature et la morphologie du matériau final.

Le comportement thermique de la phase β-$AlF_{2.6}(OH)_{0.4}$ a fait l'objet d'une étude approfondie qui a mis en avant les différents mécanismes de pyrohydrolyse et de déshydroxylation. Cette étude a permis d'isoler le premier exemple des particules de type coeur-couronne AlF_3-Al_2O_3.

L'ensemble des matériaux synthétisés ici, ont été caractérisés en termes d'acidité de surface par adsorption de molécules sondes. Chacun de ces composés possède un comportement acide particulier qui peut se résumer comme suit :
La surface de β-$AlF_{2.6}(OH)_{0.4}$ (HTB) présente une forte hétérogénéité en terme de force de sites de Lewis. Cette hétérogénéité a été attribuée à la présence des groupements OH et plus

particulièrement aux espèces de type $AlF_{6-x}(OH)_x$ identifiées par RMN du noyau ^{27}Al. Les sites présentant la plus forte acidité de Lewis ont été attribués à des défauts de surfaces liés à la taille nanométrique du matériau et à des sites penta-coordonnés récemment révélés par des calculs ab initio. Ce composé possède aussi une acidité de Brønsted qui, contrairement à son acidité de Lewis, révèle un caractère très homogène en terme de force et donc de configuration de site. Il a été supposé que cette homogénéité était due à la localisation particulière des groupements OH dans la structure, la surface reflétant la périodicité du cristal.

La surface de l'hydroxyfluorure de type pyrochlore $AlF_{1.8}(OH)_{1.2}$ reflète parfaitement l'effet du fluor sur l'acidité de Lewis. L'acidité de Lewis du pyrochlore se situe en effet entre celle d'une alumine γ et celle de β-$AlF_{2.6}(OH)_{0.4}$. Les groupements OH possèdent une acidité de Brønsted relativement faibles. Toutefois, une forte acidité de Brønsted a été détectée dans cette phase puisque suffisamment élevée pour protoner la pyridine. Une étude complémentaire utilisant l'adsorption de CO a confirmé la forte acidité de Brønsted liée à la présence d'eau résiduelle en surface. Cette étude a aussi confirmé la plus faible acidité des groupements OH de la pyrochlore par rapport à ceux présents dans la phase HTB.

Le composé lacunaire $Al_{0.82}\square_{0.18}F_{2.46}(H_2O)_{0.54}$ présente un comportement acide dépendant de son état d'hydratation. Après activation à 300°C, la surface présente à la fois une forte acidité de Lewis et de Brønsted. A plus haute température : 400 et 500°C, les sites forts de Lewis sont convertis en sites beaucoup faibles. Ce comportement a été relié au fait que la surface tendait vers celle de α-AlF_3 rhomboédrique qui possède effectivement une faible acidité de Lewis. Au contraire des sites de Lewis, ceux de Brønsted sont toujours présents et aussi forts à 500°C mais en moindre quantité. Ceci a mis en évidence la stabilité de l'eau dans ce composé qui s'explique par la force des liaisons hydrogène.

Finalement, l'importance de la surface spécifique sur le nombre de site acides a été parfaitement démontrée. De même, une diminution de la taille des particules s'est avérée concomitant avec une augmentation du nombre des sites forts de Lewis quelle que soit la composition du matériau. Ceci a mis en avant l'effet de l'échelle nanométrique sur la structure de la surface.

Nous avons ainsi montré le potentiel de la synthèse micro-ondes dans l'obtention de matériaux divisés présentant une large gamme d'acidité. L'utilisation de différents solvants organiques ou encore de liquide ionique serait à envisager dans le but d'obtenir de nouvelles phases métastables.

La synthèse d'une phase de type HTB avec une surface spécifique de 125 $m^2.g^{-1}$ ainsi qu'un matériau possédant une surface spécifique de 330 $m^2.g^{-1}$ après traitement sous F_2 gazeux, permet d'ouvrir des perspectives importantes pour l'utilisation de ces matériaux en tant que catalyseur.

L'une des perspectives de ces travaux se tourne naturellement vers la confirmation de l'efficacité de ces nouveaux matériaux par le biais de tests catalytiques. Plusieurs domaines d'applications peuvent être envisagés tel que la chimie des fluorocarbones ou des hydrocarbures. L'étude relative au comportement thermique de la variété HTB a aussi ouvert des perspectives au niveau de la fonctionnalisation de ces matériaux. Les réactions de pyrohydrolyse/deshydroxylation génèrent des sites sous coordonnés qu'il serait particulièrement intéressant de fonctionnaliser avec différentes molécules organiques pour en faire varier les propriétés.

ANNEXE :

COMPARAISON ENTRE L'APPROCHE EXPERIMENTAL ET LES CALCULS Ab INITIO

Advances in structural analysis of high surface area aluminium hydroxyfluorides combining experimental data and theoretical approach

Damien Dambournet, Alain Demourgues, Christine Labrugère, Alain Tressaud
Institut de Chimie de la Matière Condensée de Bordeaux-CNRS, Université Bordeaux 1. 87, Avenue du Dr. A. Schweitzer, 33608 Pessac cedex, France.
Marco Daturi, Alexandre Vimont, Hervé Leclerc, Jean-Claude Lavalley
Laboratoire Catalyse et Spectrochimie, UMR 6506, CNRS-ENSICAEN-Université de Caen, Boulevard du Maréchal Juin, F-14050 Caen Cedex, France.
Christine L. Bailey, Sanghamitra Mukhopadhyay, Adrian Wander, Nicholas M. Harrison
Computational Science and Engineering Department, STFC, Daresbury Laboratory, Daresbury, Warrington, WA4 4AD, United Kingdom
Department of Chemistry, Imperial College London, London, SW7 2AZ, United Kingdom

1. Introduction

The field of nanoscopic metal fluorides is a growing area of research thanks to the peculiar properties of such compounds. Some of these materials have indeed been shown to have a high Lewis acidity[1,2] comparable to that of the widely used Swarts catalyst based on antimony pentafluoride.[3] High surface area aluminium fluorides may be an attractive alternative in numerous reactions including hydrofluorocarbon production through halogen exchange.[4] In this scope, new routes comprising of plasma fluorination of aluminosilicate[5] or a sol-gel process[1] have been developed leading to X-ray amorphous aluminium fluorides with unreached high surface areas, *i.e.* 200 m^2g^{-1}. Recently, aluminium fluorides with surface areas in excess to 300 m^2g^{-1} have been prepared by optimizing the sol-gel process[6] or by treating the sol-gel fluorides by a microwave solvothermal synthesis.[7] Such a route has also been successfully applied for the preparation of nanosized crystallized aluminium hydroxyfluorides exhibiting the hexagonal tungsten bronze[8] (labelled HTB or β-) and the pyrochlore[9] type

[1] Kemnitz, E.; Groß, U.; Rudiger, S.; Shekar, C. S. *Angew. Chem. Int. Ed.* **2003**, 42, 4251-4254.
[2] Ruediger, S. ; Groß, U. ; Feist, M.; Prescott, H. A. ; Chandra Shekar, S. ; Troyanov S. I.; Kemnitz, E. *J. Mater. Chem.* **2005**, *15*, 588.
[3] Olah, G. A. *J. Org. Chem.* **2005**, *70*, 2413.
[4] Kemnitz, E. and Menz, D. *Prog. Solid State Chem.* **1998**, *26*, 97. Manzer, L and Rao, V. *Science.* **1990**, *249* 1215. Manzer, L and Rao, V. *Advances Catal.* **1993**, *39*, 329. Corbin, D and Rao, V. 2000. U.S. Patent 6,040 486.
[5] Delattre, J. L.; Chupas, P. J.; Grey, C. P.; Stacy, A. M. *J. Am. Chem. Soc.* **2001**, 123, 5364.
[6] Rudiger, S.; Eltanany, G.; Groß, U.; Kemnitz. E. *J Sol-Gel Sci Techn.* **2007**, *41*, 299.
[7] Dambournet, D.; Eltanamy, G.; Vimont, A.; Lavalley, J-C.; Goupil, J-M.; Demourgues, A.; Durand, E.; Majimel, J.; Rudiger, S.; Kemnitz, E.; Winfield, J. M.; Tressaud, A. *Chemistry – A European Journal.* **2008**. DOI: chem.200701831
[8] Dambournet, D.; Demourgues, A.; Martineau, C.; Pechev, S.; Lhoste, J.; Majimel, J.; Vimont, A.; Lavalley, J-C. ; Legein, C.; Buzaré, J-Y.; Fayon, F.; Tressaud, A. *Chem Mater.* **2008**, *20*, 1459.

structures as well as a new hydrate with the ReO_3 structure.[10] By comparison between various Al-based fluorides polymorphs including ill-crystallized, crystallized and hydroxyfluorides phases, it has been shown that the formation of the strongest Lewis acid sites can be directly correlated to the surface area and are therefore size-dependent.[7] Such experimental results are deduced from the adsorption of pyridine as a probe molecule and are in good agreement with molecular dynamics simulations performed on cubic α-AlF_3 nanoparticles, *i.e.* < 3 nm.[11] This latter work has highlighted the fluoride lability and surface reconstructions that occur at such a nano-scale resulting in the formation of strongly under-coordinated species. Nevertheless, the occurrence of four-fold coordinated Al^{3+} ions at the surface of such materials is still questionable. Taking into account the advantage in working with high surface area materials, it is also of great interest to probe in detail the surface structure of aluminium-based fluorides at the atomic scale. In this scope, *Ab initio* calculations have recently been used to model the surface structures of such materials and to rationalise the reactivity of both X-ray amorphous HS-AlF_3 and crystalline AlF_3 materials.[12,13,14] In order to model the material under conditions similar to those that occur during catalytic reactions, the stability of an α-AlF_3 surface has been predicted as a function of H_2O and HF partial pressures and temperatures.[15] It was shown that OH^- groups can substitute surface fluoride ions and water molecules can adsorb at the surface. Purely fluorinated AlF_3 materials are therefore suggested to be extremely hard to obtain under catalytic reaction conditions. High surface area aluminium hydroxyfluorides[8,9] are hence of great interest as their surface appears to be similar to those of AlF_3 materials under working conditions and can be considered as benchmarks for a deeper understanding of more complex materials, such as the X-ray amorphous HS-AlF_3.[1]

The present study will therefore consider two aluminium hydroxyfluorides with the following chemical composition: $AlF_{1.7}(OH)_{1.3}$ and $AlF_{2.6}(OH)_{0.4}$ presenting the pyrochlore and the HTB structure, respectively. Their networks exhibit quite similar arrangements with a one dimensional and a three-dimensional hexagonal tunnel system for the HTB and the

---

[9] Dambournet, D.; Demourgues, A.; Martineau, C.; Durand , E.; Majimel, J.; Vimont, A.; Leclerc, H.; Lavalley, J.-C.; Daturi, M.; Legein, C.; Buzaré, J.-Y.; Fayon, F.; Tressaud, A. *J. Mater. Chem.* **2008**. ASAP Article; DOI: 10.1039/B718856K

[10] Dambournet, D.; Demourgues, A.; Martineau, C.; Durand, E.; Majimel, J.; Legein, C.; Buzaré, J-Y.; Fayon, F.; Daturi, M.; Tressaud, A. *Submitted to J. Am. Chem. Soc*.

[11] Chaudhuri, S.; Chupas, P.; Morgan, B. J.; Madden, P. A.; Grey, C. P. *Phys. Chem. Chem. Phys.* **2006**, *8*, 5045.

[12] Wander, A.; Searle, B. G.; Bailey, C. L.; Harrison, N. M. *J. Phys. Chem. B.* **2005**, *109*, 22935.

[13] Wander, A.; Bailey, C. L.; Searle, B. G.; Mukhopadhyay, S.; Harrison, N. M. *Phys. Chem. Chem. Phys*. **2005**, *7*, 3989.

[14] Wander, A.; Bailey, C. L.; Mukhopadhyay, S.; Searle, B. G.; Harrison, N. M. *J. Mater. Chem.* **2006**, *16*, 1906.

[15] Mukhopadhyay, S.; Bailey, C. L.; Wander, A.; Searle, B. G.; Muryn, C.A.; Schroeder, S. L. M.; Lindsay, R.; Weiher, N.; Harrison, N. M. *Surf Sci*. **2007**, *601*, 4433.

pyrochlore, respectively **(Figure 1)**. Experimental data will be presented and compared with *ab-initio* calculations. Prior to the surface structure investigation, the structural relationships between the bulk framework of the HTB and the pyrochlore structures will be studied, aiming to understand the role of OH groups on the final stabilized structure. The distribution and properties of the OH groups within the bulk material will be considered. The acidic properties of the surface of these materials have been characterised using CO as a probe molecule. Experimental data will be analyzed with the support of *ab inito* calculations of CO adsorbed on the HTB structure. Finally, an attempt to rationalize the reactivity of X-ray amorphous HS-AlF_3 material will be exposed.

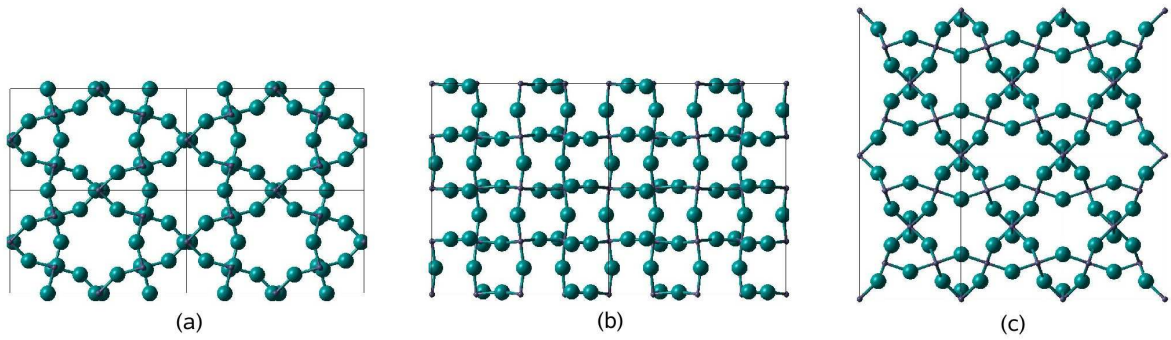

Figure 1. Network of the HTB structure along (a) the c-axis, (b) the a-axis. (c) Structure of the pyrochlore phase.

2. Experimental and computational methods

2.1 Samples preparation and characterizations. Microwave-assisted synthesis has been used to prepare the pyrochlore and the HTB phases. It has been shown that the stabilization of the polymorph was strongly correlated to the R=[HF]/[Al] molar ratio used. The pyrochlore and the HTB type structures were indeed obtained for R = 2 and 3, respectively.[8] The chemical compositions have been determined using the combination of elemental analysis, FTIR and NMR spectroscopies leading to $AlF_{1.7}(OH)_{1.3}$ and $AlF_{2.6}(OH)_{0.4}$ compositions for the pyrochlore and the HTB phase, respectively. The HTB and pyrochlore phases exhibits surface areas of around 80 and 140 $m^2.g^{-1}$ with coherence domains of 15 and 12 nm, respectively.[8,9]

X-ray photoelectron spectroscopy measurements were performed with a VG 220 i-XL ESCALAB with a non-monochromatized Mg source (1253,6 eV) at 100 W. Analysed area was around 200 μm diameter. The insulating character of the powder needed low energy (4-6 eV) electron compensation. Surveys and high resolution spectra were recorded with pass

energy of 150 eV and 20 eV respectively. Quantification was obtained with an Eclipse processing program provided by Vacuum Generators.

FTIR spectroscopy was performed using a Nicolet Nexus apparatus equipped with an extended KBr beam splitter and a mercury cadmium telluride (MCT) detector (resolution: 4 cm^{-1}). Samples were pressed in self-supported discs (2 cm^2, ~ 20 mg) and placed into an infrared quartz cell (KBr windows) connected to a vacuum line. Samples were activated under vacuum at 573 K overnight. After activation, the acidity of the materials was studied by adsorption of CO molecule at low temperature (100 K). In situ fluorination was performed by introducing an equilibrium pressure of CHF_3. After activation at 300°C for 30 minutes, the gaz was removed by vacuum and the surface acidity investigates by CO adsorption.

2.2 Theoretical calculation details. Calculations were performed using the CRYSTAL code[16] and the B3LYP hybrid exchange functional, which has been shown to provide reliable geometric and electronic structures and energetic in a wide range of materials,[17] was used to approximate electronic exchange and correlation. Triple valence local Gaussian basis sets for Al, F were obtained from previous studies.[18]

Geometries for the clean (non hydroxylated) β-AlF_3 bulk and surface structures were taken from previous studies.14,[19] The hydroxylated surfaces were obtained by substitution of F ions for OH ions. Geometry optimization was performed by energy minimization using a damped molecular dynamics algorithm as implemented in CRYSTAL. The atomic positions were allowed to relax in all directions consistent with symmetry. The structures were taken to be converged when the residual forces on all atoms was below $1x10^{-4}$ Hartree per Bohr. CO molecules were adsorbed above the under coordinated Al ions on the HTB AlF_3 surfaces and the structure allowed to relax, as previously described. The vibrational frequencies of the molecules were computed by construction of the force constant matrix via finite differencing of the analytic gradients followed by diagonalization of the resultant dynamical matrix.[20]

[16] Dovesi R, Saunders V, Roetti C, Orlando R, Zicovich-Wilson C, Pascale F, Civalleri B, Doll K, Harrison N, Bush I, D'Arco P and Llunell M 2007 CRYSTAL 2006 Users's Manual (University of Torino)
[17] Muscat, J.; Wander, A.; Harrison, N. *Chem. Phys. Lett.* **2001**, 342, 397.
[18] Basis sets are available from http://www.tcm.phy.cam.ac.uk/ mdt26/crystal.html.
[19] Wander, A.; Bailey, C. L.; Mukhopadhyay, S.; Searle, B. G.; Harrison, N. M. *Accepted in J. Phys. Chem. C.*
[20] Pascale, F.; Zicovich-Wilson, C. M.; Lopez, F.; Civalleri, B.; Orlando, R.; Dovesi, R. J. Comput. Chem. **2004**, *25*, 888.

3. Results and Discussion

3.1 Structural features

3.1.1 Description of the structures

The pyrochlore structure[21] crystallizes in the cubic symmetry (Pm-3m) leading to a random distribution of OH/F anions in the 48f sites. The HTB form[22] crystallizes in an orthorhombic system (Cmcm) with two unequivalent Al atoms and four unequivalent F atoms. The HTB and the pyrochlore type structures can be described by the connection of building units. The pyrochlore can be described through the linkage of three and six membered-rings, the later forming a 3D inter-connected channel system. In the HTB form, anionic crystallographic sites, labelled F3 and F4, enable to connect the planes containing the three- and six-membered rings resulting in a four membered-ring generating the one dimensional hexagonal channel system along the c axis **(Fig 1.b)**. The crystallographic data obtained by Rietveld refinement for both phases are gathered in **Table 1**.

	HTB β-$AlF_{2.6}(OH)_{0.4}$		Pyrochlore $AlF_{1.7}(OH)_{1.3}$
Crystal symmetry Space Group Z	Orthorhombic Cmcm 12		Cubic Fd-3m 16
Unit cell parameters (Å) Volume ($Å^3$)	6.9681(2) 12.0360(3) 7.1434(1) 599		9.7309(1) 921
Interatomic Al-F distances(Å)	Al2-F1 Al1 / Al2 - F2 Al1-F3 Al2-F4	2×1.857(12) 4×1.77(3) / 2×1.82(2) 2×1.789(5) 2×1.804(8)	1.824(1)
Al-F-Al Angles (°)	Al2-F1-Al2 Al1-F2-Al1 Al1-F3-Al1 Al2-F4-Al2	139.4(5) 151.9(11) 173.1(2) 163.8(4)	141.12(6)

Table 1. Crystallographic data of the HTB and the Pyrochlore phases.

[21] Fourquet, J. L. ; Riviere. M. ; Le Bail, A. ; Nygrens, M. *Eur. J. Solid State Inorg. Chem.* **1988**, *25*, 535.
[22] Le Bail, A. ; Jacoboni, C. ; Leblanc, M. ; De Pape, R. ; Duroy, H. ; Fourquet, J.L. *J. Solid State Chem.* **1988**, *77*, 96.

3.1.2 Structural relationships: role of OH groups

As already mentioned, a random distribution of OH^- and F^- ions occurs in the case of the pyrochlore phase, characterized by interatomic distances of 1.824 Å lying within fluorinated and hydroxylated environments. Due to the anisotropic structure displayed by the HTB form, the occurrence of OH groups inside the network impacts clearly on the interatomic distances and angles. Previous investigations have suggested that the F1 and F2 sites are partially hydroxylated, whereas the F3 and F4 sites are fully fluorinated.

In an attempt to confirm the above hypothesis, *ab initio* calculations have been undertaken by replacing all of the same types of fluoride crystallographic sites by OH groups. This substitution can be though in terms of a gas phase H_2O molecule reacting with a crystalline F ion to form a crystalline OH ion and a gas phase HF molecule. The F/OH substitution energy for x substitutions per unit volume (at zero temperature) is equal to the difference in energy of (1) a fully fluorinated slab and x water molecules and (2) a hydroxylated slab and x HF molecules, that is:

$$E(F/OH) = E[AlF_2(OH)_{(s)} + HF_{(g)}] - E[AlF_{3(s)} + H_2O_{(g)}]$$

The energies used in this calculation are the DFT zero temperature energies of the isolated H_2O and HF gas molecules and the periodic solid state calculations of bulk AlF_3 and $AlF_2(OH)$.

Four different hydroxylated compounds were thus considered. These were obtained by replacing successively all fluorides ions present in each F1, F2, F3, F4 crystallographic sites by OH^- ions. The cell parameters and atomic positions were optimised as to minimise the total energy of the system. The energies of substitution of an OH ion for an F ion at each type of crystallographic site are displayed in **Table 2**.

Type of hydroxylation	F1 hydroxylation	F2 hydroxylation	F3 hydroxylation	F4 hydroxylation
Energy (eV)	0.3734	0.4072	0.6729	0.5113

Table 2. Substitution energy per OH for F ion in the four different anionic site of the HTB structure.

These results confirm that hydroxylation will preferentially occurs in F1 and F2 sites, F1 sites being the most stable hydroxylated site. The F1 and F2 hydroxylated bulk conformations are shown in **Figure 2.**

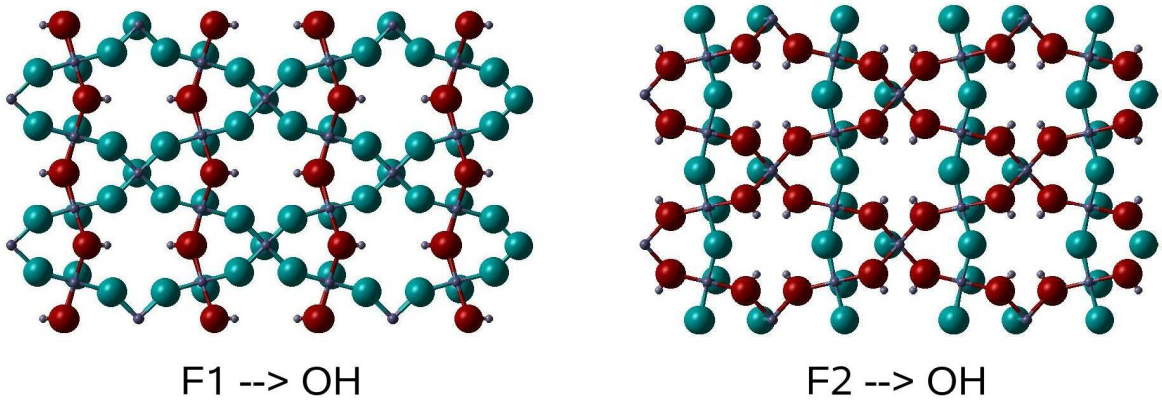

Figure 2. HTB lattice configurations after hydroxylation.

The differences in geometrical structure before and after hydroxylation, based on cell parameters, interatomics distances and angles are summarized in **Table 3.**

	β-AlF_3 (Å) (non hydroxylated)	**F1 hydroxylated (Å)**	**F2 hydroxylated (Å)**
Cell parameters			
a	7.0364	7.0645	7.1728
b	12.1850	12.2572	12.1523
c	7.2614	7.2315	7.1883
Volume	622.6	626.2	626.6
Bond Length			
Al2-F1	1.818	1.867 (Al-O)	1.855
Al2-F2	1.818	1.855	1.861 (Al-O)
Al2-F4	1.815	1.829	1.844
Al1-F2	1.817	1.813	1.893 (Al-O)
Al1-F3	1.815	1.829	1.841
Bond Angle			
Al2-F1/OH1-Al2	150.8 (148.7)	141.2	152.9
Al1-F2/OH2-Al2	150.8 (148.3	157.1	137.2
Al1-F3-Al1	179.7 (166.4)	179.1	178.7
Al2-F4-Al2	179.8 (165.5)	178.9	179.0

Table 3. Optimized crystallographic data of calculated HTB structures with F1 and F2 hydroxylated sites.

It can be seen that the substitution of F ions for OH ions leads to an increase of the interatomic distances at both the hydroxylated site and at the neighboured fluorinated site. Since the multiplicity of F2 (16) sites is higher than that of F1 (8) sites, F2 hydroxylation leads to a greater increase in the interatomic distances. Additionally, the occurrence of OH

groups results in smaller Al-OH-Al angles compared to the Al-F-Al ones. Such a feature was suggested in previous studies.[8,23] The strain induced by the lowering of the hydroxylated site angle is compensated by the increase of the Al-F-Al angle of the nearest anionic site.

The Al-OH-Al angles found in the hydroxylated HTB material are close to those found in the pyrochlore type structure, *i.e.* 141°. The hydroxylation of the HTB type structure is favoured for the anionic sites which form the structural pattern, *i.e.* three- and six-membered rings, found in the pyrochlore. This observation may explain, at least in part, why increasing the OH/F molar ratio in the synthesis process favours the formation of the pyrochlore structure.[8]

The calculated Al2-OH1-Al2 angle (Table 3) is close to the experimental Al2-F1-Al2 angle, confirming the partial hydroxylation. Contrarily, the calculated Al1-OH2-Al1 angle is lower that the experimental one suggesting that this site contains a relatively small amount of OH groups.

3.1.3 Aluminium environments

From a local point of view, both structures consist of corner-sharing $[AlF_{6-x}(OH)_x]$ octahedra. High field ^{27}Al NMR spectroscopy enables the identification and the quantification of such species, leading to a better description of both frameworks. The pyrochlore phase displays $AlF_{6-x}(OH)_x$ species, where x ranges from 0 to 6, whereas in the HTB phase x values range from 2 to 6 because of the occurrence of pure fluorinated F3 and F4 sites.[8,9] The estimated content of the various $AlF_{6-x}(OH)_x$ species is gathered in **Table 4**.

$AlF_{6-x}(OH)_x$ species	Pyrochlore $AlF_{1.7}(OH)_{1.3}$ (%)	HTB β-$AlF_{2.6}(OH)_{0.4}$ (%)
AlF_6	3.3	41
$AlF_5(OH)$	15.2	41
$AlF_4(OH)_2$	29	15
$AlF_3(OH)_3$	29.6	3
$AlF_2(OH)_4$	17	---
$AlF_1(OH)_5$	5.2	---
$Al(OH)_6$	0.7	---

Table 4. The estimated content for the various $AlF_{6-x}(OH)_x$ species in both pyrochlore and HTB phases matching with experimental results from high field ^{27}Al NMR.'

[23] Chupas, P. J.; Corbin, D. R. ; Rao, V. N. M.; Hanson, J. C.; Grey, C. P. *J. Phys. Chem. B.* **2003**, *107*, 8327.

To gain more insight into the description of both phases, X-ray photoelectron spectroscopy has been used to probe the electronic structure of the Al^{3+} ions in particular the nature of the Al-F/OH bonding. Such a technique is sensitive to the perturbation induced by anions in the vicinity of the cation. The presence of strong electronegative anions such as fluoride ions leads to an increase of the Al 2p binding energies.[24] The Al 2p XPS spectra are displayed in **Figure 3** and the data are summarized in **Table 5**.

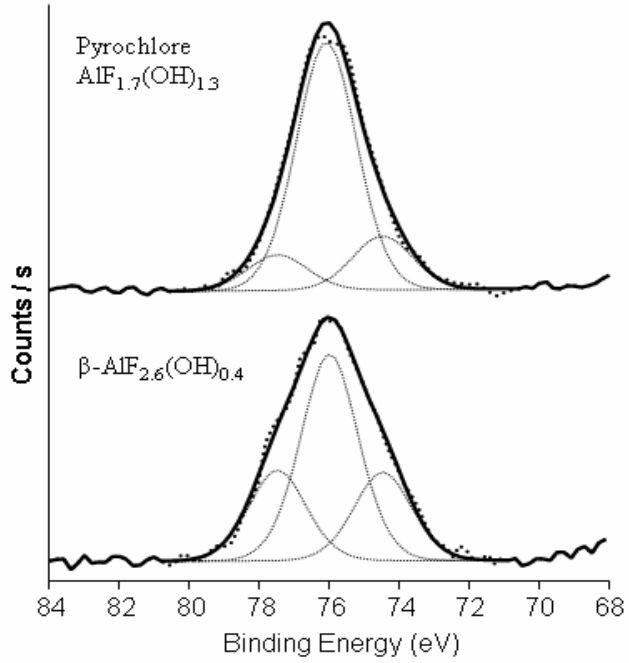

Figure 3. Al2p XPS spectra of the HTB and pyrochlore phases.

Sample	Al2p BE (eV) with corresponding relative intensity FWHM: 2.1eV		
	77.4 eV	76.0 eV	74.4 eV
β-$AlF_{2.6}(OH)_{0.4}$	24%	54%	22%
Pyrochlore $AlF_{1.7}(OH)_{1..3}$	10.5%	73.5%	16%

Table 5. Al2p XPS data of the HTB and the pyrochlore phases. The values show relative shift to lower binding energies as the Al ion is hydroxylated.

[24] Böse, O.; Kemnitz, E.; Lippitz, A.; Unger, W.E.S. *Fresenius J Anal Chel.* **1997**, 358, 175.

The Al 2p XPS spectra of both phases can be fitted into three components at 77.4, 76 and 74.4 eV. Those components can be aligned to each other with 0.1eV as a standard deviation. It should be noted that three components have also been detected for the F1s BE occurring at 686.8, 685.7 and 684.7 eV (±0.2). It appears that the electronic density around Al^{3+} ions is more homogeneous in the pyrochlore that in the HTB phase. The electronic state heterogeneity of Al^{3+} ions in the HTB phase can be rationalized regarding the large range of interatomic distances, as revealed by the Rietveld refinement (Table 1), distances lying between 1.78 and 1.85 Å. Such a disparity is assigned to the occurrence of hydroxylated sites, *i.e.* F1 and F2 sites, which are assumed to induce an electronic state heterogeneity around the Al^{3+} ions. Since a statistic OH/F distribution occurs in the pyrochlore phase, the resulting Al^{3+} ions electronic state is characteristic of a mixed F/OH anionic environment. This leads to complementary information regarding X-ray diffraction which gives average interatomic distances due to the cubic symmetry. These results also show the flexibility of the HTB-type structure regarding the heterogeneity of the Al^{3+} electronic density state.

3.2 Stable surfaces and crystal morphology

The relative energies of the (100), (010) and (001) surfaces of HTB AlF_3 have been recently calculated using the CRYSTAL code. These energies have been used, along with the approximation that the crystal has $P6_322$ symmetry, and the use of the Wulff plot[25] to predict the equilibrium crystal morphology of an HTB crystallite.19 This leads a prediction that 59% of the {010} surfaces, 42% of the {001} surfaces and 3% of the {100} surfaces will be exposed. This result is consistent with the experimental observation confirming the low stability of the (100) surface. Information on the microstructure of the solid has been obtained from an X-ray line broadening analysis which has enabled an accurate calculation of the micro-strains ($\Delta d/d$) and the coherence domains.[26] Such an analysis has been performed on both the HTB and pyrochlore phases highlighting X-ray line broadening effects arising from coherence domains and micro-strains. It has been revealed that the pyrochlore possesses an isotropic crystallite shape whereas the HTB crystallites present a platelet shape with the short dimension along the a-axis[8,9] confirming the *ab initio* calculations. Such a model clearly indicated that the (100) surface exhibits the lowest stability.

[25] Wulff, G. Z. *Kristallogr.* **1901**, *34*, 449.
[26] Line Broadening Analysis Using Fullprof: Determination of Microstructural Properties. Rodriguez-Carvajal, J; Roisnel, T. EPDIC8 Uppsala. 2002.

The predicted structures of the (100) and (010) surfaces, within a (1x1) cell, are shown in **Figure 4.a**. and b respectively. The (100) surface, which is not thermodynamically stable, consists of alternate six-fold and five-fold coordinated Al^{3+} ions in which the five-fold coordinated Al^{3+} ions are bound to 5 bidentate ("bridging") F ions and the 6 fold Al^{3+} ions are bound to an additional monodentate ("dangling") F ion. The (010) surface which is predicted to dominate on HTB crystallites, consists of five-fold coordinated Al^{3+}.

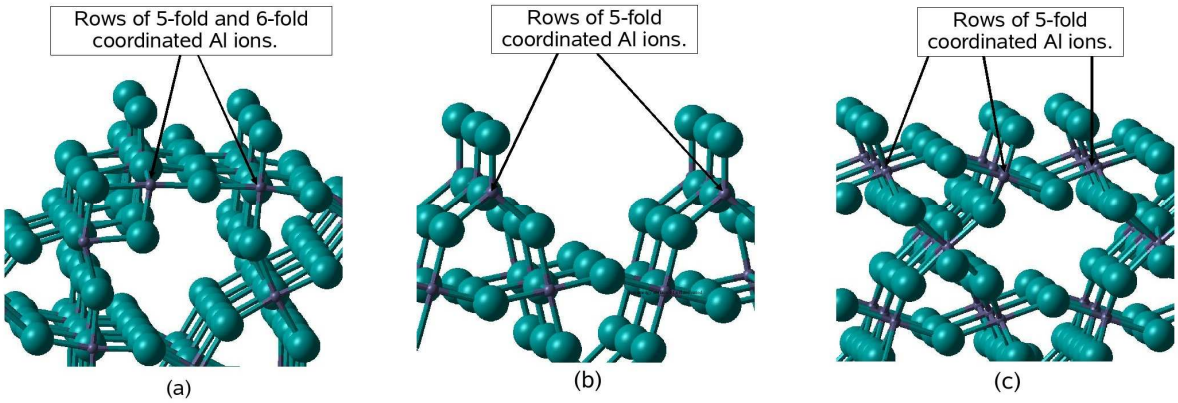

Figure 4. (a) The HTB AlF_3 (100) surface. (b) The HTB AlF_3 (010). (c) The Pyrochlore AlF_3 (001) surface.

For comparison, the surface structure of a pure fluorinated pyrochlore (100) surface has also been predicted **(Figure 4.b)**. The Al ions at the surface of the pyrochlore are all coordinated to 4 bidentate F ions and one monodentate F ion, as occurs at the (010) HTB surface. It has been shown previously that this type of Al binding at the surface is energetically favoured at AlF_3 surfaces.[24] Interestingly, the predicted AlF_3 pyrochlore (100) surface exhibits only five-fold coordinated Al^{3+} ions.

Previous studies of NH_3 adsorption[27] have shown that the Al ions that are bound to 5 bidentate F ions display the strongest Lewis acidity. We therefore probe both these types of sites and those that occur on the dominate surface.

[27] Bailey, C.; Mukhopadhyay, S.; Wander, A.; Searle, B.; Harrison, N. M. 2008 in preparation.

3.3 Acidic properties through CO adsorption

3.3.1 Experimental data

The acidic properties have been studied by adsorption of carbon monoxide at low temperature (~100K). FTIR spectroscopy is used to detect the interaction between CO and the surface. CO is considered as an ideal spectroscopic probe molecule due to it weak basic character. In this way, the inductive effect of CO is limited and it allows the discrimination of the nature and the strength of the acidic sites.

Several regions can be distinguished according to the shift observed on the stretching mode of CO in the gas phase (ν(CO)=2143 cm^{-1}): (i) bands at ν(CO)<2150 cm^{-1} are ascribed to physisorbed species, (ii) bands between 2150-2180 cm^{-1} characteristic of Brønsted acid site or weak Lewis acid sites and (iii) bands at ν(CO)>2180 cm^{-1} characteristic of Lewis acid sites, the higher the wavenumber, the stronger the Lewis acidity. Normalized IR spectra of saturated CO adsorbed at the surface of the pyrochlore and the HTB phases are displayed in **Figure 5.**

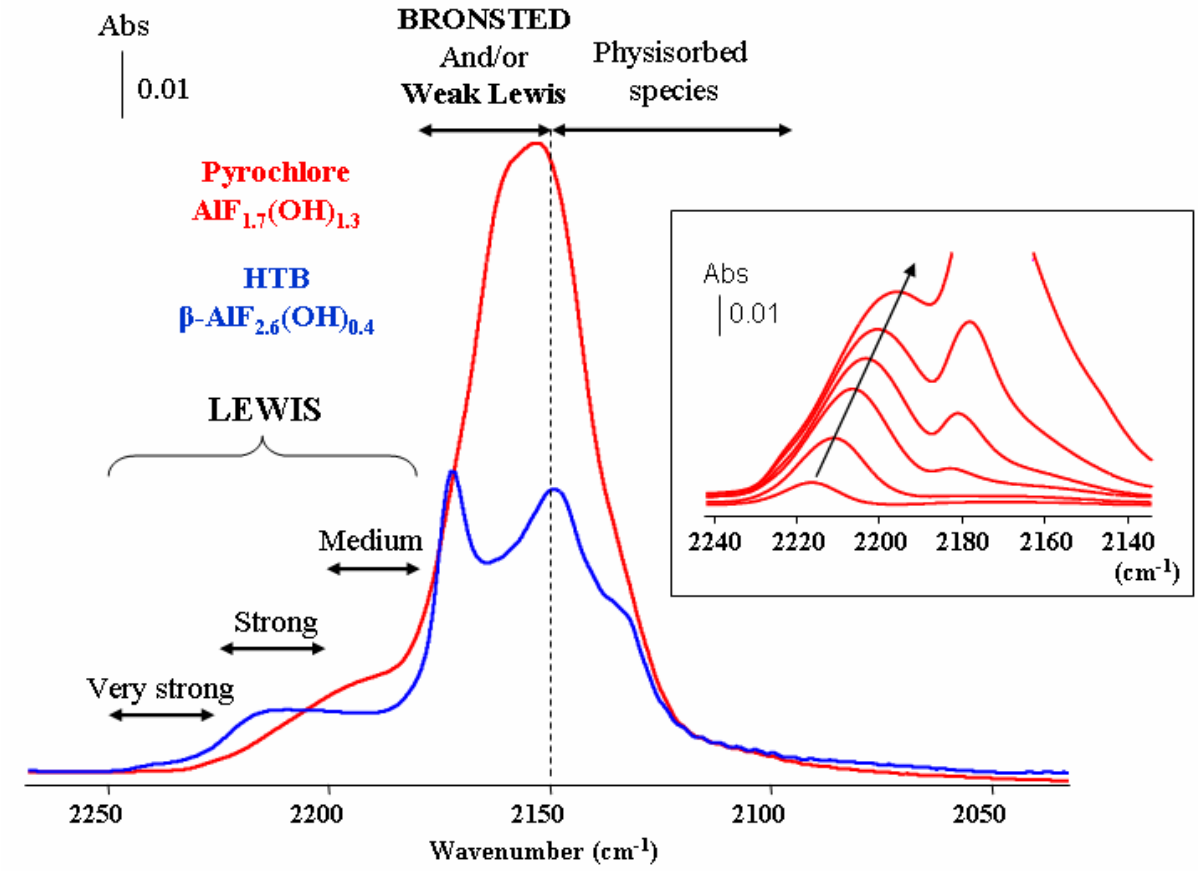

Figure 5. Comparison between normalized IR spectra of adsorbed CO on HTB and pyrochlore phases. IR spectra are recorded after activation at 573 K and an introduction of an equilibrium pressure of CO (266 Pa). Inset: successive addition of small CO doses on the pyrochlore surface.

A previous study[28] related to CO adsorption on the HTB surface has revealed a large heterogeneity of Lewis acid sites with the occurrence of five distinct sites lying in a large range of frequency. Contrarily, the Lewis acidity displayed by the pyrochlore surface occurs in a narrow frequency range. This is well evidenced when CO is adsorbed using successive additions of small amounts as shown in the Inset of the Figure 5. For low CO coverage, a weak band centred at around 2215-2220 cm^{-1} is detected. Going to higher CO doses, a broad band starts to appear at 2215 cm^{-1} and shifts downward to 2195 cm^{-1} for increasing CO doses. After saturation, in addition to the broad band centred around 2195 cm-1, a shoulder is detected at around 2220 cm^{-1}. As for the Lewis acidity, the Brønsted behaviour of both phases differs drastically. While the HTB surface displays one homogenous Brønsted site characterized by a band at 2173 cm^{-1}, the Brønsted behaviour of the pyrochlore is heterogeneous with CO frequency lying between 2181 and 2165 cm^{-1}. Such heterogeneity is in part due to remaining water molecules which act as a strong Brønsted acid site.[29] Structural OH groups generate weak Brønsted acidity with ν(CO) band lying from 2171 to 2165 cm^{-1}. **Table 6** summarizes the various acidic sites displayed by both phases.

Compound	ν(CO) (cm^{-1}) *(Δν(CO))*	
	Lewis acidity	Brønsted acidity
HTB	Site A : 2235 *(92)* Site B: 2220-2215 *(77-72)* Site C: 2200 *(57)* Site D: 2183 *(40)* Site F: 2166 *(23)*	Site E: 2173 *(30)*
Pyrochlore	2215-2195 *(72-52)* *Shoulder 2215-2220*	2165-2181 *(OH groups: 28-22)*

Table 6. Characterization of ν(CO) adsorbed on the HTB and the pyrochlore surfaces.

Aiming to understand the various acidic behaviours display by both phases, in situ fluorination using CHF_3 has been performed prior to CO adsorption. The use of a fluorinating agent allows the conversion of the accessible Al-OH bonds into Al-F bonds and therefore

[28] Dambournet, D.; Leclerc, H.; Vimont, A.; Lavalley, J-C.; Nickkho-Amiry, M.; Winfield, J. M.; Daturi, M.; Tressaud, A.; Demourgues, A. *Submitted to Phys. Chem. Chem. Phys.*
[29] Daturi, M. *In preparation.*

enables getting some information on the impact of the anionic environment on the acidity. **Figure 6** displays the IR spectra of adsorbed CO on the pyrochlore and HTB phases with and without in situ fluorination.

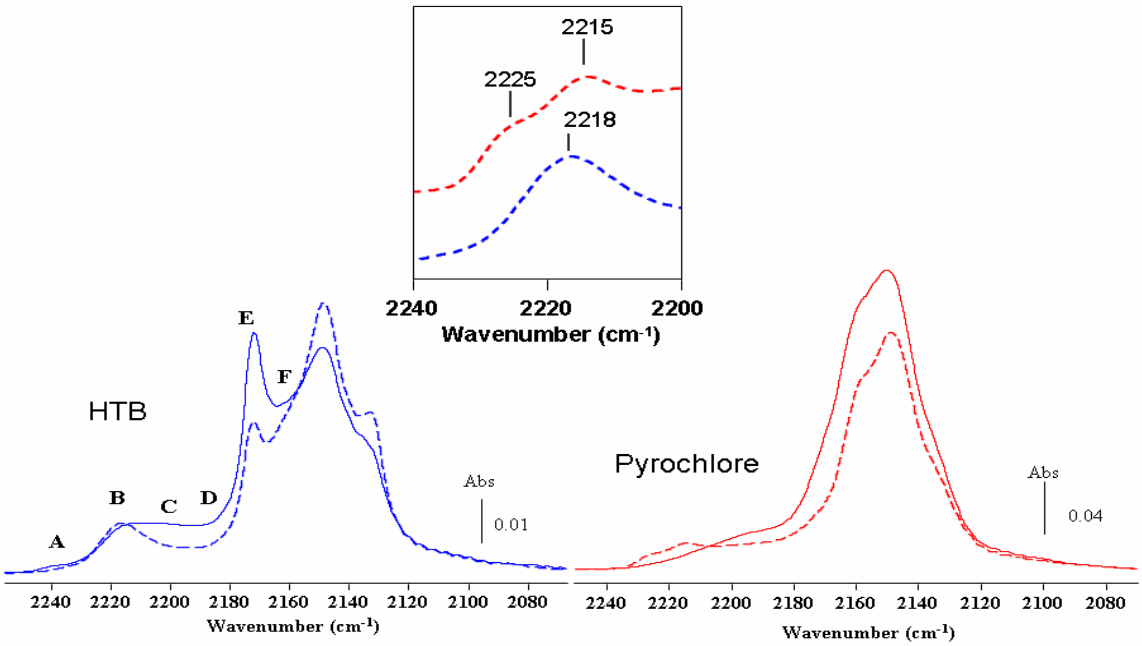

Figure 6. Effect of in situ post-fluorination using CHF_3 on the pyrochlore and HTB surface acidities. IR spectra recorded after activation at 573 K and an introduction of an equilibrium pressure of CO (266 Pa) without (full line) and with (dotted line) CHF_3 treatment. Insert: CO adsorption on strong Lewis acid sites.

In general, a decrease in the Brønsted contribution is observed as well as the conversion of weak/medium Lewis acid sites into strong ones. It should be noted that the extension coefficient varies according to the wavenumber of the ν(CO) band. The area of the converted bands is therefore not completely retransmitted. In the case of the HTB surface, the very weak site A surprisingly disappears upon fluorination. The intensities of the Lewis acid sites labelled C, D and F decrease whereas the site B intensity increases and shifts slightly towards a higher wavenumber. The decrease in intensity of the sites C, D and F after fluorination suggests that these sites are surrounded by a mixed anionic environment OH/F. On the contrary the site B is stable upon fluorination suggesting a pure fluorinated site. Concerning the pyrochlore phase, in situ post-fluorination led to the appearance of two strong Lewis acid sites located at 2215 and 2225 cm^{-1} on going with the weakening of the broad band initially detected at around 2195 cm^{-1}.

3.3.2 Ab initio calculations and assignments

In order to better understand how the strength of a Lewis site depends on it as local geometry and the hydroxylation of neighbouring anionic sites, a*b intio* calculations were performed on the HTB AlF_3 (100) and (010) clean and hydroxylated surfaces. The CO stretching frequency was calculated after adsorption on (100) and (010) surface sites labelled as $AlF_{5-x}(OH)_x$ site where x lies between 0 to 5. The local geometry of the sites at which CO was adsorbed above are shown in **Figure 7** and each of the neighbouring F ions has been labelled.

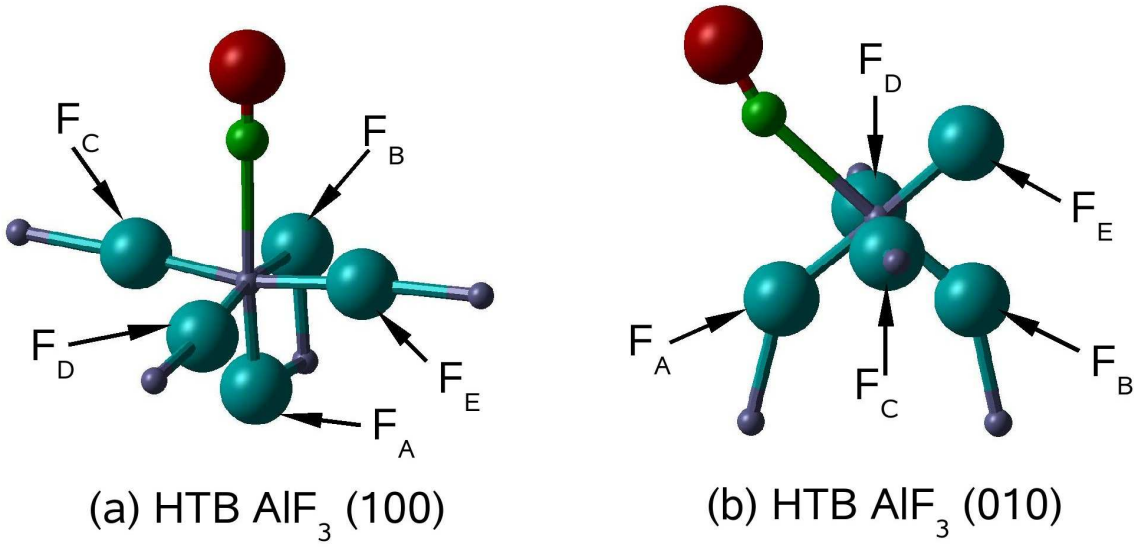

Figure 7. The local structure of the non hydroxylated surface sites on (a) the (100) surface and (b) the (010) surface. after adsorption of CO. Full surface calculations were performed; these pictures just show the local structure of the adsorption site.

The effect of substituting the F ions for OH ions in several different combinations was considered. The resultant shifts in the CO stretch frequencies are displayed in Table 6. The resultant local geometries after adsorption of CO at a selection of these sites are shown in **Figure 8**.

The calculated CO stretching frequency in the gas phase was 2220 cm^{-1} as compared to 2143 cm^{-1} as found experimentally; this is in-line with previous calculations at this level of theory.[30] The shifts in the CO stretching frequency have therefore been scaled by 0.965 (2143/2220) to take into account the discrepancy of the CO stretch frequency between experiment and theory. The resultant calculated CO shifts obtained after adsorption on the various sites are shown in **Table 7**.

[30] http://srdata.nist.gov/cccbdb/

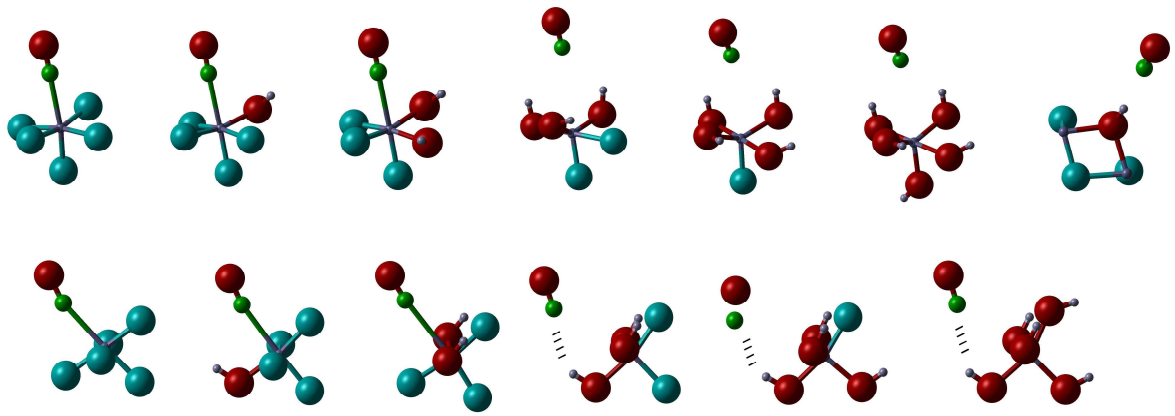

Figure 8. The local structure of the surface sites after adsorption of CO. The top row shows structures of the sites on the (100) surface while the bottom rows shows structures that occur on the (010) surface. Full surface calculations were performed; these pictures just show the local structure of the adsorption site.

The largest shift occurs for CO adsorbed to an AlF_5 site on the metastable (100) surface, a shift of 94 cm^{-1} is predicted, this type of site has hence been assigned to the peak that is observed at the A site (Figure 6). Experimentally, only a low concentration of this type of site was observed, this is in agreement with the experimental observation and *ab initio* prediction that only a small amount of the (100) surface is exposed on HTB crystallites. Furthermore, it has previously been shown that it is energetically favourable for this surface microfacet to the (010) surface. The fluorination process being exothermic, this should favour the surface reconstruction and may explain the disappearance of the A site.

The calculated CO shift for adsorption to the non hydroxylated site on the (010) surface is 75 cm^{-1}. This type of site can hence be assigned to the peak that occurs at the B site since the later was prove to be insensitive to the fluorination process. Additionally, the number of B sites is far greater than A sites in agreement with the HTB crystallite morphology.

On both the (100) and (010) surfaces, substitution of the F ions for OH ions in the vicinity of the AlF_5 motifs results in a reduction in the CO stretch frequencies in agreement with experimental results.

An interesting point is that the position of the substituted OH group in $AlF_{5-x}(OH)_x$ species impacts on the Lewis strength (Table 7). As observed in the bulk, when an F ion is substituted for an OH ion the resultant Al-OH-Al angle is always smaller than the equivalent Al-F-Al angle. If the Al-F-Al angle is small (*i.e.* the F_A and F_B ions) then the change in the angle after OH substitution is relatively small and the change in the CO shift is correspondingly small. This shift in the CO frequency is assigned to the observed peak at site C for Al sites on the

(010) surface and to site B for Al sites on the (100) surface (only a low intensity of (100) sites is predicted).

100	Al environment	Substituted F ions	shift in ν(CO) (cm^{-1})
a	AlF_5	-	94
b	AlF_5	nearby OH dangling	77
c	$AlF_4(OH)$	F_A	88
d	$AlF_4(OH)$	F_B	79
e	$AlF_4(OH)$	F_C	65
f	$AlF_3(OH)_2$	F_B, F_C	66
g	$AlF_2(OH)_3$	F_B, F_C, F_D	17
h	$AlF_1(OH)_4$	F_B, F_C, F_D, F_E	21
i	$Al(OH)_5$	F_A, F_B, F_C, F_D, F_E	13
j	Brønsted	F_B	24
010			
k	AlF_5	-	75
l	$AlF_4(OH)$	F_A	64
m	$AlF_4(OH)$	F_B	68
n	$AlF_4(OH)$	F_C	59
o	$AlF_4(OH)$	F_E	42
p	$AlF_3(OH)_2$	F_C, F_D	24
q	$AlF_3(OH)_2$	F_A, F_C	42
r	$AlF_3(OH)_2$	F_A, F_B	60
s	$AlF_3(OH)_2$	F_A, F_E	28
t	$AlF_3(OH)_2$	F_B, F_C	52
u	$AlF_3(OH)_2$	F_B, F_E	35
v	$AlF_3(OH)_2$	F_C, F_E	36
w	$AlF_2(OH)_3$	F_A, F_B, F_C	29
x	$AlF_2(OH)_3$	F_A, F_B, F_E	27
y	$AlF_2(OH)_3$	F_A, F_C, F_D	21
z	$AlF_2(OH)_3$	F_C, F_D, F_E	4
aa	$AlF(OH)_4$	F_A, F_B, F_C, F_D	20
bb	$AlF(OH)_4$	F_A, F_C, F_D, F_E	7
cc	$Al(OH)_5$	F_A, F_B, F_C, F_D, F_E	9

Table 7. Shifts in CO frequency, referring to the gas phase, for adsorption onto an Al^{3+} ion bound to 5 bidentate F ions.

If the Al-F-Al angle is close to 180^o (i.e. at the F_C and F_D ions on both surfaces and the F_E ion on the (100) surface) then the change in the angle is much greater, leading to a greater distortion of the surface, consequently the decrease in the CO shift is much greater and can be assigned to the observed peak at site D for Al sites on the (010) surface. If more than one of

these F ions is replaced by an OH group then the distortion induced at the surface is large enough such that the CO will preferentially bind via one or more OH ions (*i.e.* at a Brønsted site) if they are available, this type of adsorption is assigned to the peak at site E. On the (010) surface such a Brønsted site may not be available if the OH ions preferentially hydrogen bond to the nearby monodentate F or OH ions (structures *p and w* in Table 6). Consequently, the CO binds very weakly to the Al ion, this type of site is assigned to the peak that occurs at site F. On the (010) surface, if the monodentate F ion (F_E) is replaced with an OH ion the CO stretch frequency is much reduced. It is thought that this is caused by changes that occur in the electrostatic field in the vicinity of the CO molecule as a result of this OH substitution.
In the course of understanding the acidic behaviour of both phases, previous results obtained from high field ^{27}Al NMR could be take into account. Even if this technique belong to the bulk, it can be assumed that the identified $AlF_{6-x}(OH)_x$ species (Table 4) can be present at the surface in an under-coordinated state. While all $AlF_{5-x}(OH)_x$ species can be predicted to occur on the pyrochlore surface, it can be assumed that the HTB one contains only AlF_5, $AlF_4(OH)$, $AlF_3(OH)_2$, $AlF_2(OH)_3$ type species. Additionally, the contribution of the metastable surface (100) has been prove to be very weak and hence except for the A site, the assignments of the various sites can be assumed to arise from the (010) surface. An attempt of CO assignment of the HTB phase is shown in the **Table 8**.

Site label and shift (cm^{-1})	Al environment
A(92)	AlF_5 (100) surface
B(77-72)	AlF_5
	$AlF_4(OH)$ (F_{B-})
C(57)	$AlF_4(OH)$: F_A, F_C
	$AlF_3(OH)_2$: F_A+F_B, F_B+F_C
D(40)	$AlF_4(OH)$: $F_{E,}$
	$AlF_3(OH)_2$: F_a+F_C, F_B+F_E, F_C+F_E
F(23)	$AlF_3(OH)_2$: F_C+F_D
E(30) Brønsted	$AlF_3(OH)_2$: F_A, F_E

Table 8. Assignment of the various CO stretching frequency

The above assignments of the CO shift frequency made according to *ab intio* data is in agreement with the assumption that the identified $AlF_{6-x}(OH)_x$ species can be present at the surface in an under-coordinated state.

At this level, it appears clearly that the Lewis heterogeneity exhibits by the HTB phase is due to (i) the various surface structure which can occur on a crystallite and characterized by different acidic strength and (ii) the anionic heterogeneity.

Although calculations have not been performed for the pyrochlore surface our analysis of the HTB surface enables an interpretation of the pyrochlore adsorption spectra (Figure 6). The local structure of the pyrochlore surface is predicted to be similar to the (010) surface and due to its cubic symmetry, the surface structure is isotropic. The occurrence of only one type of surface structure is confirmed by the absence of the CO shift at 92 cm^{-1} that occurs on the HTB structure characterizing the metastable (100) surface. The feature that contrasts with the HTB phase is the apparent Lewis strength "homogeneity" characterized by a broad band centred at 52 cm^{-1} with the occurrence of a shoulder at around 77 cm^{-1}. The broadness feature of the band is ascribed to the anionic heterogeneity. The shoulder observed at 77 cm^{-1} is indicative of the occurrence of some few AlF_5 Lewis acid sites. The Lewis acidic behaviour of the pyrochlore is dominated by the CO shift that occur at around 52 cm^{-1} and can be related to $AlF_4(OH)$ and $AlF_3(OH)_2$ sites. Such assignments are in full agreement with XPS and NMR data which have evidenced mostly the occurrence of mixed F/OH species. Contrarily to the HTB phase, the pyrochlore contains some richly hydroxyl species, *i.e.* $AlF_2(OH)_4$, $AlF(OH)_5$. These types of species should act as Brønsted sites.

3.3.3 Interpretation of the reactivity of the solid acid HS-AlF_3

The solid acid X-ray amorphous HS-AlF_3 has been recently studied using CO adsorption.[31] It has been evidenced that the HS-AlF_3 surface mostly contains strong Lewis acid sites characterized by an intense and broad ν(CO) band occurring at around 2220 cm^{-1} ($\Delta\nu(CO)\sim77cm^{-1}$) after CO saturation. Such sites are similar to the site B found in the HTB β-$AlF_{2.6}(OH)_{0.4}$ ascribed to the AlF_5 site that occur on the (010) surface as shown in Figure 6b. Additionally, using small CO doses, some few very strong Lewis acid sites have been detected at a CO shift occurring at around 90 cm^{-1}. It has previously been suggested that such sites consist of a four-fold coordinated Al^{3+} ions, *i.e.* AlF_4.31 In this study we suggest that such a site can be assigned to the AlF_5 site found in the metastable (100) surface in which the Al ion is bound to 5 bidentate ions, as shown in Figure 6a. The above assignments enable the understanding of the reactivity as well as the mapping of the HS-AlF_3 surface.

[31] Krahl, T.; Vimont, A.; Eltanamy, G.; Daturi, M.; Kemnitz, E. *J. Phys. Chem. C.* **2007**, 111(49), 18317.

The surface structure of the X-ray amorphous HS-AlF_3 resembles those found on the HTB. It contains both the (100) and (010) surface-type structure. The main difference between both compounds is the relative contribution of the (100) surface-type over the whole surface contribution. The high surface area, low crystallite size and the amorphous feature of HS-AlF_3 enables the stabilization and a greater surface contribution of the metastable and highly Lewis acidic (100) surface. Finally, it may be that reactions that are catalysed by HS-AlF_3, but not HTB AlF_3 require a high concentration of the sites that occur on the (100) type-surface. Furthermore, if such sites occur adjacent to one another this may result in an inductive effect or enable larger molecules to bind via multiple adsorption sites.

Conclusion

The present work has compared two hydroxyfluorides exhibiting the HTB and the pyrochlore type structure using experimental and *ab initio* data. The stabilization of either phase has been related to the Al-X-Al angle (X=F, OH). Hydroxyl groups tend to form small angles leading to the stabilization of three- and six-membered rings building the pyrochlore type structure. In the case of the HTB phase, the hydroxylation preferentially occurs in the same structural pattern constituting the pyrochlore phase highlighting the structural effect of the hydroxylation. While the aluminium electronic density of the pyrochlore phase appears homogenous and characterized by a mixed F/OH environment, those of the HTB appear heterogeneous with hydroxylated, mixed F/OH and fluorinated environments due to preferential hydroxylation and anisotropic structure.

The prediction of the morphology of an HTB crystallite matched with experimental results from X-ray line broadening analysis and HRTEM. Such results have evidenced that the HTB surface exposed mainly the (010) type surface and that the (100) surface is metastable and weakly exposed. The prediction of the surface structure of a purely fluorinated pyrochlore revealed a structure similar of those found on the (010) HTB type surface.

The acidity of the surface Lewis sites have been characterised from experimental and theoretical CO adsorption studies. This has led to the identification of the local structure of very strong Lewis acid sites on the metastable (100) surface. Understanding the structure of these active sites may enable real perspectives for the selection of fluoride-based catalysts. The next challenge will be to move toward high surface area materials with the development of shape selective synthesis to improve the contribution of such metastable and Lewis acidic (100) type surfaces. Another possibility is the synthesis of more anisotropic structures such as κ-AlF_3 in order to stabilize new surface structures.